

Spring 2015

Photoassociative Spectroscopy of Ultracold Argon and Krypton Confined in a Magneto Optical Trap

Maha Khaled Omar
Old Dominion University

Follow this and additional works at: https://digitalcommons.odu.edu/physics_etds



Part of the [Atomic, Molecular and Optical Physics Commons](#)

Recommended Citation

Omar, Maha K.. "Photoassociative Spectroscopy of Ultracold Argon and Krypton Confined in a Magneto Optical Trap" (2015). Doctor of Philosophy (PhD), dissertation, Physics, Old Dominion University, DOI: 10.25777/a743-4154
https://digitalcommons.odu.edu/physics_etds/113

This Dissertation is brought to you for free and open access by the Physics at ODU Digital Commons. It has been accepted for inclusion in Physics Theses & Dissertations by an authorized administrator of ODU Digital Commons. For more information, please contact digitalcommons@odu.edu.

PHOTOASSOCIATIVE SPECTROSCOPY OF
ULTRACOLD ARGON AND KRYPTON CONFINED IN
A MAGNETO OPTICAL TRAP

by

Maha Khaled Omar
B.S. 2006, Tanta University, Egypt
M.S. 2012, Old Dominion University


A Dissertation Submitted to the Faculty of
Old Dominion University in Partial Fulfillment of the
Requirements for the Degree of

DOCTOR OF PHILOSOPHY

PHYSICS

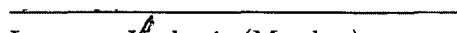
OLD DOMINION UNIVERSITY
May 2015

Approved by:


Charles I. Sukenik (Director)


Gail E. Dodge (Member)


Jozef Dudek (Member)


Leposava Juskovjc (Member)


Richard Gregory (Member)

ABSTRACT

PHOTOASSOCIATIVE SPECTROSCOPY OF ULTRACOLD ARGON AND KRYPTON CONFINED IN A MAGNETO OPTICAL TRAP

Maha Khaled Omar
Old Dominion University, 2015
Director: Dr. Charles I. Sukenik

Creating ultracold molecules has attracted considerable interest in the last decade. Once created, such molecules can be used for precision spectroscopy or to study chemical reactions at ultracold temperatures. Several techniques have been developed to produce ultracold molecules; the most common is photoassociation where two ultracold atoms collide in the presence of light that induces a free-bound transition to an excited molecular state. Photoassociation can also be used to perform spectroscopy in order to map out the ro-vibrational levels of a molecular state. In this dissertation, we report on our Photoassociative Spectroscopy (PAS) studies conducted separately in argon and krypton. For each species, we have studied transitions near two different atomic limits $ns[3/2]_2 \rightarrow np[5/2]_2$ and $ns[3/2]_2 \rightarrow np[5/2]_3$ where $n = 4$ for argon and $n = 5$ for krypton. The former atomic transition is called the “quench transition” since it forms a strong coupled channel to the ground state. As a result for this strong coupling the original atomic sample is degraded and quenched. The latter transition is the one used to cool and confine the atoms and is known as the “trapping transition.” Spectroscopy near the trapping transition in argon was studied previously in our group [1] and specific features were observed in the spectrum. At the time, the features were not definitively identified, but more than one explanation was suggested for further testing. One possible explanation was that these features were a result of resonances happening at “doubly-excited” molecular levels. The population of such states could take place as a result of absorbing two photons of the same frequency which causes photoassociation. In this dissertation we report on a series of experiments that were performed to study and conclusively identify the origin of those features. These experiments led to the conclusion that the features in the spectra were an artifact of otherwise undetectable frequency sidebands on our semiconductor diode laser. Once identified as such, a new laser was constructed to

repeat the spectroscopy measurements in argon and take new measurements in krypton that would be free from laser artifacts. In those spectra, no specific vibrational features were observed and resolved in either species. Results were consistent with published results obtained by other groups using other noble gases. Finally, we report on our attempts to perform PAS on a quench transition in order to confirm results obtained for krypton by another group [2]. We were not able to observe any photoassociation signal for both argon and krypton on this transition. We were able to observe similar effects to those reported in Ref. [2] but we attribute these to artifacts from an acousto-optic modulator and not as arising from molecular structure.

Copyright, 2015, by Maha Khaled Omar, All Rights Reserved.

ACKNOWLEDGMENTS

I would like to start by thanking God for giving me the strength and patience to accomplish this work. It took me almost six years to finish this work and I thank God for helping me to get this far. This can only lead me to realize how patient Dr. Sukenik was as a great advisor and mentor. I would like to thank Dr. Sukenik for all his help during my research and more importantly for giving me a great and wonderful experience to work on this experiment. Working on it was very rewarding and a great learning experience and although most of the time it was also very frustrating, I really do believe that I can only learn from my failure and I am very grateful to him for that. While writing this dissertation, I realized after reading all my lab notes that there was one person that was standing by me for most of the lab work and he indeed taught me a lot about both experiment and theory. To him, I am very thankful for all his efforts and patience that allowed me to bring the experiment to where it is today. That is why I would like to thank Will Williams (our now ex-postdoc) for every thing he taught me. I would never have been here without him. I would like also to thank all my group members whether they have moved on or are still working on their PhD research. Those are Gambhir Ranjit, Eman Ahmed, Aye Lu Win, Jack Mills and Grady White. Thanks for all of their help and for forming a nice environment to work in. I also would like to thank all my committee members. Dr. Gail Dodge, Dr. Josef Dudek, Dr. Leposava Vuskovic and Dr. Richard Gregory. They are indeed a great role model for me and I feel such an amazing honor to have them on my committee. As for my family, I really think that today there only two people who could be even more proud of what I have accomplished so far than me. I think the best gift I can give my parents now is this PhD dissertation. I could not have been here without their support and help in addition of course to my sister. I also would like to thank my family and especially my son, Yaseen, for giving me the time and the quiet environment to finish the work. Last but not least I would like to thank all the friends that I have made during my graduate school years: Delicia Malin, Annette Guzman-Smith, Jan Drake, Donika Plyku, Dasuni Adikaram, Suba DeSilva, Milka Nikolic, Rocio Olave and Ana Samolov, and others. They all made the Physics Department such a warm and loving second home to me.

TABLE OF CONTENTS

	Page
LIST OF TABLES	viii
LIST OF FIGURES	xviii
 Chapter	
1. INTRODUCTION	1
1.1 PREVIOUS WORK INVOLVING PHOTOASSOCIATION SPEC- TROSCOPY OF NOBLE GASES	2
1.2 OVERVIEW OF THIS DISSERTATION	7
2. THEORETICAL OVERVIEW	9
2.1 LASER COOLING AND TRAPPING OF THE ATOMS	9
2.2 DOPPLER LIMIT AND SUB-DOPPLER COOLING	24
2.3 THE MAGNETO OPTICAL TRAP (MOT)	27
2.4 ATOMIC STRUCTURE	32
2.5 MOLECULAR STRUCTURE	34
2.6 MOLECULAR WAVE-FUNCTIONS	36
2.7 FRANK-CONDON THEORY	45
2.8 COLD MOLECULAR PRODUCTION	51
2.9 THE LEROY-BERNSTEIN FORMULA	54
2.10 ION PRODUCTION IN THE MOT	58
2.11 PHOTOASSOCIATION SPECTRA	61
3. EXPERIMENTAL SETUP	65
3.1 THE ATOMIC BEAM	67
3.2 MAGNETIC FIELDS AROUND THE MOT	75
3.3 THE LASER SOURCES	77
3.4 DATA COLLECTION / DETECTION TABLE	113
4. RESULTS AND DISCUSSION	122
4.1 EXPERIMENT 1: TWO COLORS PA EXPERIMENT IN ARGON .	123
4.2 EXPERIMENT 2: INVESTIGATING THE FEATURES ON THE ARGON PA SPECTRUM	138
4.3 EXPERIMENT 3: CORRECTED PA SPECTRUM FOR BOTH AR- GON AND KRYPTON	152
4.4 EXPERIMENT 4: STUDY OF PURELY LONG RANGE STATES FOR BOTH ARGON AND KRYPTON	158
5. CONCLUSION AND PROSPECTS FOR THE FUTURE	168

BIBLIOGRAPHY 169

VITA 176

LIST OF TABLES

Table	Page
1. This table illustrates every noble gas element with photoassociation spectroscopy published data and a summary of references to the papers of the published data. For helium and krypton the second set of references are for experiments performed around the quench transition.....	3
2. This table illustrates the different settings for both argon and krypton for Zeeman slower magnetic field coils.....	74
3. This table illustrates the AOM circuits part numbers and settings used in our experiment. The two different frequency settings for both the slower and trap AOMs are for argon/krypton respectively.	86
4. This table illustrates the different frequency values used for different PA experiments.	99

LIST OF FIGURES

Figure	Page
1. The graph to the left shows the data from Ref [3] for the PA experiment in xenon. It shows no resolved vibrational features. It is in agreement with our PA scans for low intensity. The graph to the right shows the neon PA scans from Ref [4]. β is the density-dependent loss rate due to collisions between trapped atoms. The data shown do not resolve any vibrational features.	4
2. The graph to the left shows the data from Ref [5] for the PA experiment in krypton. It shows no resolved vibrational features. The graph to the right shows the data from Ref [2] for the PA experiment in krypton around the quench transition. It shows one resolved vibrational feature around -160 MHz.	5
3. The data shown for argon PA in Ref. [1] used a diode laser as the PA laser. The graph to the left is for longer scans (up to 10 GHz) at higher PA intensities. The right graph is for shorter scans (~ 1.5 GHz) and at lower PA intensities.	5
4. The left graph shows the data from the helium PA experiment Ref [6] and three vibrational series of states is shown on the top. It is also important to note that the part from -10 GHz to -3.5 GHz is a scan of laser intensity $1.2 * 10^5 I_{sat}$ and the part from -3.5 GHz to 0 GHz is a scan of laser intensity $7.5 * 10^4 I_{sat}$. The graph on the right shows data for long range states [7]. The graph shows the vibration sub-level at $\nu = 4$ in the molecular potential 0_u^+ . The curves show a) the peak optical density, b) the number of atoms and c) a Lorentzian fit of the temperature of the atoms in the MOT cloud after the PA action and then giving the atomic cloud time to expand.	7
5. Spontaneous emission following absorption occurs in random directions, but absorption from a light beam occurs along only from one direction. . .	16
6. The magnetic field inside the Zeeman slower. The figure on the left (a) is the single polarity design, while the figure on the right (b) shows the the design incorporating both positive and negative magnetic fields. The latter design is the one used in our experiment.	22
7. The six counter propagating beams set up for the optical molasses technique of cooling down a cloud of atoms.	24

8.	The effect of red detuned beams on an atom in the atomic cloud. For the right side the atom is at rest so there is no Doppler shift in the resonance energy that the atom can see. For the left side graph with the atom in motion there is a Doppler shift to the incident light that the atom sees. . .	25
9.	The graph shows how two circularly polarized counterpropagating beams of opposite polarization direction (σ^+ and σ^-) combine to form linearly polarized light [8].	28
10.	The graph shows the set up for the Magneto-Optical Trap (MOT). It shows the two anti-Helmholtz coils with a cross section of the shape of the magnetic field. It also shows the orientation of the six counter-propagating circularly polarized laser beams.	29
11.	The graph shows the effect of the magnetic field on a simplified two level atom in one of the three dimensions. This is of course applicable in the other two dimensions. The transition takes place between $J = 0$ to $J = 1$. The direction of the magnetic field is shown with the energy shifts of the atomic levels resulting from the application of this magnetic field.	31
12.	Argon atomic structure. This structure only includes atomic transitions that were studied during our experiments.	33
13.	Krypton atomic structure. This structure only includes atomic transitions that were studied during our experiments.	35
14.	The green dashed curve represents the harmonic oscillator potential. The black curve represents the diatomic potential curve. The red wave-functions represent the probability distribution of the electrons in each vibrational state. The blue dashed wave-functions represent the probability distribution for a classical oscillator which is confined inside the potential well [9]. The probabilities are shown for $\nu = 1, 2, 3$	45
15.	The electronic transitions between the vibrational levels in different molecular potentials. The figure illustrates the Frank-Condon Principle. Transitions from $\nu = 1$ sub-states are more likely to start from the middle of the potential well. Transitions to other higher vibrational levels are more likely to happen around turning points.	47
16.	Digram of the long range interaction potential between two atoms as a function in the internuclear separation for different atomic energy level limits.	50

17. The upper curves represent the diatomic potential curves for Kr around the asymptotes $5s(3/2)_2+5p(5/2)_2$ and $5s(3/2)_2+5p(5/2)_3$, for $\Omega = 0, 1, 2$. The asymptote $5s(3/2)_2 + 5p(5/2)_2$ is taken as the zero energy for the curves [10]. The lower curves represent the diatomic potential curves for Ar [11] around the asymptote $4s(3/2)_2 + 4p(5/2)_2$ and the asymptote $4s(3/2)_2 + 4p(5/2)_3$, for $\Omega = 0, 1, 2$ 51
18. Current techniques for producing cold molecules. The values for temperature and density are provided from experimental data taken with every single technique[12]. 53
19. The graph shows the ions created in the MOT during collisions between metastable state atoms. The Penning (PI) and the Associative ionization (AI) processes are shown. 59
20. The figure shows the photoassociative ion production. The probability of ions being created depends on the frequency of the incident photons. The blue line is used for blue detuned beams and the red line is used for the red detuned beam. The orange line is for on resonance beams. The dashed lines are for photon absorption transitions and the straight lines are for non-radiative ion production. 62
21. An outline for the science/MOT table with the different stages that the atomic beam goes through. 67
22. An outline for the rf discharge circuit with all of the components explained in detail in the text. 70
23. The figure to the left shows the outline of the discharge tube components. The right figure shows the actual set up in the lab. 71
24. Pictures for different steps of mounting the rf quartz tube. The top left picture is the torr seal picture which is currently used. The top right one is the quick flange connector that did not sustain as low pressure as we needed. The bottom left one is the shape of the tube after mounting the rf coil around it. The bottom right picture is the rf tube in its final setup after connection with the T-shaped connector to the two gas lines. 73
25. This figure is taken from the dissertation of H. Busch [13]. It includes the measurements that he did while building the magnetic field assembly and the velocity of the atoms leaving the Zeeman slower. 76
26. The graph to the left shows the magnetic field coils added to our science chamber. The graph to the right shows the theoretical magnetic field as a function of the distance from the center of the chamber in the X , Y and Z direction. Note that $\frac{dB_x}{dx} = \frac{dB_y}{dy} = \frac{1}{2} \frac{dB_z}{dz}$ to satisfy Maxwell equations [14]. 76

27.	The External Cavity Diode Laser (ECDL) configurations. The left figure is for Littrow configuration while the right figure is for Littman-Metcalf configuration.	79
28.	Geometry of a tapered semiconductor amplifier chip [15].	80
29.	The schematic diagram of the laser path in the Ti:S head	82
30.	This figure shows the optics layout used in creating our MOT lasers. The lasers from the master is given by the green line. The lasers from the first slave or the Zeeman slower laser is given by the blue line. The beams from the second slave or the trap laser is given by the red line which becomes orange after the second AOM. The beams from the AOM are divided into zeroth order (dashed lines) and first order (straight lines). The APP symbol is short for Anamorphic Prism Pair. ISO is short for optical isolator. AOM is short for Acousto-Optical Modulator.	84
31.	This diagram shows a typical circuit used to control the AOM. The 15 Volts voltage divider is home built. VCO stands for the voltage controlled oscillator that generates an rf signal that can be monitored through the AUX output. The switch is an rf switch used to turn the first order on and off using a TTL signal. The rf signal is amplified and fed into the AOM where it generate rf wave through changing the crystal's refractive index and hence the direction of the output beam.	86
32.	A photograph from our set up for the two ECDL cavities used as our PA laser sources. The figure on the left is for the Littrow / short ECDL cavity with cavity length ~ 2.8 cm. The figure on the right is for the Littman-Metcalf / Long ECDL cavity with a cavity length of ~ 8.5 cm. . .	89
33.	The PA laser layout for both cavities. The figure also illustrates the dual operation between the two lasers so that the switch between the two is almost instantaneous compared to the stability time of the MOT.	92
34.	A circuit diagram showing the modifications made to the lock box to enable the feed forward feature. The output of this modification is added as a modulation on the current controller.	92
35.	A layout of the optics used for the Titanium Sapphire monitoring and PA alignment. As shown in the next section the output from this PA will be combined with another beam. It goes through a switching AOM for further launching to the science chamber.	93

36. A layout of the tapered amplifier output for 1) beam diagnostics. That includes both the spectrum analyzer or the wavemeter. The same fiber was coupled for either one. 2) The second part of the output was sent to beat lock technique to enable a continuous scan of the PA laser over the whole range. 3) The third part is coupled into the PA fiber that delivers the PA light to the science chamber PA port. 95
37. The optics layout for the reference laser. The “fake” Zeeman slower feature was added for further testing that will be explained later in the next chapter. The reflected polarization from the PBS is sent to the beat lock. This produces the beat frequency required for our beat lock. The dashed line is the zeroth order of the AOM. It is important to note that the frequency and the sign of the “picked” first order were changed along our experiment to cover more frequency range. 98
38. The optics layout for the saturation absorption signal for both the MOT master laser and the reference laser. The graph shows a three dimensional set up. The green beam from the MOT master laser is in the X/Y plane and the red beam from the reference laser is in the Y/Z plane. 100
39. The graph to the left shows a block diagram of our lock circuit. The graph to the right shows the theoretical output of the saturation absorption cell “red” and the error signal used to lock the lasers “green”. 101
40. A graph for our saturation absorption output signal used in the lab is shown in red. The error signal used in locking the laser is in green. The blue ramp signal is the signal fed in the piezo to scan the laser across the resonance. 103
41. A schematic diagram of the beat lock. The part in the dashed rectangle is the second stage divider. The beat lock can work for small ranges ~ 1 GHz without the second stage. For higher frequency ranges ~ 4 GHz the second stage is added to further divide the beat frequency to be within our electronics range. The dashed green line between the laser and the fiber launcher indicates going through optics. The beam goes through optics into the tapered amplifier and then further optics until eventually the PA and reference laser beams are combined on the fiber launcher. 105

42. This figure shows the layout of the optics delivering the laser beams necessary for our experiment. The green line is meant for the Zeeman slower beam. The black straight line is for the trap beam used alternatively between Ar and Kr. The dashed line is meant for the dual operation between Ar/Kr. The red beam represents the PA beam. It is also important to note that the ports are numbered and each port is described in detail in the text. It is also important to mention that there is another dimension that is not included in the graph as PBS 2 splits the trap beams between the x-y plane and the vertical z-direction. 109
43. The figure to the left shows the third dimension in the figure 42. The Z-direction is distinguished from the X-Y plane beams by giving it a different color (orange versus black). The figure to the right shows the accurate measurements of the PA beam diameter along its path. 110
44. The top image is a photo of the channeltron configuration that is used in our set up. This was used by G. Ranjit in his thesis. The photo is from his thesis [16]. The bottom image shows the ion detector's connections. . . 115
45. A schematic diagram of the timing scheme of our experiment. It is important to note that no specific duration values were assigned because we changed them between different experiments. We will give details of the specific values for each separate experiment later. It is also important to note that the repetition of these cycles is what creates the data point that we see on our graphs by adding the data collected from all cycles. 119
46. The output from our frequency calibration instrumentation. The output on the left is from the 300 MHz spectrum analyzer as shown in black. On the same graph a sine wave fit from which the position of the maxima and minima are determined and a difference of 150 MHz frequency step is found. This fit has a root mean square error of 0.0027. On the right, the output from the photo-detector to the saturation absorption with a Gaussian fit is shown. From this fit, the zero point in frequency is determined. This fit has a root mean square error of 0.1425. 125
47. A basic two color photoassociation ion counts signal. The blue signal is for only a MOT PA sent to the MOT and parked at -160 MHz and at 650 μ W. Since the laser is not scanning it is a straight line. The green line is for the Ti:Sapphire PA laser scanning for \sim 4 GHz at 1 mW. The red line is the combined ion signal when the two PA beams are sent to the MOT at the same time. The deviation of the ion counts is \pm 100. The x-axis represents the frequency detuning from resonance. 126

48. The graphs show the effect of changing the MOT PA power by using different Ti:Sapphire PA powers. The MOT PA detuning is -160 MHz. From the top, the Ti:Sapphire powers are 0.5, 1, 1.5 mW respectively. . . . 127
49. The graphs show the effect changing the MOT PA power at different detuning. The Ti:Sapphire power is 1 mW. From the top, the MOT PA detuning goes as +50, +75, +100 MHz. 128
50. The graphs show the effect of the detuning on the spectrum. The Ti:Sapphire power is 1 mW. From the top, the MOT PA power goes as 650, 800, 20, 6 μ W respectively. Only when MOT PA detuning was +125 MHz, the MOT PA power was 100 μ W. 129
51. The graphs show the features dependence on the MOT density. The MOT density was changed by changing the Zeeman slower beam power. The Ti:Sapphire power is 1 mW. From the top, the MOT PA detuning goes as +50, +75, +100 MHz respectively. From the top, the MOT PA power goes as 20, 20, 30 μ W respectively. 130
52. A schematic for the two PA beams before being combined at the MOT site. It is important to note that we used the red path for the Ti:Sapphire PA and the green path for the MOT PA. To exclude the alignment dependence, the two beams were combined before the fiber and sent through the red path where they were perfectly overlapped. 134
53. The graphs show features dependence on the PA beams polarization. From the top, the Ti:Sapphire power (mW)/ MOT PA detuning (MHz)/ MOT PA power (μ W) combinations are (1.2/+50/27), (1/+100/varying), (1.3/-212/660) respectively. For the second graph, both the orientations for the retroreflection polarization are shown. 136
54. The graphs show the dependence of the -3.4 GHz feature on the MOT density. The MOT density was changed by changing the MOT trap laser beams detuning. The graphs were taken at PA beam power of 80 mW. With a beam waist of 90 μ W. This is an intensity of $4.9 \times 10^5 I_{sat}$ and with retro reflection included $I=9.75 \times 10^5 I_{sat}$. The different colors for each detuning represent different scans that were taken to guarantee reproducibility and exclude artifacts from any discharge pressure fluctuation. 140
55. The graph shows scan from the Ti:Sapphire laser source. The graph was taken at PA beam power of 30 mW. The x-axis is the red frequency detuning from resonance. Zero frequency detuning is at resonance. 141
56. The graphs show the bandwidth measurements for both the Ti:Sapphie laser and the diode laser. The measurement shows that the diode lasers have higher bandwidth than the Ti:Sapphire laser. 142

57. The first graph shows the check of the scan of the Ti:Sapphire alone (~ 30 mW) against the scan from the Ti:Sapphire combined with the laser of the unseeded tapered amplifier (3 mW). It is apparent that the only effect of the tapered amplifier laser is to deplete the MOT atoms at every frequency. The second graph shows the difference between scans made using (L-ECDL) and (LM-ECDL). Both of the two scans were done using a 100 mW of PA power. Different colors on every curve correspond to different scans to assure the reproducibility of these features. 145
58. The graphs show the effect of adding artificial sidebands on the laser in (L-ECDL) versus no sidebands. The blue is for no sidebands where one dip appear at ~ 5 GHz. The red is for adding sidebands at 2.6 GHz where three dips appeared at (~ 2.6 GHz, 5 GHz, 5.8 GHz). The green is for adding sidebands at 3.1 GHz where three dips appeared at (~ 3.1 GHz, 5 GHz, 7 GHz). 146
59. The graphs show the different tests made on the 170 MHz dip feature. The first graph tested the ECDL cavity effect (Littman-Metcalf versus Littrow). The second graph tested the AOM scattering effect (AOM frequencies 64 MHz and 84 MHz). The third graph tested the rf signal broadcast effect from the rf discharge cell (153 MHz and 145 MHz). Different colors show different scans to guarantee reproducibility of the data. 147
60. The graph is used to show the effect of changing the Zeeman slower laser beam detuning on the dip. When the laser beam detuning changes from 162.5 MHz to 148.0 MHz, the dip position is displaced by the same amount. 148
61. The graphs show the effect of adding a new laser beam that is always on to resemble the effect of the Zeeman slower laser beam. The "fake" Zeeman beam was set at two different frequencies of -140 MHz for the first graph and at -125 MHz for the second graph. The first graph shows a broadening of the 160 MHz dip which is due to having two dips at -160 MHz and -140 MHz combined together, but not resolved. The second graph shows two separate dips at -160 MHz and -125 MHz. The second graph also shows the angular effect of having the fake Zeeman slower beam at 90° angle to the true Zeeman slower versus having it collinear with the PA laser beam. 149
62. The graph shows the polarization dependence of the 160 MHz feature. The polarization of the PA beam was changed between linear and circular and no change in the feature was observed. 150

63. The graphs show the photoassociation spectrum for argon for higher power limit (top graph) and low power limit (bottom graph). Each single graph is labeled by its own intensity expressed in terms of saturation intensity (1.44 mW/cm^2). The top graph has frequency range between $\sim -5 \text{ GHz}$ and $\sim +1.5 \text{ GHz}$. The bottom graph has frequency limits between -1.5 GHz and $+0.5 \text{ GHz}$ 155
64. The graphs show the photoassociation spectrum for krypton for higher power limit (top graph) and low power limit (bottom graph). Each single graph is labeled by its own intensity expressed in terms of saturation intensity (1.36 mW/cm^2). The top graph has frequency range between $\sim -5 \text{ GHz}$ and $\sim +1.5 \text{ GHz}$. The bottom graph has frequency limits between -1.5 GHz and $+0.5 \text{ GHz}$ 156
65. These scans are using a timing scheme where the trap is turned off for $17 \mu\text{s}$ and the PA is turned on for $5 \mu\text{s}$. The delay between when the trap turns off and the PA turns on was changed between $12 \mu\text{s}$ and $2 \mu\text{s}$. In the graph, the dashed lines are for the PA signal and the solid curves are for the MOT background signal. 159
66. The graphs show the effect of having a different timing schemes on the PA signal. The dashed lines are almost straight to resemble the PA signal detected. The MOT background signals which are the solid curves show that the MOT recovery time is affected by the PA frequency. Those scans were taken at power of $120 \mu\text{W}$ which corresponds to $5 \times 10^3 I_{sat}$ in intensity terms. It is also important to note that they were taken with no mechanical shutter added. The main difference between the two graphs is in the delay of reading the MOT background counts. 160
67. Those graphs show the effect of the 0^{th} order of the AOM on the MOT background signal. The graph shows the dashed lines as the PA signal which is still a straight line. It also shows the MOT background signal when the AOM is on and off and when the light is blocked. Those scans were taken at PA power of $120 \mu\text{W}$ which corresponds to $5 \times 10^3 I_{sat}$ in intensity terms. 162
68. This graph shows the Multichannel Scaler for both $ns[3/2]_2 \rightarrow np[5/2]_3$ for argon and krypton (red and green respectively) against $ns[3/2]_2 \rightarrow np[5/2]_2$ for argon and krypton (dashed blue and dashed yellow respectively). The timing scheme is trap off at bin 20 and on at bin 60. PA is on at bin 30 and off at bin 50. 163

69. The graphs show the Multichannel scaler signal as observed in the $4s[3/2]_2 \rightarrow 4p[5/2]_3$ trapping transition for argon. It is a relation between the bin number and the ion counts. The trap beams were turned off at bin 20 and back on at bin 60. The PA was turned on at bin 30. For the top graph the duration of the PA on time was changed. For the bottom graph the PA was turned off at bin 50. For all of these graphs the bin width was $10.24 \mu\text{s}$ and it was allowed to add for 32,767 records. . 165
70. The graphs show the Multichannel scaler signal for argon. The top graph was taken for focused beam so the beam waist was $90 \mu\text{m}$ and the bottom graph is for unfocused beam so the beam waist was 1.1 mm. The power is shown on the graph as well as the PA frequency detuning while taking the graph. The timing scheme is trap off at bin 20 and on at bin 60. PA on at bin 30 and off at bin 50. 166
71. The graphs show the Multichannel scaler signal for krypton. The top graph was taken for focused beam so the beam waist was $90 \mu\text{m}$ and the bottom graph is for unfocused beam so the beam waist was 1.1 mm. The power is shown on the graph as well as the PA frequency detuning while taking the graph. The timing scheme is trap off at bin 20 and on at bin 60. PA on at bin 30 and off at bin 50. 167

CHAPTER 1

INTRODUCTION

Studying ultracold molecules has been attracting increasing interest for more than a decade. Being ultracold (< 1 mK) enables the exclusion of the effects of the Doppler broadening which is important for precision spectroscopy. In the ultracold regime, the molecules are not moving with high speeds. Consequently, they are also much easier to control during chemical interactions or even collisional and scattering processes. Observing these interactions and studying their dynamics gives us very good insight about the quantum systems and quantum interactions. Trapping ultracold samples employing forces derived by light scattering requires having cycling transitions which many atoms have. On the other hand such transitions are not as accessible in molecules as in atoms. A number of techniques, however, have been developed to produce cold and ultracold molecules. Some techniques begin with warm molecules and cool them down. However, other techniques start with cold atoms and combine these cold atoms into a cold molecule. The latter technique has been the most widely applied to date. For the production of diatomic molecules, the process involves using one or more photons to excite pairs of free atoms into a bound, excited molecular state. This excited molecular state can later decay to a bound, ground state molecule. Because this mechanism uses a photon to assemble the molecule, it is known as “photo-association” (PA).

In the research reported here, we have performed photoassociative spectroscopy using noble gases (argon and krypton). We start from ultracold ^{40}Ar or ^{84}Kr atoms in a magneto-optical trap (MOT). We then scan a photoassociative spectroscopy laser and observe ion production as a measure of the production of excited, bound molecular states. The PA laser was scanned by changing the detuning of the laser around two different frequencies. Each of these two frequencies corresponds to an atomic resonance transition in the elements (Ar and Kr). The PA laser intensities were also varied in order to produce a power map of photoassociation spectrum. Our studies focus primarily on spectra obtained near the “trapping transition” used to cool and confine the atoms. We also will report on studies near a second nearby transition, known as a “quench transition”. We have found that as we scan the PA

laser we get a very wide peak corresponding to the excitation of many closely spaced molecular vibrational levels. Our experiments did not, however, resolve individual vibrational levels, consistent with results from other groups as discussed below.

1.1 PREVIOUS WORK INVOLVING PHOTOASSOCIATION SPECTROSCOPY OF NOBLE GASES

Photoassociation Spectroscopy has mainly been performed on ultracold alkali atoms [17, 18, 19, 20, 21, 22, 23, 24, 25, 26, 27, 28, 29, 30, 31, 32, 33, 34, 35, 36, 37, 38, 39, 40, 41, 42, 43]. Most of these experiments report seeing some vibrational features on their photoassociation spectrum [23, 24]. The features are normally attributed to the vibrational sub structures on the diatomic molecular potential wells. Experiments were performed on lithium [25, 26], on sodium [27, 28, 29, 30, 31, 32, 33], on potassium [34, 35, 36], on cesium [37, 38, 39, 40] and on rubidium [41, 42, 43]. Similar, but far fewer experiments have been conducted in the noble gas elements. A major difference between alkali-based and noble gases experiments is that for the noble gases atoms originally are in a metastable state. For alkali atoms the transitions from ground states can be driven by commercially inexpensive lasers. On the other hand, noble gases require a huge amount of energy to drive such transitions from ground states. That is why noble gas atoms are usually pumped to a higher metastable state from which, transitions can be driven by our laser sources. Those metastable states are higher excited states of relatively long lifetime (60 s for Ar and 85 s for Kr). The long lifetime is enough for us to perform our experiments without having to deal with excitation from ground states. This crucial difference between the two types of experiments creates a complication in our detection methods. In noble gases, the atoms are cooled and as a result they have very small translational energy, however they start the experiment in higher excited states. That is why the probability of ion production is higher in noble gases even in the absence of any photon absorption. Because the two atoms already start off in high states, the exchange of their energy during collisions is enough to produce an ion. This in turn creates a high background ion signal on our detectors that has to be carefully accounted for. The PA spectra obtained in the noble gas experiments were always able to show population to excited molecular potentials. The problem with those spectra is that they were never able to resolve between vibrational sublevels in the molecular potentials. This is a true observation for most noble gas experiments except for helium. This is in agreement

TABLE 1: This table illustrates every noble gas element with photoassociation spectroscopy published data and a summary of references to the papers of the published data. For helium and krypton the second set of references are for experiments performed around the quench transition.

Element	References	Notes
He	[6],[44]	Photoassociation spectroscopy on trap transitions and vibrational features reported
	[7]	Photoassociation spectroscopy on quench transitions and vibrational features reported missing
Ne	[4],[45],[46]	Photoassociation spectroscopy around trapping transition and no vibrational features reported
Ar	[1]	Photoassociation spectroscopy around trapping transitions and some non real features were reported
Kr	[5]	Photoassociation done around trapping transitions and no features were reported
	[2]	Photoassociation done around quench transition and some features were reported
Xe	[3],[47]	Photoassociation spectroscopy around the trapping transitions and no vibrational features reported

with our data that we show here since we were not able to resolve any vibrational structures in our PA spectra. Some noble experiments performed on Ar and Kr claim detecting some of these levels and we will compare our data with them later in the thesis.

To better explain the noble gas PA spectra, we will start by explaining a summary of the findings for every noble gas element. We will describe the discrepancies between our experiment and the reported experiment and how our data either agree or disagree. We will start with xenon. Refs [3, 47] were mainly focused on studying the shielding effects and the antisymmetry in the ion production between the red and the blue side. The red side of the spectrum is when the laser frequency is less than the resonance frequency. The blue side of the spectrum is when the frequency is higher than resonance. Optical shielding happens as a result of absorbing a blue photon that drives the two atoms apart thus shielding their interaction. Although the study of the vibrational structures on the spectrum was not the main focus of these papers, all the published spectra show similar features to the ones produced

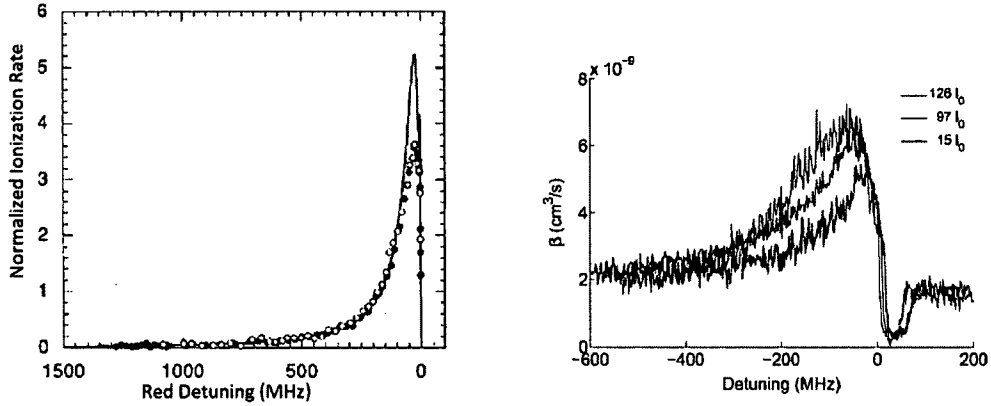


FIG. 1: The graph to the left shows the data from Ref [3] for the PA experiment in xenon. It shows no resolved vibrational features. It is in agreement with our PA scans for low intensity. The graph to the right shows the neon PA scans from Ref [4]. β is the density-dependent loss rate due to collisions between trapped atoms. The data shown do not resolve any vibrational features.

by our experiment. The spectrum that they report in their data as shown in Fig. 1, shows antisymmetry between red and the blue laser detuning as they scan the frequency of the PA laser. In their experiment, they call it the control laser. It is also important to note that their spectra does not extend as far in frequency as the work we report.

Second we will show the PA spectra for krypton. Two photoassociative spectroscopy experiments were done. One looked at photoassociation around the trapping transition [5] and the other investigated the quench transition [2]. The study in Ref[5] mainly focused on the antisymmetry between the red and the blue part of the spectrum. Their spectrum is shown in Fig. 2 with no recorded resolved vibrational structures. On the other hand, a detailed theoretical and experimental study of molecular vibrational structures around the quench transition was introduced in Ref [2]. The paper reports vibrational features around -160 MHz with respect to the quench resonance transition. Our experiment showed similar effect on our spectrum, although our features were not real vibrational features. We will show our results when we present our experimental data in section 4.4.

The photoassociation spectroscopy around the trapping transition for argon was

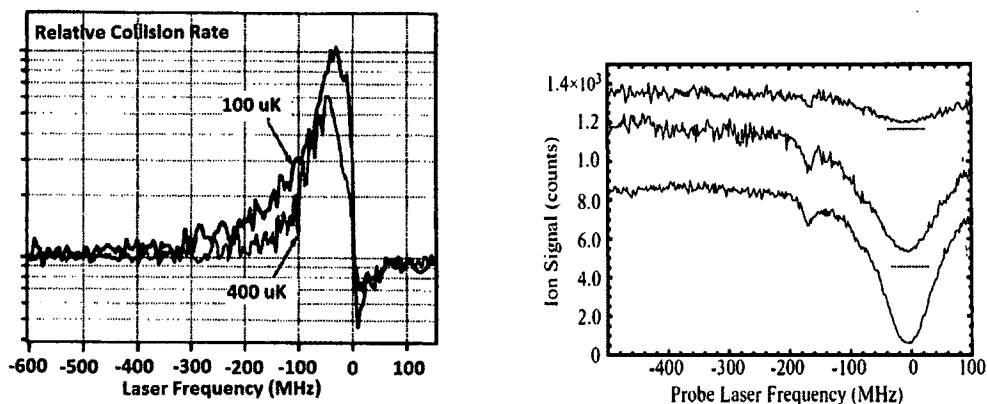


FIG. 2: The graph to the left shows the data from Ref [5] for the PA experiment in krypton. It shows no resolved vibrational features. The graph to the right shows the data from Ref [2] for the PA experiment in krypton around the quench transition. It shows one resolved vibrational feature around -160 MHz.

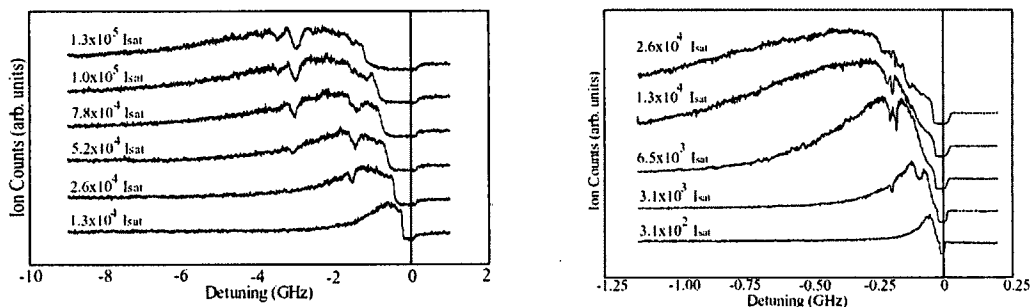


FIG. 3: The data shown for argon PA in Ref. [1] used a diode laser as the PA laser. The graph to the left is for longer scans (up to 10 GHz) at higher PA intensities. The right graph is for shorter scans (~ 1.5 GHz) and at lower PA intensities

studied by Shaffer [1] on the same apparatus that we used in this thesis work. Features reported in his experiments as possible vibrational resonance on the molecular spectrum are shown in Fig. 3. Part of this dissertation is a detailed follow-on study of the original features observed in [1] to identify their origin. Careful investigation of such features confirms that they were artifacts of the spectroscopy laser system. After building a new laser system and excluding the artifacts we were able to take additional argon spectra that does not show any resolved vibrational structures.

The PA experiments in neon [4, 45, 46] have a very similar set up to our experiment and were aimed to look for any vibrational features on the neon molecular potentials. Figure 1 shows no vibrational resonances in those spectra. The main difference between our system and the system reported in Ref [4, 45, 46] is that we were able to apply higher spectroscopy laser intensity. Our data agree with the neon spectra. We both obtain the same spectrum shape with no resolved vibrational features.

The PA experiments for helium were done on both the trapping transitions and other transitions looking at long range states. The long range states are molecular potential minima that take place at large internuclear distances. In other words, if molecules were to exist in those states, there will be an attraction force between the two atoms although the distance between them is very large $\sim 30a_0$, where a_0 is the Bohr radius. The first PA experiment done in Ref [44] did not resolve any vibrational features. On the other hand, the helium PA experiment shown in Ref [6] was able to show some vibrational features on their PA spectrum. The vibrational structures associated with three groups were observed as shown in Fig. 4 using the ion detection technique. In Ref [7], long range states were studied. In this experiment, two research groups collaborated to look for the long range states in the molecular potential in helium. One of them was able to detect the vibrational features. Their detection method was using the (MOT) temperature measurement technique. The measurement was used as a sign of heating effects in the MOT due to the PA beam. The other group used an ion detection method similar to the method used in our research. They reported this technique an unsuccessful method since the ion production probability from those states are very low. They quote *The Utrecht group has also tried to observe the purely long-range states that we study here, near the D_0 line, but without success. We believe their lack of a result is explained by the fact that they monitor the ion production rate, which is strongly reduced for these states.* Their data are shown in Fig. 4 where the intensity is expressed in terms of the so called saturation intensity I_{sat} ,

$$I_{sat} = \frac{\pi hc}{3\lambda^3\tau}, \quad (1)$$

where c is the speed of light, h is Planck's constant, λ is the light wavelength and τ is the excited state lifetime. This intensity is used as a normalization of the intensity.

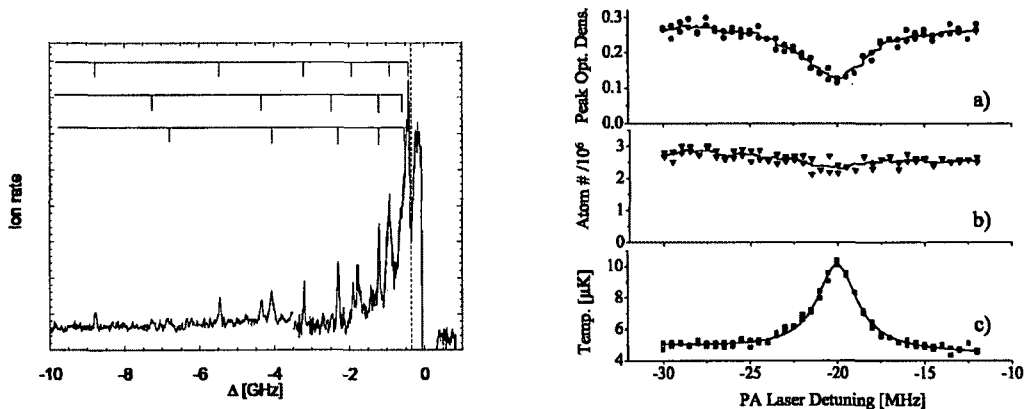


FIG. 4: The left graph shows the data from the helium PA experiment Ref [6] and three vibrational series of states is shown on the top. It is also important to note that the part from -10 GHz to -3.5 GHz is a scan of laser intensity $1.2 * 10^5 I_{sat}$ and the part from -3.5 GHz to 0 GHz is a scan of laser intensity $7.5 * 10^4 I_{sat}$. The graph on the right shows data for long range states [7]. The graph shows the vibration sub-level at $\nu = 4$ in the molecular potential 0_u^+ . The curves show a) the peak optical density, b) the number of atoms and c) a Lorentzian fit of the temperature of the atoms in the MOT cloud after the PA action and then giving the atomic cloud time to expand.

It depends on the specific transition targeted and the specific wavelength of light used. Every atom will feel the scattering force from a photon beam with different strength depending on how close the laser frequency is to the atomic transition. This information is expressed in the I_{sat} term.

1.2 OVERVIEW OF THIS DISSERTATION

In Chapter 2, we focus our interests on explaining the theory used in explaining the forces forming the MOT. We highlight the scattering force since the understanding of these forces will help later in the analysis part of our spectrum. The chapter then explains the molecular potential targeted in our spectroscopy. We briefly explain the quantum equations used in forming those potentials. We also introduce the vibrational and rotational sublevels. The chapter ends with the idea of the PA and PAS as they are crucial to our experiments.

Chapter 3 describes details of our experimental apparatus and the conditions under which the data were taken. Details of our vacuum system, laser sources and

locking circuits in addition to our ion detection and data collection methods used for both frequency calibration and ion (signal to noise) improvements are presented.

In Chapter 4, we describe every experiment we performed in detail. We describe the specific conditions under which the data were taken. Each of the four experiments that we performed is described separately in a section. Every section ends with a conclusion and motivation for the following experiment.

In the last chapter, we introduce future prospects of our experiment in light of our current modifications and results. That will show the importance of our data as part of a long term goal of using photo-association to create both homonuclear and heteronuclear ultracold molecules.

CHAPTER 2

THEORETICAL OVERVIEW

2.1 LASER COOLING AND TRAPPING OF THE ATOMS

It is well known that a light beam carries momentum and that the scattering of light by an object produces a force. This property of light was first demonstrated by Frish (1933) through the observation of a very small transverse deflection (3×10^{-5} rad) in a sodium atomic beam exposed to light from a resonance lamp. With the invention of the laser, it became easier to observe effects of this kind. Laser greatly enhances the strength of the force by the use of intense and highly directional light fields. This was demonstrated by Ashkin (1970) with the manipulation of transparent dielectric spheres suspended in water. The results obtained by Frish and Ashkin raised the interest of using light forces to control the motion of neutral atoms. Although the understanding of light forces acting on atoms was already established by the end of the 1970s, unambiguous demonstration of atom cooling and trapping was not accomplished before the mid 1980s [48]. The first laser cooling experiments were carried out on ions that were trapped by electric fields and then cooled by laser radiation. In contrast, it is difficult to confine atoms at room temperature, or above, because of the smaller electromagnetic forces on neutral particles. Therefore the pioneering experiments used light forces to slow atoms in an atomic beam and then confined the cold atoms with the help of a magnetic field. The great success of laser cooling led to the award of the 1997 Nobel prize in physics to Steven Chu, Claude Cohen-Tannoudji and William Phillips [14].

The combination of laser cooling and atom trapping has produced astounding new tools for atomic physicists. Most of the experiments require the exchange of momentum between atoms and an optical field, usually at a nearly resonant frequency. The energy of the light $\hbar\omega$ changes the internal energy of the atom, and the angular momentum l changes the orbital angular momentum of the atom, as described by the well-known selection rule $\Delta l = \pm 1$. By contrast, the linear momentum of the

light $p = \hbar\omega/c = \hbar k$ cannot change the internal atomic degrees of freedom and therefore must change the momentum of the atoms in the laboratory frame. The force resulting from this momentum exchange between the light field and the atoms can be used in many ways to control atomic motion [49]. In this section we discuss some fundamental aspects of light forces and schemes employed to cool and trap neutral atoms. The equations' derivation followed references [8, 9, 14] where a more detailed derivation can be found in those references.

To describe the interaction of a two-level atom with radiation we shall use a semi-classical treatment, i.e. the radiation is treated as a classical electric field but we use quantum mechanics to treat the atom. We shall calculate the effect of an oscillating electric field on the atom from first principles. The Fermi's Golden rule only gives the steady-state transition rate and therefore does not describe adequately spectroscopy experiments. Those experiments utilize highly monochromatic radiation, e.g. radio-frequency radiation, microwaves or laser light, in which the amplitudes of the quantum states evolve coherently in time. In such experiments the damping time may be less than the total measurement time so that the atoms never reach the steady state [14]. We start from the time-dependent Schrodinger equation,

$$-i\hbar \frac{\partial \Psi}{\partial t} = H\Psi, \quad (2)$$

where H is the Hamiltonian and it has two parts,

$$H = H_0 + H_I(t). \quad (3)$$

The part of the Hamiltonian that depends on time, $H_I(t)$, describes the interaction with the oscillating electric field that perturbs the eigenfunctions of H_0 ; the unperturbed Hamiltonian. The unperturbed eigenvalues and eigenfunctions of H_0 are just the atomic energy levels and wavefunctions. We write the wavefunction for the level with energy E_n ,

$$\Psi_n(r, t) = \psi_n(r)e^{-iE_n t/\hbar}. \quad (4)$$

As an example, let us consider a system with only two levels. The spatial wavefunctions satisfy,

$$\begin{aligned} H_0\psi_1 &= E_1\psi_1, \\ H_0\psi_2 &= E_2\psi_2. \end{aligned} \quad (5)$$

These atomic wavefunctions are not stationary states of the full Hamiltonian, $H = H_0 + H_I(t)$, but the wavefunction at any instant of time can be expressed in terms of them as follows,

$$\begin{aligned}\Psi(r, t) &= c_1(t)\psi_1(r)e^{-iE_1t/\hbar} + c_2(t)\psi_2(r)e^{-iE_2t/\hbar}, \\ \Psi(r, t) &= c_1|1\rangle e^{-i\omega_1t} + c_2|2\rangle e^{-i\omega_2t},\end{aligned}\tag{6}$$

where the second equation is in Dirac ket notation with $c_1(t)$ and $c_2(t)$ written as just c_1 and c_2 respectively, and $\omega_1 = E_1/\hbar, \omega_2 = E_2/\hbar$. From the normalization condition c_1 and c_2 satisfy $|c_1|^2 + |c_2|^2 = 1$. The perturbation part of the Hamiltonian comes from the oscillating electric field of the electromagnetic radiation $\vec{E} = \vec{E}_0 \cos(\omega t)$. Here we need to differentiate between two symbols. The first symbols are E_1 and E_2 as being the energy eigenvalues for the unperturbed system. The second symbols \vec{E} and \vec{E}_0 are the electric field and the electric field amplitude vectors. The perturbation corresponds to the energy shift of an electric dipole $-e\vec{r}$ in the electric field, where \vec{r} is the position of the electron with respect to the atom's center of mass (I have assumed that the electric dipole moment arises from a single electron but we can generalize it by adding the atom's electrons dipole moments). The perturbation part of the Hamiltonian is,

$$H_I(t) = e\vec{r} \cdot \vec{E}_0 \cos(\omega t).\tag{7}$$

This perturbation mixes up the two atomic states. After substituting Eqns 6 and 7 into Eqn 2 we get:

$$\begin{aligned}i\dot{c}_1 &= \Omega \cos(\omega t)e^{-i\omega_0t}c_2, \\ i\dot{c}_2 &= \Omega^* \cos(\omega t)e^{i\omega_0t}c_1.\end{aligned}\tag{8}$$

where $\omega_0 = (E_2 - E_1)/\hbar$ and the Rabi frequency Ω is

$$\Omega = \frac{\langle 1|e\vec{r} \cdot \vec{E}_0|2\rangle}{\hbar} = \frac{e}{\hbar} \int \psi_1^*(r) \vec{r} \cdot \vec{E}_0 \psi_2(r) d^3r.\tag{9}$$

This treatment assumes that the amplitude of the electric field is uniform over the atom so that it can be taken outside the integral over the atomic wavefunctions, i.e. that E_0 does not depend on r . It is important to note that the phase of the light wave is actually $(\omega t - \vec{k} \cdot \vec{r})$, where \vec{r} is the coordinate vector relative to the atoms center of mass (taken to be the origin) and \vec{k} is the wavevector. The dipole approximation assumes that the variation of phase $\vec{k} \cdot \vec{r}$ is small over the atom ($ka_0 \ll 2\pi$). This is

equivalent to $\lambda \gg a_0$, i.e. the radiation has a wavelength much greater than the size of the atom. Thus, for radiation linearly polarized along the x-axis, $\vec{E} = |E_0|\hat{e}_x \cos(\omega t)$, we obtain

$$\Omega = \frac{eX_{12}|E_0|}{\hbar}, \quad (10)$$

where

$$X_{12} = \langle 1|x|2 \rangle. \quad (11)$$

We can write Eqn. 8 as:

$$\begin{aligned} i\dot{c}_1 &= \Omega \{e^{i(\omega-\omega_0)t} + e^{-i(\omega+\omega_0)t}\} c_2/2, \\ i\dot{c}_2 &= \Omega^* \{e^{-i(\omega-\omega_0)t} + e^{i(\omega+\omega_0)t}\} c_1/2. \end{aligned} \quad (12)$$

For most cases of interest, the radiation has a frequency close to the atomic resonance at ω_0 so the magnitude of the detuning is small, $|\omega_0 - \omega| \ll \omega_0$, and $\omega_0 + \omega \sim 2\omega_0$. This is the rotating-wave approximation. Applying this approximation to equations 12, we can find that the term with $(\omega + \omega_0)t$ oscillates very fast and therefore averages to zero over any reasonable interaction time and the equations 12 become,

$$\begin{aligned} i\dot{c}_1 &= \Omega e^{i(\omega-\omega_0)t} c_2/2, \\ i\dot{c}_2 &= \Omega^* e^{-i(\omega-\omega_0)t} c_1/2. \end{aligned} \quad (13)$$

The assumption that the electric field is along \hat{e}_x makes the component of the expectation value of dipole along this direction,

$$-eD_x(t) = - \int \Psi^\dagger(t) e x \Psi(t) d^3r. \quad (14)$$

Using the wavefunction expression in Eqn. 6 and substituting from Eqn. 10, we get

$$\begin{aligned} D_x(t) &= \int (c_1\psi_1 e^{-i\omega_1 t} + c_2\psi_2 e^{-i\omega_2 t})^* x (c_1\psi_1 e^{-i\omega_1 t} + c_2\psi_2 e^{-i\omega_2 t}) d^3r, \\ &= c_2^* c_1 X_{21} e^{i\omega_0 t} + c_1^* c_2 X_{12} e^{-i\omega_0 t}, \end{aligned} \quad (15)$$

where $\omega_0 = \omega_2 - \omega_1$. From Eqn. 11, we see that $X_{21} = (X_{12})$, and also $X_{11} = X_{22} = 0$. This can clearly be viewed by recalling that the wavefunctions are symmetric about

the origin. When we add the x variable to the integral, the integral will be odd and eventually vanish. To calculate this dipole moment induced by the applied field, we need to know the bilinear quantities $c_1^*c_2$ and $c_2^*c_1$. We can write the density matrix as,

$$|\Psi\rangle\langle\Psi| = \begin{pmatrix} c_1 \\ c_2 \end{pmatrix} \times \begin{pmatrix} c_1^* & c_2^* \end{pmatrix} = \begin{pmatrix} |c_1|^2 & c_1c_2^* \\ c_2c_1^* & |c_2|^2 \end{pmatrix} = \begin{pmatrix} \rho_{11} & \rho_{12} \\ \rho_{21} & \rho_{22} \end{pmatrix}. \quad (16)$$

Off-diagonal elements of the density matrix or coherences represent the response of the system at the driving frequency ω . It appears in the dipole moment expression in Eqn. 15. The diagonal elements $|c_1|^2$ and $|c_2|^2$ are the populations. We can define the new variables \tilde{c}_1 and \tilde{c}_2 as

$$\begin{aligned} \tilde{c}_1 &= c_1 e^{-i\delta t/2}, \\ \tilde{c}_2 &= c_2 e^{i\delta t/2}, \end{aligned} \quad (17)$$

where $\delta = \omega - \omega_0$ is the detuning of the radiation from the atomic resonance. This transformation does not affect the populations ($\tilde{\rho}_{11} = \rho_{11}$ and $\tilde{\rho}_{22} = \rho_{22}$) but the coherences become $\tilde{\rho}_{12} = \rho_{12} \exp(-i\delta t)$ and $\tilde{\rho}_{21} = \rho_{21} \exp(i\delta t) = (\tilde{\rho}_{12})^*$. In terms of these coherences the dipole moment is

$$\begin{aligned} D_x(t) &= X_{12} \{ \rho_{12} e^{i\omega_0 t} + \rho_{21} e^{-i\omega_0 t} \}, \\ &= X_{12} \{ \tilde{\rho}_{12} e^{i\omega t} + \tilde{\rho}_{21} e^{-i\omega t} \}, \\ &= X_{12} (u \cos \omega t - v \sin \omega t). \end{aligned} \quad (18)$$

Here we have assumed that X_{12} is real which is true for transitions between two bound states of the atom because the radial wavefunctions are real and the integration over the angular momentum eigenfunctions also gives a real contribution to the matrix element (selection rules). The coherences $\tilde{\rho}_{12}$ and $\tilde{\rho}_{21}$ give the response of the atom at ω , the angular frequency of the applied field. The real and imaginary parts of $\tilde{\rho}_{12}$ multiplied by 2 are

$$\begin{aligned} u &= (\tilde{\rho}_{12} + \tilde{\rho}_{21}), \\ v &= -i(\tilde{\rho}_{12} - \tilde{\rho}_{21}). \end{aligned} \quad (19)$$

We can rewrite Eqn. 13 after using the definition of δ as

$$\begin{aligned} i\dot{c}_1 &= \Omega e^{i\delta t} c_2/2, \\ i\dot{c}_2 &= \Omega^* e^{-i\delta t} c_1/2. \end{aligned} \quad (20)$$

Taking the time derivative of Eqn. 17

$$\begin{aligned}\dot{\tilde{c}}_1 &= \dot{c}_1 e^{-i\delta t/2} - \frac{i\delta}{2} c_1 e^{-i\delta t/2}, \\ \dot{\tilde{c}}_2 &= \dot{c}_2 e^{i\delta t/2} + \frac{i\delta}{2} c_2 e^{i\delta t/2}.\end{aligned}\tag{21}$$

Substituting $\tilde{c}_1, \tilde{c}_2, c_1$ and c_2 , we get:

$$\begin{aligned}i\dot{\tilde{c}}_1 &= \frac{1}{2}(\delta\tilde{c}_1 + \Omega\tilde{c}_2), \\ i\dot{\tilde{c}}_2 &= \frac{1}{2}(\Omega\tilde{c}_1 - \delta\tilde{c}_2).\end{aligned}\tag{22}$$

The time derivative of the “new” coherences is

$$\begin{aligned}\dot{\rho}_{12} &= \dot{\tilde{c}}_2^* \tilde{c}_1 + \tilde{c}_1^* \dot{\tilde{c}}_2, \\ \dot{\rho}_{21} &= \dot{\tilde{c}}_1^* \tilde{c}_2 + \tilde{c}_2^* \dot{\tilde{c}}_1.\end{aligned}\tag{23}$$

We can write it after simplification as

$$\begin{aligned}\dot{\rho}_{12} = \dot{\rho}_{21}^* &= -i\delta\rho_{12} + \frac{i\Omega}{2}(\rho_{11} - \rho_{22}), \\ \dot{\rho}_{22} = -\dot{\rho}_{11} &= \frac{i\Omega}{2}(\rho_{21} - \rho_{12}).\end{aligned}\tag{24}$$

The later equation is consistent with the normalization $\rho_{11} + \rho_{22} = 1$ condition.

We can also write them in terms of u and v as

$$\begin{aligned}\dot{u} &= \delta v, \\ \dot{v} &= -\delta u + \Omega(\rho_{11} - \rho_{22}), \\ \dot{\rho}_{22} &= \frac{\Omega v}{2}.\end{aligned}\tag{25}$$

If we define $w = \rho_{11} - \rho_{22}$ then we can rewrite those equations as

$$\begin{aligned}\dot{u} &= \delta v, \\ \dot{v} &= -\delta u + \Omega w, \\ \dot{w} &= -\Omega v.\end{aligned}\tag{26}$$

A two-level atom has an energy proportional to the excited-state population, $E = \rho_{22}\hbar\omega_0$ Ref. [14]. Introducing the spontaneous emission effect can be simplified by treating it as a damping force. Let us consider a classical system of harmonic oscillator with driving force $F(t)\cos(\omega t)$. The system has a natural frequency ω_0 . It suffers from a friction force $-\alpha\dot{x}$. Newton’s second law will yield an equation of motion as follows

$$\ddot{x} + \beta\dot{x} + \omega_0^2 x = \frac{F(t)}{m} \cos(\omega t), \quad (27)$$

where $\beta = \alpha/m$. The solution to this equation can be on the form,

$$x = U(t)\cos(\omega t) - V\sin(\omega t), \quad (28)$$

where U is the component of the displacement in phase with the force and V has a lead of $\pi/2$ with respect to the force. Substituting Eqn. 28 into Eqn. 27, and comparing the terms with the $\cos(\omega t)$ and $\sin(\omega t)$ on both sides we find

$$\begin{aligned} \dot{U} &= (\omega - \omega_0)V - \frac{\beta}{2}U, \\ \dot{V} &= -(\omega - \omega_0)U - \frac{\beta}{2}V - \frac{F(t)}{2m\omega}. \end{aligned} \quad (29)$$

Damping by spontaneous emission can be introduced into the quantum treatment of the two-level atom by comparison with the damping of a classical system. We introduce a damping term into Eqn. 25 to give

$$\dot{\rho}_{22} = \frac{\Omega v}{2} - \Gamma \rho_{22}, \quad (30)$$

where Γ is the damping rate. In the absence of the driving term ($\Omega = 0$) this gives exponential decay of the population in level 2, i.e. $\rho_{22}(t) = \rho_{22}(0)\exp(-\Gamma t)$. By analogy with the classical oscillator, we see that the coherences u and v have a damping factor of $\Gamma/2$ and Eqns. 26 become the optical Bloch equations

$$\begin{aligned} \dot{u} &= \delta v - \frac{\Gamma}{2}u, \\ \dot{v} &= -\delta u + \Omega w - \frac{\Gamma}{2}v, \\ \dot{w} &= -\Omega v - \Gamma(w - 1). \end{aligned} \quad (31)$$

For $\Omega = 0$ the population difference $w \rightarrow 1$. These optical Bloch equations describe the excitation of a two-level atom by radiation close to resonance for a transition that decays by spontaneous emission. The steady-state solution ($\dot{u} = \dot{v} = \dot{w} = 0$) is established at times which are long compared to the lifetime of the upper level ($t \gg \Gamma^{-1}$). The solution takes the form

$$\begin{pmatrix} u \\ v \\ w \end{pmatrix} = \frac{1}{\delta^2 + \Omega^2/2 + \Gamma^2/4} \begin{pmatrix} \Omega\delta \\ \Omega\Gamma/2 \\ \delta^2 + \Gamma^2/4 \end{pmatrix}. \quad (32)$$

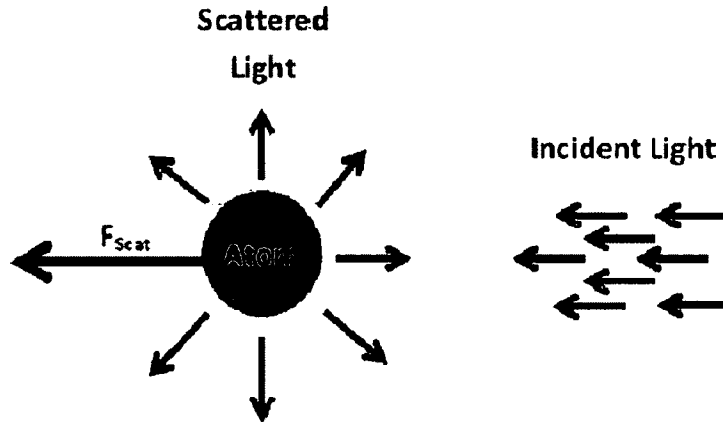


FIG. 5: Spontaneous emission following absorption occurs in random directions, but absorption from a light beam occurs along only from one direction.

These show that a strong driving field ($\Omega \rightarrow \infty$) tends to equalize the populations $w \rightarrow 0$. The steady state gives an upper level population of

$$\rho_{22} = \frac{1 - w}{2} = \frac{\Omega^2/4}{\delta^2 + \Omega^2/2 + \Gamma^2/4}, \quad (33)$$

where for high intensity, i.e. $\Omega \rightarrow \infty$, $\rho_{22} \rightarrow 1/2$. The light force exerted on an atom can be of two types: a dissipative, “scattering force” and a conservative, “dipole force.” The scattering force arises from absorption of light and spontaneous emission. On the other hand, the dipole force arises from the electric dipole interaction between the oscillating electric field component in the incident detuned radiation and the dipole moment of the atoms. The following section will explain in detail the scattering force with an explanation towards the end of the major difference between the two forces.

2.1.1 THE SCATTERING FORCE

The scattering force arises from the impulse experienced by an atom when it absorbs or emits a quantum of photon momentum. When an atom scatters light, the resonant scattering cross section can be written as $\sigma_{sca} = \lambda_0^2/2\pi$ where λ_0 is the on-resonant wavelength. A detailed derivation for this equation can be found in Ref. [50]. In the optical region of the electromagnetic spectrum the wavelengths of light are on the order of several hundreds of nanometers, so resonant scattering cross sections

become quite large 10^{-9}cm^2 Ref. [48]. Each photon absorbed transfers a quantum of momentum $\hbar\vec{k}$ to the atom in the direction of light propagation (the magnitude of \vec{k} is $2\pi/\lambda$ of the wave vector associated with the optical field). The spontaneous emission following the absorption occurs in random directions; over many absorption-emission cycles, it averages to zero. As a result, the net spontaneous force acts on the atom in the direction of the light propagation, as shown schematically in Fig. 5. The saturated rate of photon scattering by spontaneous emission (one half the reciprocal of the excited-state lifetime) fixes the upper limit to the force magnitude. This force is sometimes called radiation pressure, spontaneous force or radiative optical force. It follows from the conservation of momentum that when an object absorbs radiation its momentum changes. The force on the object equals the rate of change of momentum. Therefore the force equals the rate at which the light delivers momentum. Lasers produce well-collimated monochromatic beams of light that can slow atoms in an atomic beam. Each absorbed photon gives the atom a kick in the direction opposite to its motion and spontaneously-emitted photons go in all directions. That is why the scattering of many photons gives an average force that slows the atom down. The magnitude of this scattering force equals the rate at which the absorbed photons impart momentum to the atom or in other words the photon momentum multiplied by the scattering rate of the photons. The scattering rate equals $R_{scatt} = \Gamma\rho_{22}$ where ρ_{22} is used to express the fraction of the atoms in the level 2. The scattering force is given by

$$F_{scatt} = \hbar k \frac{\Gamma}{2} \frac{I/I_{sat}}{1 + I/I_{sat} + 4\delta^2/\Gamma^2}, \quad (34)$$

where $I/I_{sat} = 2\Omega^2/\Gamma^2$ [50]. As $I \rightarrow \infty$ the force tends to $\Gamma\hbar k/2$. The total scattering rate of light from the laser field saturates to $\Gamma/2$ at high intensities because the populations in the upper and lower levels both approach 1/2. This force is the main tool used in laser cooling atoms in our set up.

So far we have assumed that the intensity of the light (i.e. the amplitude of the applied electric field) is constant. This is not the case for Gaussian beam in which the intensity is strongest at the center of the beam and fades away at the edges. The consideration of the gradient of the beam intensity creates another type of force which is called the dipole force. To recall the derivation of the scattering force definition, we started by an applied electric field \vec{E} . The field induces a dipole moment of $-e\vec{r}$

on an atom. The interaction energy of this dipole with the electric field is

$$U = e\vec{r} \cdot \vec{E}, \quad (35)$$

where E is the magnitude of \vec{E} . For an induced dipole moment, $e\vec{r} = -\epsilon_0\chi_a\vec{E}$, where ϵ_0 is vacuum's permittivity and χ_a is the atom's polarizability. The interaction energy will be $U = -1/2\epsilon_0\chi_a\vec{E} \cdot \vec{E}$. For a linearly polarized electric field, oscillating with an angular frequency ω and propagating in the z-direction, the electric field can be expressed as $\vec{E} = E_0 \cos(\omega t - kz)\hat{e}_x$, where k is the wavevector and equals $2\pi/\lambda$. The force is given by $\vec{F} = -\vec{\nabla}U$. This leads to

$$F_z = -\frac{\partial U}{\partial z} = -ex \left(\frac{\partial E_0}{\partial z} \cos(\omega t - kz) + kE_0 \sin(\omega t - kz) \right). \quad (36)$$

To get the time average of the force over many oscillations (quantum mechanically), we need to do the integration $\bar{F}_z = -\int \Psi^\dagger(t) F_z \Psi(t) d^3r dt$. Following the same steps as the derivation before for the scattering force we will end up with

$$\begin{aligned} \bar{F}_z &= \frac{-e\chi_a}{2} \left(u \frac{\partial E_0}{\partial z} - v E_0 k \right), \\ &= F_{dipole} + F_{scatt}, \end{aligned} \quad (37)$$

which will lead to the forms of the scattering and the dipole force as follows

$$F_{scatt} = \frac{\hbar k \Gamma}{2} \frac{\Omega^2/2}{\delta^2 + \Omega^2/2 + \Gamma^2/4}, \quad (38)$$

which in accordance with Eqn. 34. The dipole force takes the form

$$F_{dipole} = -\frac{\hbar \delta}{2} \frac{\Omega}{\delta^2 + \Omega^2/2 + \Gamma^2/4} \frac{\partial \Omega}{\partial z}. \quad (39)$$

Now that we have derived both the two force equations we can clearly see that the two forces are fundamentally different. The scattering force vanishes for atoms at rest in a standing wave because for two counter-propagating beams the atoms can absorb light from either of the two beams and the average momentum transfer is zero. This force is dissipative because the reverse of the spontaneous emission is not possible and therefore the action of the force can not be reversed [8]. As the light intensity increases this force saturates at $\hbar k \Gamma/2$. It also results from the out of phase component of the dipole interaction which is originated in the definition of v [14].

On the other hand the dipole force is a conservative force and can be used to trap atoms. It can be increased by increasing the intensity but it can not be used to cool down the atoms [8]. This force results from the in-phase component of the dipole.

2.1.2 THE ZEEMAN SLOWER

One of the ways we use the scattering force to pre-cool the atoms and slow them down before they could be loaded into the atomic trap is the Zeeman slower. Loading the atomic traps for noble gases is different from alkali atomic trap loading. It is hard to use the laser light that targets atomic transitions starting from the ground state. These lasers are mostly high energy and very expensive to use in wide experimental scale. That is why before the atoms' cooling and trapping process starts, the atoms are loaded into a metastable state. Atomic electronic transitions from metastable states are easier to achieve using an inexpensive diode laser. During this stage the atoms gain kinetic energy. The problem with this technique is that the number of atoms populated in the metastable state with a small enough velocity is small. This makes it hard to trap the atoms directly in the atomic trap without slowing them down to more efficient capture speed for the atomic trap.

As described above, when an atom interacts with laser light directed against its motion it starts to slow down as long as it continues to scatter photons. The scattering force will remain maximized until the detuning between the light and the resonance frequency is large enough i.e. δ is large enough. This can be a result of the velocity change of the atom due to the slowing down process. The velocity change affects the Doppler frequency difference and as a result changes δ . That is why to slow an atomic beam we need to constantly compensate for the change in the Doppler shift of the light frequency. This compensation keeps the light resonant with the atom and hence a strong radiation force throughout the slowing process. There are several ways to do that. One is by continuously changing the frequency of the slowing laser so that it matches the change in the Doppler shift frequency (this is called chirp cooling). Another method is by adding a position dependent magnetic field. Changing the strength of the magnetic field which in accordance will change the Zeeman shift in the energy level in a way to cancel the Doppler shift, thereby keeping the atoms in resonance with a single frequency slowing laser beam. The latter is the technique we use in our lab.

This technique was first developed by Phillips et al. in 1982 [51]. It was found to be more effective in creating slow atomic beams than other methods. As a result, it has been widely used as a pre-cooling stage in MOTs [52, 53]. Another important aspect of its application is that certain metal elements used in optical clocks, such as Sr and Yb have very low vapor pressures at room temperature [54]. That makes it really hard to trap them directly from a background gas. In such case, a Zeeman-slowed atomic beam is usually the only choice to obtain a high flux of slow atoms for subsequent laser cooling. In this section we will show how this “Zeeman slower” works. For an atom starting from $x = 0$ and traveling a distance x , it will end up with a velocity $v(x)$ at this new position. The atom starts with a velocity v_0 at $x = 0$. Using principle equations of motion with the assumption of constant acceleration, we can find that

$$v^2(x) = v_0^2 - 2ax. \quad (40)$$

When the atoms leave the Zeeman slower their velocity will be slowed down to $v = v_f$. The atom’s slowing process happens over a distance range which is $2a = v_0^2 \left(1 - \frac{v_f^2}{v_0^2}\right) / L_0$ from Eqn. 40. When we use this expressions for a and substitute them in the Eqn. 40 we get

$$v(x) = v_0 \left(1 - \frac{x}{L_0} \left(1 - \frac{v_f^2}{v_0^2}\right)\right)^{\frac{1}{2}}. \quad (41)$$

Now consider that the atom is immersed in a magnetic field $B(x)$. Because of the atom’s motion, the atom will be excited by a different frequency ω than its original resonance frequency ω_0 . ω_0 is the resonance frequency of the atoms at rest. The difference between the two frequencies $\omega - \omega_0$ can be expressed in terms of the atom’s velocity as $k v$. This is a result of the Doppler effect, where k is the wavevector. Since the atoms in the Zeeman slower is slowing down, its new resonance frequency is changing as well. That is why the magnetic field along the atom’s path needs to change. Hence the Zeeman shift in the energy levels due to the interaction with the magnetic field $E - E_0 = \mu_B B(x)$ changes accordingly. μ_B is a universal constant called the Bohr magneton. The magnetic field changes in such a way that matches the change in the resonance frequency due to the Doppler effect. We can express it in mathematical form as

$$\omega + kv = \frac{\mu_B B(x)}{\hbar} + \omega_0. \quad (42)$$

From these equations we can get a formula for the magnetic field required to compensate for the change in the atom's velocity. The magnetic field equation in the Zeeman slower is

$$B(x) = \frac{\hbar(\omega - \omega_0)}{\mu_B} + \frac{\hbar kv_0}{\mu_B} \left(1 - \frac{x}{L_0} \left(1 - \frac{v_f^2}{v_0^2}\right)\right)^{\frac{1}{2}}. \quad (43)$$

This expression is for the shape of the magnetic field that is usually applied to slow down the atoms. The direction of this magnetic field is along the axis of the solenoid x . A graph for this equation is shown in Fig. 6(a). It is important to recall that the slowing laser beam is also sent counter propagating to the atom's velocity along the slower axis as well. A practical problem with this magnetic field design is that it requires a very high current to generate large field, at least towards the beginning of the Zeeman slower. Also an atom moving slower than v_0 will still traverse the Zeeman slower. It will travel with the same velocity along the slower and opposite to the laser beam until it reaches a certain point. This point is where the Zeeman shift meets the Doppler shift and that is when the process of slowing of this specific atom starts. This means that the Zeeman slower has the ability to slow down almost any atom as long as it is entering with velocity lower than v_0 .

To overcome the problem of high current that is present in the design in Fig. 6(a), a modification to the magnetic field is added. This is simply achieved by adding another magnetic field in the opposite direction at the end of the slower. This is shown in Fig. 6(b). This is the shape of the field that we are applying in our experiment [13]. Having the magnetic field in the latter layout has several advantages: (1) It allows us to use much lower currents because we do not need as high magnetic field at the entrance of the slower. This decreases the heat created by the coils and hence lessens requirements for cooling the magnet. (2) In the overlap region between the two coils the magnetic field goes down to zero which provide a good place for adding additional pumping along the line. (3) Down the stream from the Zeeman slower at $x \gg L_0$ the contributions from the two reverse magnetic field cancel out. This maintains very small stray field after the Zeeman slower especially at the atomic trap position. (4) The atoms leave the Zeeman slower with a well-defined velocity. This allows them to travel to the science chamber where they get

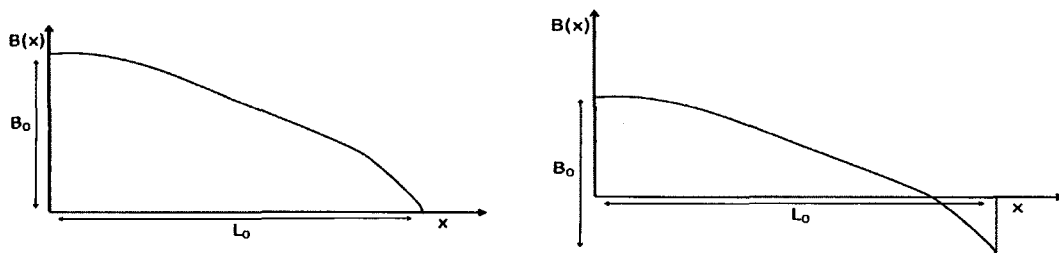


FIG. 6: The magnetic field inside the Zeeman slower. The figure on the left (a) is the single polarity design, while the figure on the right (b) shows the design incorporating both positive and negative magnetic fields. The latter design is the one used in our experiment.

captured with the MOT beams. The different magnetic field configurations require different slowing light detuning.

2.1.3 OPTICAL MOLASSES

Trapping and slowing atoms opened the gates for countless experiments involving a variety of topics [12, 55, 56]. Many experiments involve studying the interaction of light with just one atom or interactions involving just two atoms. Trapping ions (charged atoms) may be somewhat straight forward to think of in terms of their strong interactions with both magnetic and electric fields. Neutral atoms on the other hand since they are electrically neutral, their trapping using magnetic and electric fields is not always as feasible. Several types of traps have been developed. By far the most common is the magneto-optical trap (MOT) that relies on the scattering force to both cool and confine (trap) the atoms. First we start by describing the cooling part of the trap which is mainly achieved by creating an “optical molasses”. Consider an ensemble of atoms in a vapor at room temperature. In a gas sample the atoms are moving randomly in all directions. Therefore to be able to cool those atoms to very low temperature, the laser beams have to be applied in all three Cartesian directions [57]. The common configuration used is to use six beams counter propagating in three Cartesian directions. There are others that use fewer beams, but are not as convenient experimentally. These beams are red detuned i.e. tuned with a frequency below atomic resonance. The reason for the red detuned lasers is explained later. The configuration for optical molasses is shown in Fig. 7.

To understand the physics of optical molasses consider the 1-dimensional case of two counter-propagating, red-detuned laser beams as shown in Fig. 8. For atoms that are extremely cool or almost at rest in the center (the right side case of Fig. 8), the beams are not in resonance with the atomic transitions so the probability of their absorption is very small. As a result, the scattering force from the two beams is very small. Equation 34 shows that the scattering force is inversely proportional to the square of the detuning. The scattering forces resulting from the two counter-propagating beams will balance each others causing the atom to remain in place confined in the center of the cloud. For atoms trying to escape from this cloud (having enough velocity to move away from the center), these atoms have a Doppler shift in their resonance frequency because of their motion. The scattering rate from one of the two counter propagating beams will be much greater than the other beam. This beam is the beam moving towards the atom. The beam gives the atom a kick as a result of the scattering force pushing it back towards the atomic cloud. As an example let us assume that the atom is trying to escape from the trap and moving to the right with velocity v as in left side of Fig. 8. The atom will see the laser beam moving to the right (towards it) as if it has frequency $\omega + kv$. It will see the laser beam moving to the left (in the same direction as the atom's motion) as if it has frequency $\omega - kv$. As a result, the frequency of the first beam will be bigger than the frequency of the second beam. In scattering force terms, the scattering force resulting from the interaction with the first beam is larger than the scattering force resulting from the second. This only means that the forces pushing the atoms to the left (back to the center) are much larger than forces pushing the atoms to the right (away from the trap). This technique can be extended to 3 dimensions by using 3 pairs of counter-propagating laser beams. It is important to note that this type of interaction results from Doppler shift of the atomic resonance transition. In other words, this interaction depends on the atoms velocity and hence it creates only a slowing effect not a trapping technique.

Because of velocity dependence, the scattering force is a dissipative force or a friction force which will ultimately slow the atoms down enough to be trapped in the center. This technique is what is called Optical Molasses. This techniques was demonstrated for the first time in 1985 by *Chu et al* [58]. This effect can be explained mathematically [14] by

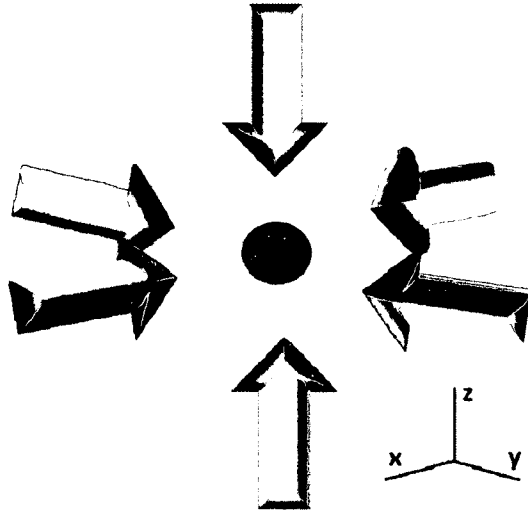


FIG. 7: The six counter propagating beams set up for the optical molasses technique of cooling down a cloud of atoms.

$$\begin{aligned}
 F_{molasses} &= F_{scatt}(\omega - \omega_0 - kv) - F_{scatt}(\omega - \omega_0 + kv), \\
 &\simeq F_{scatt}(\omega - \omega_0) - kv \frac{\partial F}{\partial \omega} - [F_{scatt}(\omega - \omega_0) + kv \frac{\partial F}{\partial \omega}], \\
 &\simeq -2kv \frac{\partial F}{\partial \omega}.
 \end{aligned} \tag{44}$$

Here I have assumed very low velocities $kv \ll \Gamma$. To find the partial derivative to the scattering force

$$\begin{aligned}
 F_{scatt} &= \hbar k R_{scatt} \equiv \hbar \frac{\omega}{c} R_{scatt}, \\
 \frac{\partial F}{\partial \omega} &= \frac{\hbar}{c} \left(R_{scatt} + \omega \frac{\partial R_{scatt}}{\partial \omega} \right).
 \end{aligned} \tag{45}$$

The second term is about $\omega/\Gamma \simeq 10^8$ larger than the first one. Assuming very low intensities (much lower than the saturation limit) $I/I_{sat} \ll 1$, we can find the molasses force as

$$F_{molasses} = 4k^2 v \hbar \frac{I}{I_{sat}} \frac{2\delta/\Gamma}{[1 + (2\delta/\Gamma)^2]^2}. \tag{46}$$

So that this force become a damping force, the whole term expression has to have a minus sign. This can only take place when $\delta < 0$ or $\omega - \omega_0 < 0$. That is the reason the light that is sent to the atoms is red detuned or with a frequency less than the resonance frequency.

2.2 DOPPLER LIMIT AND SUB-DOPPLER COOLING

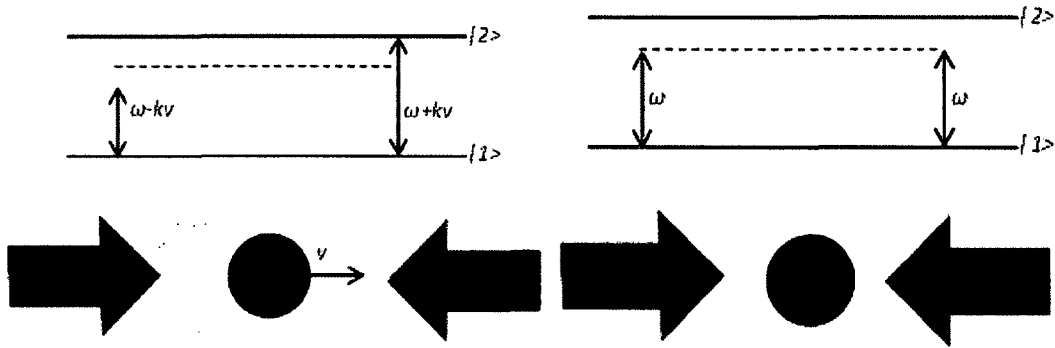


FIG. 8: The effect of red detuned beams on an atom in the atomic cloud. For the right side the atom is at rest so there is no Doppler shift in the resonance energy that the atom can see. For the left side graph with the atom in motion there is a Doppler shift to the incident light that the atom sees.

So far we have claimed that in an optical molasses technique, the atoms can continuously decelerate to $v = 0$. This is clearly unphysical result since achieving zero Kelvin is impossible. This can be understood by considering the kinetic energy of an atom moving along a line. The kinetic energy can be expressed as $\frac{1}{2}mv^2 = \frac{1}{2}k_B T$, where k_B is Boltzmann constant and T is the system's temperature in Kelvins. The fact is that in addition to this cooling process (optical molasses), there is a heating process associated with it. The heating mechanism is one of the limitation that controls the final velocity of the atoms. To better understand heating processes, we start by considering the fluctuations in the absorption process of the photon. This fluctuation rises because atoms does not always absorb the same number of photons in the same period of time t . Each photon absorption is followed by a spontaneous emission process. The number of such events is given by $N = R_{scatt}t$ [14]. On the other hand the spontaneous emission process also suffers from fluctuations. These emission fluctuations cause the atoms to go through recoil kicks in random directions. The number of such kicks is again given by $N = R_{scatt}t$. Every recoil kick gives the atoms a velocity increase $\bar{v}^2 = Nv_r^2$, where v_r is the velocity corresponding to the recoil energy E_r . The recoil energy is given by $E_r = (1/2)Mv_r^2 = \hbar^2k^2/(2M)$. If we combine the effects of both absorption and emission fluctuations, we can express the velocity as $\bar{v}^2 = 2R_{scatt}tv_r^2$. For an atom in two counter-propagating beams, the fluctuation effect is cumulative. This is a reasonable approximation at low intensities where saturation is not significant. This causes an extra factor of 2 from the two

beams so $\bar{v}_{heat}^2 = 4R_{scatt}tv_r^2$.

For our optical molasses technique, the balance between the heating and cooling processes takes place when $\frac{d}{dt}(\frac{1}{2}M\bar{v}^2) = 0$. This equals

$$\begin{aligned} \frac{d}{dt}(\frac{1}{2}M\bar{v}^2) &= \frac{d}{dt}(\frac{1}{2}M[\bar{v}_{heat}^2 - \bar{v}_{cool}^2]), \\ &= 4R_{scatt}\frac{1}{2}Mv_r^2 - Mv\frac{dv}{dt}, \\ &= 4R_{scatt}\frac{1}{2}Mv_r^2 - vF_{molasses}, \\ &= 0. \end{aligned} \tag{47}$$

The terms v_{cool} and v_{heat} were labeled to differentiate between the heating effect term and the cooling effect term. The condition of zero derivative takes place when

$$v^2 = Mv_r^2 \frac{2R_{scatt}}{4k^2\hbar(I/I_{sat})(-2\delta/\Gamma)} [1 + (-2\delta/\Gamma)^2]. \tag{48}$$

Substituting for R_{scatt} and v_r while taking into account low intensity beams $I/I_{sat} \ll 1$ and the fact that $\frac{1}{2}Mv^2 = \frac{1}{2}k_B T$, we find

$$k_B T = \frac{\hbar\Gamma}{4} \frac{1 + (2\delta/\Gamma)^2}{-2\delta/\Gamma}. \tag{49}$$

This function has a minimum when $2\delta/\Gamma = -1$ or $\delta = -\Gamma/2$. At this detuning the temperature is the least possible temperature reached by optical molasses. This temperature is called the Doppler cooling limit T_D and is given by

$$k_B T_D = \frac{\hbar\Gamma}{2}. \tag{50}$$

This was expected to be the limit for cooling using optical molasses. However, experimental measurements found much lower temperatures under certain conditions, in particular when the Earth's magnetic field was canceled out [14]. This can only be explained by considering other cooling mechanisms such as Sisyphus Cooling. In this cooling technique, degenerate energy levels $|JFM_F\rangle$ are taken into account rather than using the two-level model of an atom.

Dalibard and Cohen-Tannoudji [59] discussed a model of sub-Doppler cooling where the light polarization is circular. In this case, the two counter propagating beams are orthogonal and circularly polarized. The resulting optical electric field is constant in magnitude and linearly polarized. The direction of the linear polarization rotates through an angle of 2π over one optical wavelength [8]. A graph showing the

rotating polarization direction is shown in Fig. 9. Let us consider a basis where the quantization axis rotates in space so that it is always along the direction of the optical electric field. In this basis, the light shifts are independent of position and only π transitions are allowed. This is because there is no component of the optical field perpendicular to the quantization axis. The spatially uniform light shifts preclude spatially varying potential.

However, cooling force required for cooling below the Doppler limit originate from the motion of the atom through a region of rotation of the quantization axis. As an example, let us consider atoms with ground state configuration corresponding to $J = 1$. For atoms at rest, excitation will redistribute the population among the magnetic substates according to the local direction of the linearly polarized light. $M_J = 0$ sublevel will be populated stronger than $M_J = \pm 1$. As for moving atoms, they will experience rotation of quantization axis. That is why the population of the ground substates will follow the polarization direction. States with $M_J = +1$ will be more populated than $M_J = -1$ states for atoms traveling towards σ^+ beams. Reference [59] calculated the Clebsch-Gordan coefficient for $M_J = 1$ sublevel scattering σ^+ beam to be six times larger than for σ^- beam. After atoms in $M_J = 1$ sublevel absorb the σ^+ , they undergo spontaneous emission back to $M_J = 1$ sublevels. Atoms traveling towards σ^- beam will scatter more light if they are in $M_J = -1$ levels. Thus going through more recoil kicks in the opposite direction.

To summarize, the atomic motion is clearly damped. The cooling here does not depend on the difference in the Doppler shifts of the two laser beams as in Doppler cooling. In this case, the cooling is caused by the imbalance in population following the field polarization.

2.3 THE MAGNETO OPTICAL TRAP (MOT)

The most widely used trap for neutral atoms is a hybrid of sorts, employing both optical and magnetic effects (though the forces are purely optical). Making a MOT was first demonstrated in 1987 [60]. The operation of a MOT depends on both inhomogeneous magnetic fields and radiative selection rules to exploit both optical pumping and the strong radiative forces. The radiative interaction provides

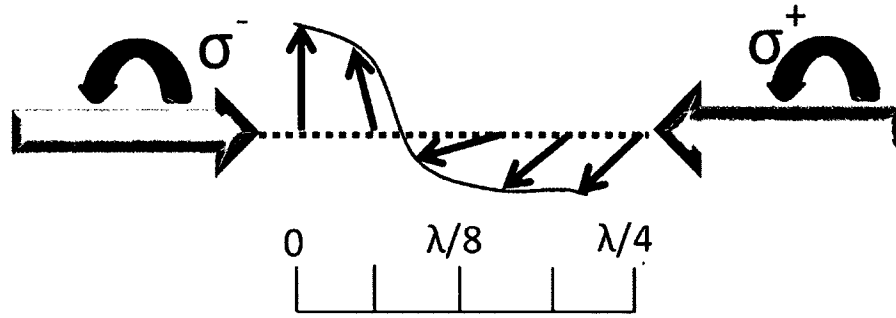


FIG. 9: The graph shows how two circularly polarized counterpropagating beams of opposite polarization direction (σ^+ and σ^-) combine to form linearly polarized light [8].

cooling (described above) that helps in loading the trap, and enables very easy operation. The MOT is a very robust trap that does not depend on precise balancing of the counter-propagating laser beams or on a very high degree of polarization. The magnetic field gradients are modest and can readily be achieved with simple, air-cooled coils. The trap is easy to construct because it can be operated with a room-temperature cell for many atoms (like alkali atoms that are captured from the vapor). It can also be used for noble gas trapping with slight modification (loading from an atomic beam). Furthermore, low-cost diode lasers can be used to produce the light appropriate for many atoms. That is why the MOT became one of the least expensive and widely used ways to make atomic samples with temperatures below 1 mK.

The MOT set up is shown in Fig. 10. The MOT is formed by a magnetic field gradient which is usually much less than the one used by a purely magnetic trap. At the center of the magnetic field three sets of perpendicular, counter-propagating beams intersect. These six beams are chosen so that they are red-detuned and circularly polarized for reasons that we will explain later. Every two counter-propagating beams are circularly polarized in opposite handedness σ^+ and σ^- . The magnetic field gradient is produced by a quadrupole magnetic field. The field is created by a pair of anti-Helmholtz coils (a pair of coils with current in each coil flowing in the opposite direction to the current in the other coil). This field gradient creates a null field at the center and a gradient close to the center that is linear with displacement from the center. The magnetic field is used to Zeeman shift the energy levels of the atom. The

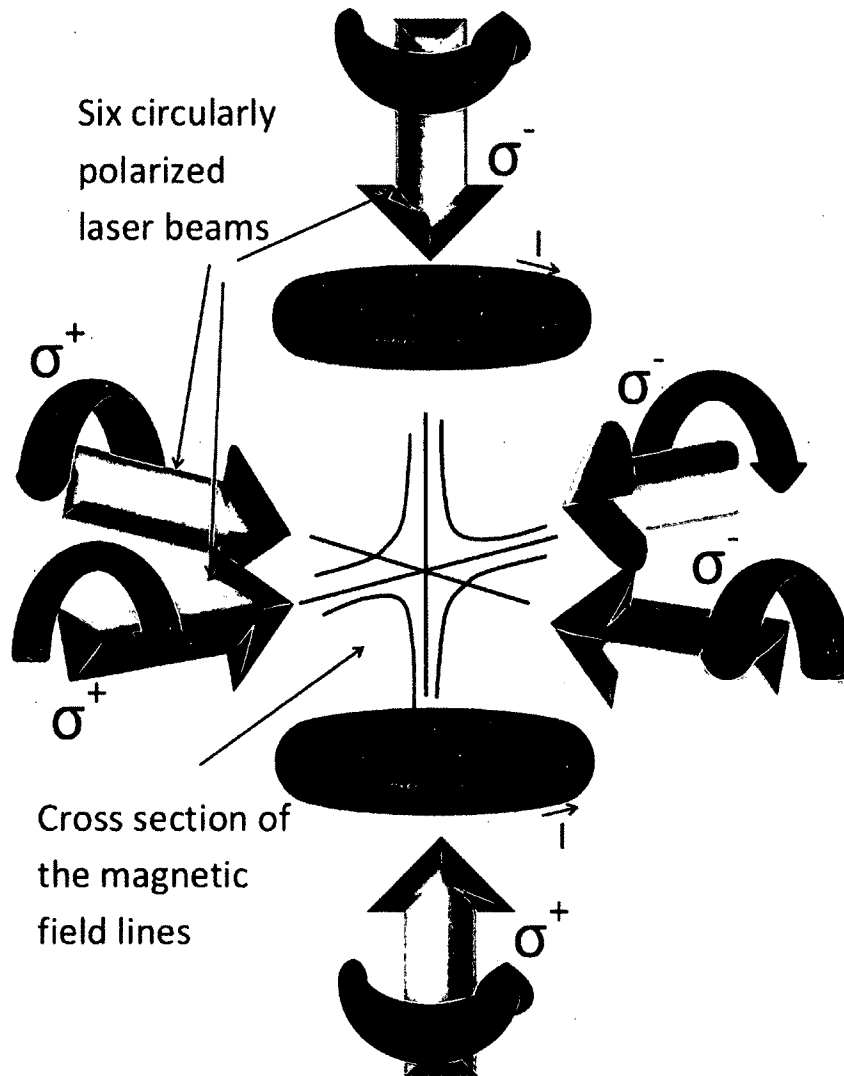


FIG. 10: The graph shows the set up for the Magneto-Optical Trap (MOT). It shows the two anti-Helmholtz coils with a cross section of the shape of the magnetic field. It also shows the orientation of the six counter-propagating circularly polarized laser beams.

Zeeman shift is proportional linearly with the radial displacement from the center of the trap, which along with the circularly polarized light impose the position dependent trapping part of the MOT as explained below. The six laser beams provide a dissipative force that depends on the atoms velocity. This force causes the atoms to be slowed down (cooled) so that they ultimately can be trapped in the MOT. The position dependent magnetic field causes a position dependent Zeeman shift which in turn gives rise to a position dependent optical force. It is this position dependence that provides the spatial confinement (trapping) component to the MOT. Optical molasses alone will slow atoms, but will not spatially confine them.

To be able to understand the operation of the MOT in greater detail, consider atoms which have a cycling transition between $J = 0$ and $J = 1$. An energy diagram to illustrate this system is shown in Fig. 11. When we apply the quadrupole magnetic field, the Zeeman energy shift will split the energy levels of $J = 1$ to $M_J = -1, 0, +1$ and the level $J = 0$ will remain the same. Let us investigate what happens in one of the three coordinates for example the z -axis (i.e. consider the one-dimensional case). The x and y axis should behave the same as the quadrupole field has the same behavior around the center for the x, y and z directions (though not the exact same gradient).

Let us start with the region where the magnetic field is pointing in the $z > 0$ direction. The energy levels splitting will be such that the $M_J = -1$ will have a lower energy than the atomic resonance cyclic transition. This corresponds to $J = 0$ & $M_J = 0$ and $J = 1$ & $M_J = 0$ (the Zeeman shift will be zero for $M_J = 0$). The beam incident from from $z > 0$ has σ^- polarization which matches the $M_J = 0$ to $M_J = -1$ transition, hence the scattering force between them is higher. Since the beam is red detuned from resonance, the scattering force between this beam and the atoms escaping from the trap will push the atoms back to the trap. This “kick” takes place because the atoms are moving opposite to the beam so that their Doppler shift matches light detuning. These two effects combined will cause the scattering force between the beam coming from $z > 0$ and atoms moving at $z > 0$ to be much larger than for other atoms along the same direction. In other words, the atoms at $z > 0$ location will have a cycling transition which is between $J = 0$ & $M_J = 0$ and $J = 1$ & $M_J = -1$. The same happens at $z < 0$. The Zeeman shifts flips so that now the cycling transition is between $J = 0$ & $M_J = 0$ and $J = 1$ & $M_J = +1$.

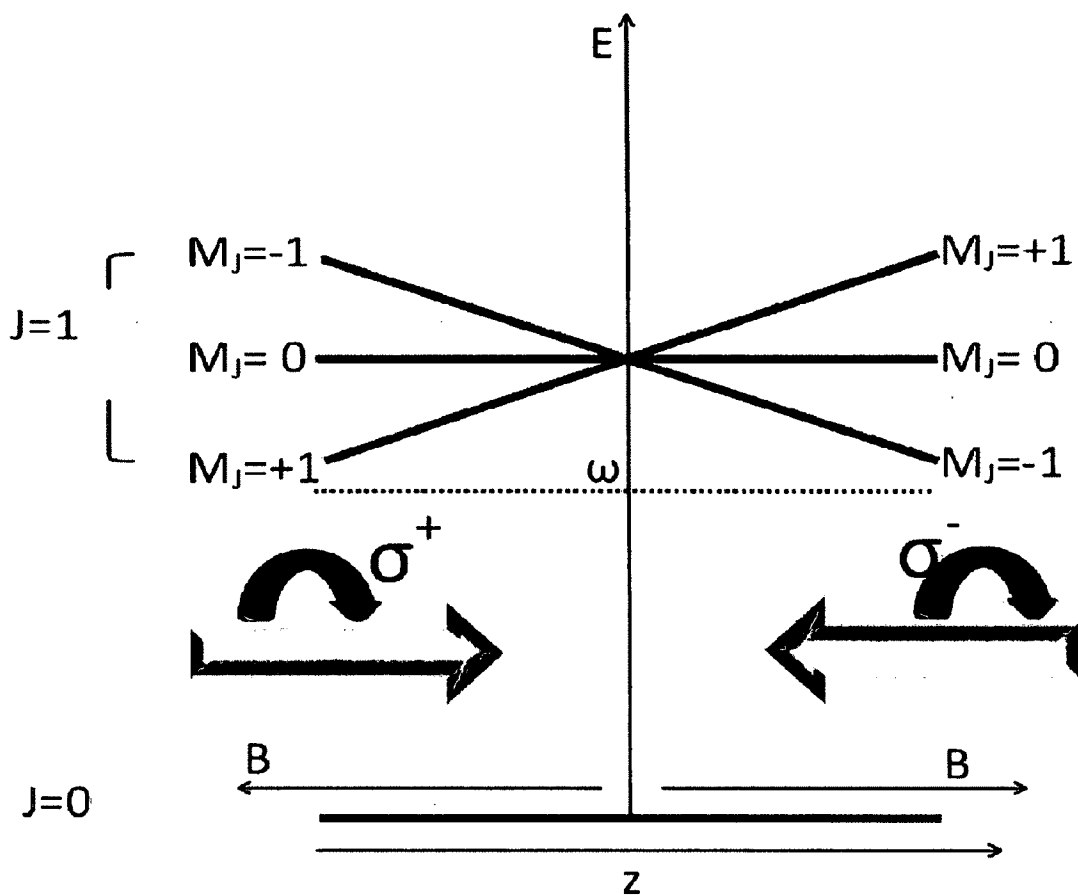


FIG. 11: The graph shows the effect of the magnetic field on a simplified two level atom in one of the three dimensions. This is of course applicable in the other two dimensions. The transition takes place between $J = 0$ to $J = 1$. The direction of the magnetic field is shown with the energy shifts of the atomic levels resulting from the application of this magnetic field.

We can express the MOT forces mathematically using Eqn. 34 after replacing the detuning δ with the new detuning $\delta \pm kv \pm g_J \frac{\mu_B}{\hbar} \frac{dB}{dz} z$. The first term in the new detuning was added because of the Doppler shift which is the same case as in the optical molasses. The second term is added because of the Zeeman shift of the energy levels. This is the same case as the Zeeman slower only here we just kept the linear term in the magnetic field. For simplicity we can write the Zeeman term as $\beta_m z$, where $\beta_m = g_J \frac{\mu_B}{\hbar} \frac{dB}{dz}$ and μ_B is the Bohr magneton. The scattering force at $z > 0$ will take the form

$$F_{scatt}^{\sigma^-}(z > 0) = \hbar k \frac{\Gamma}{2} \frac{I/I_{sat}}{1 + I/I_{sat} + 4(\delta - kv - \beta_m z)^2 / \Gamma^2}. \quad (51)$$

Similarly, we can write the force at $z < 0$ as

$$F_{scatt}^{\sigma^+}(z < 0) = \hbar k \frac{\Gamma}{2} \frac{I/I_{sat}}{1 + I/I_{sat} + 4(\delta + kv + \beta_m z)^2 / \Gamma^2}. \quad (52)$$

We can add these two forces to get the MOT force

$$\begin{aligned} F_{MOT} &= F_{scatt}^{\sigma^-}(\omega - \omega_0 - kv - \beta_m z) - F_{scatt}^{\sigma^+}(\omega - \omega_0 + kv + \beta_m z), \\ &\simeq F_{scatt}(\omega - \omega_0) - kv \frac{\partial F}{\partial \omega} - \beta_m z \frac{\partial F}{\partial \omega} - [F_{scatt}(\omega - \omega_0) + kv \frac{\partial F}{\partial \omega} + \beta_m z \frac{\partial F}{\partial \omega}], \\ &\simeq -2kv \frac{\partial F}{\partial \omega} - 2\beta_m z \frac{\partial F}{\partial \omega}, \\ &\simeq -\alpha v - Kz. \end{aligned} \quad (53)$$

The last equation is the same as a damped harmonic oscillator motion equation. The dissipative force term is coming from the Doppler energy shift (optical molasses). The trapping term (position dependent term) is coming from the magnetic and polarization effect on the atoms. It is also important to mention that to be able to do the previous approximations we had to assume that the Zeeman shift and Doppler shift are very small $\beta_m z \ll \Gamma$ and $kv \ll \Gamma$. Deriving these equations we only took into account one direction (z-direction). Similar effect happens in both x and y directions. When we take into account the three directions of x, y and z we find that a MOT is anisotropic since the restoring force along the z axis of the quadrupole field is twice the restoring force in the xy plane. This can be proved from Maxwell's equations $\nabla \cdot B = 0$ we can analyze it in x, y and z as $\frac{dB_x}{dx} = \frac{dB_y}{dy} = \frac{1}{2} \frac{dB_z}{dz}$.

2.4 ATOMIC STRUCTURE

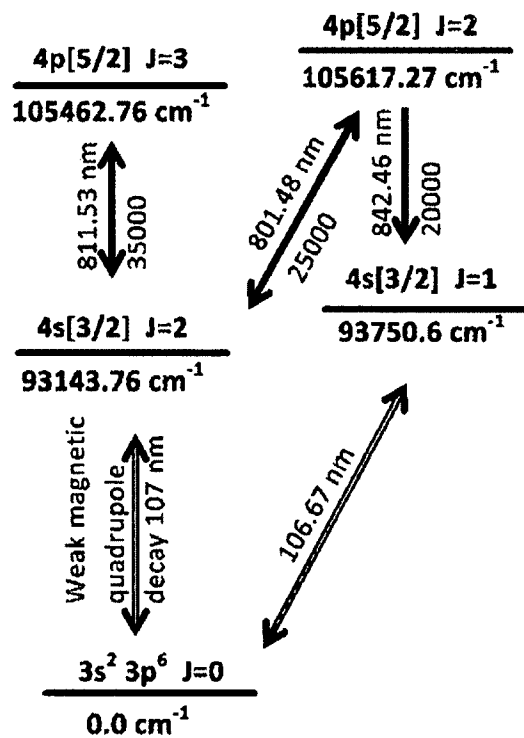


FIG. 12: Argon atomic structure. This structure only includes atomic transitions that were studied during our experiments.

In our thesis work, we focus our research on noble gases, explicitly argon (Ar) and krypton (Kr). An atomic diagram for both the elements with a focus on the transitions used in our experiment is shown in Fig. 12 for the Ar element and in Fig. 13 for the Kr element. The first excited state of noble gases are energetically very high compared to say, alkali atoms. That is why they would require lasers with photons in the vacuum ultraviolet in order to make transitions from the ground state. Such light sources either do not exist or are not practical. To overcome this problem, the atoms are pumped into the first metastable state (in our lab by using a radio frequency (rf) discharge). The metastable state serves as a “virtual ground state” that the atoms can cycle to and from during their cooling process. Since it has relatively long lifetime (tens of seconds), the atoms can stay there long enough to complete most experiments. The metastable state has theoretical lifetime of 60 s for Ar and 85 s for Kr. The lifetime was measured experimentally to be 38 s for Ar and 28.3 s for Kr [61]. Those metastable state atoms usually have the electronic configuration of $S[\frac{3}{2}], J = 2$. The cooling cyclic transition is usually $(S[\frac{3}{2}] \rightarrow P[\frac{5}{2}], J = 2 \rightarrow J = 3)$.

In our photoassociative spectroscopy experiments described in Chapter 4, we usually scan our lasers around an atomic transition limit. The main idea of the experiments is to excite pairs of nearby atoms. Our experiment is focused around two types of transitions: 1) the trapping transition and 2) a quench transition. The trapping transition as was mentioned in the previous paragraph is the transition used in cooling and trapping the atoms. This transition has the form of $(S[\frac{3}{2}] \rightarrow P[\frac{5}{2}], J = 2 \rightarrow J = 3)$.

The quench transitions on the other hand has the form $(S[\frac{3}{2}] \rightarrow P[\frac{5}{2}], J = 2 \rightarrow J = 2)$. The reason these transitions are called quench transitions is that those transitions strongly couple the metastable state to a new state. This state is in turn strongly coupled to the ground state. This means that a very large percent of the atoms that are excited using this transition will eventually end up in the ground state. As a result, they will immediately be lost from the MOT. Atoms in the ground state are “blind” to the trapping transition. The only way to load them back into the MOT is to channel them back to the rf discharge. There, they would get pumped into the metastable state where they can be further cooled down into the MOT using the trapping transition.

2.5 MOLECULAR STRUCTURE

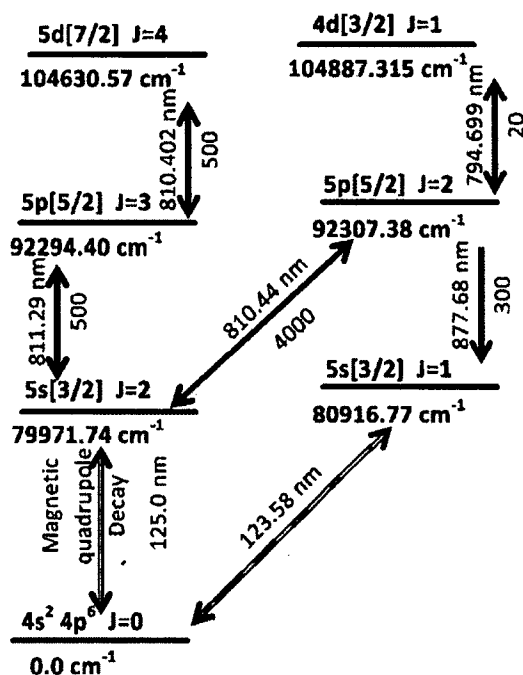


FIG. 13: Krypton atomic structure. This structure only includes atomic transitions that were studied during our experiments.

Molecules are groups of more than one atom that combine together with attractive forces and interactions to form bonds between the individual atoms. We will focus our study here on diatomic molecules as this is our main focus in our Photo Association (PA) experiments. The molecular character and the way the bonds between the atoms are formed depend to large extent on the internuclear distance between the two atoms.

When two atoms combine to form a molecule, the electronic clouds start to diffuse as they come together. From the physics stand point the easiest theoretical way to model this system is to deal with it initially as two separate atoms. We already know their wave-functions solutions to Schrodinger's equation. We can then treat the electronic cloud diffusion as a perturbation to the system. Unfortunately as the atoms get closer, the perturbation gets larger ND this approach breaks down. For short separation between the atoms the chemical bond gets really strong and the electron clouds are really distorted. The explanation of the molecular wave-functions must include summation over many atomic wave-functions terms. This is chemistry.

As the distance between the atoms gets longer, the chemical bonds starts to weaken. Examples of these electrostatic interactions include the van der Waals or dipole-dipole interactions. As the distance between the atoms increase the separate atomic electronic clouds become less disturbed. These types of “long range” molecules are very appealing to physicists as they allow molecular quantities to be calculated from atomic parameters. The internuclear distance in these types of molecules is often about $20a_0$ or greater, where a_0 is the Bohr radius.

Another very important aspect in studying long range molecules is that vibrational levels in molecular potential wells can be approximated by quantum harmonic oscillator. This is true for low levels of vibrational excitation but for higher levels the molecular vibration is highly anharmonic [62]. Their electronic position expectation value is highest around the classical turning points. This follows by considering the expectation value of position for a classical oscillator [9]. We say that electrons in these states “like” to spend most of their time in the outer “longer distance turning point”. This shows the importance of studying long range molecules.

On the other hand, “purely” long range states form a very important feature of some molecules. They result in some molecular potential curves which have both inner and outer turning points. In the purely long range states, the turning points happen to take place at large internuclear separation. Their potential wells are not crossed by another higher level well. The distance between the nuclei is so long that effects from chemical bonds can be neglected. Photoassociation spectroscopy (PAS) of ultracold atomic sample forms a very useful tool to map these levels (both long range and purely long range). PAS has the enough resolution (for most of the cases) to distinguish between those levels as we will explain later.

2.6 MOLECULAR WAVE-FUNCTIONS

The molecular spectroscopy is a powerful tool for studying both simple and complex molecules. By studying the x-ray diffraction patterns from molecules we can understand that inner electrons in closed shells are tightly bound to the nucleus. It is only the outer lying electrons or what we can call the valence electrons that form the electronic cloud and hence the molecular bond. The way this charge distribution is arranged provides the binding force [9]. To be able to analyze this cloud distribution, we need to solve the electron’s wave equations. We can distinguish between three types of motion of the electron. The first type arises from the electrostatic

interaction. This interaction can either be attractive between the electrons and the nuclei or it can be the electrons' mutual repulsive interaction. Molecules possess a series of molecular potentials that characterize the overall energy of the molecular state. Unlike a single atom that only supports discrete energy levels describing the orbital motion of the electron, a molecular potential well may support vibrational and rotational states. This means that molecules have two additional degrees of freedom when compared to atoms. The vibrational motion (second type) of the nuclei about their equilibrium position forms a splitting to the electronic potential wells. The rotational motion (third type) of a diatomic molecule will produce an even finer splitting within each of the vibrational energy levels.

In order to fully understand molecular structure and dynamics, a quantum treatment is needed. From solutions to the quantum equations we can analyze molecular spectra. Molecular spectra carry a lot of information about atoms forming molecules as well as the way atoms interact and form a chemical bond. A challenge of studying molecular spectra is that the structures are sometimes extremely complicated. This may cause calculations to be demanding which can make it hard to connect experiment and theory. It is not uncommon to have to make certain approximations to calculations in order to make them tractable. We will try to briefly go over them here as understanding them will be a key element in understanding the goals of our experiments. Below, we will follow the treatments given in Ref. [9, 63, 64, 65].

The Born-Oppenheimer Approximation separates the Hamiltonian of the molecules. It uses the assumption that the nuclei are heavy compared to the electron cloud moving around them. This means that we can consider the nuclei stationary during the electron transitions. We can apply this approximation when solving the Schrodinger equation. The Hamiltonian for a system of electrons forming an electron cloud around two nuclei A and B i.e. diatomic molecule can be written as

$$\begin{aligned}
 H &= T_N + T_e + V, \\
 T_N &= \sum_{n=A,B} -\frac{\hbar^2}{2M_n} \nabla_n^2, \\
 T_e &= -\frac{\hbar^2}{2m} \sum_i \nabla_i^2,
 \end{aligned} \tag{54}$$

where T_N is the kinetic energy term due to the two nuclei (A,B). For higher than diatomic nuclei, this summation will be extended to include all the nuclei. T_e is the electron cloud kinetic energy term where the sum is over the total number of electrons

from the two atoms. V is the potential energy term formed from the electrostatic interaction. This interaction can be divided into interaction between nuclei and electrons and electrons' mutual interactions. We can express it as

$$V = \frac{Z_A Z_B e^2}{4\pi\epsilon_0 R} + \sum_{i>j} \frac{e^2}{4\pi\epsilon_0 |r_i - r_j|} - \sum_{n=A,B} \sum_i \frac{Z_n e^2}{4\pi\epsilon_0 |r_i - r_n|}. \quad (55)$$

The first term express the repulsive interaction between the two nuclei. Z_A and Z_B are the numbers of protons inside the nuclei in the form of the atomic number. R is the distance between the two nuclei. e is the magnitude of the proton or the electron charge. The second term represents the mutual repulsion between every two electrons at positions r_i and r_j . The summation in that term is a double summation over i and j where we drop the term when they both equal each other. The condition $i > j$ is to ensure that the same electron pair is not counted twice. The last term is the attractive potential between every nucleus at positions r_A and r_B and the electron cloud. That is why it is a double summation over the number of electrons and then for both the nuclei.

The main idea of the next step in this separation technique is to be able to write the wave function as a product of two functions. One function is "nuclear" ψ_N that depends on R and the another one is "electronic" ψ_e that depends on r_i . Since we are going to assume stationary nuclei then R is a constant. We write the molecular wave function as

$$\Psi_{molecular}(r, R) = \psi_e(r, R)\psi_N(R). \quad (56)$$

It is important to note that the ψ_e depends on R as a parameter so for every value of R there is a set of wave functions. These functions form a complete set that represents the motion of electrons in the electrostatic potential. The potential is due to the nuclei from one side and to the rest of the electronic cloud from the other side. After separating the variables, we can write the Schrodinger equation as

$$\begin{aligned} H_e \psi_e &= \left(-\frac{\hbar^2}{2m} \sum_i \nabla_i^2 - \sum_{n=A,B} \sum_i \frac{Z_n e^2}{4\pi\epsilon_0 |r_i - r_n|} + \sum_{i>j} \frac{e^2}{4\pi\epsilon_0 |r_i - r_j|} \right) \psi_e = E_e(R) \psi_e, \\ H_N \psi_N &= \left(\sum_{n=A,B} -\frac{\hbar^2}{2M_n} \nabla_n^2 + E_e(R) + \frac{Z_A Z_B e^2}{4\pi\epsilon_0 R} \right) \psi_N = E_{total} \psi_N. \end{aligned} \quad (57)$$

To be able to perform this separation, we needed to evaluate the $\nabla_i^2 \Psi_{molecular}$ and $\nabla_n^2 \Psi_{molecular}$. The first can be written as

$$\nabla_i^2 \Psi_{molecular} = \psi_N \nabla_i^2 \psi_e. \quad (58)$$

Since ψ_N is a function in R only, then we can consider it as a constant in regards to ∇_i^2 . On the other hand,

$$\nabla_n^2 \Psi_{molecular} = \psi_e \nabla_n^2 \psi_N + (\nabla_n \psi_e)(\nabla_n \psi_N) + \psi_N \nabla_n^2 \psi_e \approx \psi_e \nabla_n^2 \psi_N, \quad (59)$$

where here we used the Born-Oppenheimer Approximation. Since the electronic changes takes place almost instantly compared to the nuclear changes, we consider the nuclei fixed when we investigate the electronic motion. That is why we can neglect $\nabla_n \psi_e$ compared to $\nabla_n \psi_N$. That is the reason we end up neglecting the first two terms and end up with two separated equation.

For now, let us try to solve the electronic equation as this solution will give us the shape of the molecular potential. One of the methods used in solving this equation is using the Molecular Orbital model (MO). In this theory, we assume that the molecular orbit is formed from linear combination of the atomic orbits. That is why it is sometimes termed (MO- LCAO). As an example, we can find the molecular orbits for H_2^+ by forming a linear combination of the atomic orbits of the hydrogen atom. The atomic hydrogen ground state can be expressed in atomic units as $\phi(1s) = \pi^{-1/2} \exp(-r)$. If we looked at the H_2^+ molecule, it has a center of symmetry. We can write the molecular orbits as a linear combination of atomic orbits as follows

$$\begin{aligned} \psi_1 &= \frac{1}{\sqrt{2}} (\phi_A + \phi_B), \\ \psi_2 &= \frac{1}{\sqrt{2}} (\phi_A - \phi_B). \end{aligned} \quad (60)$$

The coefficient $\frac{1}{\sqrt{2}}$ in front of the two equations is coming from the normalization condition. It can be written as

$$\int |\psi_i|^2 dr = 1, \quad i = 1, 2. \quad (61)$$

The two wave-functions ψ_1 and ψ_2 form now a basis from which we can derive the molecular energy of the molecular system. We can use the variational method

to find the molecular energy. The molecular energy of the first two states can be written as

$$E_{1,2}(R) = \frac{\int \phi_{1,2}^* H \phi_{1,2} dr}{\int |\phi_{1,2}|^2 dr}. \quad (62)$$

We can also use the perturbation theory for a degenerate system to find the energy. To find the second order correction to the energy levels, we solve the secular determinant

$$\begin{vmatrix} H_{AA} - E & H_{AB} - ES \\ H_{AB} - ES & H_{BB} - E \end{vmatrix} = 0, \quad (63)$$

where

$$\begin{aligned} H_{ij} &= \int \phi_i^* H \phi_j dr, \\ S &= \int \phi_A^* \phi_B dr. \end{aligned} \quad (64)$$

Our Hamiltonian here has the special form because we are dealing with two hydrogen atoms so $Z_A = Z_B = 1$ and we only have one electron in the electronic clouds. The Hamiltonian can be written as

$$H = -\frac{\hbar^2}{2m} \nabla_i^2 - \frac{e^2}{4\pi\epsilon_0|r - r_A|} - \frac{e^2}{4\pi\epsilon_0|r - r_B|} + \frac{e^2}{4\pi\epsilon_0 R}. \quad (65)$$

After solving Eqn. 62, we can see that there are two behaviors: 1- For ψ_1 , there is a minimum in energy which is characteristic of an attractive potential of a stable molecule. 2- For ψ_2 , the energy of the system increases as R decreases which is a sign of a repulsive potential or unstable molecule. The state of ψ_2 is usually written with a * sign i.e. ψ_2^* to enforce that it is an anti-bonding state. This was an example for a very simple system of diatomic molecule.

For systems with higher number of electrons, we start from combinations of the atomic orbitals and build up the molecular orbits. Then we start filling up these molecular orbitals in the same way we do in the atomic analogous orbitals. When we build up the molecular orbitals out of the atomic ones, the angular momentum (orbital and spin) component along the internuclear axis is conserved. Also, the single orbital can not take more than two electrons with opposite spin according to Pauli exclusion principle.

Let us start with two atoms A and B with orbital angular momenta L_A, L_B . Their components along the internuclear axis are λ_A, λ_B . The molecular orbital angular momentum is L and its component along the internuclear axis is $\Lambda = \lambda_A + \lambda_B$. In atomic orbitals, we have the notation $\sigma, \pi, \delta, \phi, \dots$ for $\lambda = 0, 1, 2, 3, \dots$. For molecular orbitals, we have $\Sigma, \Pi, \Delta, \Phi, \dots$ for $\Lambda = 0, 1, 2, 3, \dots$. Also, if the spin of each atom is s_A and s_B , then they will combine to form a molecule with spin $\vec{S} = \vec{s}_A + \vec{s}_B$. The z-component of \vec{S} is Σ . It is conventional to choose the z-direction along the internuclear axis. In the same way we introduce the spin-orbit interaction in atoms we again have the same interaction in molecules. Its effect is to introduce a perturbation to the Hamiltonian $\hat{H} = A\vec{L}\cdot\vec{S}$. The combination between \vec{L} and \vec{S} produces the total electronic angular momentum \vec{J} . Its projection along the internuclear axis gives $\Omega = \Lambda + \Sigma$. Another very strong analogy between the atomic and molecular system is for the hyperfine interaction. The introduction of the nuclear spin \vec{I} and the interaction between \vec{I} and \vec{S} produce a further perturbation to the molecular Hamiltonian $H'' = a_{hf}\vec{I}\cdot\vec{S}$. Connected to the hyperfine interaction a hyperfine quantum number $\vec{F} = \vec{I} + \vec{S}$. We usually write the molecular levels using the notation $^{2S+1}|\Lambda|_J$. Where the $2S + 1$ is the multiplicity of the orbital. In case when $S = 0$, the multiplicity of the state is 1 and it is called a singlet state. However, when $S = 1$, the multiplicity is 3 and we have a triplet state.

Other symbols are added to the molecular orbital notation. They come from the symmetry of the electronic charge cloud under reflection through different symmetry elements. For example, the \pm symbol added sometimes to the Σ orbits. It represents the symmetry and antisymmetry of the wave-function under reflection through a plane containing the internuclear axis. This symmetry only exist for the Σ orbitals with the + sign corresponds to the symmetric wave-function and the - sign represents the antisymmetric case. Another symmetry character is the effect of the inversion of the electronic cloud through the center of symmetry. The center of symmetry is at the midpoint of the distance between the two nuclei. This symmetry only exists for homo-nuclear molecules when both the two nuclei are in the same electronic state. This symmetry is expressed as g/u sign, where g expresses the symmetric states (gerade) and u expresses the antisymmetric state (ungerade).

When looking at the molecular levels notations, we see that there are letters in front of each symbol. The ground molecular state is usually given by X notation. For all the excited states that share the same multiplicity as the ground state, they

are arranged in ascending order with capital letters notation A, B, C, D, \dots . For the excited states with the other multiplicity, they can be labeled in small letters as a, b, c, d, \dots .

Considering the available transitions between these energy levels enables us to analyze the molecular spectrum. We start by calculating the dipole matrix element $\langle \Psi_\alpha | \mu | \Psi_\beta \rangle$ for a transition between two states (α and β), where μ is the electric dipole moment. The electric dipole transition is the strongest transition in the interaction with the electromagnetic waves. The analytical solution for these matrix elements in the molecular case become more and more complicated. That is why it is helpful to use the symmetry properties. After applying the symmetry conditions, we can come out with certain rules: 1) $\Delta\Lambda = 0, \pm 1$. 2) In the transitions where the ground and the excited state are both Σ , the transitions between different \pm symmetry are not allowed. Only $+\leftrightarrow+$ and $-\leftrightarrow-$ transitions are allowed. 3) In Homo-nuclear molecules, only u states can be connected with g states, so only $u \leftrightarrow g$ transitions are allowed.

2.6.1 ROTATIONAL MOTION

When we introduce the rotational motion in the molecular orbital solution, we can, at least to a first approximation, treat the molecule as a rigid rotator. With this assumption in mind, we can consider the internuclear distance as being constant R . Hence, we can separate the rotational kinetic energy part in the Hamiltonian. The kinetic energy of the rigid rotator is $T = J^2/(2I)$ where J is the angular momentum of the rotator and I is its moment of inertia. I is given by $I = 2mR^2$ where m is the reduced mass of the molecule. In quantum mechanics, the total angular momentum is quantized and we can write J^2 as $J(J+1)\hbar^2$. Therefore, the rotational energy is written as

$$E_{rot} = \frac{\hbar^2}{2mR^2} J(J+1) = BJ(J+1), \quad (66)$$

where $B = \hbar^2/(2mR^2)$.

Now to consider the available transitions in a pure rotational state, we need to solve the matrix elements of the electric dipole transition $\langle \Psi_{JM} | \vec{\mu} \cdot \vec{E} | \Psi_{J'M'} \rangle$ [63]. We will use that $\vec{\mu} = \mu_0 (\sin\theta\cos\phi \hat{x} + \sin\theta\sin\phi \hat{y} + \cos\theta \hat{z})$. This means that $\vec{\mu} \cdot \vec{E} = |\mu_0||E| (\sin\theta\cos\phi + \sin\theta\sin\phi + \cos\theta)$. Calculating the matrix element will be

$$\begin{aligned}
\langle \Psi_{JM} | \vec{\mu} \cdot \vec{E} | \Psi_{J'M'} \rangle &= |\mu_0| |E| \int_0^{2\pi} \int_0^\pi P_J^M(\cos\theta) e^{-iM\phi} \\
&\times (\sin\theta \cos\phi + \sin\theta \sin\phi + \cos\theta) P_{J'}^{M'}(\cos\theta) e^{+iM'\phi} \sin\theta d\theta d\phi.
\end{aligned} \tag{67}$$

This integral will vanish unless 1) $\Delta J = \pm 1$ or 2) $\Delta M = 0, \pm 1$. For the molecule to have pure rotational spectrum it must have a permanent dipole moment $\mu_0 \neq 0$. For the first selection rule, there is an exception when the transition happens in $\Lambda \neq 0$ levels. This takes place when the electronic transition is accompanied by an opposite and equal change in the nuclear angular momentum which will add up to no change in J . That is why we can replace the first selection rule by two cases: a) $\Lambda = 0, \Delta J = \pm 1$ and b) $\Lambda \neq 0, \Delta J = 0, \pm 1$. In addition to that, the third selection rule implies that for homo-nuclear molecules there is no pure rotational spectral lines as these molecules do not have a permanent dipole moment. For these molecules the rotational spectrum is observed on top of the electronic spectrum [9]. The pure rotational spectrum will be generated from molecules moving between molecular levels with a total angular momentum change $J \leftrightarrow (J + 1)$. The photon's energy will be

$$h\nu_{(J+1) \rightarrow J} = E_r(J + 1) - E_r(J) = 2B(J + 1). \tag{68}$$

This result could be interpreted that the rotational levels are equally spaced and displaced by $2B/h$. This is the ideal case. When we start taking into account the effects of the vibration of the nuclei and the change of the internuclear distance, then this will create a more complicated spectrum. The change of the internuclear distance usually takes place as a result of centrifugal force in the rotating molecule which is called centrifugal distortion. The effect of the centrifugal distortion is to add $-2DJ^2(J + 1)^2$ to the rotational energy, where $D = \hbar^4/2m^2R^6K$ and K is the force constant for the vibrational motion [63].

2.6.2 VIBRATIONAL MOTION

The second splitting in the molecular energy levels is a result of the molecular vibrational motion. We start by assuming no translational or rotational motion by the two nuclei in the molecule and so the only available motion is the vibrational motion. We can approximate it with a simple harmonic motion. The vibration of the nuclei about their equilibrium position will cause the internuclear distance to vary

from R to r . The Hamiltonian of the molecule as a function of r can be written as a Taylor expansion series around R [63]. This is shown as

$$H(r) = H_0 + \left(\frac{\partial H}{\partial r}\right)_{r=R} (r - R) + \frac{1}{2} \left(\frac{\partial^2 H}{\partial r^2}\right)_{r=R} (r - R)^2 + \dots \quad (69)$$

The higher order terms were neglected compared to the first three terms. The second term vanishes. This is because the potential has a minimal at the equilibrium internuclear distance R which will make the first order derivative vanishes. We can now write the perturbation part of the Hamiltonian due to the vibrational motion as

$$H'_{vib} = \frac{1}{2} K (r - R)^2, \quad (70)$$

where K is the vibrational restoring force constant. K can be written as

$$K = \left(\frac{\partial^2 H}{\partial r^2}\right)_{r=R} \quad (71)$$

The energy shifts due to this perturbation gives

$$E_{vib} = \hbar\omega \left(\nu + \frac{1}{2}\right), \quad \omega = \sqrt{\frac{K}{m}}, \quad (72)$$

where ν is a the vibrational quantum number and can take 0, 1, 2, 3, Analysis of the molecular spectrum arising from the vibrational motion leads to the selection rule $\Delta\nu = \pm 1, \pm 2, \pm 3, \dots$. We can see that by looking at the dipole matrix element for the transition. In this case since the change is coming from r then integration will be simplified to be only over μ as it will change with r . In other words, we can simplify the integration $\langle \Psi_\alpha | \vec{\mu} \cdot \vec{E} | \Psi_\alpha \rangle$ so that we can only consider integration over μ or $\langle \nu | \mu | \nu' \rangle$. With expanding the μ around R with Taylor expansion, we can get

$$\mu(r) = \mu_0 + \left(\frac{\partial \mu}{\partial r}\right)_{r=R} (r - R) + \frac{1}{2} \left(\frac{\partial^2 \mu}{\partial r^2}\right)_{r=R} (r - R)^2 + \frac{1}{6} \left(\frac{\partial^3 \mu}{\partial r^3}\right)_{r=R} (r - R)^3 + \dots \quad (73)$$

We should note that as we go into higher order terms, they get smaller by orders of magnitude. When we use this expansion in the integration, we will get the selection rules. From the term with $(r - R)$, we can drive the condition $\Delta\nu = \pm 1$. From

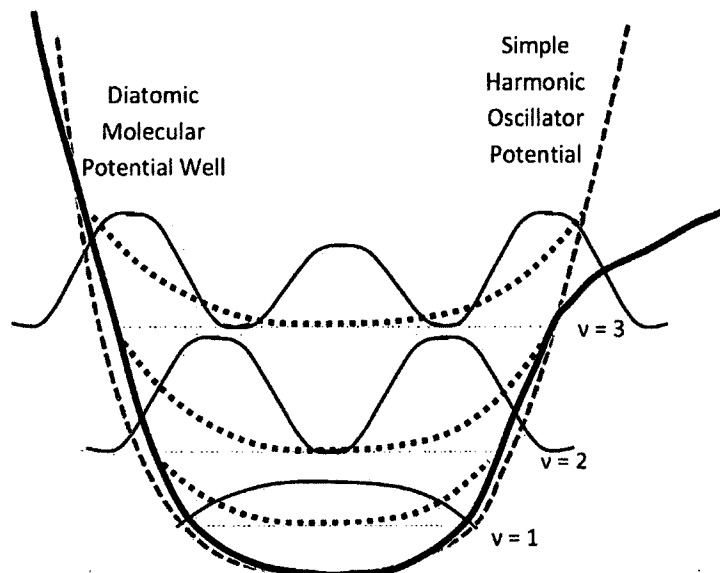


FIG. 14: The green dashed curve represents the harmonic oscillator potential. The black curve represents the diatomic potential curve. The red wave-functions represent the probability distribution of the electrons in each vibrational state. The blue dashed wave-functions represent the probability distribution for a classical oscillator which is confined inside the potential well [9]. The probabilities are shown for $\nu = 1, 2, 3$.

the term with $(r - R)^2$, we get the condition $\Delta\nu = \pm 2$ and so on. That is why the spectral line with $\Delta\nu = \pm 1$ are stronger and easier to see than $\Delta\nu = \pm 2$.

2.7 FRANK-CONDON THEORY

We mentioned before that there are selection rules for transitions between two vibrational states that belong to the same molecular level. For transitions between two vibrational states belonging to different molecular structure potentials, a few considerations come into play. The first consideration is imposed from the assumption that the masses of the nuclei are much bigger than the masses of the electrons. That is why the nuclei motion will be much slower than the electron motion. From this assumption, it is safe to say that the nuclei are considered almost stationary during the electronic transitions. That is why on the molecular potential curves, the transitions are denoted by vertical line between the two potentials to resemble the same internuclear separation R as a consequence of having stationary nuclei. This is the Frank-Condon principle.

The second assumption rises as a result of the probability distribution of electrons in real diatomic molecules. In real diatomic molecules, the vibrational potential is deviated from the pure harmonic oscillator case as shown in Fig.14. The diatomic potential well $w(x)$ can be written as a Taylor expansion around the potential minimum $x = a$. $w(x) = w(a) + (x - a)w'(a) + \frac{1}{2}(x - a)^2w''(a) + \dots$. Since the point a is a minimum so $w'(a) = 0$ and $w''(a) > 0$. Substituting this into the Schrodinger equation we get the linear harmonic oscillator equation

$$\frac{d^2\psi}{d\xi^2} + (\lambda - \xi^2)\psi = 0, \quad (74)$$

where

$$\xi = \alpha x, \quad (75)$$

$$\alpha = \left(\frac{mk}{\hbar^2}\right)^{1/4}$$

The solution to this equation takes the form of Hermite Polynomials. The probability distribution of the electrons in the vibrational states will take the form shown in the Fig. 14. From studying those probability distributions, we can note that the probability is highest for the first vibrational state around the middle of the well. Also for the first state, the probability around the turning points is very small. As we go higher and higher in vibrational states, the probability around the turning point gets higher and higher as the motion approaches the classical limit.

Using the Frank-Condon principle [9, 63] and the vibrational probability distribution, we can interpret which transitions will have higher probability. Let us study the vibrational structures in different molecular potentials illustrated in Fig. 15. We can see the absorption and emission spectrum observed by applying the Frank-Condon Principle. For example, the transitions starting from the $\nu = 1$; for this state the electron has higher chance of being located around the middle. When this electron goes up “vertically”, it will meet the states $\nu = 6$ and $\nu = 7$ around their turning points where they have the high electronic density. Similarly, for emission spectrum, we start from $\nu = 1$ (high probability around middle) and end at $\nu = 4$ and $\nu = 5$ (high probability around turning points). Another transition that does not happen to or from the ground state is shown and we can see that it happens between the two turning points. That is where the electronic distribution is highest or in other words where electrons spend more time.

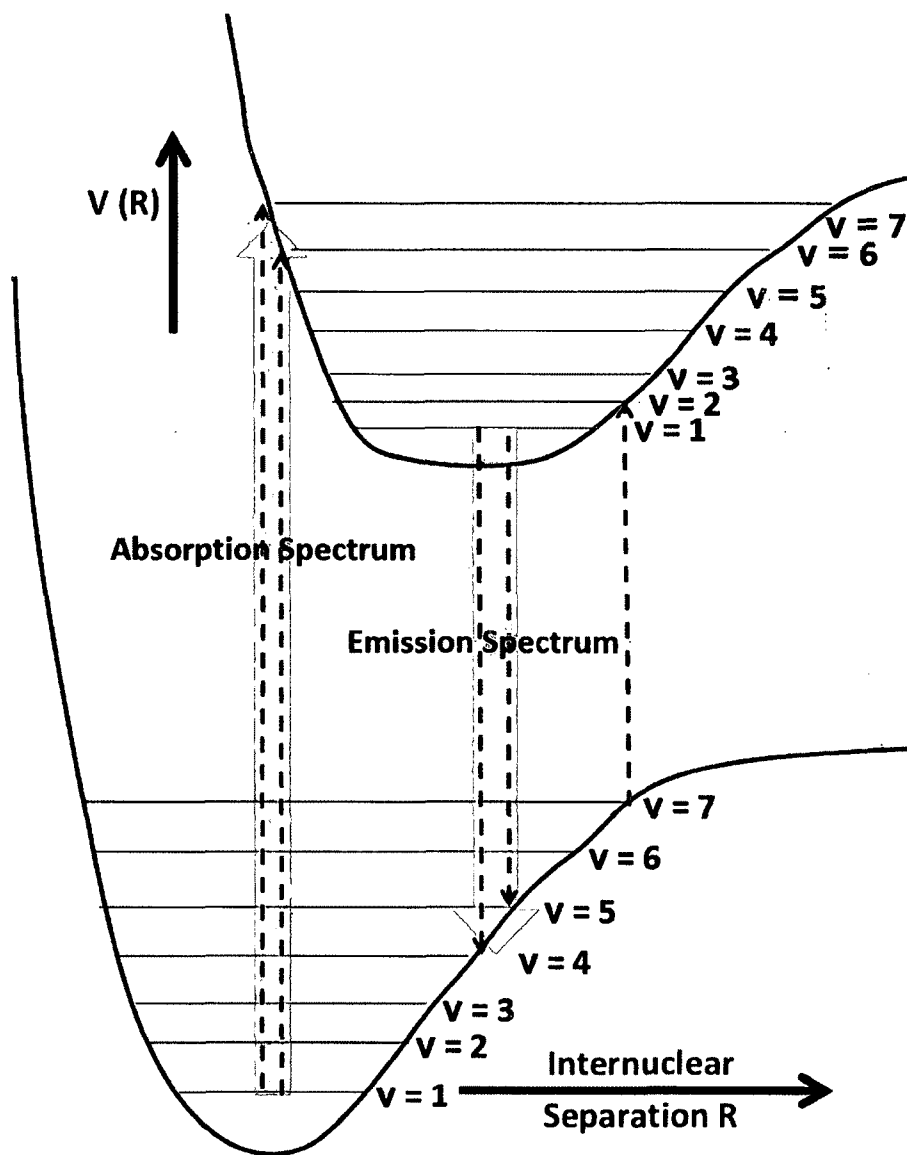


FIG. 15: The electronic transitions between the vibrational levels in different molecular potentials. The figure illustrates the Frank-Condon Principle. Transitions from $\nu = 1$ sub-states are more likely to start from the middle of the potential well. Transitions to other higher vibrational levels are more likely to happen around turning points.

2.7.1 LONG RANGE INTERACTIONS

One of the molecular structures that we are interested in here is the long range and the purely long range state. The structure of the molecule along with the chemical and physical properties depend mainly of the internuclear separation. At large internuclear separations, the molecular potential can be derived using the interaction between the potential of the separated atoms [9]. When two atoms in s state form a molecule, the interaction potential rises from the attraction between the induced dipole in each atom. This interaction is called van der Waals interaction and can be expressed mathematically in terms of $-C_6/R^6$, where C_6 is a van der Waals dispersion coefficient. Mathematically, we can obtain the $1/R^6$ dependence from solving the perturbation second order energy shift as

$$E^{(2)} = \sum_{j \neq 0} \frac{\langle \psi_0 | V | \psi_j \rangle \langle \psi_j | V | \psi_0 \rangle}{E_0 - E_j}, \quad (76)$$

where $\psi_0 = \psi_{1s}(r_{1A})\psi_{1s}(r_{2B})$ and ψ_j are the wavefunction of the intermediate states. In this case the ψ_j s are of the form $\psi_{nlm}(r_{1A})\psi_{n'l'm'}(r_{2B})$, with n and $n' \neq 1$. The energy denominator is given (in atomic units) by $(E_0 - E_j) = (-1 + 1/2n^2 + 1/2n'^2)$, with both n and n' greater than 1. This means that the denominator is always negative. This derivation was done for Hydrogen atoms and the expansion to other atoms is possible following the same technique. The potential operator used in the brackets are obtained from Eqn. 55 for two Hydrogen atoms. The numerator is positive and behaves like $1/R^6$. This will lead to a van der Waals long range interaction between the two Hydrogen atoms in ground states. The potential here has the form of the interaction energy between two dipoles as

$$V = \frac{1}{R^3} \left[D_1 \cdot D_2 - 3 \frac{(D_1 \cdot R) \cdot (D_2 \cdot R)}{R^2} \right], \quad (77)$$

where D_1 is the dipole moment formed by the proton and electron from the first atom. D_2 is the dipole moment formed by the proton and electron from the second atom. It is important to note that the first order energy shift vanishes for such states. This is because the matrix elements of the angular dependent terms are zero when taken between spherically symmetric wavefunctions [9].

Generally, we can tie the van der Waals interaction potential in long range states to three effects [65]. The first effect comes from the dispersion effect of perturbing the ground molecular state by higher states. The second effect is the induction effect

which comes from the non-spherical charge distribution in molecules that induce a dipole moment. The third effect which arises when the molecule has a dipole moment of its own. When the two atoms are identical but in different energy levels symmetry considerations can change the leading term of the potential from $1/R^6$ dependence to $1/R^3$.

In homo-nuclear molecules, when one of the two atoms is in the P state and the other one is in the S state, then the potential is coming from resonant dipole-dipole interaction [8]. This is the case for either alkali-metal or metastable noble gas atoms. Classically, this corresponds to an inductive force. In other words, the charge distribution of one atoms is being perturbed by the field set by the permanent moment of the other atom. The resulting induced moments interact with the permanent moments. A detailed derivation of the interaction potential can be found in Ref. [66]. This type of interaction can be attractive or repulsive depending on the orientation of the dipole in each atom relative to the other atom. The resonant dipole-dipole potential interaction can be expressed as $\pm C_3/R^3$. The \pm sign is used to give the potential the attractive and the repulsive character and C_3 is the potential constant.

For hetero-nuclear molecules, when one of the atoms is in the S state and the other one is in the P state, then the interaction between these two atoms behaves as $1/R^6$. In some alkali molecules and noble gases in their metastable state, when the two constituent atoms are in excited states, there would be some contribution from a $1/R^5$ term (for example, two atoms in a P state) [66].

The usual theoretical method is to put empirical forms with constants that are determined from experiment. For the molecules that we are studying in our experiment, they are homo-nuclear molecules for nobles gases (Ar and Kr). One molecular state consists of two s state atoms with potential interaction as $1/R^6$. The second molecular state arises from one S atom and one P atom. It has its long range behavior as $1/R^3$. A diagram of the long range interaction potential is shown in Fig. 16.

To summarize, when the two atoms are in the $S+S$ state, the interaction between them takes the form of van der Waals interaction or R^{-6} . This is the original state of our noble gas atoms. When the two atoms are identical and in the $S+P$ state, the interaction between them takes the form of dipole-dipole interaction or C_3/R^3 . This is the case for the first atomic excitation of the sample. When the two atoms are in the $P+P$ state, the interaction between them takes the form of quadrupole-quadrupole

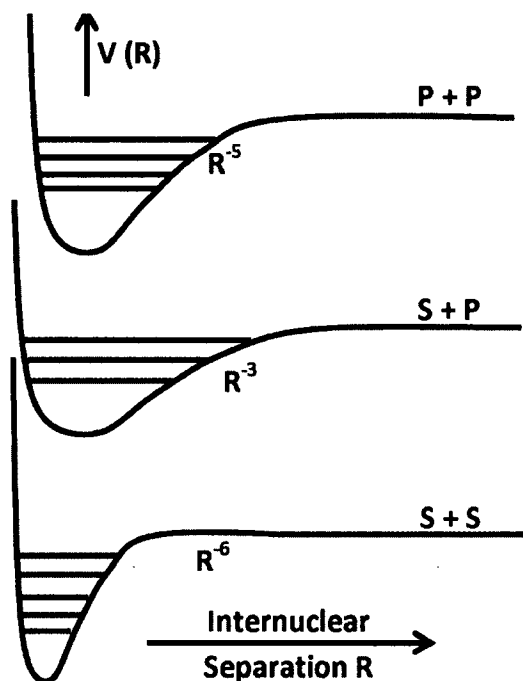


FIG. 16: Diagram of the long range interaction potential between two atoms as a function in the internuclear separation for different atomic energy level limits.

interaction or R^{-5} . This is the case for our system of doubly atomic excited states. Every potential curve branches out at small R to repulsive and attractive curves. These curves further branch to different angular momentum components. Combining all of these effects create very complex potential maps. Example for these maps is shown in Fig. 17 for both argon and krypton.

Studying these molecular potentials in more detail produces the very fascinating features of long range and purely long range states. “Long range states” are produced when the outer turning points in the molecular attractive potential happen at very large internuclear distances. The turning point takes place close to the dissociation limit, which resembles the point where the two atoms have minimal interaction and no more form a molecule. That makes molecular characters very close to the free atoms character. In theoretical terms, molecular parameters at this point can be approximated using atomic terms. On the other hand, “pure long range states” result from the application of the non crossing rule in the molecular levels. The von Neumann-Wigner non-crossing rule [9] states that in order for two levels to have the

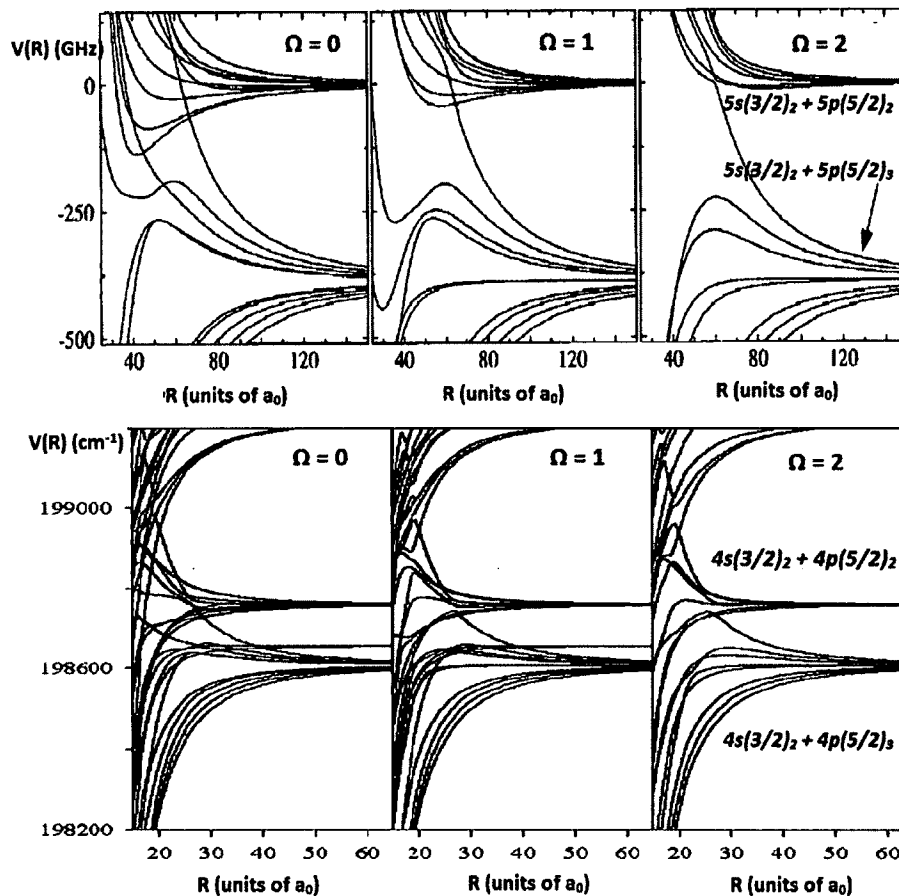


FIG. 17: The upper curves represent the diatomic potential curves for Kr around the asymptotes $5s(3/2)_2 + 5p(5/2)_2$ and $5s(3/2)_2 + 5p(5/2)_3$, for $\Omega = 0, 1, 2$. The asymptote $5s(3/2)_2 + 5p(5/2)_2$ is taken as the zero energy for the curves [10]. The lower curves represent the diatomic potential curves for Ar [11] around the asymptote $4s(3/2)_2 + 4p(5/2)_2$ and the asymptote $4s(3/2)_2 + 4p(5/2)_3$, for $\Omega = 0, 1, 2$.

same energy, they must have different symmetry. Different symmetries correspond to two electronic terms having different values of Λ , different parities g/u , different multiplicity or terms Σ^+ and Σ^- . Non-crossing between a low energy repulsive curve and a higher energy attractive potential well result in very shallow minima on the repulsive curves. They are shown on some potential curves in Fig. 17. These minima can support molecular structures at much longer internuclear separation than in chemical compounds $\sim 70a_0$. In other words, stable molecules can be created at these minima where the internuclear distance is order of magnitude higher than in normal chemical molecules.

2.8 COLD MOLECULAR PRODUCTION

Photo-associative spectroscopy (PAS) of ultra-cold atoms provides a very strong tool of studying molecular structure. The most fascinating fact about this type of PAS is that the original sample of atoms is really cold to begin with (less than 1 mK). This means that the spread in kinetic energy of the atoms is minimal. In other words, spectrum does not suffer from the thermal broadening of the atomic levels. This very important feature assures a very high resolution in the spectrum. Another important advantage of PAS is that the two atoms that feature our starting point are free (unbound). The two atoms get excited to higher energy levels by a red detuned beam. If they are close enough, they start accelerating towards each other moving towards the minimum of the molecular potential. When it is time for the two atoms to return to their original “ground” state, they will emit a photon. They return either to the molecular bound state or to molecular repulsive state creating two separated atoms. By monitoring the energy of the photon incident and the photon emitted, we can always calculate the binding energy of the stable molecule. The binding energy is calculated relative to the separated atoms extreme which gives a good measure of the absolute binding energy.

The reason of PAS' importance is that since it starts off from cold atoms, the molecules created are transitionally cold as well. That provides a very strong tool to create cold molecules alternative to cooling a sample of hot molecules by different techniques. Those molecular cooling techniques vary between optical deceleration, Stark deceleration, buffer gas cooling and many more techniques that the reader can find more detailed description of in Ref. [12]. Figure 18 shows different cooling techniques of the molecules. They were not able experimentally to provide as low temperatures and velocity distribution as provided by the photo-association techniques.

As we explained before, the atomic collisions and the photo-association processes between two free atoms depend on the initial state of the two atoms. Attractive potentials are curves which show a minimum and hence can support a stable molecule. Along this potential minimum, vibrational sub-level splitting takes place. For every minimum shown in Fig. 16, vibrational sub-levels build up. Those sub-levels are so closely spaced that their measurements require a very high resolution technique. Another important advantage of PAS is that it is able to map out these vibrational levels since it has high enough resolution.

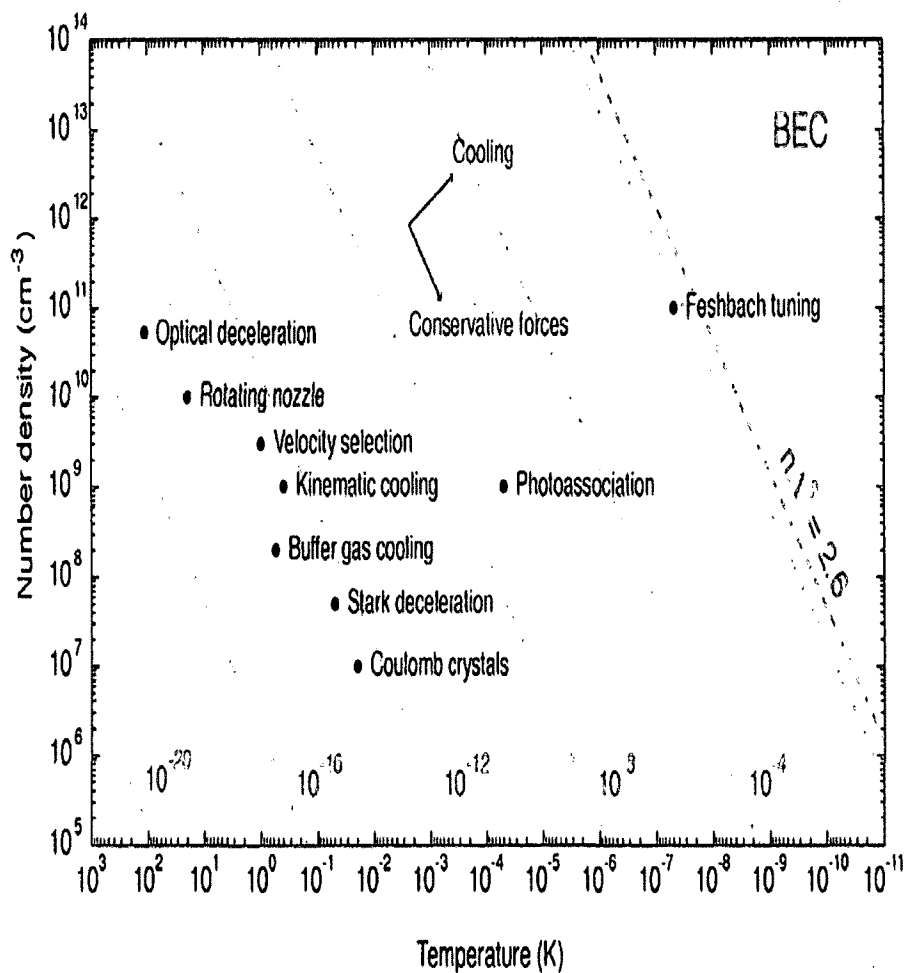


FIG. 18: Current techniques for producing cold molecules. The values for temperature and density are provided from experimental data taken with every single technique[12].

Another important aspect of applying PAS is populating long range states and purely long range states. These levels are easily excited from the two free atom regime than from the compound molecular regime since they happen near the dissociation limit. Finally, PAS can also provide an important tool in atomic lifetime precision measurements and in ground state scattering length determination. The scattering length parametrizes the extreme low-energy scattering properties and is connected to the phase shift atoms experience in a collision. The sign of the scattering length determines the stability of the Bose-Einstein condensate [62].

2.9 THE LEROY-BERNSTEIN FORMULA

Many theoretical models were introduced that help to analyze the vibrational and rotational features that appear on the diatomic molecular spectrum. Those models help to analyze the features of the molecules by looking at the spectrum and then calculating the molecular potential constants from it. These formulas can be used to calculate the potential constants from the frequencies at which vibrational or rotational features appear in the spectrum. To understand this more, let us explain one of these formulas that is applicable when the spectra are near the dissociation limit. A detailed explanation of different theoretical techniques is explained in [67].

There are two ways to link between the molecular parameters and the electronic wavefunctions. The first way is the semi-empirical method. This method provides a physical picture that explains the molecular parameters. The second method is the ab initio method which relies on quantum chemistry providing a much more complicated picture. It uses the experimental values to test the accuracy of these methods. The LeRoy - Bernstein formula starts from a semi-classical method called the (Jeffreys-Wentzel-Kramers-Brillouin) method or JWKB method. This method starts from the Schroedinger equation as

$$\hbar^2 \frac{d^2\psi}{dR^2} + \{2\mu[E - V(R)]\}\psi = 0. \quad (78)$$

We assume that the solution to this equation takes the form

$$\psi = \exp[iX(R)/\hbar]. \quad (79)$$

Substituting this in the Schroedinger equation, we have

$$-\frac{\hbar^2}{2\mu} \left\{ -\psi(R) \left[\frac{X'^2(R)}{\hbar^2} - \frac{iX''(R)}{\hbar} \right] \right\} = [E - V(R)]\psi(R), \quad (80)$$

where $X'(R)$ and $X''(R)$ are the first and second derivative of $X(R)$ with respect to R . From this equation we can have

$$X'^2(R) - i\hbar X''(R) = 2\mu[E - V(R)]. \quad (81)$$

If we expand the phase function $X(R)$ in powers of \hbar , we can have

$$X(R) = X_0(R) + \hbar X_1(R) + \frac{\hbar^2}{2} X_2(R) + \dots \quad (82)$$

From which we can calculate the first and the second derivatives as follows

$$\begin{aligned} X'^2(R) &= [X'_0(R) + \hbar X'_1(R)]^2, \\ X'^2(R) &= X_0'^2(R) + \hbar^2 X_1'^2(R) + 2\hbar X'_0(R)X'_1(R), \end{aligned} \quad (83)$$

$$-i\hbar X''(R) = -i\hbar X_0''(R) - i\hbar^2 X_1''(R).$$

We then substitute this in Eqn. 81 and compare the terms with the same order of \hbar . For \hbar orders of 0, 1, 2 respectively, we will have

$$\begin{aligned} X_0'^2(R) &= 2\mu[E - V(R)], \\ 2X'_0(R)X'_1(R) - iX_0''(R) &= 0, \end{aligned} \quad (84)$$

$$X_1'^2(R) - iX_1''(R) = 0.$$

From the first and second equations, we have

$$\begin{aligned} X_0(R) &= \pm \int \sqrt{2\mu[E - V(R)]} dR, \\ X_1'(R) &= \frac{i X_0''(R)}{2 X_0'(R)}, \end{aligned} \quad (85)$$

$$X_1(R) = i \ln \left[\sqrt{X_0'(R)} \right].$$

When we substitute this in the wavefunction, we get

$$\begin{aligned}
\psi_{\pm}(R) &= \exp [iX(R)/\hbar], \\
&= \exp [iX_0(R)/\hbar + iX_1(R) + \dots], \\
&\simeq \frac{1}{\sqrt[4]{2\mu[E-V(R)]}} \exp \left[\pm i/\hbar \int \sqrt{2\mu[E-V(R)]} dR \right],
\end{aligned} \tag{86}$$

where the factor $\frac{1}{\sqrt[4]{2\mu[E-V(R)]}}$ is a result from the normalization condition for the wavefunction. It is also very important to note that the JWKB formula is good between the two turning points in the potential well. Let us call them R_1 and R_2 . The turning points are points where $E - V(R) = 0$ and hence beyond which the electron can not exist classically. The region $R_1 < R < R_2$ is the part of the potential where $\psi(R)$ is non zero and real. It is also the part where $\psi(R)$ has the oscillatory behavior. That is why it is very valuable to write the wavefunction in a real form as

$$\begin{aligned}
\psi(R) &= \frac{B}{\sqrt[4]{2\mu[E-V(R)]}} \sin \left[\frac{1}{\hbar} \int_{R_1}^R \sqrt{2\mu[E-V(R)]} dR + \frac{\pi}{4} \right], \\
&= \frac{B'}{\sqrt[4]{2\mu[E-V(R)]}} \sin \left[\frac{1}{\hbar} \int_R^{R_2} \sqrt{2\mu[E-V(R)]} dR + \frac{\pi}{4} \right].
\end{aligned} \tag{87}$$

The two equations represent the solution around the two turning points. They ensure the proper connections around $R = R_1$ and $R = R_2$ respectively. The connection between the two will yield the Bohr-Sommerfeld quantization condition where $B' = B(-1)^\nu$. The numerical evaluation of the integral will yield

$$(\nu + 1/2)\pi = \frac{\sqrt{2\mu}}{\hbar} \int_{R_1}^{R_2} \sqrt{E - V(R)} dR. \tag{88}$$

The LeRoy-Bernstein method [68] starts off from this formula. It applies this equation in the case of long range interaction for vibrational structures that are near the dissociation limit. The spectra that we will report later are comprised of scans about 6 GHz around the atomic transition. The dissociation frequency is the light frequency corresponding to exciting to two separate atoms i.e. the atomic transition limit. This makes the accessible vibrational structures by our laser near the dissociation frequency. We can approximate our potentials as power series of the inverse of the internuclear separation distance R as

$$V(R) = D_e - \sum_n \frac{C_n}{R^n}. \quad (89)$$

where D_e is the dissociation limit and the n is the strength of the interaction between the two atoms. The n order depends on the two electronic structures of the separated atoms as

- $n = 1$ for Coulomb potential interaction between two charged atoms.
- $n = 2$ for interaction between a charged atom and a permanent electric dipole attached to an electronic state to the other atom.
- $n = 3$ for dipole interaction between either two atoms with permanent dipole moment or between two identical atoms in different electronic states and their angular momenta should be different by 1.
- $n = 4$ for interaction between a neutral atom and a charged atom or ion.
- $n = 5$ for quadrupole-quadrupole interaction between neutral atoms that have a non-zero angular momentum.
- $n = 6$ for van der Waals interactions between two induced dipoles.

The LeRoy-Brenstein Formula evaluates these potentials coefficients C_n and D_e to get a better picture of the interaction potential between the two atoms. if we take the derivative of Eqn. 88 with respect to $E(\nu)$ which is the energy of the vibrational state ν , we will have

$$\frac{d\nu}{dE(\nu)} = \frac{\sqrt{2\mu}}{2\pi\hbar} \int_{R_1}^{R_2} [E(\nu) - V(R)]^{-1/2} dR. \quad (90)$$

At the turning point R_2 , the energy of the vibrational level is given by

$$E(\nu) = V(R_2) \simeq D_e - \frac{C_n}{[R_2]^n}. \quad (91)$$

We can rewrite the integral with the potential term as

$$\frac{d\nu}{dE(\nu)} \simeq \frac{\sqrt{2\mu}}{2\pi\hbar} \int_{R_1}^{R_2} [E(\nu) - D_e + \frac{C_n}{R^n}]^{-1/2} dR. \quad (92)$$

The evaluation of this integral is explained in [67, 68]. After evaluation of the integral we have

$$\frac{d\nu}{dE} = \zeta_n [D_e - E(\nu)]^{\frac{n+2}{2n}}, \quad (93)$$

$$\zeta_n = \frac{2\pi\hbar n}{\sqrt{2\mu}} \frac{1}{\sqrt[n]{C_n}} \frac{\Gamma(1 + 1/n)}{\Gamma(1/2 + 1/n)}.$$

If we express $m = 2n/(n - 2)$, then we can rewrite the relation between $E(\nu)$ and ν as

$$\begin{aligned} \frac{dE}{d\nu} &= m \left[\frac{\zeta_n}{m} \right]^m (\nu_D - \nu)^{(n+2)/(n-2)}, \\ E(\nu) &= D_e - \left[\frac{\zeta_n}{m} \right]^m (\nu_D - \nu)^m, \end{aligned} \quad (94)$$

where ν_D is the energy level corresponding to the dissociation limit. The application of this method on the experimental data are used by applying $E(\nu + 1)$ and $E(\nu)$ to approximate $\frac{dE}{d\nu}$. This method can also be extended to include the rotational substructure as well [67, 69].

2.10 ION PRODUCTION IN THE MOT

Before explaining the details of PAS technique used in our experiment, let us describe one of the complications of our PAS technique. This will help us when explaining PAS to tell the real from the artifact signal. As we will describe in the next chapter, in our experiment, our detection method is through ion detection. That is why it is very important to understand the sources of ions produced in our experiment which are:

1. The discharge ions.

The atoms we are using in our experiment are noble gases and they need to be excited to the metastable state from the ground state. From the metastable state, they go through further optical transitions and then are loaded to the MOT. An rf discharge is used to pump the atoms into the metastable state.

The main idea of the rf discharge is to establish a high potential across the gas that causes atoms to ionize. As the electrons accelerate towards the electrodes, they ionize more and more atoms through collisions. During collisions, the energy transfer is high enough to excite the atoms to the metastable state. By understanding the rf discharge [70], we can see that not only can the atoms

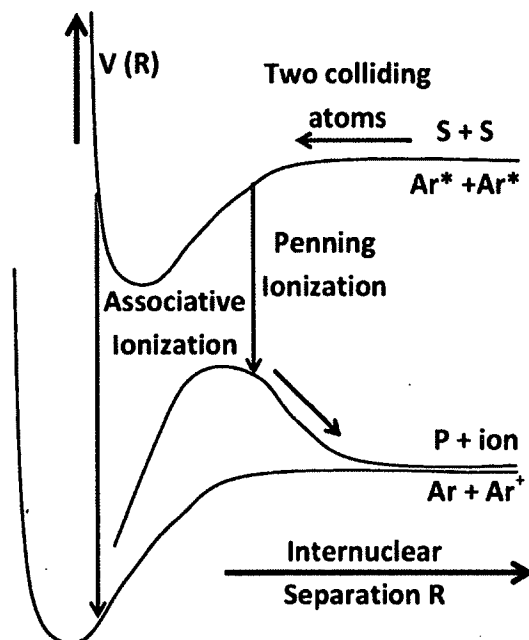


FIG. 19: The graph shows the ions created in the MOT during collisions between metastable state atoms. The Penning (PI) and the Associative ionization (AI) processes are shown.

excite to the metastable state, but also this rough environment can create ions (both single atom ions and molecular ions). These rf discharge ions are detected on our detection techniques. They form our background on our ion signal.

2. The MOT ions.

Inside the atomic cloud in the MOT, some atoms are very close to each other. In addition to having short internuclear distances, the atoms goes through constant collisions with both each other and the MOT trapping beams. During our data collection, the trapping beams are off. This means that for our discussion of collected ions during spectrum measurement, we can neglect interaction with the laser cooling and trapping beams. On the other hand, colliding metastable state noble gas atoms can still ionize.

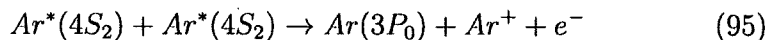
Fig. 19 shows two ions creating processes that take place in the MOT even without the presence of any light. The graph shows the molecular potential for both two atoms in their metastable states. For example, argon is shown in the

Fig. 19 but it is important to understand that the same discussion holds for krypton as well. The lower curve is for the interaction potential between one argon atom in its ground state and one singly ionized argon atom.

We should mention here that the energy used to pump two argon atoms in their metastable state is greater than the energy consumed to ionize one atom. It is also important to note that every molecular interaction potential has both attractive and repulsive parts to it. The attractive part leads to a stable molecule formation. When the atoms undergo interaction on the repulsive curve they start accelerating further apart from each other until they form a stable version of two separated atoms. It is important to note that both PI and AI processes are non radiative and the excess energy is carried by an electron or an atom. Whether the atoms interact along the potential curve and end up in attractive or repulsive curve will give us Associative or Penning Ionization respectively:

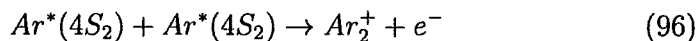
- Penning Ionization (PI):

When two atoms approach each other along the $Ar^* + Ar^*$ curve, they start accelerating towards each other. After sometime (depending on their metastable state lifetime), they may lose their energy through ionization. If they end up in a repulsive curve, they start accelerating further from each other and we get the stable separated argon ion and argon atom in its ground state. Mass spectrometer measurements done by H. Busch on our experiments shows that this technique is more dominant and creates more ions [13]. This is explained in the equation:



- Associative Ionization (AI):

When the two atoms undergo the transition to the attractive ion potential, they form a stable molecular ion of argon. So that the atoms end up in this state, the atoms have to get very close to each other in a very short period of time before their metastable state lifetime ends. This is shown in the equation:



3. Photoassociation ions.

These are the ions we are interested in and they are created by adding a PA photon to the colliding atoms. Depending on the frequency of this photon, the atoms' interaction changes and hence the number of ions created changes as well. These ions are still formed by Penning or associative ionization, but they are "light-assisted". We will explain this in more details in the next section.

2.11 PHOTOASSOCIATION SPECTRA

The course of our experiment starts from a sample of cold atoms confined in a MOT. As two atoms in the MOT approach each other, we act on them with an additional photon (PA photon). We scan the frequency of this photon over a wide range of frequencies about the resonance frequency of an atomic transition. By scanning the photon frequency, we hope to map out excited molecular states. As the frequency changes, the photon populates different molecular potentials. Molecular potential has attractive and repulsive branches. Attractive molecular potential houses vibrational sub-levels with discrete energy (the spacing between the vibrational sub-levels decreases as we go higher and higher in energy). What we were hoping to see here is the absorption of the PA photon following this somewhat discrete pattern. By studying the PA spectra, we should be able to resolve these vibrational structures especially using our high resolution technique.

In terms of ion counts, the course of our experiment starts by loading the MOT from the rf discharge, until a full MOT is loaded. This is detected as an offset on the ion counts from ions produced by the rf discharge. When the MOT is finally loaded, a higher ion count is obtained through the processes of PI and AI. The higher the density of the MOT, the closer the atoms will be to each other. This will lead to a higher rate of PI and AI and hence a higher ion count. In fact, ion count levels generated by the MOT and the discharge are constantly monitored to ensure a stable MOT and same initial conditions for all the experiments. After the MOT is fully loaded, we turn off our MOT loading beams. At the same time we send the PA photons meanwhile collecting the ions created. Figure 20 illustrates that the PA ion counts depends on the frequency of the incident PA photon as follows:

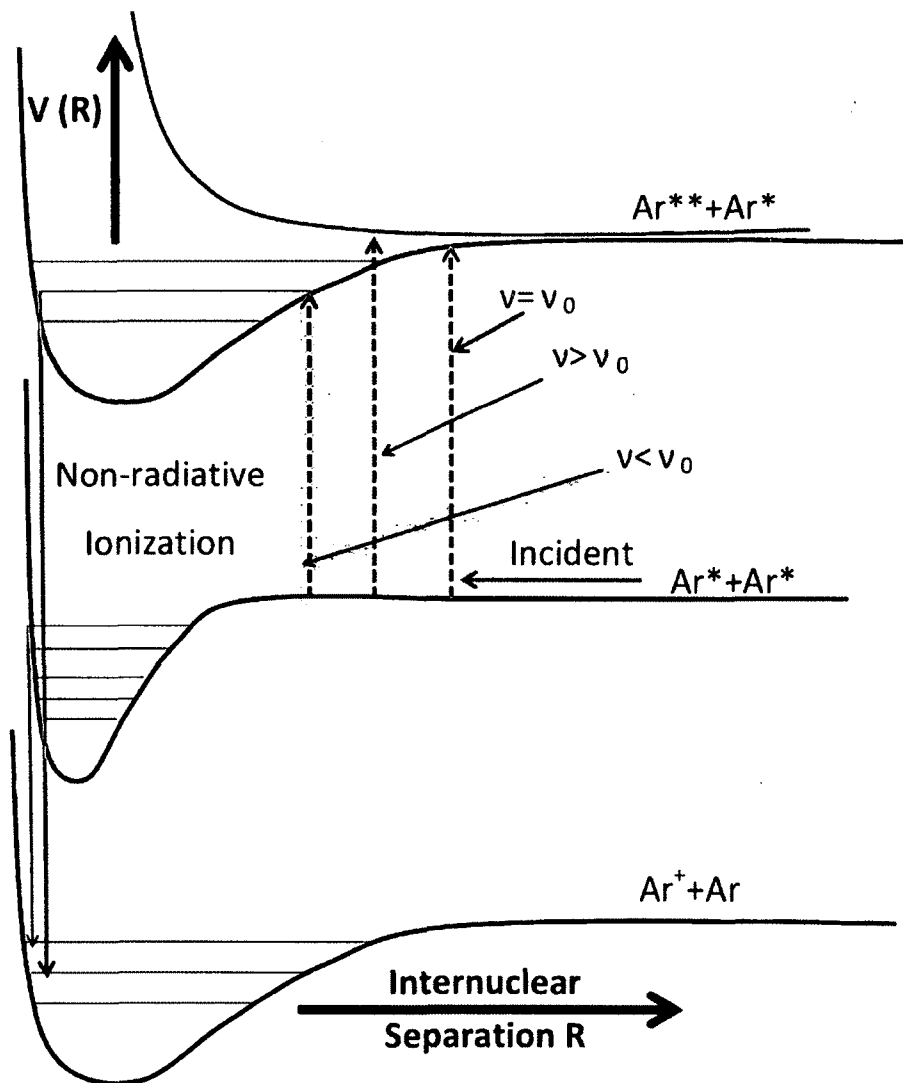


FIG. 20: The figure shows the photoassociative ion production. The probability of ions being created depends on the frequency of the incident photons. The blue line is used for blue detuned beams and the red line is used for the red detuned beam. The orange line is for on resonance beams. The dashed lines are for photon absorption transitions and the straight lines are for non-radiative ion production.

- Resonance Photons ($\nu = \nu_0$):

At this frequency, the detuning of the PA beam is zero $\delta = 0$. Using Eqn. 34, we see that the scattering force is maximum at resonance. This means that the light has the maximum force of kicking the atoms out from the trap. Note that the MOT loading beams are off when the PA beam is on. That is why the PA beam kicks the atoms out from the expanding MOT atomic cloud. Also the molasses force Eqn. 46 will be zero, hence we can not claim that the two counter propagating PA beams will cancel each other's effect. Their effect will not be to slow down the atoms but to kick the atoms from the trap. That provides a non-ionizing loss channel for atoms in the trap. The atoms are pushed away from the trap so no PI or AI. That is why the ions created from the PA beam on resonance are even less than the counts from the full MOT. The only ion production technique left is the rf discharge ions. Essentially, the MOT is simply blown away and no atoms remain.

- Blue Detuned ($\nu > \nu_0$):

These photons may drive the atoms into the molecular repulsive curve. Along these curves, atoms need more energy to get closer and create an ion. The problem is the summation of their energy and the photon's energy is not enough to push them closer. That is why the two atoms prefer to go on the lower energy side of the curve which is at larger internuclear distances. This means that the blue detuned photon actually drives the two atoms apart and hence shields their ionization. This is called "optical shielding." The conclusion of that is that the atoms that choose to interact with the PA beam do not produce any ions. They can later relax back to the $Ar^* + Ar^*$ curve where they will remain available for PI and AI process. That is why the available ion production techniques on the blue side are from rf discharge and from PI and AI processes. The PA ion counts on the blue side is very close to the ion counts from the full MOT.

- Red Detuned ($\nu < \nu_0$):

This photon drives the atoms into their attractive molecular potential. Depending on the frequency of the PA photon, it can excite different vibrational sub-states of the molecular potential. Those states will provide a good energy state where they can get even closer. When it is time for them to de-excite, they will be close enough to form ions. This means that the atoms that interact

with the PA red detuned photons end up creating ions. As in the case for the blue detuning, the atoms that do not interact with the PA beam will remain available for PI and AI processes.

To summarize: At resonance, There is no MOT atoms and so no ion counts from either the MOT or the PA laser. At blue side, MOT ion counts are there and no extra ions produced by the PA beam. At the red side, both the MOT ions and the PA ions are created so it will have the highest number of ion counts.

CHAPTER 3

EXPERIMENTAL SETUP

The set up that we use in our noble gases photoassociation spectroscopy experiments is relatively complicated. The reason for this complication is that the requirements to get low noise data that can resolve any vibrational features are tremendous. First, we need to have a very good vacuum system that can maintain a pressure of 10^{-8} Torr. This is not as easy to achieve in our system as it is in alkali atoms because we must load the MOT from an atomic beam. The atomic beam flow is always on unlike the alkali MOT that is loaded from room temperature vapor under low pressure. The alkali gas is only loaded once and the chamber is sealed under the required pressure which it could be maintained as long as needed. Noble gases are loaded from an rf gas discharge that excites the atoms to the metastable state as we explained in the previous chapter. This implies a constant loading of the gas and as a result a constant differential pumping of the gas. The pumping is performed to maintain the required vacuum pressure in the Science Chamber. Our experiment also requires very stable laser sources with good locking techniques (sometimes this locking technique needs to be scan-able as in our beat lock). The experiment also requires a good detection technique that has high efficiency and a good signal to noise ratio. How we achieve these required conditions will be described in detail in this chapter. This chapter is dedicated to the description of our apparatus.

Since our system is complex, we are going to divide it into four main parts and then we will explain every part and its constituents in detail.

1. The Atomic Beam. This part will include an explanation of the atomic beam generation and the generation of the metastable state. It will also describe the slowing of the atoms until they are eventually captured in the MOT. It will include a description of
 - The vacuum system.
 - rf discharge source.

- Zeeman slower.
2. The Magnetic Fields (The Anti-Helmholtz Coils and The Shim Coils). This section will include an explanation of the magnetic fields used in the MOT set up. This included both the shims coils used to cancel the stray magnetic fields and the anti-Helmholtz coils.
 3. The Laser Sources. This part explains the different laser cavities used for both MOT and PA light generation. It also explains the different locking techniques used. We will end up by showing how all these light sources combine at the MOT site to perform our PAS experiment. Since this part has a lot of components we can divide it into five parts.
 - Laser Sources Explanation. This part will include an explanation of all of our sources operation techniques. This includes the External Cavity Diode Laser (ECDL), the Titanium-Sapphire laser (TiS) and the tapered amplifier.
 - MOT Laser Sources. This part will include a description of laser sources used in the MOT generation. To be specific the sources are MOT master laser, MOT Zeeman slower slave laser and MOT Trap slave laser.
 - PA Laser Sources. This part will describe the different laser sources used in generating the PA light. This includes the original PA source (Shaffer's Laser), the TiS laser, the tapered amplifier and the Littrow short cavity.
 - The Laser Locking Technique. This can be divided into the fixed locking technique and a scan-able locking technique (Beat Lock). The beat lock requires the use of a reference laser that will be explained in this section too.
 - The MOT laser beams set up. This part will describe how the MOT and the PA beams are sent into the science chamber so that we are able to form the MOT and the PAS.
 4. The Detection table. This section will explain our ion detection system and our frequency measurements and calibration systems.
 - The ion detection.

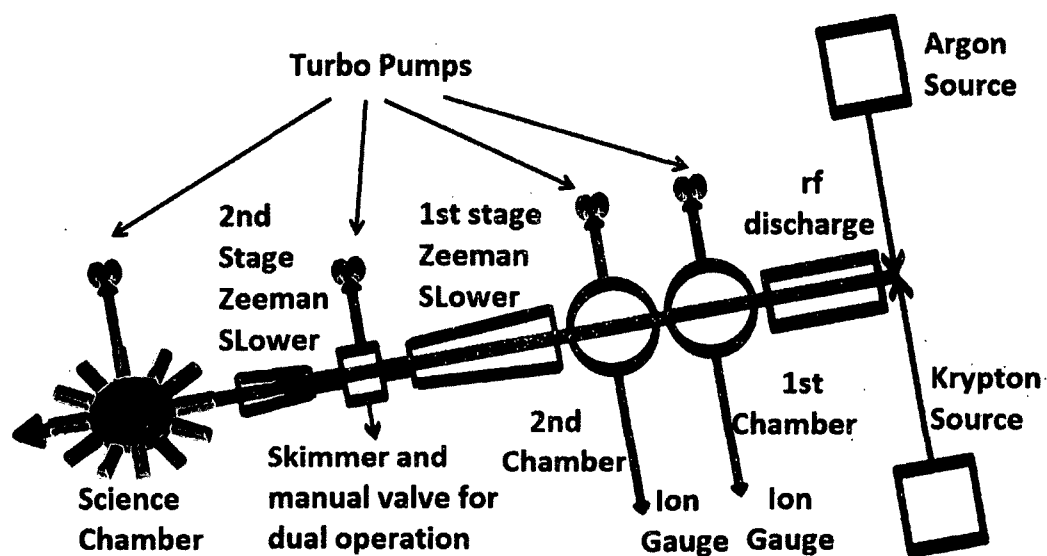


FIG. 21: An outline for the science/MOT table with the different stages that the atomic beam goes through.

- Data Collection.
- The Frequency Calibration.

3.1 THE ATOMIC BEAM

Figure 21 shows schematically the principal components of the vacuum system used in our experiments. It shows the path along which the atomic beam flows until eventually it makes it to the science chamber where the MOT is formed. For fast switching between Ar and Kr the two lines carrying the two gases are connected through a T-shaped connector to the rf discharge tube. The discharge will excite the atoms into a mixture of $(Ar^+/Kr^+, Ar_2^+/Kr_2^+, Ar^*/Kr^*, Ar/Kr)$, where the * sign stands for atoms excited in the metastable state. The system can be run in either single species (Ar or Kr) or dual species (Ar and Kr) mode. Both ground state and excited state atoms (including the metastable state of interest) as well as ions exit the rf discharge and form a thermal beam that travels down the vacuum system. For the experiments reported here, we only used one gas at a time although future extension of using the two gases at the same time is planned. The first chamber that the beam enters is pumped by a Pfeiffer vacuum pump (D-35614 Asslar Model-TC100). The

first chamber also includes a pair of deflection plates that can be used to deflect ions out of the atomic beam (although we found that the MOT loading efficiency did not seem to depend on plate voltage). This only suggests that the ions lose their energy through collisions with the chamber walls before they make it to the MOT. That is how the ions are removed from the atomic beam. For pressure monitoring, an ion gauge with dual filaments is connected to this chamber and monitored through an 843 Varian Ratiomatic Vacuum ionization Gauge. The pressure in the first chamber is kept at about 10^{-5} Torr. As the atomic beam crosses from the first chamber to the second chamber it goes through a skimmer to help for sustaining the differential pressure pumping. The second chamber is again connected to a turbo pump (Pfeifer vacuum pump D-35614 Asslar Model-TC600) for further pumping to 10^{-7} Torr. The pressure is again monitored in this chamber through a 843 Varian Ratiomatic Vacuum ionization Gauge. After the atomic beam exits the second chamber it enters the first stage of the Zeeman slower. As the atoms cross the first stage to the second stage Zeeman slower, they go through another differential pumping stage where another vacuum pump is connected (Pfeifer vacuum pump D-35614 Asslar Model-TC600). As they exit the last stage of the Zeeman slower, they enter the science chamber where the MOT is created. A turbo pump is connected to the science chamber to pump down the background pressure of the science chamber to 10^{-8} Torr. In the following sections, we will explain every step into more details.

3.1.1 THE VACUUM SYSTEM

Atoms slowing down along the atomic beam axis have two components of velocity: the radial velocity (or the divergent direction) and the longitudinal velocity. Atoms that start diverging from the collimated atomic beam can collide with the walls of the chamber and will contribute to the background pressure in the chamber. In turn, diverging atoms can collide with atoms in the atomic beam knocking them again off their course. Those atoms need to be removed from the system otherwise they just create a background that kills our metastable signal. The removal of background atoms is done over many stages. The first stage is through four turbo pumps arranged along the apparatus. The first pumps is connected to the first chamber right after the discharge (Pfeifer Vacuum D-35614 Asslar TC100 with controller TMU 262P Model: PM P02 996A). It pumps down the pressure from 10^{-3} Torr to 10^{-5} Torr. The second pump (Pfeifer Vacuum D-35614 Asslar TC600 Model: PM C01

690A with controller TMU 071P Model: PM P02 801A) is connected to the second chamber. The connection between the first and the second chamber is done through a differential pumping tube. This turbo pump pumps down the pressure from 10^{-5} Torr to 10^{-7} Torr. The third pumps is connected to the connection piece between the two Zeeman slower stages (Pfeiffer Vacuum D-35614 Asslar TC600 Model: PM C01 690 with controller TMU 071P Model: PM P02 801A). It pumps down the pressure from 10^{-7} Torr to 10^{-8} Torr. The fourth pumps is connected to the science chamber (Pfeiffer Vacuum D-35614 Asslar TC600 Model: PM C01 720 with controller TMU 071P Model: PM P02 801G). This pump was added later to cut down on background pressure and improve our signal to noise ratio on the ion detector.

The outlet of the first three pumps is connected to manual valve (KEY High vacuum products, Model: PA-75). It is aimed for separating the backing lines of these pumps from the science chamber pump for easier pump maintenance. The pressure of the outlet of the three pumps is monitored through vacuum gauge thermo couple (TC1) (Duniway Stockroom Corp Model: DST-531). The outlet of the fourth pump (the science chamber pump) is connected to another manual valve (KEY High vacuum products, Model: PA-75). The pressure of its outlet is monitored through another thermo couple (TC2) (Duniway Stockroom Corp Model: DST-531). The two backing lines after the two valves are connected through a NTZE electrically controlled vacuum valve switch for power outage safety. The switch is connected to a PVC tube line that goes to the roughing pump (rotatory vane pump) which exhausts the outlet gas to air (Adixen/ Pfeiffer Vacuum F-7400/ Pascal Series 5 to 21 m^3/h).

The pressure inside our system is monitored using three measurements: 1) The ion gauge is connected to the first chamber right after the discharge (843 Varian Ionization Gauge). It usually reads 10^{-6} Torr when the discharge is off and 10^{-5} when the discharge is on; 2) Another ion gauge is connected to the second chamber (843 Varian Ionization Gauge). It usually reads 10^{-8} when the discharge is off and 3×10^{-7} for Kr discharge and 5×10^{-7} for Ar discharge. 3) Ion Pump (Ultek D-1 pump/ controller: Perkin-Elmer Ultek combination Boostivac control) usually reads $1.5 \mu A$ when the atomic beam is running through the set up because of the rf discharge being on. The operating theory of the ion pump pressure monitoring technique is to induce a small ionization into our gas sample and then collect the ion

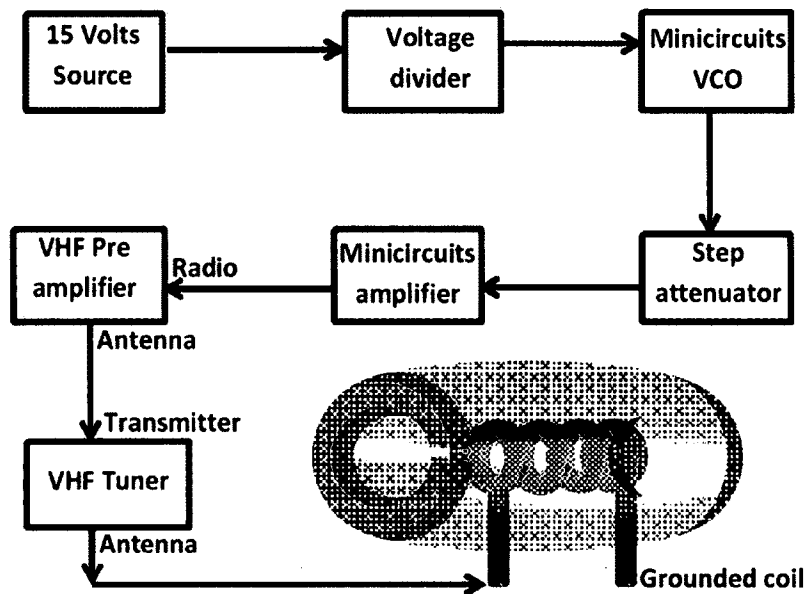


FIG. 22: An outline for the rf discharge circuit with all of the components explained in detail in the text.

created from these atoms, thereby pumping the chamber. The number of the ions created is proportional to the number of atoms originally in the background gas.

3.1.2 RF DISCHARGE SOURCE

The rf discharge source can be described into two parts. The electronic part that generates the rf frequency driving the rf discharge tube. The second part is the actual part of the system which sustains the rf discharge and as a result creates the metastable noble gas atoms.

The electronic system (first part) shown in Fig. 22 consists of a home built 15 Volt voltage divider that is connected to a voltage controlled oscillator VCO (Minicircuits ZOS-200). The VCO has an auxiliary output to monitor the frequency generated and its job is to provide a source for the rf frequency. The output of the VCO is connected to a step variable attenuator (MFJ-762) usually set to 23 dBm for gain adjustment between the VCO and the amplifier stage. The output of the attenuator is connected to a low noise rf pre-amplifier (Minicircuits ZFL-1000) to obtain a gain of 20 dBm. The output of the amplifier is connected to the radio input of the

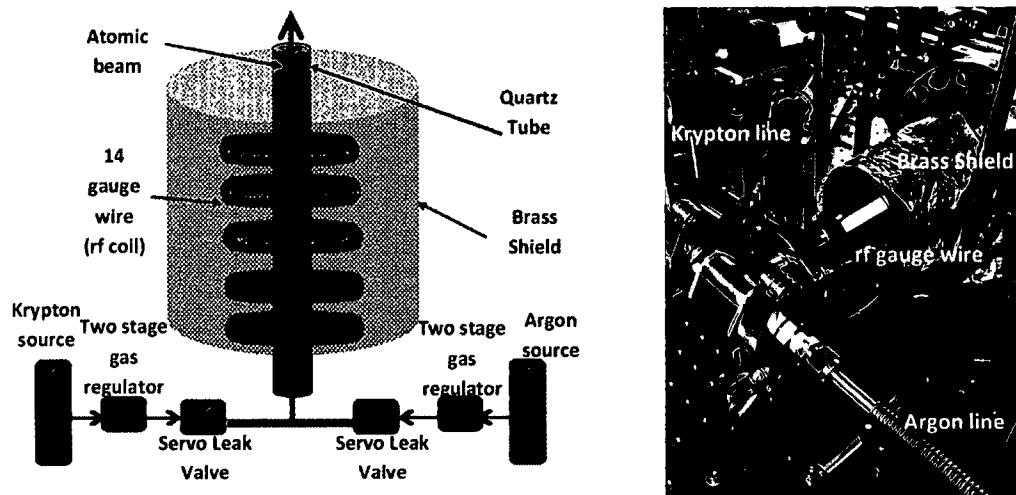


FIG. 23: The figure to the left shows the outline of the discharge tube components. The right figure shows the actual set up in the lab.

antenna amplifier (Mirage B-34-G). This amplifier has a specified operation range of 144 MHz to 148 MHz which limits our tuning range of the rf discharge. However, we found that it can be operated slightly outside this range. The antenna output of the amplifier is connected to the transmitter input of the tuner (VHF Dual band Tuner 144 - 220 MHz , Model MFJ-921). The antenna output of the tuner is connected to the rf discharge coil. These components work together to drive the discharge cell at a frequency close to 154 MHz with a very small tuning range between 145 MHz and 155 MHz.

Before we start describing the second part of the rf discharge source, it is useful to describe the noble gas sources. The argon source consists of a bottle of research grade argon connected to a two stages gas regulator (VEC model BHS 500-15-580-BV). The output of the regulator is connected to a servo valve (Granville Phillips 216). The valve is controlled by a Model 216 pressure/ flow controller. The krypton source line is very similar to the argon one. The two stages gas regulator for Kr is VWR 55850-622. The servo valve in Kr is also a servo driven valve assembly 216 series / Granville-Phillips. The two gas lines are combined at a T-Shaped connector to the quartz tube where the rf discharge takes place as shown in Fig. 23. The quartz tube is connected to the rest of the vacuum system through a torr seal epoxy to the vacuum chamber flange. The torr seal was found to sustain high vacuum much better

than the quick flange connector. Fig. 24 shows the steps followed during the rf tube mounting. The tube is surrounded by a 14 gauge coil with one side connected to the rf broadcasting circuit and the other side to ground. The coil is surrounded by a brass tube for cavity purposes. The aluminum foil added in the Fig. 23 is mainly aimed to cut down the rf noise broadcasting to the surrounding electronics. The original design was made by Hauke Busch [13] although the actual tube and the coil parts were changed during our experiment. Original design follows a paper by Lu (Chen et al).

Through power and attenuation adjusting as well as impedance matching through the antenna tuner, the rf discharge is generated in the tube. As a result of the rf discharge, an atomic beam of both atoms and ions - including metastable atoms - is formed. It was found that the maximum number of metastable state atoms is usually generated at the brightest discharge. That is why a part of the daily adjustment to the system is to adjust the power sent to the discharge to maximize the number of ion counts produced by the MOT. We should keep in mind that the detector sees ions produced either in the discharge or by metastable state atoms collisions. Both the ion counts are not associated with the MOT.

As noted above, after the atoms exit the quartz tube, they travel through the first chamber where an ion gauge is connected to monitor the pressure. This chamber has a deflection plate added to it to help with the ions deflection so that they do not end in the science chamber and interfere with the ion signal from the MOT. A second chamber follows this one with another ion gauge connected to it. The combination of the readings of the two gauges gives a good reference for the discharge operating pressure conditions from day to day.

3.1.3 ZEEMAN SLOWER

Alkali MOTs can be loaded directly from a thermal vapor. The atom's velocity distribution follows Maxwell-Boltzmann distribution. At room temperature, thermal vapor pressure is high enough that there is a sufficient density of slow atoms in the Maxwell-Boltzmann distribution to be captured by the MOT. Rubidium atoms, for example, are almost always loaded into a MOT this way. For atoms with low vapor pressures or for low numbers of atoms, it is necessary to perform one-dimensional

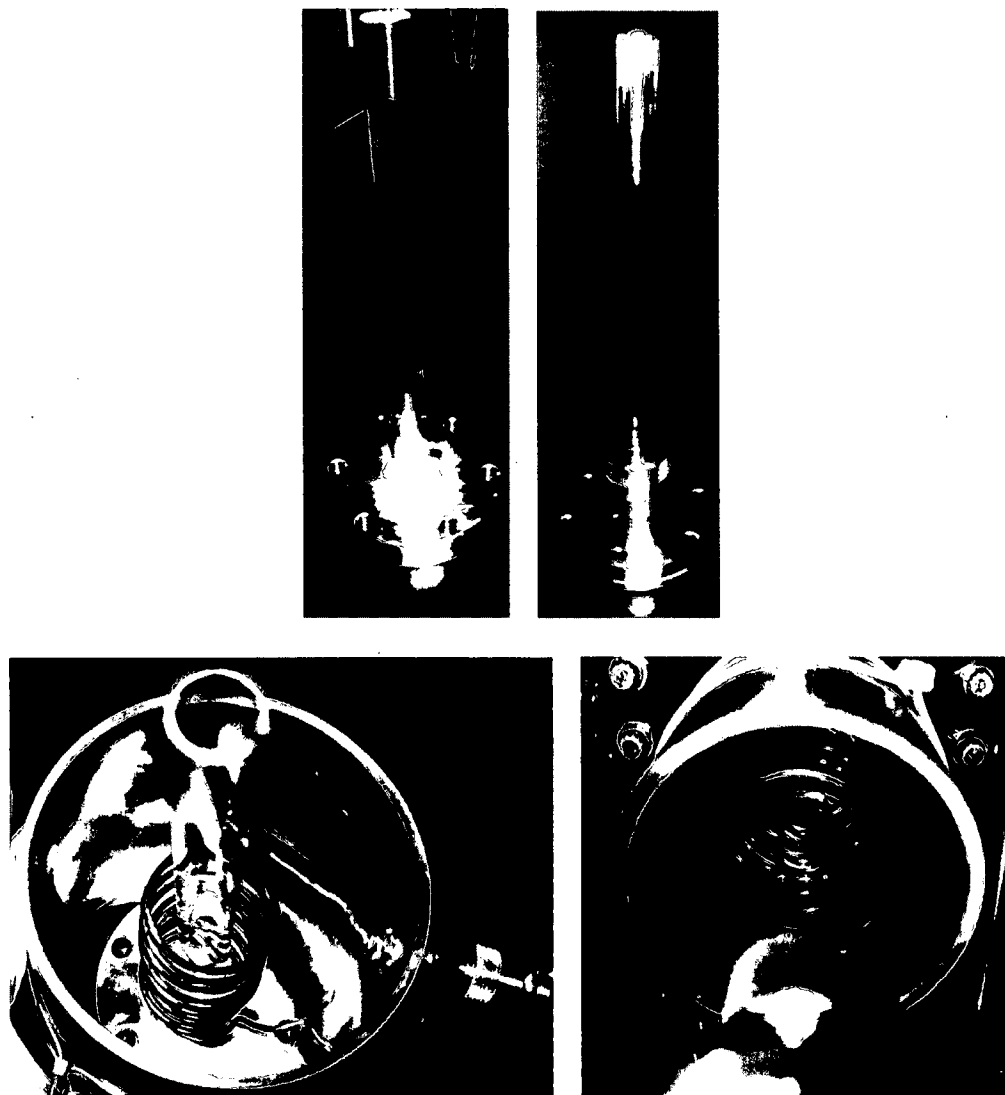


FIG. 24: Pictures for different steps of mounting the rf quartz tube. The top left picture is the torr seal picture which is currently used. The top right one is the quick flange connector that did not sustain as low pressure as we needed. The bottom left one is the shape of the tube after mounting the rf coil around it. The bottom right picture is the rf tube in its final setup after connection with the T-shaped connector to the two gas lines.

TABLE 2: This table illustrates the different settings for both argon and krypton for Zeeman slower magnetic field coils.

Parameter	Argon	Krypton
The first/long coil current	28 A	20 A
The second/short coil current	18 A	18 A
The slowing laser beam detuning	-160 MHz	-156 MHz
The slowing laser beam power	20 mW	20 mW
The slowing laser beam intensity	50 mW/cm ²	50 mW/cm ²

cooling. This increases the number of atoms that are available for MOT loading. In our case, the number of metastable state atoms in the tail of the velocity distribution of the atomic beam is too small to load the MOT. It is also important to note that the rf discharge efficiency in metastable state production is not the highest. In fact, in our experiment, the ratio of Ar^*/Ar is $\sim 10^{-4} - 10^{-5}$.

For atoms to get trapped in the MOT they must be slowed down to a speed that is slower than the MOT “capture velocity” ($v_c \equiv \gamma/k$ where γ is the decay constant of the atoms in the electronic state used for MOT loading). This capture velocity is about 50 m/s for argon. On the other hand the atoms leave the discharge with an average velocity of ~ 400 m/s. That is why if the metastable atoms were not slowed down, most of them will end up crossing the MOT region without being trapped. They will not go through enough cycles of excitation and de-excitation to cool them down sufficiently so that they are eventually trapped in the MOT. Those atoms with velocities higher than the capture velocity will end up colliding with the science chamber walls. As a result, they may end up on our ion detector creating a background count. As a summary for all these reasons, the atomic beam needs to be slowed down from 400 m/s (the velocity of the atoms exiting the discharge) to < 50 m/s (the MOT capture velocity). This is important for two reasons: 1) The method used for producing metastable atom has low efficiency. That is why we can not afford to lose the metastable atoms created because they were not slowed down enough. 2) The atoms that are not stopped before they make it to the chamber will end up as background noise on our signal. That is why in our experiment we use a Zeeman slower.

The Zeeman slower part of the experiment consists of two coils with a connector

piece between them which has: 1) A turbo pump to remove further background gas. 2) A skimmer that helps with the differential pumping. 3) A manual valve which is an added feature to our apparatus needed for the dual species operation between noble gases and alkali (Rb) atoms. The magnetic field coils were originally constructed by Busch and described in detail in [13]. As explained in the theoretical overview of the Zeeman slower, the varying magnetic field is established by wrapping a 14 gauge magnet wire around the vacuum tube carrying the atomic beam.

The magnetic field is high at the beginning of the coil and slowly decreases until it reaches the connection part. Then in the second coil, the magnetic field is in the opposite direction and increases gradually until it cuts off right at the science chamber flange. The magnetic field is established by wrapping the wire closely at the beginning and increasing the spacing between the loops as you go down the tube. This creates a magnetic field that decreases almost linearly with the distance. The opposite case happens with the small coil with loosely wrapped coils at first and then gradually decreasing the distance between the loops. This efficient way of slowing down the atoms from 400 m/s to 50 m/s has the downside of consuming high current. The current sources are a 6269B Hewlett-Packard DC Power Supply 0-40 Volts/ 0-50 A for the long coil and a 6259B Hewlett-Packard DC Power Supply 0-10 Volts/ 0-50A for the small coil. The large current produces a lot of heat that needs to be removed. To cool the Zeeman slower coils a small hose is wrapped around the coils. The ends for those coils are connected to a re-circulating water chiller that maintains a constant flow of cold water with a temperature that is usually set to 20⁰ C. The chiller model is VWR Chiller Model 1171PD. The graph for the measured magnetic field on our apparatus is shown in Fig. 25 [13].

3.2 MAGNETIC FIELDS AROUND THE MOT

We can divide the magnetic fields used in our experiment into two sets. The first set consists of the MOT magnetic field or the anti-Helmholtz coils creating the magnetic field necessary for the trapping process. The second set has the shim magnetic coils which were added to cancel the effect of stray fields.

The shim coils supplies are MPJA power supplies (HY 1802D for the shim1 coils (x-axis) / HY1802D for shim2 (y-axis) / HY 14600PS for shim3 (z-axis)). The values for the currents are adjusted as part of the MOT tweaking process that takes place regularly at least every week (adjusting the shim coils changes the position of the

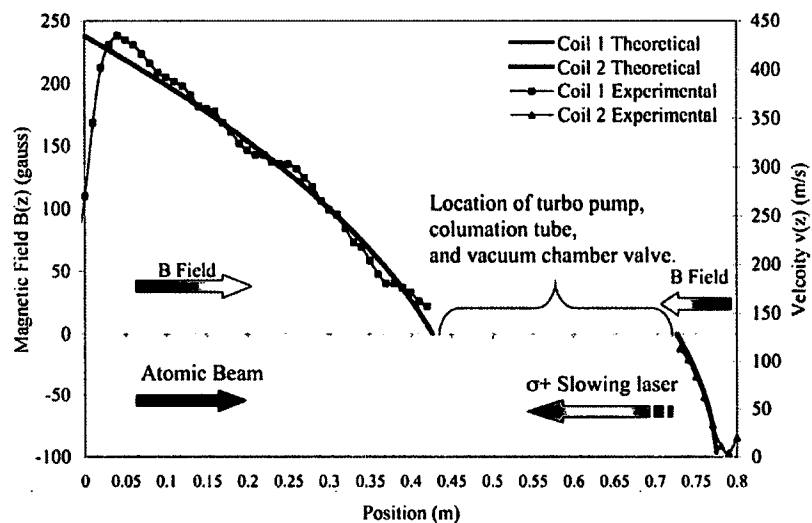


FIG. 25: This figure is taken from the dissertation of H. Busch [13]. It includes the measurements that he did while building the magnetic field assembly and the velocity of the atoms leaving the Zeeman slower.

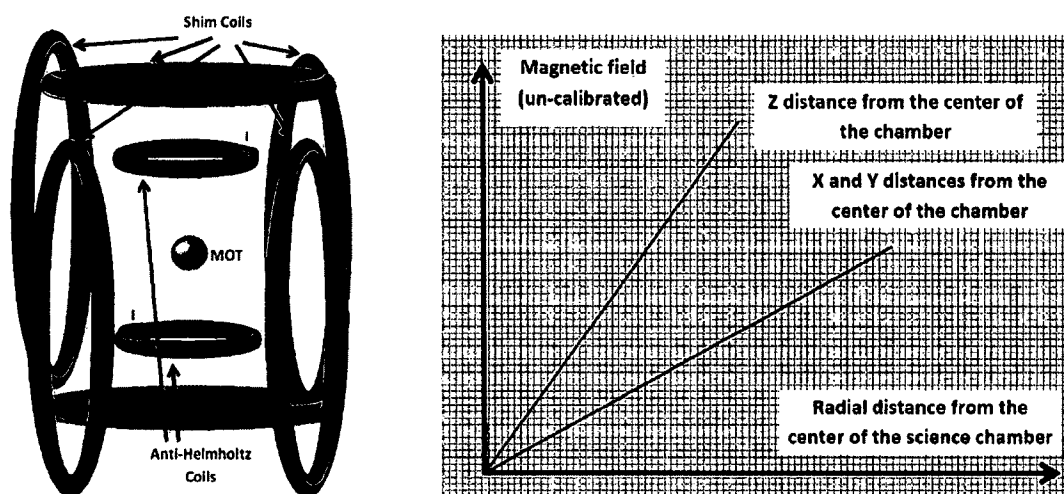


FIG. 26: The graph to the left shows the magnetic field coils added to our science chamber. The graph to the right shows the theoretical magnetic field as a function of the distance from the center of the chamber in the X , Y and Z direction. Note that $\frac{dB_x}{dx} = \frac{dB_y}{dy} = \frac{1}{2} \frac{dB_z}{dz}$ to satisfy Maxwell equations [14].

MOT slightly which requires realignment of the laser beams).

After canceling any stray magnetic field in the chamber, two anti-Helmholtz coils are added to the chamber along the z-axis. Those coils are 14 Gauge coils wrapped around the top and the bottom of the chamber. They are connected to a constant high DC current of 6 Amperes supplied from an INSTEK Laboratory DC power supply Model: PR-3060. The two coil set up is shown in Fig. 26. The coils produce a magnetic field that is shown also. The magnetic field changes linearly with the distance from the center of the chamber (in x, y and z direction). The current of 6 Amperes has the downside of creating a smaller size MOT, because of the stronger gradient than at smaller currents. The reason that we use it is that it creates higher MOT densities which are very vital for our experiment. The higher density means that the atoms start from smaller internuclear distances on average. When they undergo photoassociation, they are more likely to end up in one of the molecular potential wells that take place at small R .

3.3 THE LASER SOURCES

In photo-association experiments, atom's manipulation with lasers play a crucial rule. As a result, the characteristics of the lasers used are very important. This experiment requires the source lasers to have a small bandwidth (~ 1 MHz). The experiment also requires that we are able to scan some of the lasers over the range of many GHz with MHz step sizes for the PA laser. As for the MOT lasers locking technique, scans over the range of a couple MHz s are required. Fortunately, semiconductor diode lasers at the proper wavelength that meet these requirements are available.

3.3.1 LASER SOURCES EXPLANATION

Diode lasers have the advantages of being really affordable, along with having a wide selection of lasing wavelength available. This makes them very useful for different applications and also for the trapping and cooling of different elements. Typically the diode lasers are consisting of p-n junction (p-n junction is a stack of two sides made with semiconductor material doped with different elements on each side). The doping has the effect of changing the polarity of the stack by creating extra charge carriers on one side and creating extra vacancies on the other side. This polarity

creates potential difference between the sides and so under proper conditions creates current flow. When the charge carriers from one side combine with the vacancies from the other side, the extra energy released can be in the form of laser photons. We can change the wavelength where the diode will lase by simply changing the current and temperature of the diode. This in turn changes the potential difference between the two sides and hence the energy of the photon released. This effect enables coarse frequency tuning of the diode laser. However, the tuning range may have gaps in it and the bandwidth of the emitted laser light can be large for cw lasers. Further, the diode lasers become very sensitive to optical feedback. Optical feedback takes place when a scattered beam makes it back to the diode laser. This new beam provides some feedback to the diode that affects the wavelength at which the diode lases. That is why unfortunately for the range of sub-MHz smooth scans, we can not use the current and temperature manipulation anymore to tune the laser wavelength. To enable that kind of scan, we place our diode lasers in an external cavity to form an External Cavity Diode Laser (ECDL). The lasers are used as “master lasers” and can be injected into “slave lasers” to obtain higher output power if needed. The diode laser is placed in an external cavity Fig. 27 and with the help of a diffraction grating we can drive the laser at the frequency range we need for the experiment. This technique for controlling the laser frequency is widely used and many groups have used it over the years. There are different examples of diode lasers being coupled into external cavities of different configurations from mirrors and etalons [71] to locking it to high finesse cavities [72].

The two most commonly used configurations of an ECDL with a diffraction grating are the Littrow Cavity setup [73, 74] and Littman-Metcalf Cavity [75]. The Littman-Metcalf configuration is shown for pulsed lasers in Ref. [76, 77]. We usually have our ECDL in one of these two configurations: 1) Littrow configuration and 2) Littman-Metcalf configuration.

The Littrow cavity configuration contains a collimation lens after the diode laser at a distance about the focal length of the collimation lens. This cancels any divergence effects in the beam emitted from the diode. After the collimation lens, the beam travels to a diffraction grating with the first order diffracted beam sent back to the diode laser which provides the optical feedback. The zeroth order of the grating

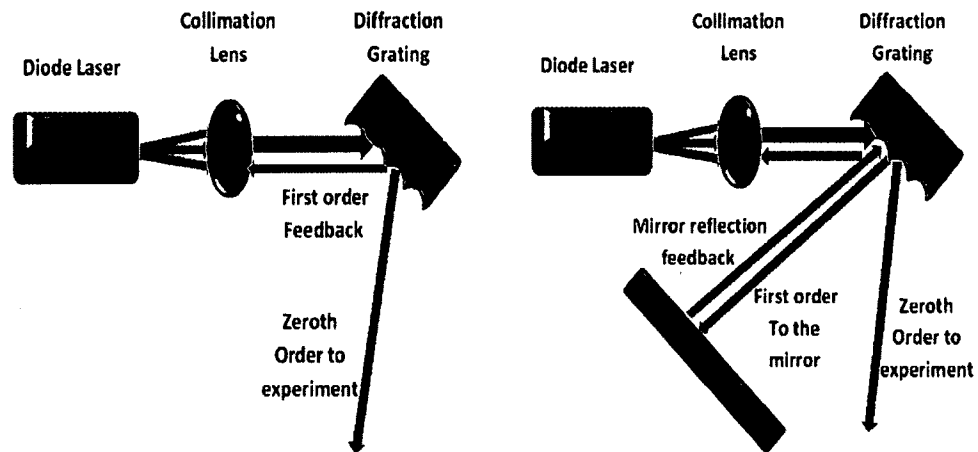


FIG. 27: The External Cavity Diode Laser (ECDL) configurations. The left figure is for Littrow configuration while the right figure is for Littman-Metcalf configuration.

reflection goes to the experiment. The main disadvantage of this configuration is that as we tune the laser or “pull it” to the desired frequency range or even when we scan it, we also change the direction of the output beam. The scanning is performed by a piezoelectric ceramic at the horizontal mount point on the grating. As the voltage on the piezo changes, it rotates the grating reflecting different diffraction colors from the grating back into the diode laser. It is important to note that these diffraction colors all belong to the same diffraction order (first order). This, in turn, changes the cavity’s frequency for which the cavity is closed and the boundary conditions are met.

The second configuration (Littman-Metcalf) on the other hand consists of collimation lens to eliminate divergence effects of the diode output beam. The laser beam then travels to the grating where the first order diffraction of the grating goes to a mirror. The mirror reflects back the beam onto the the diffraction grating and back to the diode laser to provide feedback. The zeroth order of the grating goes to the experiment. Adding the mirror on the path of the first order beam makes it easier to tune the cavity without any directional change in the output beam. In this configuration, the cavity tuning is done by changing the angle of the mirror. This means that the grating’s position is fixed and hence the output beam direction does not change. Because the optical feedback beam that reflects back to the diode laser

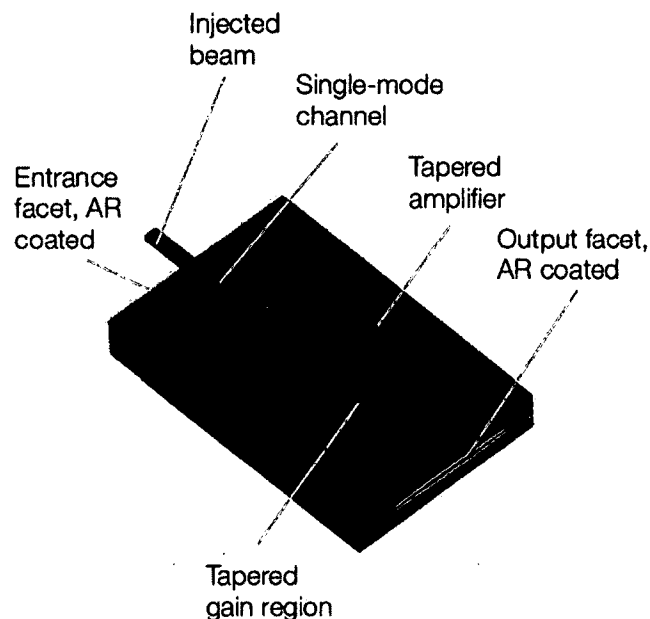


FIG. 28: Geometry of a tapered semiconductor amplifier chip [15].

undergoes grating reflection twice, we have a better control ability over the frequency range. After we “park” the laser at the needed frequency, we can scan it around that frequency. We usually achieve that by adding a ramp signal to the piezo material on the mirror mount. Here, rotation of the mirror closes the cavity for different wavelengths and hence tunes the laser.

Because the output from the master laser generally has a relatively small power and not enough to perform our experiments, we use slave lasers. For the MOT lasers we use two slave lasers. The idea of the slave lasers is to feed a laser beam with certain frequency into a second laser (like a diode laser). This actually induce the transitions in the p-n junction so that they happen at the same frequency. The result is that you get an amplification effect at the injected frequency. For the PA laser source to get high power we inject it into a tapered amplifier. The main piece in the tapered amplifier is a semiconductor chip which acts as a semiconductor optical amplifier or gain medium. The chip is shown in Fig. 28. It is essentially like a laser diode where the end mirrors have been replaced with anti-reflection coatings for single pass operation. The signal light is usually sent through a semiconductor single-mode waveguide. The waveguide mode has significant overlap with the active

(amplifying) region, which is pumped with an electric current. The injection current creates a certain carrier density in the conduction band, allowing for optical transitions from the conduction band to the valence band. The gain maximum occurs for photon energies slightly above the bandgap energy of the amplifier.

Under the optical feedback conditions the visibility function becomes dramatically different from that in the absence of the feedback which is a normal Lorentzian spectrum. A more detailed explanation is provided in Ref. [78]. For strong feedback, the multiple external cavity modes will start lasing eventually. This also takes place for longer external cavity than the coherence length of the laser. In this case, the laser spectrum will have a multiple mode distribution and the mode spacing of the spectrum is $c/2L$ where c is the speed of light and L is the length of the cavity. Those modes create what we call sidebands on the principle laser frequency. Usually those sidebands are detectable, but as we will discuss below that is not always the case. Typically, our lab has several instruments used for optical diagnostics of the laser sources. These include a wavemeter and a number of Fabry-Perot spectrum analyzers with different resolution. As we will discuss in the next chapter, it turned out that sidebands on the ECDL spectrum played a very important role in producing artifacts in our PAS. However, those sidebands were never detected on any of our frequency diagnostics.

For purposes that will become more obvious when we start explaining our data, we used several different laser sources. In particular, we wished to use a laser source different from the diode lasers. This will change the sideband characteristics without changing the frequency. For this purpose, we used a Titanium-Sapphire Laser source (Ti:S). This laser is a ring laser which is formed of a solid state crystal of Titanium-Sapphire in a bow-tie cavity. The Ti:S is pumped by a Coherent Verdi laser at $532nm$. We typically operated the laser at $811nm$. This commercial laser was capable of mode-hop free scans of up to 10 GHz. A layout of the laser path in the Ti:Sapphire source is shown in Fig. 29. More detailed explanation about Ti:S lasers can be found in Ref. [79].

3.3.2 THE MOT LASER SOURCES

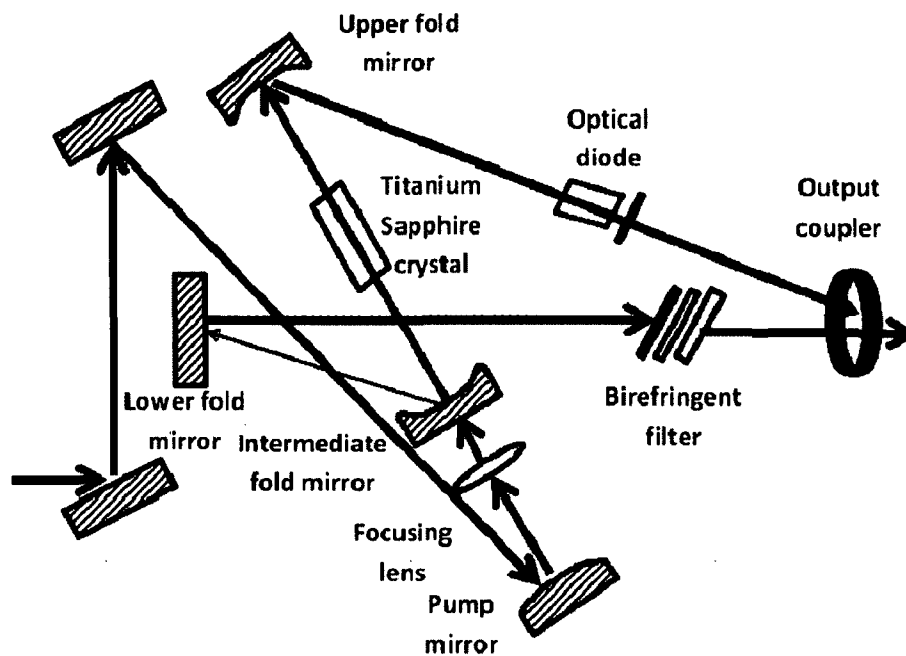


FIG. 29: The schematic diagram of the laser path in the Ti:S head

In this part of the chapter, we are going to describe different laser systems producing the beams that are later transferred to the science chamber through the optical fibers. The laser system that we are going to explain in this section include the MOT laser master that is locked at the cycling atomic transition used in MOT loading. Needless to say that this frequency value is different between argon and krypton, although they happen to be very close to each other. We will also describe the laser source used for the Zeeman slower laser which counter propagates the atomic beam and slows it down. We will also describe the laser source that provides the six circularly polarized beams (actually it is one laser beam that is split between three directions x , y and z). Every one of the three beams is reflected back “retro-reflection” to form the six counter-propagating beams. This laser source is called the MOT trap slave laser. A diagram of the layout of the three laser sources and the way they are steered into the optical fibers so that they are transmitted to the science chamber is shown in Fig. 30.

1. The MOT Master laser

Our master laser source is a Sanyo infrared diode laser that, under standard

operating conditions, has an output of 150 mW at 50°C. The model number is DL-8031-31A. The diode laser is operated at a current of 139.78 mA and the temperature controller is adjusted at 9.772 V which corresponds to 17.8°C. The diode laser is then installed in an External Cavity Diode Laser (ECDL) in Littman-Metcalf Configuration. The grating used is an Edmund Optics IR Gold Grating (Model: 43848) with 1200 Groves/mm. The mirror is mounted on three adjustable points. One of them controls the horizontal alignment and that is where a piezo electric material is mounted. When the piezo electric material is fed with a voltage ramp signal, it rotates (and translates) the mirror. As the mirror mount angle is adjusted, the diffracted color from the grating changes. This is the diffracted color that is reflected back to the diode laser. This process helps with the specific selection of the closest frequency mode to the atomic transition. Further current and temperature adjustments drives the ECDL at the specific atomic transition frequency.

The output of the ECDL is feed into a periscope which raises the beam height so that it is easier to spatially adjust the direction of the beam. Then it goes into an optical isolator (Optics for Research IO-5-810-LP/VLP-Z /38-44db) that prevents any feedback from any of the optical components. This feedback can change the frequency at which the ECDL lases. After the optical isolator (ISO) the beam goes through an Anamorphic Prism Pair. This has the effect of changing the spatial shape of the master laser beam from elliptical to a circular beam. That provides a better coupling through the optical components. The circular beam then goes through another optical isolator (OFR IO-3D-780-VLP/34-40db). The beam is then directed into the first slave through a polarizing beam splitter (PBS) and $\frac{\lambda}{2}$ waveplate. The idea of the PBS is to reflect the beam components of one linear polarization and transmits the other perpendicular components. The idea of the waveplate is to shift the phase between two perpendicular polarization components of the light wave. For $\frac{\lambda}{2}$ waveplate, this has the effect of rotating the polarization direction of the linearly polarized light. On the other hand, for elliptically polarized light this waveplate changes the polarization handedness. Similarly, the $\frac{\lambda}{4}$ waveplate transfers the linearly polarized light into elliptically polarized light. In fact, the adjustment of the angle between the polarization direction and the waveplate axes can generate a circularly polarized light. The combination of the PBS and

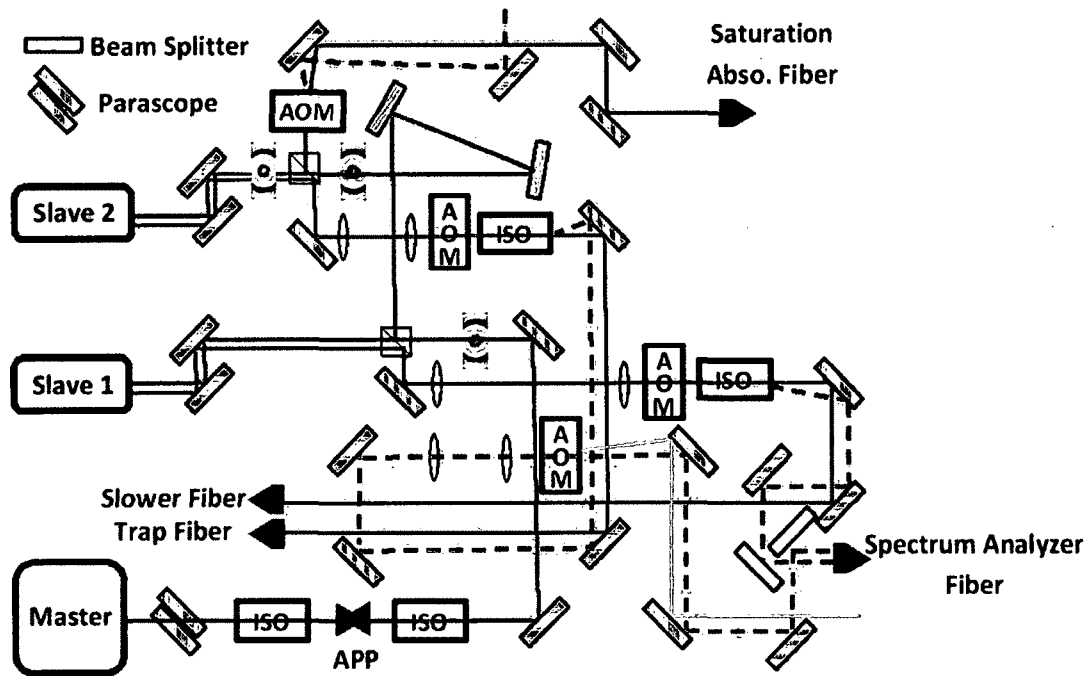


FIG. 30: This figure shows the optics layout used in creating our MOT lasers. The lasers from the master is given by the green line. The lasers from the first slave or the Zeeman slower laser is given by the blue line. The beams from the second slave or the trap laser is given by the red line which becomes orange after the second AOM. The beams from the AOM are divided into zeroth order (dashed lines) and first order (straight lines). The APP symbol is short for Anamorphic Prism Pair. ISO is short for optical isolator. AOM is short for Acousto-Optical Modulator.

the waveplates controls how much power that is feed into the first slave. It also matches the polarization between the output beam from the slave 1 and the input driving beam from the master. The injection of the master beam into the slave ensures that the slave 1 is resonating at the same frequency as the master frequency. This techniques of locking the slave laser to the same frequency as the master laser is called injection locking. The polarization matching of the two beams ensures better locking. The injection locking technique is repeated for the second slave as well. The master beam intensity left after driving the two slaves is feed into an acousto-optical modulator (AOM) (NEC C8217A). The AOM (shown in Fig. 31) is a device that depends on changing the refractive index of a transparent crystal by the oscillating mechanical pressure of a sound wave. A frequency in the the range of 100 MHz is applied to a piezo-electric transducer attached to the crystal that drives a sound wave through the crystal. The result of this is changing the direction and the frequency of some of the input power into new beams (orders of diffraction). The rest of the power of the original beam that is not affected by the the sound wave will be transmitted into almost the same original direction creating the zeroth order of diffraction. Depending on the direction of this sound wave and the incident laser the first order is diffracted with either a higher frequency than the original beam (positive first order) or lower frequency (negative first order). This process may also be thought of as the scattering of a photon off a phonon. The importance of using the AOM is that it enables fast switching of the laser beam. This takes place by applying fast switching to the driving sound wave and hence switching the first order light as well. In the master case, the laser goes through the AOM diffracting into the positive first order. The AOM is driven at frequency 81 MHz. The zeroth order is picked for the master laser monitoring purposes and the first order is picked off and sent to the saturation absorption tube to create a signal that will be used later in locking the master laser. This will be discussed into more details in the locking technique section.

2. MOT Zeeman Slower Slave Laser

This is the laser source that drives the beam used for the Zeeman slower to slow down the atoms as they propagate along the slower. The frequency of this laser is fixed using an injection locking technique. The master laser beam is injected into the slave diode laser that stimulate the transitions into the diode

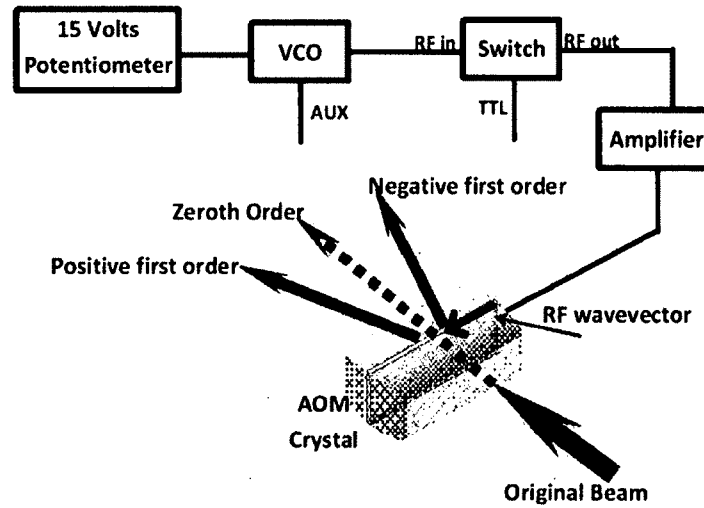


FIG. 31: This diagram shows a typical circuit used to control the AOM. The 15 Volts voltage divider is home built. VCO stands for the voltage controlled oscillator that generates an rf signal that can be monitored through the AUX output. The switch is an rf switch used to turn the first order on and off using a TTL signal. The rf signal is amplified and fed into the AOM where it generate rf wave through changing the crystal's refractive index and hence the direction of the output beam.

TABLE 3: This table illustrates the AOM circuits part numbers and settings used in our experiment. The two different frequency settings for both the slower and trap AOMs are for argon/krypton respectively.

	VCO/Switch (Minicircuit)	AOM	AOM Frequency
SA	ZOS 100 / ZYSWA-2-50DR	NEC C8217A	81 MHz
Slower	ZOS 100 / ZYSWA-2-50DR	NEC C8217A	81/75 MHz
Trap	ZOS 100 / ZYSWA-2-50DR	NEC C8217A	64/68 MHz
PA 1	ZOS 100 / ZYSWA-2-50DR	NEC C8217A	79 MHz
PA 2	ZOS 200 / ZYSWA-2-50DR	crystal tech 3299-147	190 MHz
Reference 1	ZOS 200 / ZYSWA-2-50DR	crystal tech 3299-142	190MHz

lasers at the same frequency as the master laser. The slave diode laser is a Sanyo DL-LS-2031, 150 mW diode. It is operated at a current of 159.25 A and temperature setting of 9.768 V which corresponds to 18°C using a homebuilt current and temperature controllers. The diode laser is placed in aluminum casing that is designed to minimize the effect of temperature swings on the laser.

As the beam leaves the casing, it goes through the PBS. With careful control of the polarization of the output beam from the first slave, most of the beam power is reflected through a telescope into an AOM. The AOM is fixed at 81 MHz for argon or 75 MHz for krypton (NEC Model C8217A). The output of the AOM is being coupled into an optical isolator ORF IO-3D-811-VLP-TILT-Z. The AOM's zeroth order goes through an optical fiber to be monitored on a spectrum analyzer. The spectrum analyzer ensures that the slave is following the master as well as identifies any extra noise frequencies overlapped on the laser source. The negative first order is coupled through optical fibers and sent to the science chamber to be used in slowing the atomic beam as previously described. It is important to note that the detuning of the laser beam sent to the Zeeman slower is derived relative to the saturation absorption which will be our zero reference point. That is why we need to take into account the frequency shifts from the two AOMs on the master and the Zeeman path. This makes the detuning $-81 - 81$ MHz or -162 MHz for argon and $-81 - 75$ or -156 MHz for krypton.

3. MOT Trap Slave Laser

This is the laser source producing the trap beam that later gets divided between three pairs of counter-propagating circularly polarized beams. This slave is driven at the specific transition through injection locking in the same technique as the first slave. The IR laser source itself is a Sanyo IR diode laser (DL-8141-035) with a power output of 150 mW at 50°C. In this case, the polarization of the master needs to be rotated further to lock the slave. That is why adding an extra $\frac{\lambda}{2}$ waveplate seemed to be very beneficiary in maintaining a good following lock between the master and the second slave. The output of slave 2 follows in a similar optical path to slave 1 through a PBS and then a telescope and then an AOM (NEC C8217A) and then an OFR isolator IO-3-780-PSCL. This

AOM is fixed at 64 MHz frequency for argon and 68 MHz for krypton. The AOM zeroth order is being coupled into a fiber optic to the spectrum analyzer. The two slaves are being monitored simultaneously on the spectrum analyzer. Since both the slave have their zeroth order coupled into the fiber, they appear on top of each other of the spectrum analyzer oscilloscope. The positive first order is being coupled into a fiber optic and delivered to the science chamber table as the trap beam. This creates a total detuning of the trap beam from the saturation absorption “zero frequency” of $-81 + 64$ MHz or -17 MHz for argon and $-81 + 68$ MHz or -13 MHz for krypton. It is very important to note that the Zeeman slower detuning and the trap detuning were picked so that they maximize the number of ions produced from the MOT. The number of ions is proportional to the density of the MOT. This is because the closer the atoms are together, the more likely they are to collide and undergo Penning or associative ionization, producing an ion count.

It is also important to note that in slave 2 another feature was added later on. We used the AOM’s zeroth order and delivered it through a telescope to a second AOM. There, the first order were picked and used as a PA laser beam, while the zeroth order were sent to the spectrum analyzer. In experiments discussed in the next chapter, we will call this the “MOT PA” beam to differentiate it from the usual PA beam. It is important to note that we send the PA beam into the chamber when the MOT trap beam is off. The first AOM is turned off and all the MOT trap light power is dumped into the zeroth order. The zeroth order is coupled into the second AOM which is turned on alternatively to the first AOM. Hence most of the power appears in the MOT PA beam (the first order of the second AOM).

3.3.3 THE PA LASER SOURCES

This is where we describe all our laser sources used for the PA light. The sources are extended cavity diode lasers. We have used the ECDL in its two configurations (Littman-Metcalf and Littrow). The main reason for having the two configuration is to explore the effect of sidebands. As a reminder, for the Littman-Metcalf laser, the light comes out from the diode and is diffracted from the surface of the grating. The zeroth order is sent to the experiment and the first order is diffracted back into

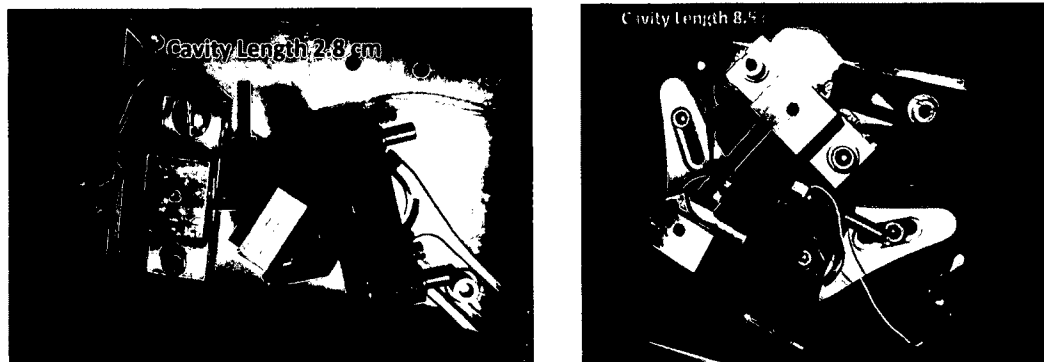


FIG. 32: A photograph from our set up for the two ECDL cavities used as our PA laser sources. The figure on the left is for the Littrow / short ECDL cavity with cavity length ~ 2.8 cm. The figure on the right is for the Littman-Metcalf / Long ECDL cavity with a cavity length of ~ 8.5 cm.

the diode again. The cavity length does not only affect the original lasing frequency but it also creates sidebands from other orders of interference as well. The frequency displacement of these sidebands from the laser frequency is related to the cavity length. For Littman-Metcalf configuration the cavity length is much larger than the Littrow configuration because of the extra reflection off the mirror. This means that the sidebands in the Littrow cavities are further from the laser frequency than in the Littman-Metcalf one. Indeed, for our Littman-Metcalf cavity the sidebands happen at 1.5 GHz from the lasing frequency. On the other hand, for the Littrow Cavity, the sidebands are about 5 GHz away from the laser frequency. Another source that we use is the Titanium-Sapphire ring laser. This source has the advantage of being monochromatic (does not have sidebands on it). Although our Ti:S laser had some technical problems that prevented it from operating at commercial specifications. For purposes of having much higher powers and saturating the PA transitions a tapered amplifier was used. We coupled the light from the two types of ECDLs alternatively into the tapered amplifier to be able to access higher powers from them and compare the results obtained using each.

1. Littman-Metcalf / Long / Shaffer's ECDL Cavity

This is the Littman-Metcalf ECDL configuration. It is composed of a Sanyo IR DL-8031-031A as the diode laser. It has an output power of 150 mW at standard operation conditions of 50°C . The grating used is an Edmund Optics

IR Gold Grating (Model: 43848) with 1200 groves/mm. The ECDL cavity length is $L \sim 6 + 2 \sim 8$ cm which places the sidebands at about $c/(2L) \sim 1.8$ GHz from the laser frequency. The diode is controlled using a homebuilt current controller set at 161.3 mA and a home built temperature controller set at 9.69 V which corresponds to temperature of 18°C. The laser comes out from the ECDL and goes through a periscope to raise the beam height. It then goes through a lens to focus the beam into an optical isolator (Toptica-Photonics Double stage isolator 60 dB 8451-101-000-81 Mod: F1-810-5TV-EOM). The output from the isolator goes through a combination of $\frac{\lambda}{2}$ wave-plate and a PBS. The effect of this PBS is to send a very slight portion of the light to a photodiode. We scan the ECDL by applying a ramp signal into the piezoelectric material. We found that when the frequency is close to the end of the cavity mode, the laser will “mode hop”, and the frequency and the intensity from the ECDL change suddenly. The piezoelectric ramp enables the scan over this range of frequencies until this range ends and the laser “mode hopes” into another range of frequencies. Back to our set up, monitoring the photodiode signal could give us a feedback if the ECDL is about to mode hop. This observation was used as a way of locking the ECDL laser in Ref. [80] to extend its scan range to ~ 25 GHz. The straight beam that goes through the PBS will go through another combination of $\frac{\lambda}{2}$ wave-plate and a PBS to clean the polarization of the beam so that it is linearly polarized. The beam is then sent through a shutter for power outage protection of the tapered amplifier. It then travel through another $\frac{\lambda}{2}$ wave-plate to fix the polarization of the light so that it matches the polarization of the tapered amplifier input fiber.

2. Litrow / Short ECDL Cavity This is an ECDL that is used as a master PA laser source alternative to the long ECDL Littman-Metcalf cavity. Since this laser cavity is in the Littrow configuration, the cavity length is much shorter than the Littman-Metcalf cavity. In fact, this cavity length is ~ 2.8 cm and as a result the sidebands of this cavity are at ~ 5 GHz away from the laser frequency. This cavity was built for two reasons. First, this cavity was used to test the source of the features that appear on our molecular spectrum. We wanted to test if they are a result of the main PA photons or they are a result of the photons at sideband frequencies that co-propagate along with them. If these features take place at the same frequencies even after changing the cavity,

then this suggests that the features are not a result of the laser sidebands. That of course does not exclude any other artifacts that are on the laser as we will explain in the next chapter. The second reason for building this laser cavity is that since the sidebands are pushed to 5 GHz, they do not interfere with our scan range. This allows us to take clean scans without any interference from the sideband photons.

The cavity consists of a Sanyo IR DL-8031-031A diode that has a power output of 150 mW at standard operational conditions. The diode is controlled using commercial controllers from ILX-Lightwave (current controller model LDX-3525 set to 132 mA and temperature controller LDT-5525 set to 10 C or 57.5 K Ω). The output of the diode is directed to a grating (Edmund Optics IR Gold Grating Model: 43848) with 1200 groves/mm. The output from this cavity goes through a pariscope and then optical isolator (OFR IO-3D-811-VLP-TILT-Z). Finally, it is redirected to follow the same path as the Littman-Metcalf beam into the tapered amplifier. The dual operation between the two lasers are made possible using a flip mirror mount. The polarization of the two laser cavities is not identical (because of mirror reflections affecting the beam polarization). That is why after flipping the mirror mount some power tweaking takes place by adjusting the polarization using the waveplates and the fiber launcher lens. The dual operation between the two diode lasers ECDLs is shown in Fig. 33.

The scan of this cavity was possible by applying a sawtooth or triangular wave to the piezoelectric transducer attached to the horizontal adjust on the grating mount. We found that it was possible to scan the cavity smoothly over ~ 1.5 GHz without a mode hop. To be able to perform our experiment, it was helpful to add a feed forward feature to the lock box used to control this cavity. The idea of this feature is to give the current controller a small current adjustment as the cavity scans in order to prevent a mode hop. The design for the modification to the lock box is shown in Fig. 34. The circuit basically uses the modulation/error signals added to the piezo as an additional modulation on the current controller. By adjusting the gain of the feed forward, we can control how big this modulation will be when added to the current. This feed forward signal is added to the current through a Minicircuits Bias-Tee (ZFBT-6G). This modification extends the scanning range of the cavity from ~ 1.5 GHz to ~ 8.5 GHz.

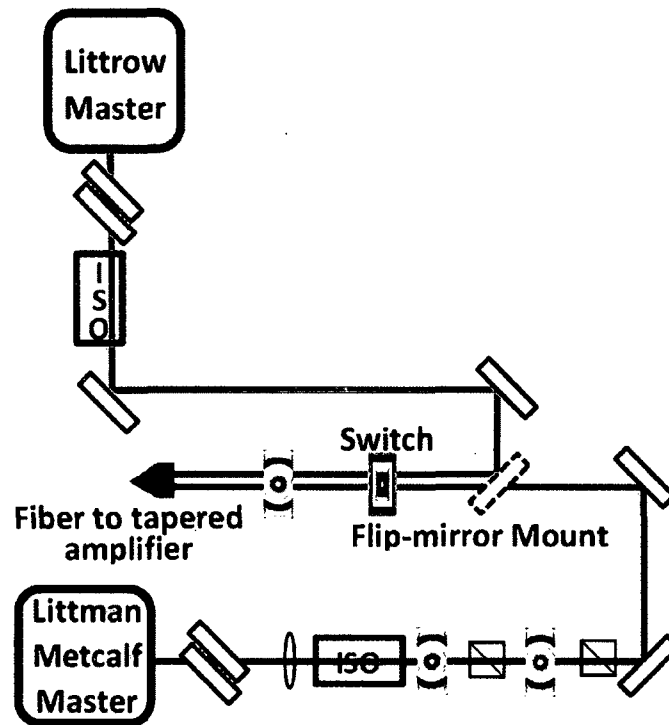


FIG. 33: The PA laser layout for both cavities. The figure also illustrates the dual operation between the two lasers so that the switch between the two is almost instantaneous compared to the stability time of the MOT.

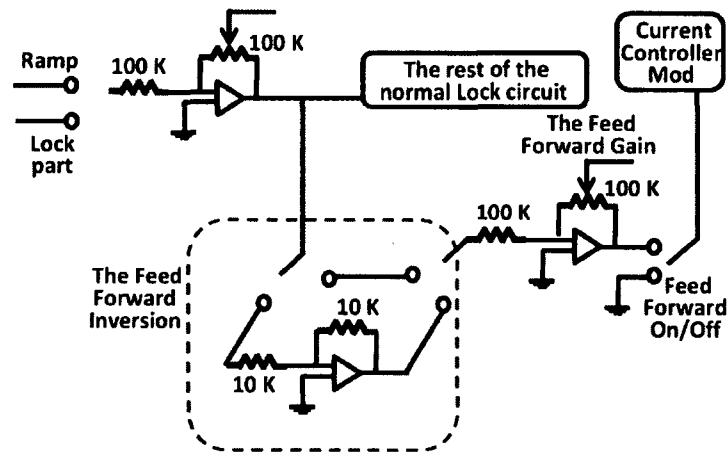


FIG. 34: A circuit diagram showing the modifications made to the lock box to enable the feed forward feature. The output of this modification is added as a modulation on the current controller.

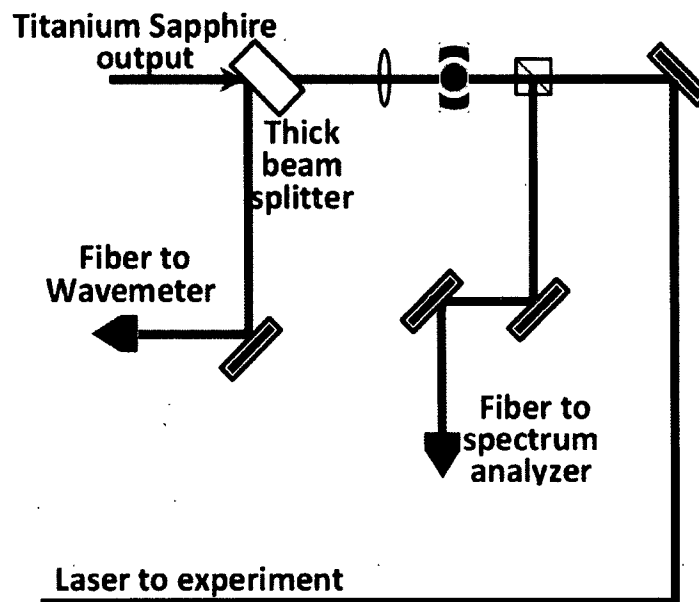


FIG. 35: A layout of the optics used for the Titanium Sapphire monitoring and PA alignment. As shown in the next section the output from this PA will be combined with another beam. It goes through a switching AOM for further launching to the science chamber.

3. The Titanium Sapphire Laser

An alternative PA laser source that is used is the Titanium-Sapphire (TiS) source. The merit of this source is that it is a ring laser (Coherent 899 ring laser) that is pumped through a Verdi laser source (Coherent Verdi-V10 10W). That is why this laser source does not suffer from the sideband disadvantage. The data were taken under typical operating condition of setting the Verdi output to 6 W for pumping the ring laser. That produced about 240 mW output from the TiS laser. The scan of the laser is performed through two etalons that are controlled using a Coherent 699/899 laser controller. The thick etalon should tune the laser frequency in 180 MHz jumps and the thin etalon scans it in 10 GHz jumps. The two etalons are walked off through the controller to cover the 10 GHz scanning range desired for our runs.

4. The tapered amplifier

One of the key factors for performing PA experiment is exciting as many atoms to the higher levels so that they can associate when they undergo an emission

process. That creates a big challenge for our experiment since this requires a high output PA intensity at the position of the trap. We can do this by creating a tighter focus for the PA beam, but this means cutting down the number of atoms that are subject to the PA beam. This is the number of the trap atoms that lie at the PA beam waist. That is why we introduced the tapered amplifier. The basic operation of it is to drive it using an input laser frequency with typically 30 mW input power. Our laser sources input about 12 mW into a fiber that is coupled to the tapered amplifier input. This means about 10 mW are directly coupled into the tapered amplifier with an 80% fiber coupling efficiency. The tapered amplifier that we are using is a Toptica Photonics BoostA tapered amplifier with an input wavelength range ~ 790 nm to ~ 820 nm, so that it will work for both argon and krypton. The tapered amplifier is controlled through a remote control via a computer desktop in our lab. The Hyperterminal control on the computer allows the laser current adjustment. During our data taking procedures, we adjust the current to about 1800 mA. At a fiber coupled input to the tapered amplifier of 12 mW, this will give fiber coupled output of 637 mW. Without the proper seeding of the tapered amplifier, the spontaneous emission from the tapered laser sources will interfere with our experiment. It will travel through the fiber and will make it to the experiment, thereby drastically changing our data. Without proper seeding, the power of the fiber coupled spontaneous emitted light is 64 mW. This delivers about 3 mW of spontaneous emitted light through the optics to the MOT. At the proper seeding, all the output power from the amplifier is locked into the input laser frequency. The specification chart for the tapered amplifier shows a maximum output power at 811nm which makes it perfect to our experiment. Since seeding the tapered amplifier with laser light without powering on the amplifier can burn the amplifier chip, a shutter was added in front of the fiber coupler. In case of power outage the light is blocked from making it to the amplifier.

After seeding the tapered amplifier properly, all the amplifier's power is coupled into a single mode frequency. The output of the tapered amplifier is fiber coupled as well. The output of this fiber is then sent into a $\frac{\lambda}{2}$ waveplate and a polarizing beam splitter. This gives us the flexibility of sending a very small portion of the output light to the beam diagnostics and the beat lock,

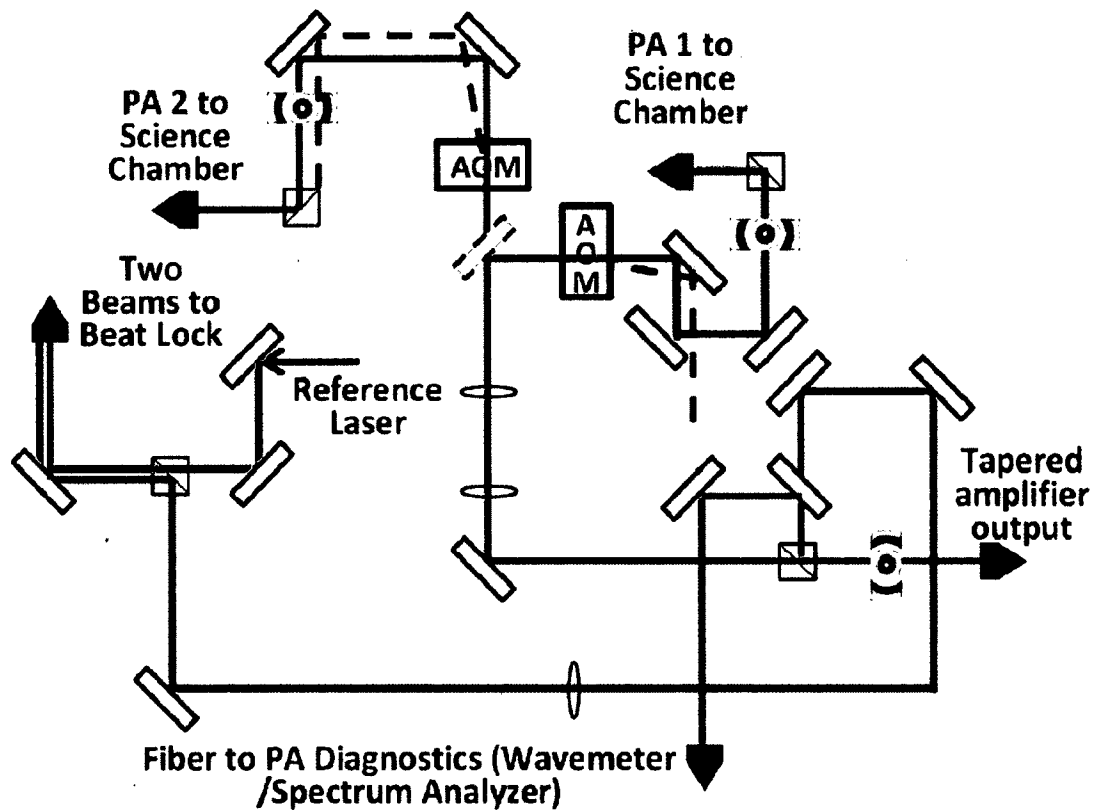


FIG. 36: A layout of the tapered amplifier output for 1) beam diagnostics. That includes both the spectrum analyzer or the wavemeter. The same fiber was coupled for either one. 2) The second part of the output was sent to beat lock technique to enable a continuous scan of the PA laser over the whole range. 3) The third part is coupled into the PA fiber that delivers the PA light to the science chamber PA port.

meanwhile sending the rest of the amplifier output to the PA portion. First, let us trace the weak part of the beam. The light goes through a beam splitter that divides the beam into a part that is fiber coupled through two mirrors. The fiber is then used as an extra monitoring for the PA beam. The monitoring is done on either our wavemeter (Burleigh Wavemeter WA-1000) or on our spectrum analyzer (Burleigh 2 GHz spectrum analyzer with a Burleigh detector amplifier DA-100 and a ramp generator Burleigh 91). The rest of the weak beam is directed into the focusing lens (Bi-Convex $f=250.00\text{mm}$, Thorlabs LB1056-B) to match the beam size between a reference laser and the PA beam. The beam is then reflected off from a polarizing beam splitter and directed into a fiber launcher to the beat lock part that will be explained later in the next section. The strong beam on the other hand is reflected into a telescope to focus the beam into an AOM. After the telescope the PA beam can go through one of two choices using a flip mirror mount. In the first choice, the beam is reflected into a (NEC AO-Modulator Model C8217A) AOM which enables a frequency change in the first order between 60 MHz and 100 MHz. In the second choice, the beam goes straight into a (Crystal Technology Model: 3200-147) AOM. This AOM enables a frequency change between 160 MHz and 190 MHz. The idea of having the two AOMs is to cover different ranges of the PA frequency. This is achieved by changing the frequency offset between the tapered amplifier zeroth order which is locked (using the beat lock) to the reference laser and the AOM first order that is being used as PA light. Another goal of having the AOMs is that they enable the PA light switching so that it is not directed onto the MOT all the time. This gives the MOT time to reload before the PA light is on it again. That is why the first order from the AOMs is then reflected through a combination of a $\frac{\lambda}{2}$ waveplate and a polarizing beam splitter into a fiber launcher. The reasons of adding this combination are first to assure that the light sent to the PA is linearly polarized and second to control the amount of light going to the experiment. Changing the PA power enables us to go over a wide power map as shown in our data. It is very important to note that throughout our preliminary data, we went over the AOM frequency ranges to exclude artifacts from the AOM diffraction orders. We tested if the features were coming from the AOM zeroth order scattering into the fiber and eventually delivered to the MOT. We also went through both the positive and

negative orders of the AOM.

3.3.4 LOCK TECHNIQUES

For our PA lock technique and so that we are able to scan the PA laser smoothly, we need to compare the PA laser to a fixed frequency laser source. The laser source has to be locked to an absolute reference (the absolute reference is usually picked to be a saturation absorption signal generated by the laser that we are using). That is why it is called the reference laser. Next, we will explain the lock technique that we use to fix the frequency of all of these lasers. Finally, we will describe our design for the beat lock that enabled us to scan for up to 8 GHz around the resonance frequency. The 8 GHz scanning range is divided as 4 GHz on the red side of the resonance and 4 GHz on the blue side with small gap between them ~ 520 MHz that could be patched using the AOM shifts.

1. Reference Laser

While scanning the PA laser, it is very important and useful to control and monitor the change in frequency accurately. That is why we built a beat lock system. It mainly works by monitoring the beat frequency signal created between two lasers. The two lasers in this case are the PA laser and a reference laser. The reference laser is used to mark a single frequency reference point which is the resonance frequency of the atomic transition. The reference laser is locked by sending the diffracted first order of an AOM to the saturation absorption (SA) cell. Using the SA signal, we can lock the reference laser to a specific atomic transition frequency or nearby frequencies. The zeroth order of the AOM is sent towards the beat lock optics where it gets compared against our PA laser. The importance of adding an AOM to the reference laser beam, rather than splitting the beam, is to give us the freedom to change the frequency offset. The frequency offset is the difference between the frequency of the reference laser and the frequency of the SA signal which is our zero frequency point. This enables us to cover a larger frequency range when we scan the PA laser.

The reference laser is a Sanyo DL-8141-035 IR diode laser placed in an ECDL in a Littman-Metcalf configuration. The grating used is an Edmund Optics IR

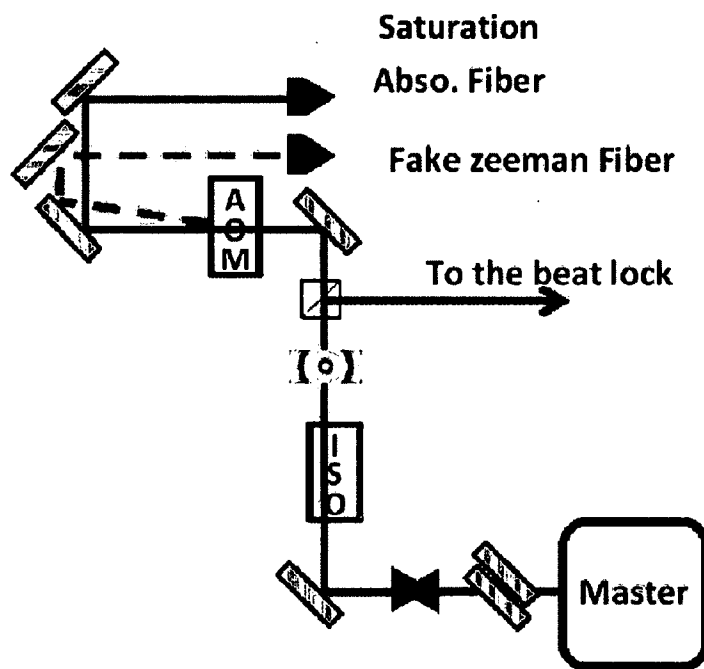


FIG. 37: The optics layout for the reference laser. The “fake” Zeeman slower feature was added for further testing that will be explained later in the next chapter. The reflected polarization from the PBS is sent to the beat lock. This produces the beat frequency required for our beat lock. The dashed line is the zeroth order of the AOM. It is important to note that the frequency and the sign of the “picked” first order were changed along our experiment to cover more frequency range.

TABLE 4: This table illustrates the different frequency values used for different PA experiments.

	Ar	Ar (quench)	Kr	Kr (quench)
λ (nm)	811.7542	801.6990	811.5131	810.6594
Energy (E^{-1})	12318.9996	12473.5100	12322.6595	12335.6369
Frequency(GHz)	369314.32	373946.42	369424.04	369813.09
Lower level	4s[3/2] J=2	4s[3/2] J=2	5s[3/2] J=2	5s[3/2] J=2
Upper level	4p[5/2] J=3	4p[5/2] J=2	5p[5/2] J=3	5p[5/2] J=2

Gold Grating (Model: 43848) with 1200 Groves/mm. A piezoelectric material is added on the mirror mount in the cavity. Applying a ramp to it enables a smooth scan over the ECDL resonating frequency. The diode laser has an output of 150 mW at 50°C standard operation. The diode laser is operated at current of -140.72 A and a temperature settings of 9.82 V which corresponds to a temperature setting of 17.5°C. The output from the master ECDL reference laser then goes through a pariscope to raise the height of the laser beam so that it is easier to vertically manipulate it. Then it goes through an anamorphic prism pair for spatial mode correction (changing the shape of the beam from elliptical to circular). Later the beam is reflected into an optical isolator (Isowave model: I-80-T4 with an isolation 38-40db). The light is then transferred into a combination of a $\frac{\lambda}{2}$ waveplate and PBS. This controls how much light is sent to the AOM and how much light is sent to the beat lock. The transmitted light is reflected into an AOM (Crystal Technology/ Model: 3200-142/13671) that is set at 190 MHz. Another AOM that was used during our preliminary data is (NEC A-O-Modulator/ Model:C8217A) for another frequency range between 60 MHz and 100 MHz. In figure 38, the negative first order is sent to the SA through an optical fiber. It is important to note that the AOM shift was changed along the experiment and swapped between positive order and negative order to cover a larger frequency range.

2. The master lasers lock

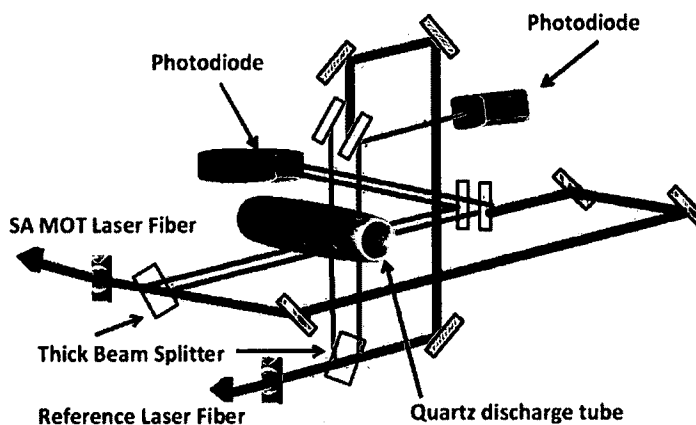


FIG. 38: The optics layout for the saturation absorption signal for both the MOT master laser and the reference laser. The graph shows a three dimensional set up. The green beam from the MOT master laser is in the X/Y plane and the red beam from the reference laser is in the Y/Z plane.

For both the MOT master laser and the reference laser, we discussed how to stabilize the ECDL so that it resonates at a frequency mode close to the atomic resonance transition. We also mentioned that through current and temperature adjustments, we can bring the cavity to this resonance frequency. Now we will explain how to keep the frequency of the ECDL fixed at this frequency throughout the course of our experiment.

To keep our lasers frequency stabilized or “locked”, a laser beam is fed into a saturation absorption spectrometer. By observing the spectrometer signal, a frequency measurement relative to the atomic transition frequency can be inferred. The spectrometer arrangement is as follows: The laser beam, usually coming from a fiber, is divided into three parts. Two weak beams reflect off a thick beam splitter and a transmitted strong beam which we call the pump beam. Then the two weak beams are aligned through the quartz tube where the discharge takes place. Some of the atoms in the tube are in the metastable state when the discharge is on. The number of atoms in the metastable state is the largest when the discharge is all tweaked up and in its brightest state. After the two beams enter the tube, they interact with the atoms in it. The interaction produces two big Doppler broadened peaks that are visible on photo-diodes. The next step is to redirect the strong beam back into the tube in a collinear

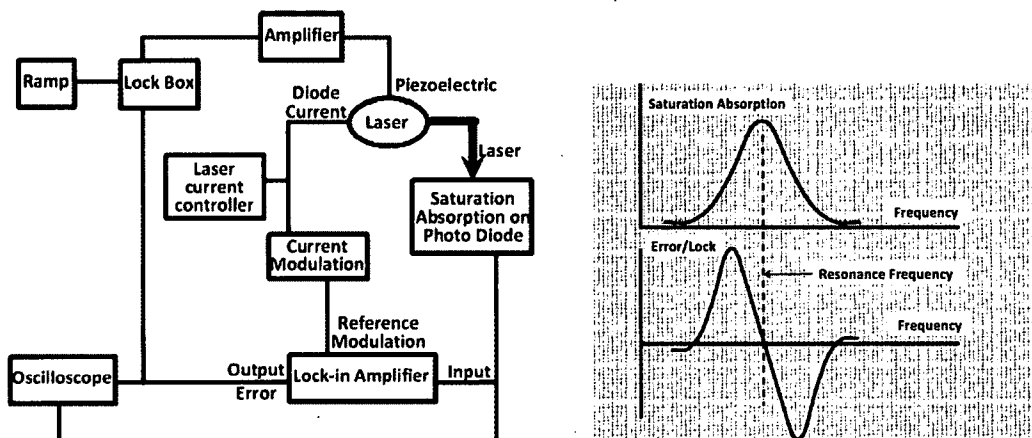


FIG. 39: The graph to the left shows a block diagram of our lock circuit. The graph to the right shows the theoretical output of the saturation absorption cell “red” and the error signal used to lock the lasers “green”.

counter-propagating direction to one of the two weak beams (which we call the probe beams). As a result of this, the Doppler broadened peak from the probe beam will show additional features which is the saturation absorption signal. This signal happens at the frequency where the atomic transitions take place (or at other places known as crossover peaks).

To better understand this, we will consider what the weak beams do and what the strong beam does separately. For the weak beams, as the laser is scanned through different frequencies, it starts to interact with different atoms. When the beam is slightly red detuned in frequency, it will interact with atoms moving towards it. As it goes to the blue frequencies, it will interact with atoms moving away from it. Only when the frequency of the weak beams is exactly the same as the resonance frequency, it will interact with non moving atoms or those moving perpendicular to the laser beam. This means that as we change the frequency of the weak beam around resonance, it will always interact with some atoms. Hence we will always see a big Doppler broadened peak around resonance. Now let us consider the strong pump beam action. Because the probe beam and the pump beam are driven from the same laser source, they have exactly the same frequency. When they are both on the red side and because they are counter-propagating, they will interact with atoms moving in different directions. This will continue to be the case except at resonance frequency when both of them

will interact with the same velocity class of atoms. Since the pump beam will have high intensity, it will saturate the transition. When the probe beam arrives, the transition is already saturated from the pump beam and the probe beam is not scattered. This appears as a small feature on top of the big Doppler feature. The comparison between the photo-diode signals that are observing the two weak beams can produce a Doppler-free saturation absorption signal. The photo-diode signals are one Doppler broadened signal from one weak beam and one Doppler broadened signal with SA feature on top of it from the probe beam.

To simplify the electronic circuit used, we have to separate the components that are fed into the laser and affect its frequency. The first part is the piezoelectric transducer connected to the mirror or the grating mount in the ECDL cavity. The second part is the current signal feeding the diode laser from the current controller. We also have to introduce a new device which is called the Lock-in amplifier. It generates a reference modulation and adds it to the laser and then it demodulates the spectroscopy signal. It does a phase sensitive comparison of the SA signal. This demodulation technique provides a signal that closely resembles the derivative of the SA signal. The result of this action is that it produces an error signal which crosses zero at the atomic resonance frequency as shown in Fig. 39. If this error signal is integrated and fed back to the laser, it will keep the laser at this specific frequency.

The circuit description for this lock is as follows: It starts by feeding the piezo on the laser ECDL with a ramp. This ramp is either a triangular or a sawtooth wave that has a frequency of 10 Hz and an amplitude of 0-10 volts. It goes through an amplifier to 0-100 V and is then fed into the piezo. The reason of the ramp is to scan the laser frequency across the resonance frequency. On the other side, the lock-in amplifier generates a small 10 kHz modulation that is added to the current of the diode laser through a current modulation box. This box allows us to adjust the amplitude of the modulation so that it is large enough for our lock, but does not broaden the laser too much. As a result of the scanning and the modulation, the SA signal will be generated. When the saturation absorption signal is fed back into the lock-in amplifier, it generates an error signal. The error signal is then fed back into a lock box to park the laser on the resonance frequency.

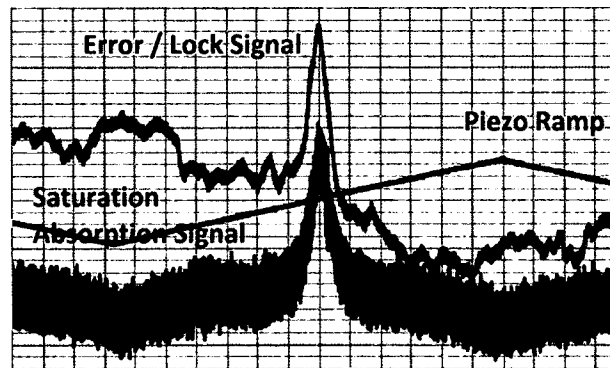


FIG. 40: A graph for our saturation absorption output signal used in the lab is shown in red. The error signal used in locking the laser is in green. The blue ramp signal is the signal fed in the piezo to scan the laser across the resonance.

3. Beat Lock

One of the biggest challenges that we had in our experiment is statistics. The PA laser cavities are placed in a metal box. Even though we try to control all of the environmental conditions of the diode laser - especially temperature - we still suffer from minor temperature fluctuations. These fluctuations in addition to other system imperfections cause our ECDL cavity laser to drift ~ 3 MHz in the course of 10 minutes. The imperfections can be due to slight diode laser power drifting, vibrations (terrestrial,.....) and noise on the piezoelectric material ramp signal just to name a few. Although this is a very small drift, it limits our data building up statistics at a fixed frequency. Every time we take one ion record ($\sim 200\mu\text{s}$), we have to wait for the MOT to reload $\sim 8000\mu\text{s}$. That is why if we want to build up enough records at the same frequency, we need to fix the laser frequency at the same value (an error of ~ 2 MHz) for up to 16000 ms. This is just for an average statistics data point (2000 record per data point). For some scans, we needed to extend this to 30000 ms. For the quench features study, we had to keep the laser frequency at the same value for 7 or 8 hours to build up enough statistics. The quench transitions kill the metastable state atoms which require us to wait until we completely reload the MOT from empty. That takes $\sim 2-3$ s before every ion record is measured. All of the reasons mentioned above imposed a strong need to lock the PA laser to a single frequency value. This value has to be 1) accurately “locked” in the

2 MHz interval and 2) we have to be able to scan this value so that we can produce a molecular spectrum.

The beat lock starts by combining the two beams from the PA laser ECDL and from the reference laser that is locked to resonance. When we combine two beams with different frequencies, they start beating against each other. The beat frequency is given by the difference between the two frequencies. We can approximate each wave ψ_1 and ψ_2 for each laser by $\psi_1 = A\cos(\omega_1 t)$ and $\psi_2 = A\cos(\omega_2 t)$. Where ω_1 and ω_2 are the two waves frequencies. Here we have assumed that the two waves have almost the same amplitude which is the case in our experiment. We assure that each wave has a transmitted power through the fiber of about 300 μ W. The addition of the two waves from simple trigonometry is $\psi_1 + \psi_2 = 2A[\cos[(\omega_1 + \omega_2)t/2]\cos[(\omega_1 - \omega_2)t/2]]$. So the small frequency will create an envelope to the large average frequency and it will be our beat frequency. The two beams are coupled into a fiber launcher and the fiber is S630-NP/ TP0071 6415. The output of the fiber is directed into 4.25 GBPS 850 nm PIN + preamplifier. The output of the preamplifier has one of two choices. First choice is when we make a scan from 0.7 MHz to 4 GHz. In this case we use a two steps dividing circuit to divide this frequency by 800 so that the output beat frequency will be in the 10 MHz range after division. This value is within our beat lock electronics range. It is then compared against a set frequency (that we set using the computer depending on where we want the PA laser frequency to be). The comparison between the two frequencies produces an error signal that can be fed into the lock box to lock the piezoelectric transducer in the ECDL at the set frequency. For example, if we need to lock the PA laser at -4 GHz from resonance, we set the computer generated value to 4000 MHz/ 800 = 5 MHz. The error signal generated from the lock box will guarantee that the laser stays at this frequency in the 2 MHz uncertainty window. When we scan the laser frequency to the next value -3.998 GHz, we set the frequency to 3998 MHz/800= 4.9975 MHz. That will change the PA laser frequency by 2 MHz. At every single frequency value, we can lock the laser long enough to build enough statistics. The laser's frequency will remain fixed as long as the laser ECDL remain locked and stable. The second choice takes place when we want to study the frequency range much closer to resonance molecular features. At this point, we need to use a dividing stage

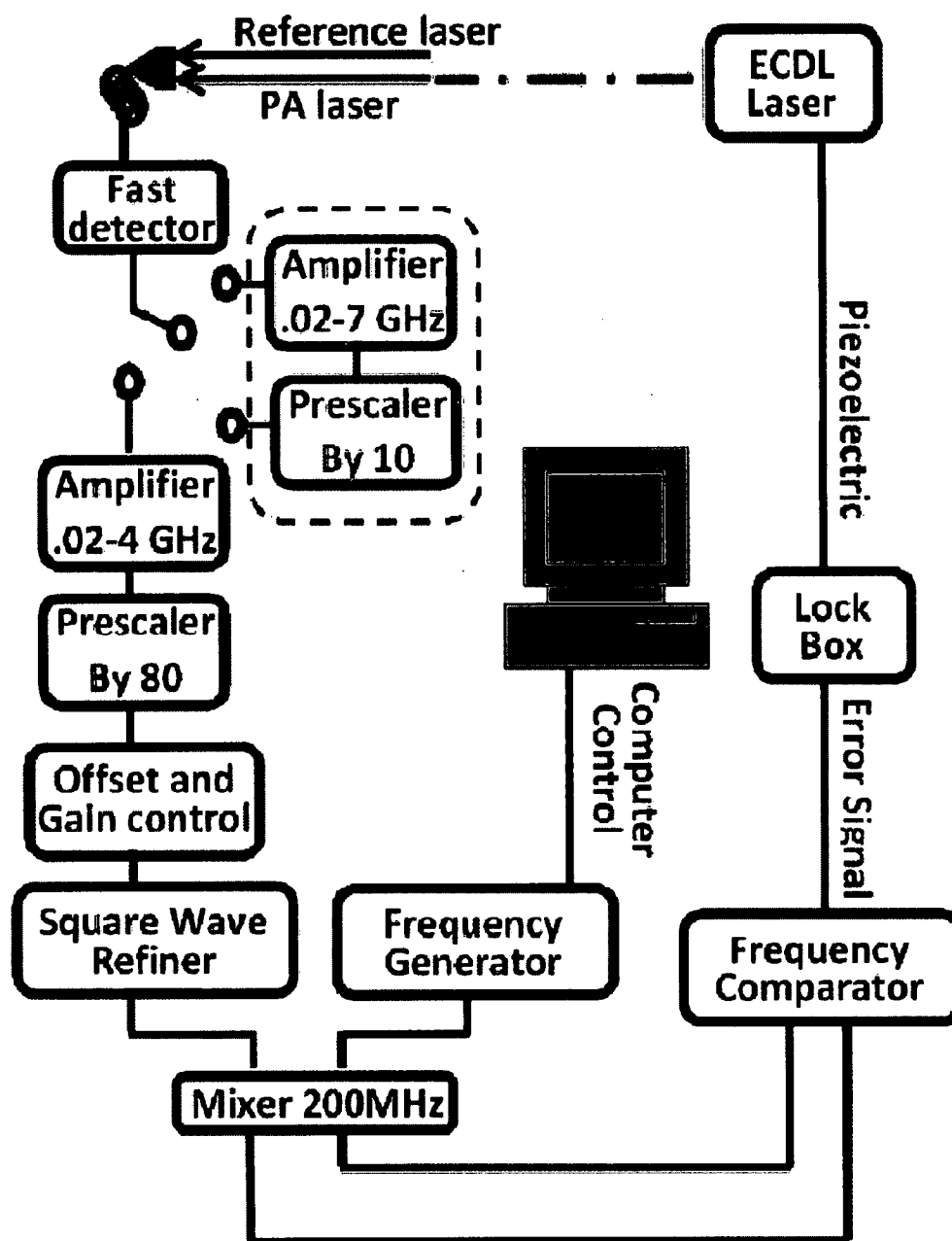


FIG. 41: A schematic diagram of the beat lock. The part in the dashed rectangle is the second stage divider. The beat lock can work for small ranges ~ 1 GHz without the second stage. For higher frequency ranges ~ 4 GHz the second stage is added to further divide the beat frequency to be within our electronics range. The dashed green line between the laser and the fiber launcher indicates going through optics. The beam goes through optics into the tapered amplifier and then further optics until eventually the PA and reference laser beams are combined on the fiber launcher.

that divides only by 80. This division will enable a scan between 70 MHz and 1 GHz. After the division, the lock circuit follows the same exact logic as the first choice division. The rest of the frequency range very close to resonance can be covered using the AOM shift. AOM shifts means using the appropriate combination of the reference laser AOM and the PA laser AOM. To summarize all of this, we label them either one stage division (by 80 covering the range .07-1 GHz) or two stages division (by 10 then by 80 covering the range .8- 4 GHz).

Figure 41 illustrates a diagram of the beat lock. Basically, the output of the fiber is sent into the preamplifier/photo detector. The output of the preamplifier goes into an amplifier (Minicircuit ZJL-7G Gain: 10 dB and in the frequency range of .02 to 7 GHz). The output of the amplifier goes into the prescaler (RF BAY / FPS-10-12 divide by 10 and in the frequency range .1 to 12.5 GHz). This is used for the two stages division. The dividing by 80 step is done using an amplifier (ZJL- 4 HG /typical gain 17.0 dB/ in the range .02 to 4 GHz). The output of the amplifier is followed by a prescaler (MC12080 dividing by either 10 or 20 or 40 or 80) which we have it set to divide by 80. The dividing by 80 stage is used for both one and two stages divider. The output of the division has the problem of having a dc offset and not being perfectly a square wave. The reason for this is that as the fast original signal (4 GHz) goes through our circuits, it transmits rf noise that is picked up later by our divided signal. Also the electronic circuit noise contribute to the generation of the bad square wave. To solve this, the signal goes through a saturating inverter signal that serves for two jobs (to cancel the dc offset and change the signal gain). The signal then passes through a logic level translator (Phillips Scientific/ 16 channel logic level translator/ NIM Model 726). The translator output is a very clean square wave at the same frequency as the input signal. The output of the division is mixed with a set frequency supplied from (Hewlett Packard 33120A/ 15 MHz) and controlled by our National Instruments Labview program. The mixer is a AD9901 (Ultrahigh Speed Phase/ Frequency Discriminator). The two outputs from this circuit is coupled into a comparator (SGS-Thomson microelectronics/ TL074 low noise quad J-FET operational amplifier). This mixer/comparator job is to look at the two frequencies (divided beat frequency and the set frequency). If one frequency is bigger than

the other, it saturates into one direction of voltage. For the other way around of frequencies combination, it saturates into the other polarity. This creates an error signal that crosses zero only when the beat frequency equals the set frequency, hence keeping the PA laser at the zero crossing frequency. The set frequency is controlled using our Labview program and supplied with different frequencies for each data point on the molecular spectrum.

3.3.5 LASER BEAMS SET UP INSIDE THE SCIENCE CHAMBER

This section will describe the way all the optics are aligned so that they send the three X, Y and Z circularly polarized beams into the chamber. We will also discuss how the Zeeman slower laser beam is sent down along the Zeeman slower axis. It will also explain the different ways we used to send the PA beam into the chamber. Next we will describe measurements of the PA beam waist along its path since knowing the PA beam shape is essential for our data analysis. This section also describes the science chamber and a detailed description of the different ports of the chamber. It is advised throughout this section to use figures 42 and 43 as two different projections of the science chamber to give a feel for the three dimensional shape of the chamber.

In the chamber schematic, the ports were numbered by labels that go between P1 and P12 with P1, P4, P7 and P12 ports labeled on the graph. The P1 port is connected to the Zeeman slower and that is where the atomic beam enters the chamber. P2 is the port where the Y-axis trap beam enters the chamber. That is why it is an anti-reflection (AR) coated window to maintain minimal power loss. P3 is connected to a T-shaped connector with the straight side as the inlet of the PA so it is an AR coated window. The right side is connected to the titanium sublimation pump. The addition of this pump helps with initial pump down of the chamber after it has been opened to air. P4 was used originally as a photomultiplier tube (PMT) monitoring port. Unfortunately, the PMT was found to be an inefficient detection method in our experiment. This is because our detector consists of a metal ring that is located really close to the MOT which causes a lot of scattering from the trap laser beam. This high scattering washes out our signal and results in a very small signal to noise ratio (500mV/5V observed on the oscilloscope). The P4 port was used throughout the experiment for different purposes of monitoring and alignment and sending auxiliary laser beams in, which will be explained in more detail later. P5 port is the X-axis inlet port. P6 is the port where our ion detector (channeltron)

is connected. P7 is the inlet of the Zeeman slower laser beam. As in the case of P3 there is a T-shaped connector with the straight part going toward the Zeeman beam (AR coated window). The right angle port is connected to the (ULTEK) ion pump. P8 is the opposite side of the Y-axis beam. P9 is the opposite side for the PA beam. So they are both AR coated windows. P10 is used as a connector to the turbo pump. The pump is directly connected to the port to improve the pumping speed and the gas flow conductivity. P11 is the opposite port of the X-axis beam (AR coated window). P12 has a camera looking at it and it serves as a good visual way for monitoring the MOT in addition to assisting with the PA alignment (as a replacement of the PMT).

The Zeeman slower laser beam: The slowing laser light is transferred through fibers from another optic table that is floating to remove noise on the laser frequency produced by terrestrial vibrations. Since the fibers that we use in transferring the light are not polarization preserving, we need to clean the beam polarization. That is why after the beam exits the fiber it goes through $\frac{\lambda}{2}$ and $\frac{\lambda}{4}$ wave-plates before it goes through a PBS. The reason for this combination is to adjust the beam polarization so that only the beam with linear polarization will go through the PBS. The wave-plates job is to rotate the beam polarization and as a result maximize the transmitted linear polarized light. The beam then goes through a telescope to increase the size of the beam waist ($\sim 0.5\text{cm}$) so it can interact with more atoms, thereby slowing down a larger number of atoms. After a couple reflections on infrared (IR) mirrors, the beam goes through a $\frac{\lambda}{4}$ wave-plate to change the linearly polarized light into circularly polarized light. The IR mirrors were aligned so that the beam travels along the tube where the Zeeman slower magnetic coils are mounted. This light is very slightly focused as it counter-propagates with the atomic beam.

The trapping laser beam: This describes the way the six counter propagating circularly polarized laser beams are delivered to the science chamber. The beam comes out from the fiber and then reflects off couple IR mirrors before going through a combination of PBS 3, $\frac{\lambda}{2}$ and $\frac{\lambda}{4}$ waveplates. Similar to the Zeeman slower beam, this cleans the laser light polarization and creates a linearly polarized light. The light then goes through a telescope to expand the beam to increase the number of atoms that the laser light interacts with. Before going through the telescope a $\frac{\lambda}{2}$ waveplates is added which determines the ratio of the light intensity that is split between the Z-axis and the X-Y plane at the PBS 2. The X-Y plane light is split

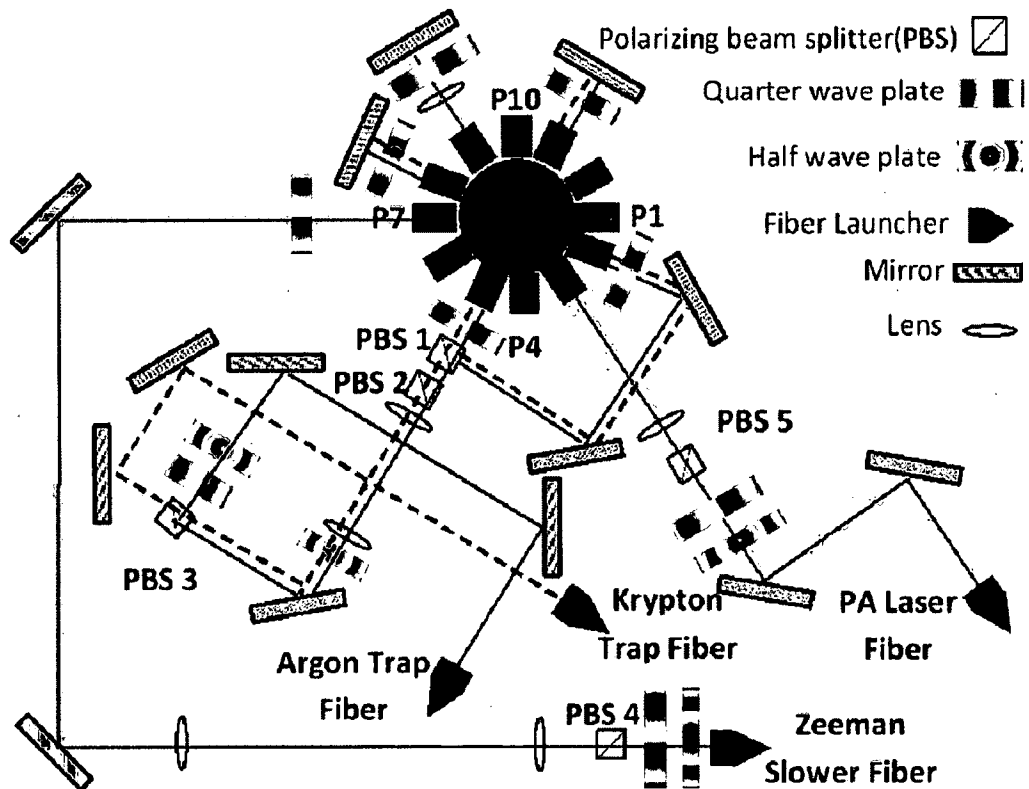


FIG. 42: This figure shows the layout of the optics delivering the laser beams necessary for our experiment. The green line is meant for the Zeeman slower beam. The black straight line is for the trap beam used alternatively between Ar and Kr. The dashed line is meant for the dual operation between Ar/Kr. The red beam represents the PA beam. It is also important to note that the ports are numbered and each port is described in detail in the text. It is also important to mention that there is another dimension that is not included in the graph as PBS 2 splits the trap beams between the x-y plane and the vertical z-direction.

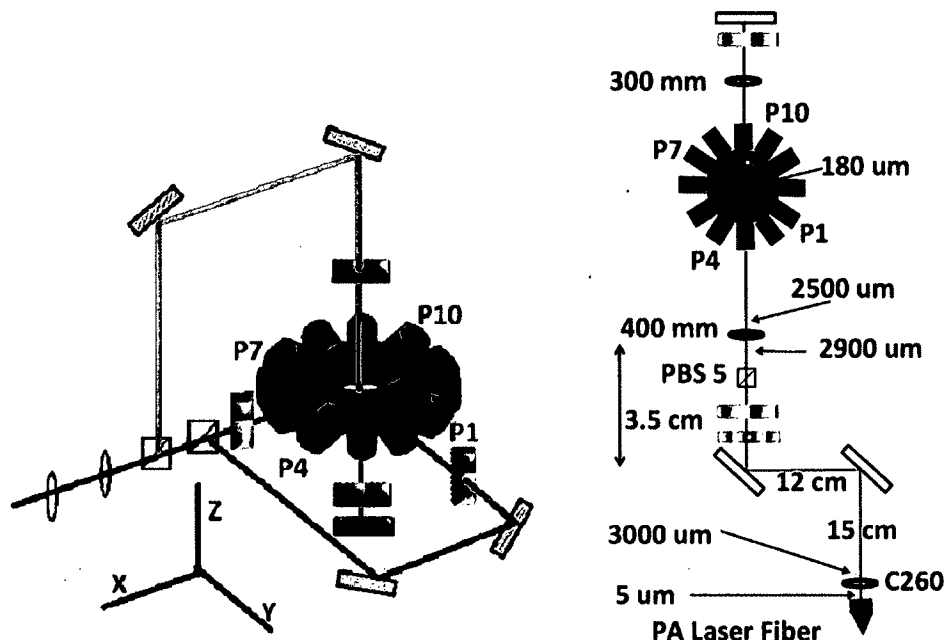


FIG. 43: The figure to the left shows the third dimension in the figure 42. The Z-direction is distinguished from the X-Y plane beams by giving it a different color (orange versus black). The figure to the right shows the accurate measurements of the PA beam diameter along its path.

between the X-direction and the Y-direction using another PBS 1. At this moment the light beam is split between X, Y, Z direction and the three beams are linearly polarized. That is why a $\frac{\lambda}{4}$ waveplate is added right before each entry window to change the linear polarization into circular polarization. As every beam exits that chamber it goes through $\frac{\lambda}{4}$ waveplate in the forward direction which will change its polarization from circular polarization into linear polarization. The beam reflects on the mirror and reflects back in the same incidence path. It goes back through the $\frac{\lambda}{4}$ waveplate and changes the polarization again from linear to circular in the opposite circular polarization direction. As part of our future design for the experiment to trapping both argon and krypton an alternative path is added. The two beams are combined at the PBS 3 and then they go through the same optics of expansion and division between different axial directions.

The PA laser beam: The PA laser light is sent through an optical fiber to a collimation lens (Thorlabs C260) of focal length 15.29 mm. The collimation length takes the beam waist right out from the fiber of $\sim 2.5 \mu\text{m}$ and expands it to 1500

μm . Then the laser travels a total distance of 30 cm. This distance is divided as 15 cm to the first mirror and 12 cm to the second mirror and 3.5 cm through the two waveplates ($\frac{\lambda}{2}$ and $\frac{\lambda}{4}$) and the PBS. This distance takes into account traveling through different materials when calculating the actual path length. The light then makes it to the first lens (a plano convex lens of focal length 400 mm (Thorlabs LA1172-B)). The lens is positioned at a distance of 400 mm from the center of the chamber where the MOT is usually located. The lens focuses the beam waist from 1450 μm before the lens to 1250 μm right after the lens and then 90 μm at the MOT location. The beam then expands again and go through a second lens (a plano convex lens of focal length 300 mm (Thorlabs LA1484)). The lens is positioned at a distance of 300 mm from the center of the chamber where the PA beam was focused to 90 μm . The beam leaves the lens almost collimated where it is reflected back to it using a mirror perpendicular to the beam. It passes again through the lens where it is focused back on the MOT location and it keeps back tracking its original path until the PBS.

The reasons for having the PA beam retro reflection are both for greater intensity of spectroscopy light and to balance the scattering forces of the PA beam near resonance. In terms of power, if we neglect the effect of power lost in all the reflections and transmission, we will end up with a beam with double the power at the MOT site. Hence, we will have a higher intensity. Higher intensity is also achieved because of the beam focusing to a tight waist. The intensity is proportional to the power and inversely proportional to the beam size. $I = 4P/\pi w^2$, where I is the intensity, P is the beam power and w is the beam waist. Focusing allows us to obtain higher intensities, but the down side to this is that since the PA beam waist is not as big, it does not interact with as many atoms. On the other hand, the atoms that do interact with it will feel a stronger intensity than they would if the beam was not focused. As for the PA beam polarization, the PA beam comes out from the combination of the two waveplates ($\frac{\lambda}{2}$ and $\frac{\lambda}{4}$) and the PBS linearly polarized. It arrives at the MOT site linearly polarized. Then, it goes through the $\frac{\lambda}{4}$ waveplate twice (forward and retro-reflection) which takes it back to linear polarization. This results in two PA beams that are linearly polarized at the MOT position with their linear polarization direction perpendicular to each other.

3.3.6 FREQUENCY CALIBRATION

Until now, we did not mention how we calculated the laser frequency to high precision. We explained the beat lock and how it was used to fix the frequency of the PA light relative to the resonance frequency. The beat lock was not the only method used to calibrate the laser frequency. Other methods were used that were not as accurate as the beat lock. However, they were well within our error bars for our spectrum in those experiments. They also did not require as high power as the beat lock. For all of those methods, the saturation absorption signal was used to know the position of our zero frequency detuning. The methods we used for frequency calibration are described below.

1. Spectrum Analyzer. Spectrum analyzers used in our experiment are built in Fabry-Perot configuration. It consists basically of two mirrors facing each other. As the input light enters the region between the two mirrors, it reflects back and forth between the two mirrors. Each time the light beam reflects through the mirrors it increases the path difference between the original beam and the reflected beam. This path difference is proportional to the distance between the mirrors. All the beams that are bouncing off the two mirrors have different path lengths. Constructive and destructive interference takes place between these beams. We will only have amplification when the beams are in phase from which we can infer the frequency of the laser. In our experiment we used two different optical spectrum analyzers.

The first one is a commercial 2-GHz Burleigh Spectrum analyzer with a Burleigh detector amplifier DA-100 and a ramp generator Burleigh 91. In this type the two mirrors are enclosed inside a casing. It is designed to minimize temperature fluctuation or any other noise sources that can affect the interferometer length. The mirrors are allowed to move using a piezoelectric transducer on the back of the mirrors. This changes the cavity length and hence scans over the different frequencies of the interferometer. It then graphs a relation between the power of the transmitted light and the frequency at which constructive interference takes place. The result is a graph which only shows peaks at the main light's frequency as well as any sidebands frequencies that are overlapped on the incident light. This takes place only if the incident light sideband frequencies are in the range of the interferometer. We use this spectrum analyzer to monitor our ECDLs single mode behavior and if there

are any modulations. The modulations can be produced due to optical feedback from optics on the table or due to electronic noise on the diode laser's controllers.

The second type is a home built spectrum analyzer. It consists of two flat mirrors and the distance between them is fixed using stainless steel rods. The rods were picked to have low temperature expansion coefficient to minimize the interferometer length swings due to temperature fluctuation. The whole assembly is placed in a transparent box for further stability. The output is monitored with a photodiode to measure the power of the output beam. The length was picked so that the spacing between the resonance orders of the interferometer is 300 MHz. In other words, the free spectral range is 300 MHz. As the PA laser was scanned, a fraction of the light was sent to the cavity and the output power was monitored. As we change the laser frequency, the power transmitted will go through constructive interference and after 150 MHz, destructive interference will take place.

2. Wavemeters. The wavemeters we used are both Burleigh WA-1000 and WA-1500. They are both Michelson interferometer based. The first one has a resolution of 100 MHz with ± 300 MHz accuracy. However the second wavemeter (WA-1500) employs a temperature stabilized HeNe laser and has a resolution of 10 MHz with ± 60 MHz accuracy. The two wavemeters are integrated into our Labview program and are used as read out for the laser frequency.

3. Network analyzer

This is an Agilent N9320B RF Spectrum Analyzer (9 kHz to 3.0 GHz). This is an rf spectrum analyzer. It requires an electric signal input which could be supplied from a fast photodetector. This spectrum analyzer is also used to monitor our beat lock performance by monitoring the divided square wave generated by the Logic level translator (Phillips Scientific / 16 channel /NIM model 726).

3.4 DATA COLLECTION / DETECTION TABLE

The photoassociation spectrum has been studied for different elements throughout the literature. Homonuclear and heteronuclear molecules were detected as features

appearing on the spectrum. In most of those experiments, the spectrum was produced by measuring the number of photon scattered from the MOT. The photons could be the trap beam photons (MOT light) scattered from the MOT itself. The MOT photon scattering helps to estimate the number of atoms in the MOT (i.e. the MOT density). This can tell us if the PA process forms a strong channel of atoms loss from the MOT by coupling them into a different state (atomic or molecular) that can not be re-trapped using the MOT light. In other words, the PA light can channel the atoms into a different atomic state that the trap lights are not resonant to, hence no MOT loading and no photon scattering. The PA light can also create a molecule which will remove two atoms from the MOT and as a result will decrease the number of photons scattered from the MOT. Another aspect of the photon detection method takes place when we know that one of the by-products of the PA process is a photon with different frequency. The photon detection technique is performed using a photomultiplier tube (PMT). The PMT depends on creating electrons using the incident “detected” photons. The electron emission stimulates further secondary electron emission from cascade dynodes. The secondary electrons stimulates further electron production until they finally make it to the anode where they are collected as an electric current. Unfortunately, in our experiment using the PMT is not informative since the scattering inside the chamber cause a poor signal to noise ratio. It is very important to note that the frequencies of the Zeeman slower, the trap and the PA photons are very close for most of our experiments. This makes it harder to trace back the source of the detected photon. In addition to that scattering from the other metal parts that exist inside the chamber creates a huge background on top of the scattering from the MOT atoms itself.

The other detection method that is used in the PA literature is ion detection. As described before, because the atoms in the MOT are close to each other and subject to constant mutual collision, ion production through Penning ionization (PI) and Associative ionization (AI) is very frequent. Adding the PA light causes further ion production that could be detected as a function of the PA laser frequency. The ion detection usually takes place using a “channeltron” or electron multiplier tubes. The channeltron we used is shown in Fig. 44. The electron multiplier’s function starts with an incident ion (or electron) on the surface of the tube creating secondary electrons. As those electrons accelerate towards the tube’s anode, they undergo constant collisions with the surfaces of the tube and create more secondary electrons.

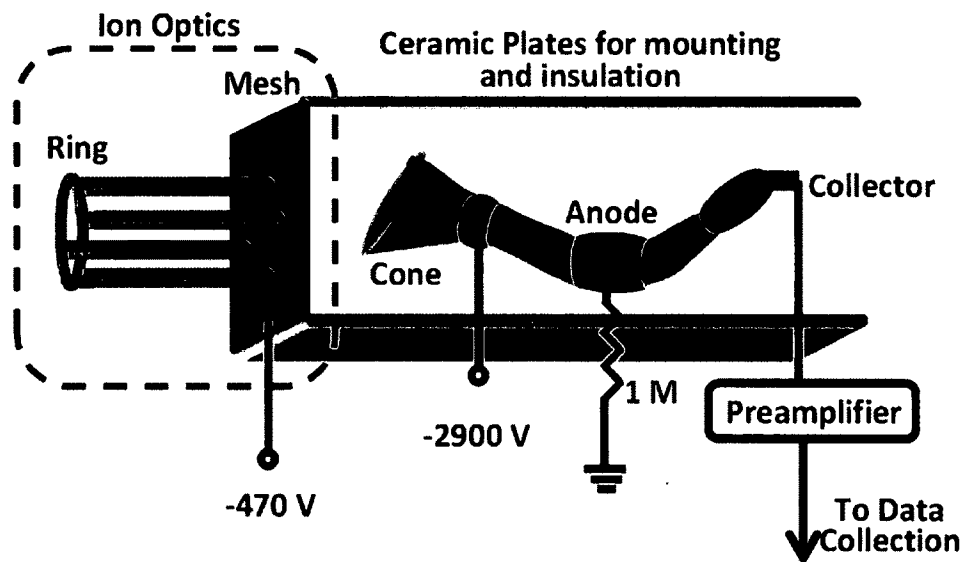
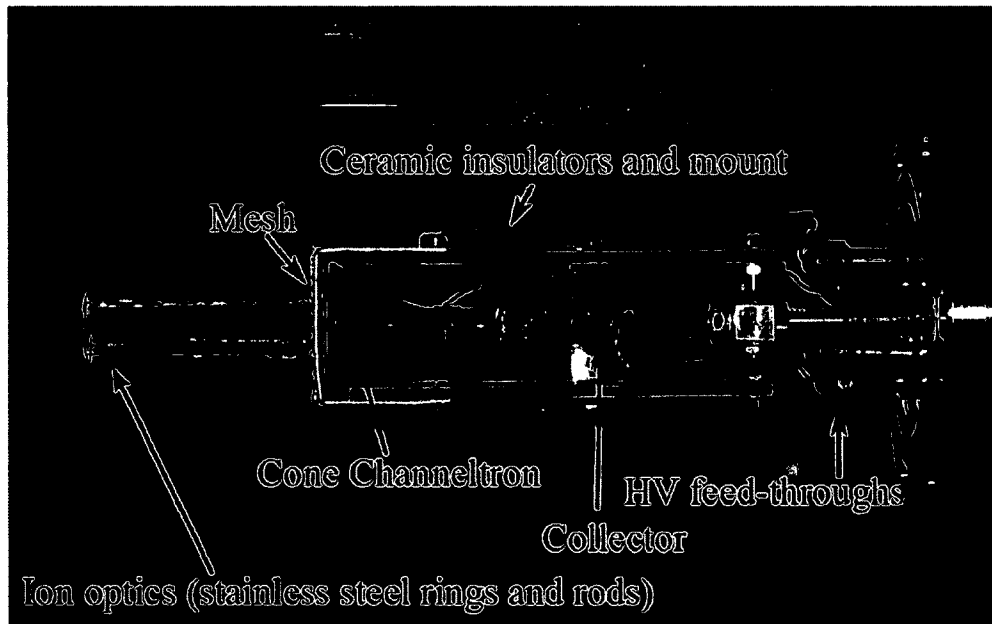


FIG. 44: The top image is a photo of the channeltron configuration that is used in our set up. This was used by G. Ranjit in his thesis. The photo is from his thesis [16]. The bottom image shows the ion detector's connections.

Every electron collision with the tube creates more secondary electrons until the electrons reach the tube's anode forming the electric current. The output current produced is proportional to the number of electrons originally incident on the front of the tube. Our specific channeltron has slight modification to it so that it has better ion collection efficiency. In front of the channeltron, homebuilt ion optics are attached to accelerate the ions towards the detector to help with the ion collection efficiency. The channeltron is usually mounted on one of the science chamber ports. These ports are relatively far from the MOT position at the center of the chamber. This means that the ions have to travel a relatively long distance before they are detected. This imposes high voltage (that the channeltron can not take) being applied to the channeltron to accelerate the ions along this large distance. That is why, we added the ion optics part to the channeltron. Another reason for having the ion optics is that the channeltron is mounted on the chamber port. It will be somewhat surrounded by the chamber's flange which will shield the electric field produced by the channeltron to pull the ions. Our ion optics consists basically of a homebuilt stainless steel ring (~ 1 cm in diameter) spot welded to four stainless-steel rods. The rods are in turn welded to a mesh (only one of the four rods is welded to the mesh). This part is supplied by a constant high negative voltage throughout the experiment. A voltage of -470 volts is supplied from a high voltage power supply (Fluke 415B). This voltage was chosen and tested to provide the best MOT ion detection efficiency. The ratio of the ion counts from the MOT to the ion counts from the background (discharge, ion collisions with the chamber walls) was measured as a function of the ring voltage. It was found to saturate at some value which was about -470 volts. The voltage is supplied through feed-through in the chamber's flange where the channeltron is mounted. The feed-through is chosen so that it maintains the vacuum pressure as well as supplies the high voltages to different parts of the channeltron without shorting as shown in Fig. 44. Ceramic hollow rods are used for wire insulation. The objective of having the ring sticking inside the chamber very close to the MOT position is that it acts as an ion lens that attracts, focuses and accelerates all the ions towards the channeltron. There is one difference between our setup and that of the previous graduate student Gambhir Ranjit. In Ranjit's apparatus, the ion optics/channeltron combination was used from one side and another ring was used from the other side. The two rings were used to field ionize the MOT atoms through high electric field pulse applied on one of the two rings. However, in our setup only the ion optics/channeltron combination

is used and only for ion collection efficiency purposes.

The electric connections on our channeltron (Galileo / 4870 V) are chosen so that they accelerate the electrons in the channeltron to cause more secondary electron production. The cone which is the front part of the channeltron is connected to (SRS Stanford Research System / Model: PS350/ 5000 -25 W) that supplies a voltage of -2900 Volts and drives a current of $.27 \mu\text{A}$. The current monitoring serves as a sign of any electric shorts on the channeltron surface. The 4000 Channeltron series has the additional feature of having an internal resistor between the collector part and the cone part. The collector is the back of the channeltron and it is electrically isolated from the rest of the channeltron. The cone part is the input of the channeltron. The internal resistor helps to draw linear output currents $10\text{-}50 \mu\text{A}$. The collector part or the anode has to be fixed at high positive voltage for negative ion detection and at ground for positive ion detection. The idea of the positive potential gradient along the channeltron is to accelerate the secondary electrons along the channeltron until they are finally collected on the collector part. To summarize, the ion optics part is connected to -470 V and the channeltron cone is connected to -2900 V . The anode part is connected to ground through a supplemental $10 \text{ M}\Omega$ resistor and finally the collector is connected to the rest of our detection circuit. Since the signal created by the channeltron is small, it is usually fed in a preamplifier before it is used in our data collection part. The preamplifier is a (SRS fast preamplifier / model: SR445A). This preamplifier has four wide bandwidth, DC coupled amplifiers designed to be used independently or cascaded to provide gains of 5, 25, 125 and 625. In our experiment we use three channels in cascade. The output of the preamplifier is changed depending on the experiment we want to perform.

One way we did our spectroscopy is to change one parameter and measure the effect of changing this parameter on the ion counts. This parameter can be the frequency (other parameters can be the delay time to try different timing schemes). The counts recorded as data points in this scheme are the integrations of ion signals produced in the whole timing cycle duration of the PA. In other words, it is the summation of the ion counts collected while the PA is on for the number of iterations specified by the experiment. In this case we used a photon counter. Some other times, we wanted to see if there is any effect of the PA beam on the MOT. This was used when the PA effect was very weak. In this case all the conditions of the experiment were kept fixed. The ion signal of the MOT was pinned in small time windows. This

was done to test if there was any effect of the PA on the MOT that is washed away in the time integration process. In these types of experiments a multichannel scaler was used for data collection.

3.4.1 THE TIMING SCHEME

Most of the experiments that we performed followed the same main outline of the timing scheme. The timing objective is to turn on the PA beam when the MOT trap beams are off to ensure that the studied molecular features are solely due to the PA photons. Also turning the trap beams off increases the atom's population in the $S + S$ states from which our PA molecular transition starts. After the PA lights are turned off, the trap lights are turned on. The MOT reloading takes place to prepare the MOT for the following PA cycle. These cycles of turning the PA lights on and off are repeated for as many times as we need to build up enough statistics. During the statistics build up time, the experimental conditions are kept fixed as much as possible, including the PA laser frequency. When the desired statistics level is reached, a single data point is produced. The time it takes to create a single data point is then the product of the ON/OFF cycle duration times and the number of cycles used to build up the statistics. The period of the PA on and the PA off parts varies depending on the specific experiment and it will be noted for each of the experiments as we describe them. The number of PA on/off cycles used to create a data point changes also according to the strength of the feature studied. It also depends whether we are close to a quench transition and we have higher probability of killing the sample before any PA signal is produced.

The pulses used to switch the AOMs (Trap / Zeeman /PA) and trigger the data collection (photon counter/multichannel scaler) are shown in Fig. 45. They are produced using a Quantum Composers 9520 series 8-channels pulse generator.

3.4.2 DATA COLLECTION

Collecting the data from the preamplifier output was done by one of two devices: 1) photon counter, or 2) multichannel scaler.

1. Photon Counter

The photon counter's job is to add up the number of counts that the channeltron

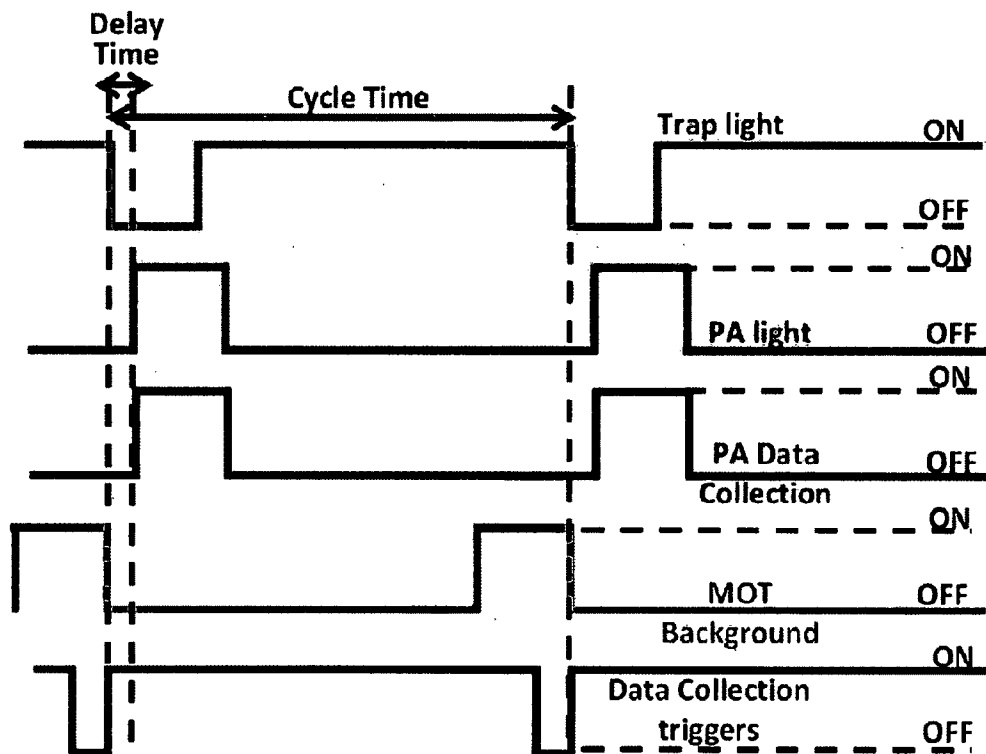


FIG. 45: A schematic diagram of the timing scheme of our experiment. It is important to note that no specific duration values were assigned because we changed them between different experiments. We will give details of the specific values for each separate experiment later. It is also important to note that the repetition of these cycles is what creates the data point that we see on our graphs by adding the data collected from all cycles.

sends during a duration of time that we can specify in the ON/OFF cycle. It can also add up the counts from cycles up to some number of cycles to create one data point. The data point can be fed to the computer using a Labview program. When the trap beam is OFF and the PA beam is ON, we ask the photon counter gate A to sum the number of counts coming from the channeltron. The delay of the photon counter's gate can be specified to match the delay of the PA beam as well as the PA beam duration. After that we ask the photon counter to trigger for some number of cycles (T trigger/T SET). This adds up the statistics from the cycles to create the data point. The number of cycles is usually some number between 2000 cycles to 20000 cycles depending on the desired statistics. After the photon counter is done, it saves the data number until the computer asks for it using the Labview program. It is important to note that there is some dead time between each data point addition process and the following addition process. This is called the DWELL time (the minimum DWELL time setting is 2 ms). It is also important to note that the time it requires the photon counter to finish one data point is calculated. We then input it into the Labview program as the milliseconds to wait time which changes from experiment to experiment. If this number was not calculated right, the counter will keep sending the same data point until it is ready to output the new point. The photon counter is a SRS gated photon counter, Model SR400.

Since the photon counter has two channels, it gives us the ability to look at the MOT counts before each PA shot as well as looking at the PA counts. This is very important since it enables us to ensure that every PA shot starts from the same initial conditions of the MOT. In case of any change in the PA signal, we can eliminate the MOT or discharge effects by looking at the MOT signal before the arrival of the PA. Gate B follows the same technique as Gate A. They both share the same settings except for the delay of their measurements.

2. Multichannel Scaler

The multichannel scaler (MCS) was very useful in the quench experiments because the signals were very small and weak. We wanted to investigate whether there is any effect of the PA that is canceled by the fact that the metastable

atoms are being quenched. The multichannel scaler was a SRS Multichannel Scaler Model SR 430. The scaler enabled the use of different bin width. As the counts from the channeltron arrived to the MCS they were grouped into different bins depending on the time of their arrival. The bin width could be selected from 5 ns, 40 ns, 80 ns, 160 ns, 320 ns, 640 ns, 1.28 μ s, 2.56 μ s, ... 10.486 ms. The bin width was changed in our experiments and we will give the single bin width for every data graph in the next chapter. Every bin could add up to 32,767 records. Every record is created in one ON/OFF cycle. The result is a histogram of the added MOT counts along the ON/OFF cycles.

CHAPTER 4

RESULTS AND DISCUSSION

In this chapter we will explain every experiment we performed in our study for the PAS of both argon and krypton. In the process of looking for any molecular resonances in our PA spectrum, we performed four experiments. The first two experiments were performed using argon gas only. The latter two were done for both argon and krypton. Looking for molecular features on our PA scans took many steps. When studying PA for noble gases, especially argon, reference [1, 11] reported seeing some features on the spectrum. They were speculatively assigned to two photons molecular effects. In fact, in the thesis work, it was assumed that the two photons share the same frequency. Their PA features shown in Fig. 3 [1, 11] could be grouped into four features around four frequency detunings. Two features appear in the high intensity spectra at -1.7 GHz and -3.4 GHz. Another two features in the low intensity spectra at -170 MHz and \sim -80 MHz. For the last feature, we were not able to reproduce it. It was of minor interest since it only appeared on one of the PA spectrum shown in Fig. 3.

It is important to note that the data taken in Ref. [1, 11] used the same apparatus we had in our experiment. The apparatus was later used by another student Gambhir Ranjit where most of the parts were taken down. As a result, many of the operating conditions (detection, laser sources, the whole lab and optical tables set up, the vacuum system,) were changed. Our original goal was a close up study of these “potential” molecular features and hopefully later trapping those molecules. As we started our experiment, we realized that the features detected in those spectrum were no longer reproducible.

That was why the starting point for our study was to search for those features. We started with a two photon spectrum experiment. The two photons were allowed to have different frequencies (two colors PA experiment). By doing this, we were hoping to cover more molecular features by having different frequencies as an extra degree of freedom. During the course of this study, the data suggested that our ECDL lasers are not as monochromatic as we thought. In other words, their actual main lasing frequencies have sidebands on them. Although the sidebands were weak

enough that they were not visible on any of our optical diagnostic equipment, their effects were quite strong on our PA process. In terms of power ratios, the sidebands are 10^{-6} weaker than the main ECDL frequency at most.

The second experiment performed was aimed at studying every molecular feature reported in Ref. [1, 11] to investigate their origin. The study was aimed at studying the nature of these features along with measuring the frequency of the photons causing them to appear. In this case, we were able to measure the frequency with much greater resolution than before. During the two experiments, we gained a better understanding for our system. We also binned the artifacts that could alter our molecular spectrum because of otherwise undetectable laser sidebands.

For the the third and the fourth experiments, we built a new ECDL to exclude the artifacts on our spectrum. We then took PA spectra for both argon and krypton, searching for discrete molecular features. The PA spectra were done around two different atomic limits. The trapping transition frequency limit was covered in experiment 3: “corrected PA spectrum for both argon and krypton”. The quench transition frequency limit was covered in experiment 4: “quench transition study for both argon and krypton”.

4.1 EXPERIMENT 1: TWO COLORS PA EXPERIMENT IN ARGON

This experiment was done using two photons for the PA light. The first photon originated from the Titanium Sapphire laser which we were able to scan over a 1 GHz range. The second photon was coming from the “locked” MOT lasers as a pick off from the second slave (trap slave). The laser trap beam going to the MOT passes through an AOM where the positive first order is picked up and sent to the MOT through the fiber. At the MOT site, this beam acts as a trap beam i.e. the beam that is later divided into six counter propagating beams. The zeroth order is then redirected into another AOM and the “new” first order is coupled into a fiber launcher. It is then sent to the MOT as a PA beam and to differentiate this PA beam from the Titanium Sapphire PA beam, we call it “MOT PA” beam. Now it is very important to mention two notes. First, the MOT PA beam detuning is the sum of the second AOM detuning and the trap beam zeroth order detuning (-81 MHz). The later is the difference between the master laser zeroth order and first order that is sent to the saturation absorption and locked at zero frequency reference point.

Since the trap slave laser follows the master laser the two lasers zeroth order share the same frequency. The second term in the MOT PA detuning is the frequency shift created by the MOT PA AOM. We were able to change it between two ranges (60 MHz to 100 MHz) and (130 MHz to 210 MHz). The two ranges and both the positive and the negative AOM orders were used to allow for a wider range of MOT PA frequency range. The second important note is the switching scheme for our experiment. We made sure that the maximum amount of power was dumped into the MOT PA beam only when the Titanium Sapphire PA was on. In other words, the two PA beams followed the same on/off scheme. This was checked using our Thorlabs fast photo detectors (DET100A and DET36A Si Biased detector). It was mounted in front of the fiber delivering the PA beams to the MOT and the photo detectors were connected to an oscilloscope and monitored against the trigger signals to the photon counter. To explicitly explain the AOM timing scheme, we start from the trap AOM which turns OFF during our PA beam ON time. When the trap AOM is OFF all the trap beam power is dumped into the zeroth order which passes through the MOT PA AOM. During the trap AOM OFF time the MOT PA AOM is ON and that dumps most of the light power into the first order MOT PA light.

The frequency calibration for this experiment was done using a Labview program. The program read a data acquisition card connected to a data acquisition box where the saturation absorption signal and the 300 MHz spectrum analyzer were connected. A part of the PA beam was sent to the rf discharge tube to get a saturation absorption signal. The purpose of the saturation absorption signal is to record the zero point in the frequency range. Another part of the PA beam was coupled into the 300 MHz spectrum analyzer producing sine wave like signal with the peaks 300 MHz apart. The wave was then transferred to the Labview program and it helped to estimate a 300 MHz steps in the spectrum. A typical saturation absorption signal and a 300 MHz cavity signal are shown in Fig. 46. The two signals were later fed into a Mathematica code where the saturation absorption signal was fit with a Gaussian distribution function. Using this fit, the zero frequency detuning (resonance frequency) was estimated. This helped since our saturation absorption signal was observed on top of a Doppler broadened peak. The 300 MHz signal was fit with a sine wave function and the wave peaks position was again calculated. The

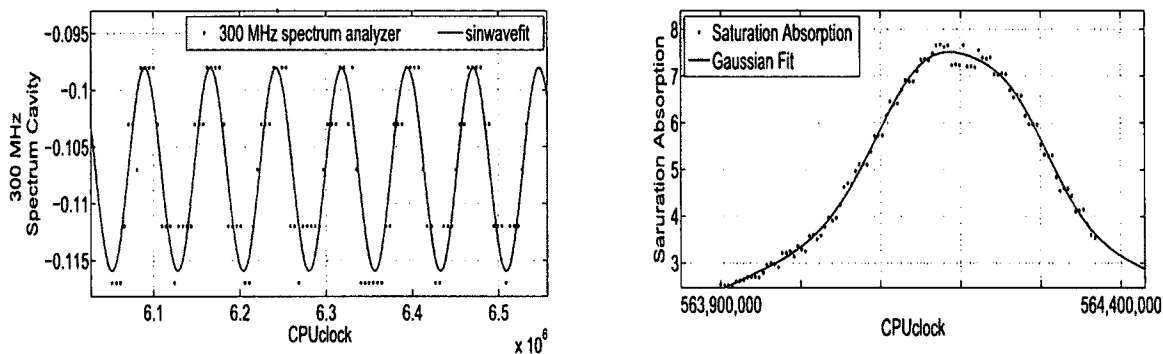


FIG. 46: The output from our frequency calibration instrumentation. The output on the left is from the 300 MHz spectrum analyzer as shown in black. On the same graph a sine wave fit from which the position of the maxima and minima are determined and a difference of 150 MHz frequency step is found. This fit has a root mean square error of 0.0027. On the right, the output from the photo-detector to the saturation absorption with a Gaussian fit is shown. From this fit, the zero point in frequency is determined. This fit has a root mean square error of 0.1425.

output of the code was a processed file of the ion counts as a function of the calibrated frequency.

Three degrees of freedom are available for this experiment. The typical data that we got from this experiment are shown in Fig. 47. This experiment had more than one degree of freedom and we were mainly concerned with three of them. 1) We changed the power of the Ti:Sapphire PA at constant MOT PA power and detuning. 2) We changed the power of the MOT PA at constant Ti:Sapphire power and MOT PA detuning. 3) We changed the MOT PA detuning at different Ti:Sapphire and MOT PA powers. Changing the powers had the effect of changing the strength of the observed features. If the MOT PA beam was the only PA beam present, the number of the ions created will be constant. This is because they are created in the same way they are created from a constant power PA beam and at the same frequency. That is why the ion counts of only the MOT PA constitute a DC offset in the ion signal. The Ti:Sapphire effect as it scans through the frequency from the red side to resonance to blue is a gradual increase in the ion counts. At the resonance frequency, a sharp decrease to zero takes place. As we move to the blue side frequency, the ion counts start to increase gradually until it settles down at a constant value. This value

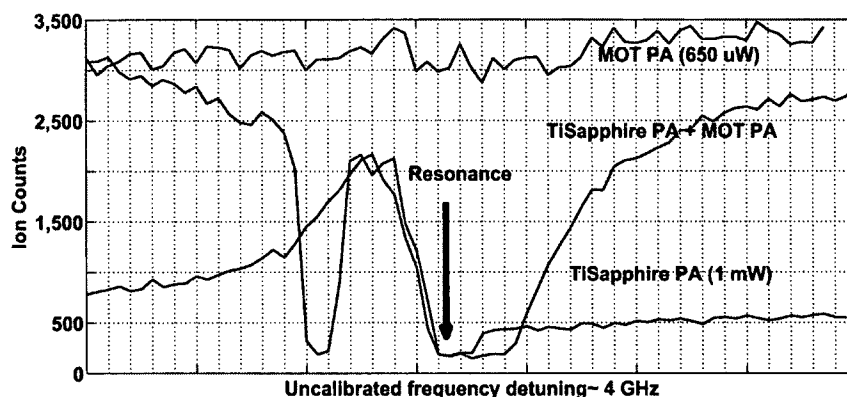


FIG. 47: A basic two color photoassociation ion counts signal. The blue signal is for only a MOT PA sent to the MOT and parked at -160 MHz and at $650 \mu\text{W}$. Since the laser is not scanning it is a straight line. The green line is for the Ti:Sapphire PA laser scanning for ~ 4 GHz at 1 mW. The red line is the combined ion signal when the two PA beams are sent to the MOT at the same time. The deviation of the ion counts is ± 100 . The x-axis represents the frequency detuning from resonance.

represents the ion counts from the MOT atoms interaction (Penning ionization (PI) and Associative Ionization (AI)). The combined effect of both the two PA beams is a slight increase of the ion counts offset (created by the MOT PA). It also creates some extra features that appear at some specific frequencies depending on the MOT PA detuning. Finally, a decrease to zero as the Ti:Sapphire scans through resonance is observed and a slight increase on the blue side until the ion counts level reaches the offset again.

Changing the power of the Ti:Sapphire PA or the power of the MOT PA Figs. 48 and 49 increases the strength of the extra features observed on the molecular scan. Changing the MOT PA detuning changes the shape of the scans as shown in Fig. 50. To better understand the shapes of the different scans we need to differentiate between two cases: Case 1) happens when the MOT PA is locked to the red side. In this case, the MOT PA produces an extra ion counts and as a result create a positive high offset in ion counts. Case 2) happens when the MOT PA is locked on the blue side. In this case, the MOT PA creates optical shielding and the ion counts offset is very small compared to case 1.

The timing scheme for this experiment was varied. Trap OFF duration is $400 \mu\text{s}$ and delay is $0 \mu\text{s}$. The PA beam (both the TiS and the MOT PA) ON duration

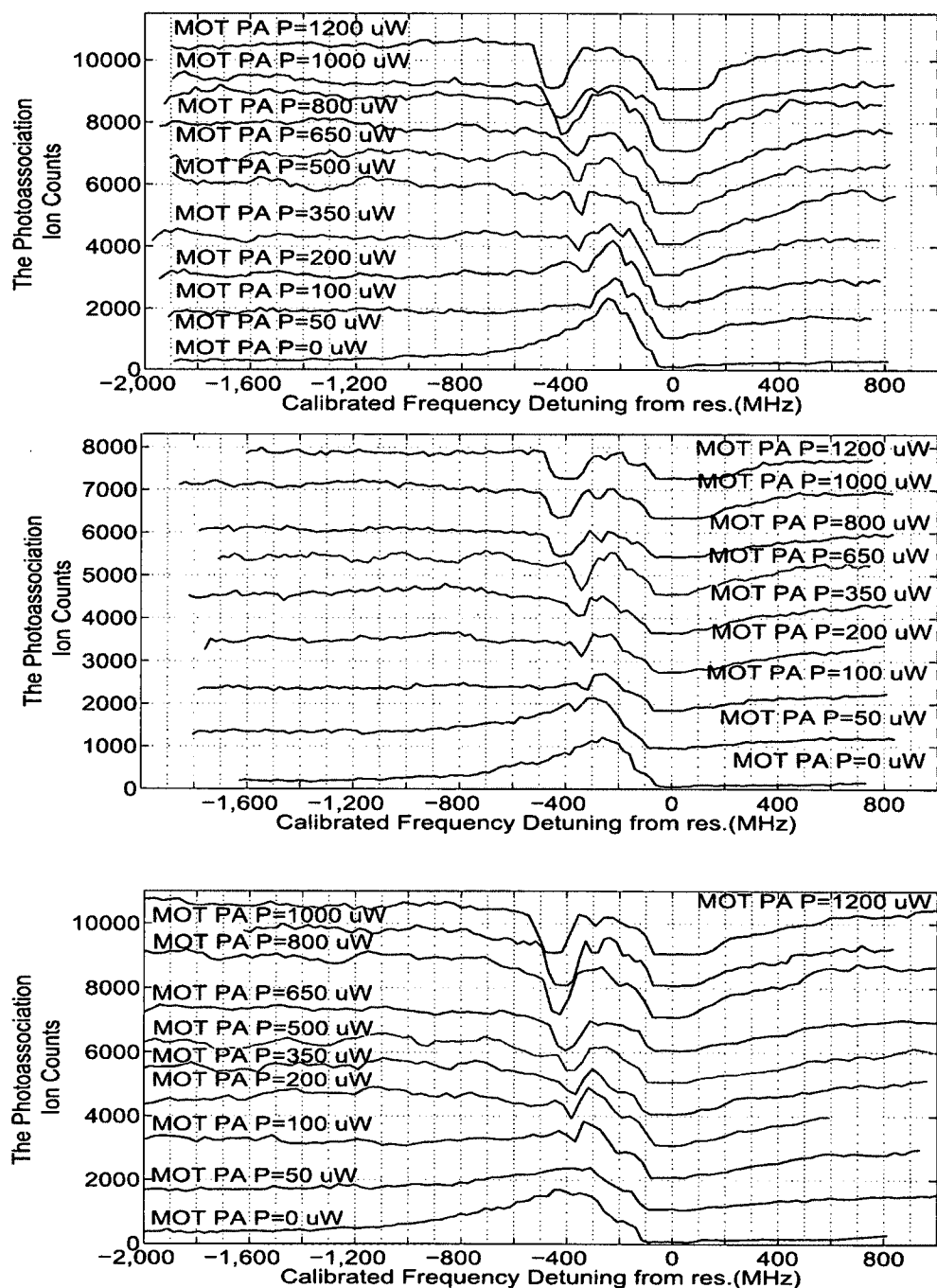


FIG. 48: The graphs show the effect of changing the MOT PA power by using different Ti:Sapphire PA powers. The MOT PA detuning is -160 MHz. From the top, the Ti:Sapphire powers are 0.5, 1, 1.5 mW respectively.

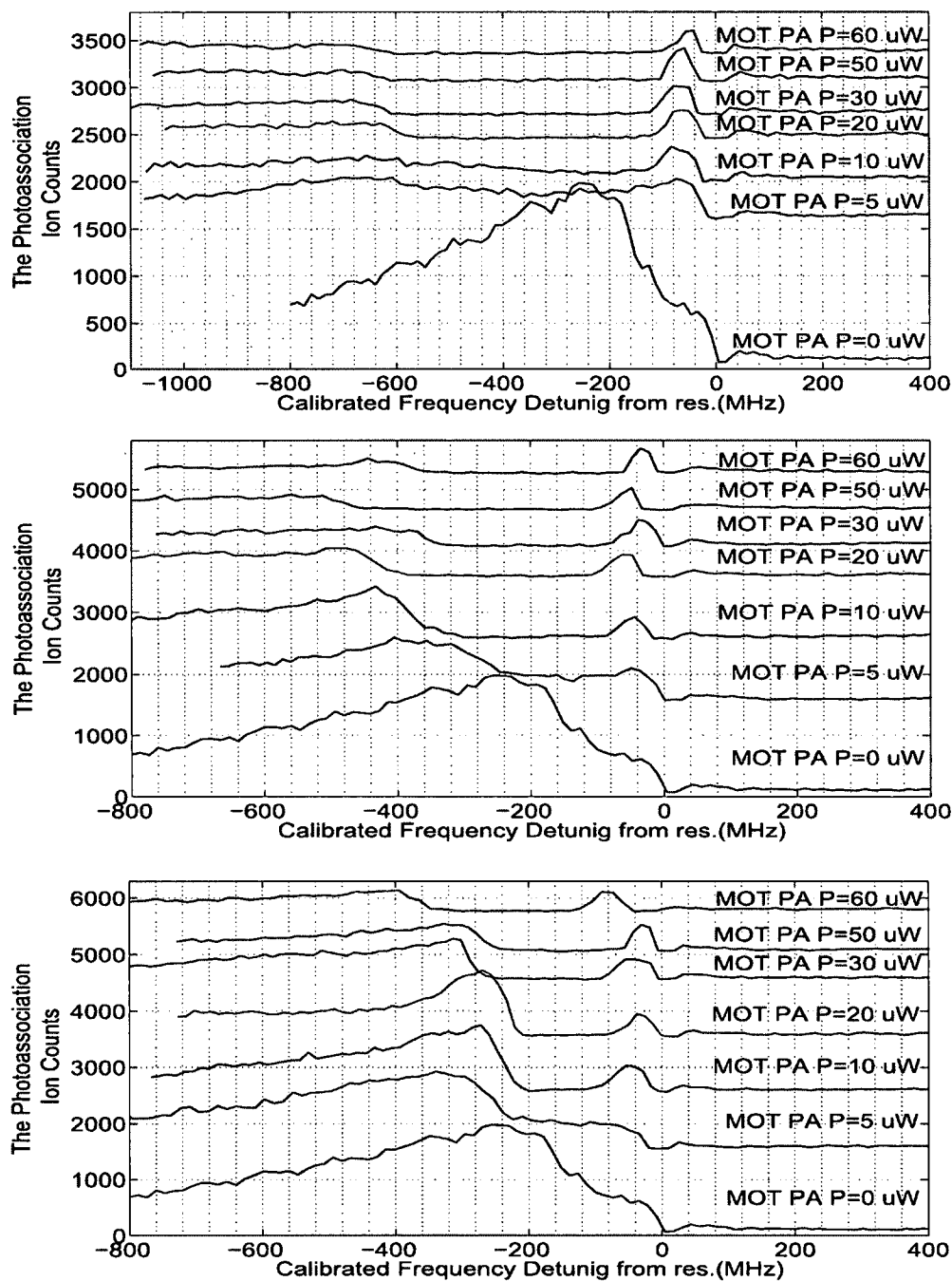


FIG. 49: The graphs show the effect changing the MOT PA power at different detuning. The Ti:Sapphire power is 1 mW. From the top, the MOT PA detuning goes as +50, +75, +100 MHz.

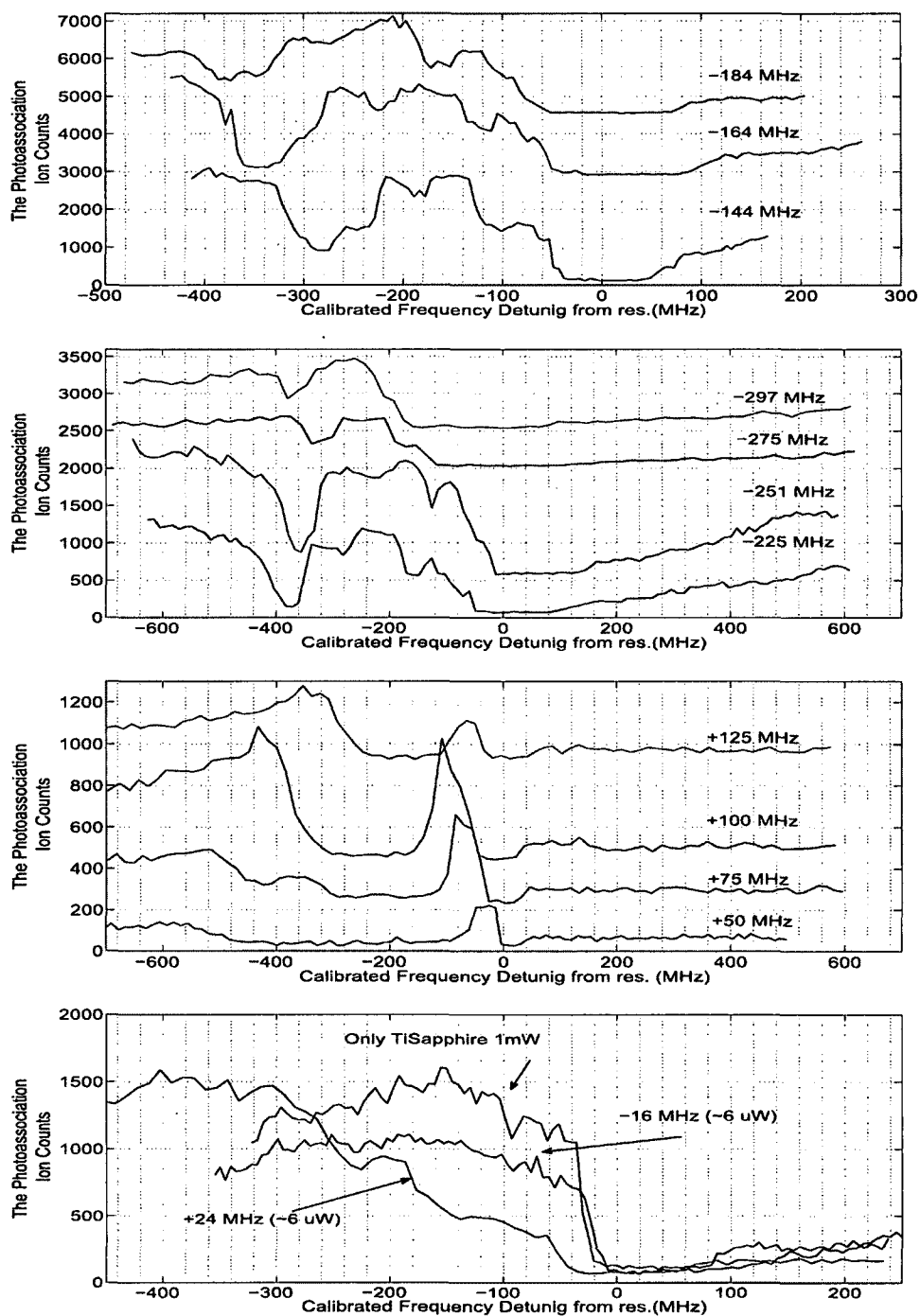


FIG. 50: The graphs show the effect of the detuning on the spectrum. The Ti:Sapphire power is 1 mW. From the top, the MOT PA power goes as 650, 800, 20, 6 μ W respectively. Only when MOT PA detuning was +125 MHz, the MOT PA power was 100 μ W.

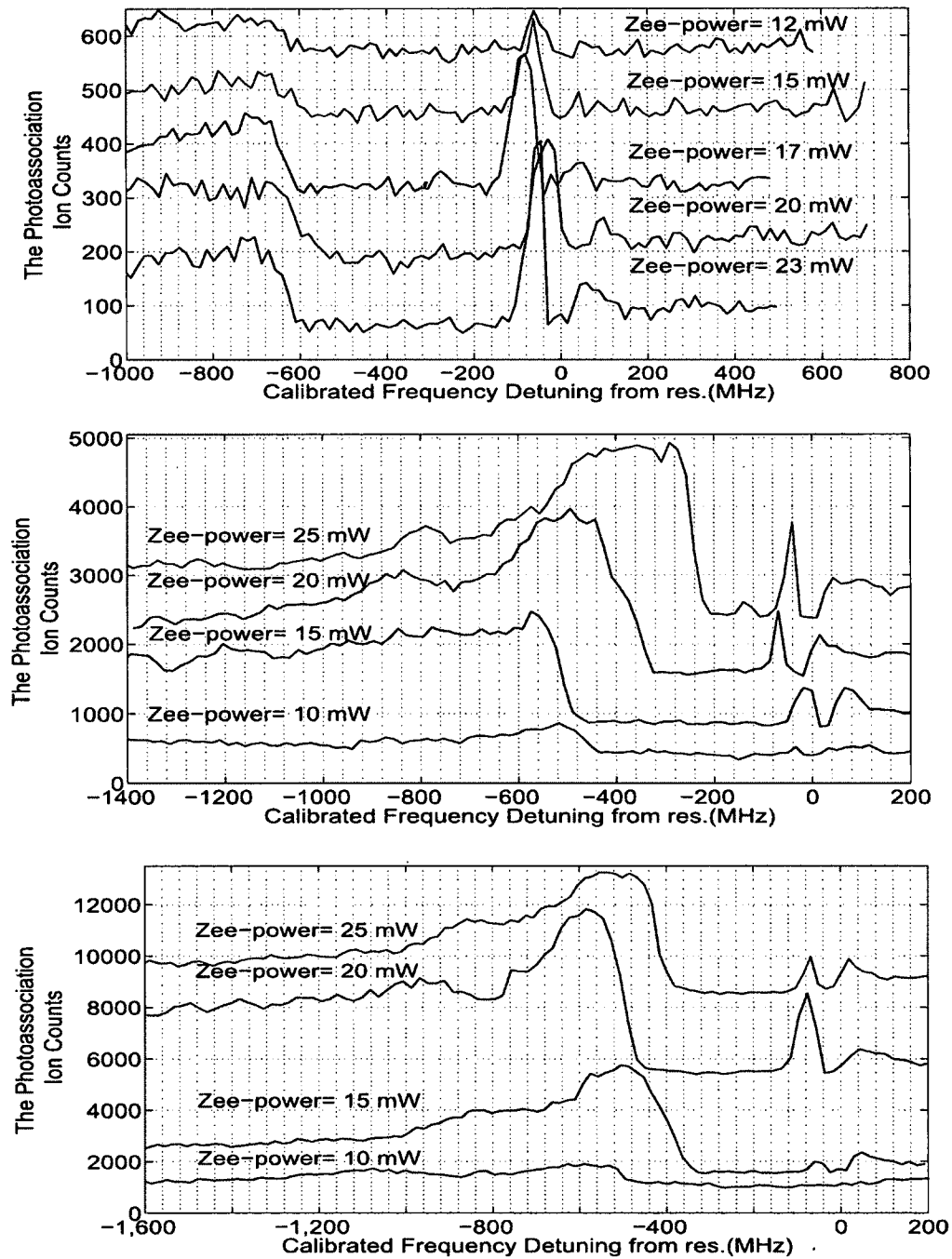


FIG. 51: The graphs show the features dependence on the MOT density. The MOT density was changed by changing the Zeeman slower beam power. The Ti:Sapphire power is 1 mW. From the top, the MOT PA detuning goes as +50, +75, +100 MHz respectively. From the top, the MOT PA power goes as 20, 20, 30 μ W respectively.

is 200 μs and the delay is 30 μs . The photon counter Channel A was triggered so that it is ON for 200 μs and delay 30 μs . The photon counter Channel B was on for 200 μs and the delay was 900 μs . Channel B served as a background measurement for the MOT to see how much it was affected by the PA ON period. The 30 μs delay for the PA and Channel A was tested and changed to 0 μs during our preliminary data. It was not recorded to have any effect on the features that appeared on our scans. The reason for choosing this time scheme was to follow the time scheme used in Ref. [1, 11]. This whole timing was repeated every 2000 μs . The trap beams were turned ON for 2000 - 400 = 1600 μs . The PA and the photon counter channel A were turned OFF for 2000-200-30 = 1770 μs before the beginning of the new triggering cycle. Finally, the photon counter channel B was not counting for 1800-900-200=500 μs before the new trigger signal arrives. It waits for 900 μs before it can count again. The photon counter readings were added for 2000 records to create one data point (T set 2E03).

During our experiment, the timing scheme was changed to test the effect of the timing scheme on the observed features. The PA and photon counter channel A ON duration was tested versus the number of counts. It was observed that as the duration increases the number of PA ion counts increases until it reaches 300 μs where it starts to remain the same with any duration increase. The Trap OFF duration was tested. It was found that as the trap OFF duration increases the PA ion counts is almost the same for the duration between 200 μs to 400 μs . The delays of the PA and channel A were also tested. There was no effect on having the delays between 0 μs to 40 μs on the PA ion counts. However, this effect started increasing and becoming more pronounced when the delay reached 70 μs . Testing the PA ON window was done while keeping the PA duty cycle the same. The duty cycle is the ratio between the time the PA is ON to the cycle duration. Examples of duty cycles are 200 μs PA ON to 2000 μs cycle duration, 150 μs PA ON to 1500 μs cycle, 20 μs PA ON to 200 μs cycle and 50 μs PA ON to 500 μs cycle duration. For all the tests we made it was found that the best timing scheme was trap OFF/PA ON / Channel A ON for 200 μs with 0 μs delay. Channel B was recorded with a 900 μs delay. The whole cycle duration was 2000 μs .

It is important to note that changing the timing scheme only affects the signal to noise ratio in the molecular scans. In all of these timing schemes the features were visible. The idea of changing the timing scheme was trying to minimize the duration

for the whole scan without affecting the resolution of the features.

The PA beam spatial characteristics were varied. The beam spatial characteristics was studied for this experiment in detail. Since we have two beams, we needed to make sure that both the two PA beams were delivered to the MOT with the same alignment condition. This will ensure the same scattering force direction for both the two beams. The PA beams were then retro reflected back on their original path to balance the scattering force and get twice as much power effect at the MOT site.

A schematic of the optics layout for the PA lasers is shown in Fig. 52. The Ti:Sapphire laser was coupled through the fiber to translate it to the science chamber. The PA beam output from the fiber had a beam diameter of $5 \mu\text{s}$ and then it was let through a C240TME lens ($f=8 \text{ mm}$ NA-0.5 Mounted Geltech Aspheric lens). The PA beam was then directed through mirrors, ($\frac{\lambda}{2}$ and $\frac{\lambda}{4}$) waveplates and a PBS. This was done to correct for the beam polarization and steer the beam to the MOT site. This happens along a $\sim 30 \text{ cm}$ distance which takes the beam diameter to 0.413 mm . Then the beams were allowed to go through a 400 mm lens placed 400 mm away from the center of the chamber where the MOT is. The optics alignment was picked so that it makes the PA beam diameter at the MOT site 0.266 nm . Then, it was sent to the retro reflection optics where it passed through a 300 mm lens placed 300 mm away from the center of the chamber. It goes through a $\frac{\lambda}{4}$ waveplate which rotates the PA beam polarization from linear to circular. The beam is then reflected on a mirror that is placed to directly reflect it back on its original path. It goes back through the $\frac{\lambda}{4}$ waveplate to rotate the beam back into linear polarization.

The way the two PA beams were combined also differed. Originally, the two beams were combined at the MOT site as shown in Fig. 52. The beams were launched from the two fibers through two different fiber launcher whose collimation lenses were picked to match the two PA beam sizes at the MOT position. The two beams were separately steered into a PBS where they were combined and sent through the 400 mm lens to focus them on the MOT. Before the two beams were sent into the PBS, they separately passed through ($\frac{\lambda}{2}$ and $\frac{\lambda}{4}$) waveplates. The waveplates' job was to control how much power was dumped from the two beams separately. It also ensured that the portion of the beam that was sent to the science chamber as PA was almost clean in terms of polarization direction. In fact, the Ti:Sapphire laser

was linearly polarized in the P-polarization and the MOT PA was linearly polarized in the S-polarization. This means that the two beams were linearly polarized and their linear polarization direction was perpendicular to each other at the MOT site. The “combined” PA beam (Ti:Sapphire and MOT PA) traveled through the optics to be focused on the MOT. It was expanded at the other side of the chamber where it retro reflected back onto the MOT. During aligning the PA beams, a careful testing of the two PA beams was done to ensure having the two beams on top of each other and aligned with the MOT.

Combing the two PA beams at the MOT had two disadvantages. First, the two beams had linear polarization directions that were perpendicular to each other. Second, there was always an uncertainty of not having the two beams perfectly on top of each other. That is why, during our experiment, we combined the two beams before launching them into the fiber. This alignment way ensured that the two beams are already collinear at the MOT since they depart from the same fiber to couple into the same optics until they reach the MOT. Accordingly, all artifacts that could rise from small angle between the two beams is excluded. Another advantage of combing the two beams before the fiber is to ensure they have the same polarization when they arrive at the MOT to exclude the features’ polarization dependence. In this alignment way, the two beams were combined at a PBS before the fiber. That is why they had perpendicular linear polarization directions as they enter the fiber. The PA beams then traveled through a non polarization preserving fibers. The output of the two beams then traveled through the lenses and the ($\frac{\lambda}{2}$ and $\frac{\lambda}{4}$) waveplates until they reached the PBS cube. Their linear polarization was cleaned so that the only polarization that reached the MOT is a P-linear polarization direction. This could be achieved since the PBS used to combine the beams does not have 100% efficiency. As a result, the two PA beams sent into the fiber do not have exactly orthogonal polarizations. Instead, each beam has both components of polarization. This inefficiency effect of the PBS combined with the non polarization preserving fiber effect are enough to make the two beams share the same polarization at the MOT site.

Another aspect for the beam polarization testing was studied in Fig. 53. Instead of sending the two beams as linearly polarized beams, the beams were sent as circularly polarized light. Also the retroreflection beam polarization dependence

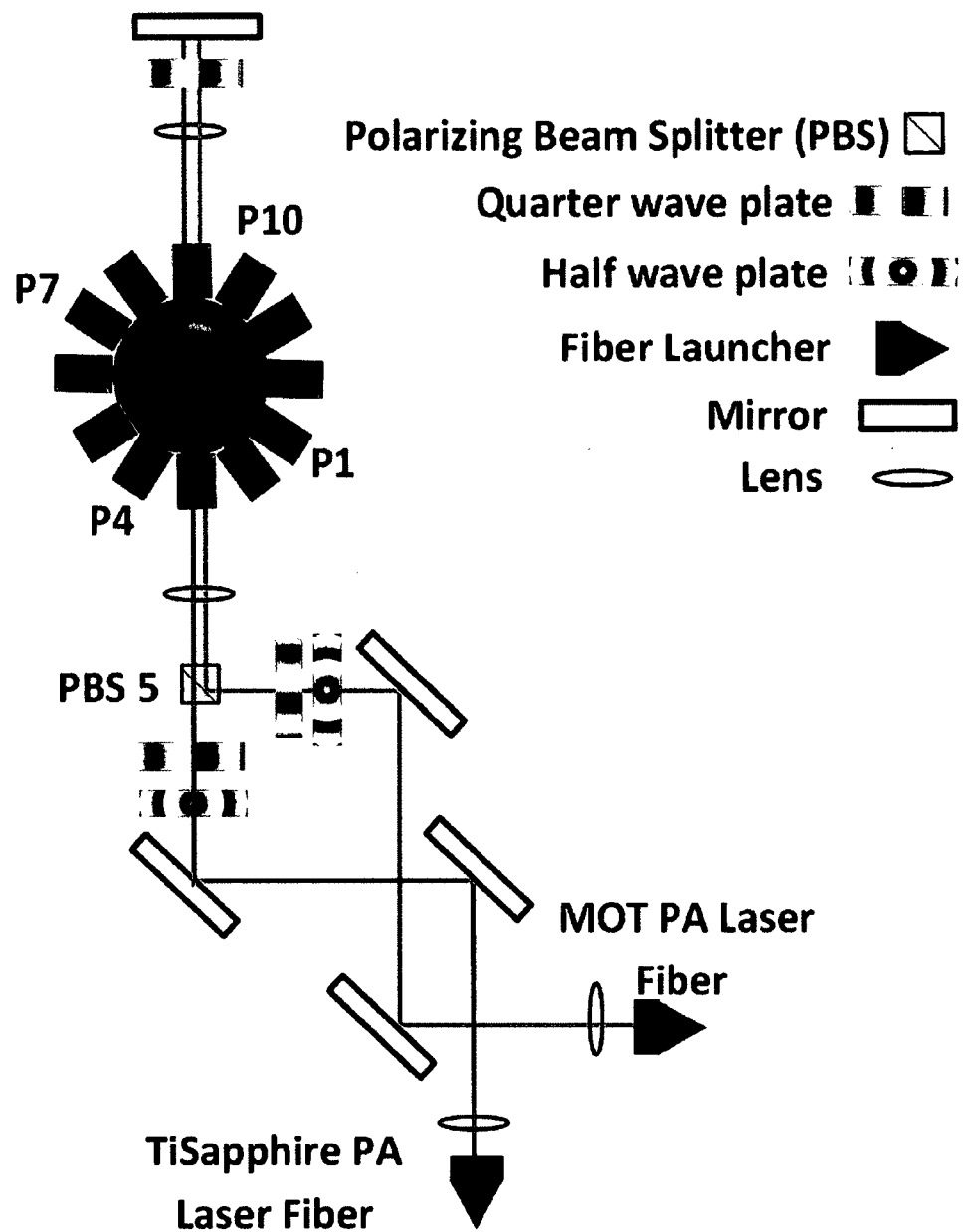


FIG. 52: A schematic for the two PA beams before being combined at the MOT site. It is important to note that we used the red path for the Ti:Sapphire PA and the green path for the MOT PA. To exclude the alignment dependence, the two beams were combined before the fiber and sent through the red path where they were perfectly overlapped.

was tested. Usually the retroreflected beam would pass twice through a $\lambda/4$ waveplate which results in a $\pi/2$ polarization difference between the incident beam and the retroreflected beam. To test the dependence on the retro reflection polarization, the scans were taken both with and without the $\lambda/4$ waveplate. The features were always observed with those two techniques which suggests almost no polarization dependence.

The two color PA experiment error estimate.

While plotting the molecular scans, there was some window of uncertainty. The first uncertainty was coming from the frequency calibration uncertainty as shown in Fig. 46. This uncertainty can be in the range of ~ 100 MHz. The second uncertainty can be generated from the ion counts. This can be attributed to two types of fluctuations. The first type is due to the statistical deviation of the ion counts from the channeltron. This ranges in ± 100 counts. The second type is due to system conditions drifts. The drifts can be in the rf discharge power which can affect the number of the metastable atoms created. The drift can also be due to slight laser beam power drift. This type of fluctuation takes place over a long period of time. It is usually visible as a gradual change in the ion counts level. To give a feel for this change, the fluctuation can be over the range of 300 counts along the whole scan. In other words, the scan DC level can start at zero and over the period of the scan it can go up to 300 counts DC level.

The two color PA experiment Conclusion

When we started this experiment, we were hoping to cover as many two color photon combinations as possible. This was done in a hope to duplicate the special features observed on Shaffer's scans shown in Fig. 3. Not only did we not observe the same features but also we got different features. The main conclusion that we gained from this experiment can be made clear if we study two different scanning techniques delivering the same combination of photons. One of the scans is where the MOT PA is parked on the red side (for example at -160 MHz) and the other is where the MOT PA was parked on the blue side (for example at +100 MHz). These scans are shown in Fig. 50. The first scan does not show any features when the MOT PA was at -160 MHz and the Ti:Sapphire PA at +100 MHz. However, in the second scan, when the MOT PA is parked at a +100 MHz, a strong features appears when

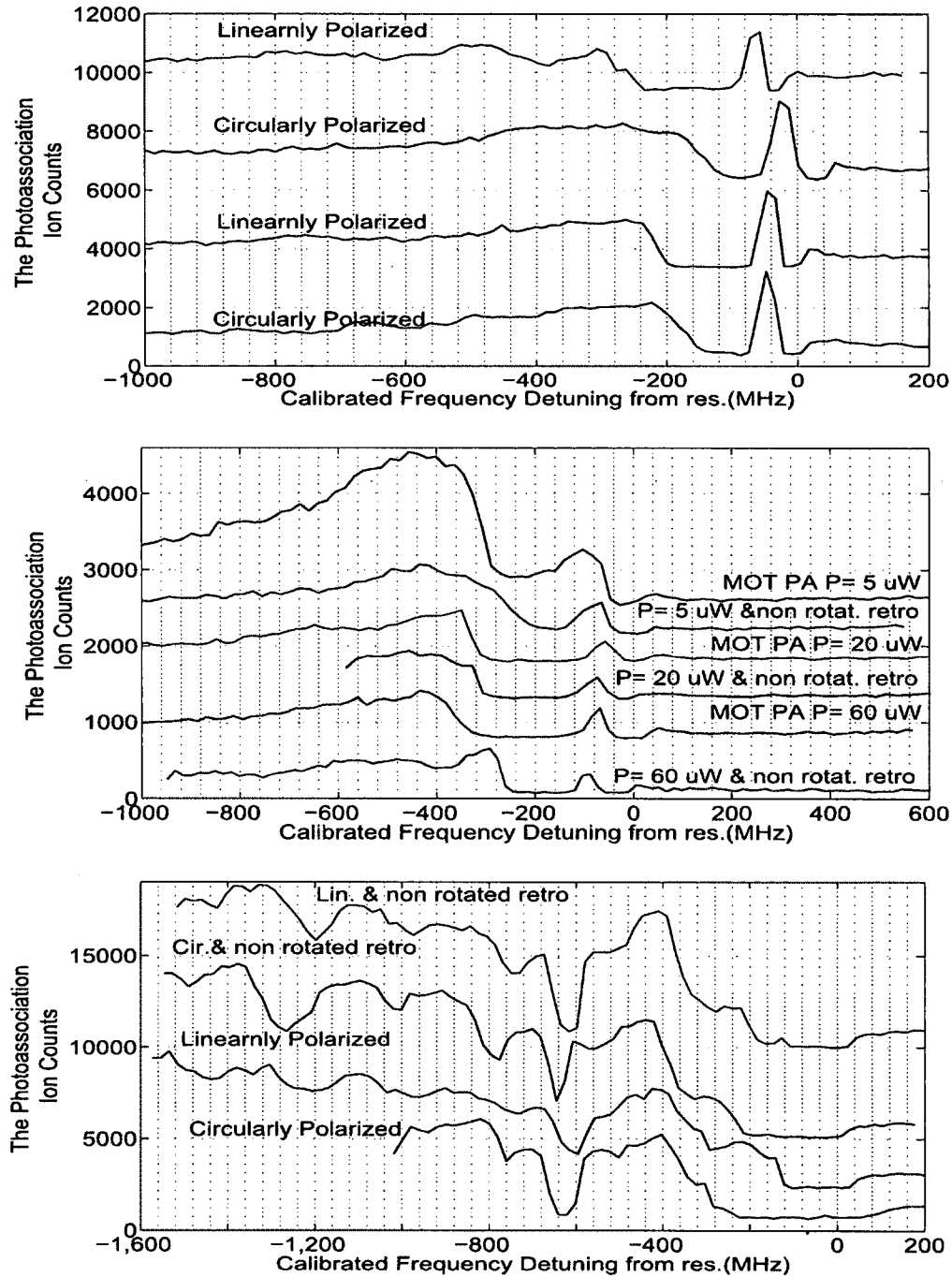


FIG. 53: The graphs show features dependence on the PA beams polarization. From the top, the Ti:Sapphire power (mW)/ MOT PA detuning (MHz)/ MOT PA power (μ W) combinations are (1.2/+50/27), (1/+100/varying), (1.3/-212/660) respectively. For the second graph, both the orientations for the retroreflection polarization are shown.

the Ti:Sapphire scans through -160 MHz. The atoms should not care what is the photon laser source. They should only care what is the photon frequency. From this observation, we concluded that one of the two lasers sources is not monochromatic and there are sidebands that exist on our ECDL and hence on our MOT PA light. This means that the features observed are not a result of only the “main” frequencies. They are resulted from the combined effect of the MOT PA sideband photons and the Ti:Sapphire photon. With this conclusion, we had to go back and try to duplicate the ECDL source used to get the data in Fig. 3.

4.2 EXPERIMENT 2: INVESTIGATING THE FEATURES ON THE ARGON PA SPECTRUM

This experiment mainly focused on studying the features observed on the PAS for argon shown in Fig. 3. The main challenge was trying to reproduce the features on these scans. Both Ti:Sapphire laser source and diode lasers in ECDL were used. Two ECDLs were used in two different configurations (i.e. Littrow and Littman-Metcalf configurations). Before we start explaining the nature of each of the features shown in Fig. 3 independently, it is good to try and group them into categories. That will help in tracking every single dip and explaining its source. Looking closely at Fig. 3, we can group the dips into four groups. The first group of dips can be confined about ~ -3.5 GHz. Note: we can now claim that those features were dips since we will prove that the reason for their occurrence is due to the introduction of an escape channel for the atoms from the MOT. This channel is much stronger than all of the effects produced from the photoassociation beams for reasons that will become clear as we explain our findings. The second group of “dips” can be located at ~ -1.5 GHz. Both of these dips can be observed on the high power long scan curve that cover ~ 12 GHz of scan range (from -10 GHz to $+2$ GHz). As for the low power “relatively short” scan curve (~ 1.5 GHz range, from -1.25 GHz to $+0.25$ GHz), we can locate another two features. One that happens at ~ -200 MHz and one that happens at ~ -100 MHz. The later feature was only produced on one curve of the scans. That is why we neglected it in our study especially because for all our high resolution scanning technique, we were never able to reproduce it consistently enough to study it again.

One of the challenges that we faced in this experiment is to optimize the MOT density since all of these features are highly dependent on MOT density. Let us recall Eqn. 34, where the scattering force is inversely proportional to the laser light detuning. That is why the size of the dips were studied at different MOT trap light δ . It was found that the size optimizes at about -16 MHz (as shown in Fig. 54) where it was fixed for the rest of the experimental procedures. Also the timing scheme for this experiment was fixed as the trap turns off for $200 \mu\text{s}$ where the PA beam is turned on. Meanwhile the photon counter ion collection channel A was turned on. This cycle repeats every $2000 \mu\text{s}$ and the ion counts from 2000 cycles add up to form one data point. For the low power scans, it was found that as the PA laser got

closer to resonance, the scattering force became so strong that it basically killed all of the atom sample trapped in the MOT. That is why the atoms needed more time to reload. The only adjustment made to our timing scheme during the low power scans was that the Trap off/ PA on cycle was repeated every 8000 μs instead for 200 μs for high power. As a reminder, we will rewrite the scattering force equation since it is crucial part in our understanding of this section. The scattering force is given by

$$F_{scatt} = \hbar k \frac{\Gamma}{2} \frac{I/I_{sat}}{1 + I/I_{sat} + 4\delta^2/\Gamma^2}, \quad I/I_{sat} = 2\Omega^2/\Gamma^2. \quad (97)$$

To boost up the effect of the PA at the MOT site, we changed the PA beam waist at the MOT position from 0.13 mm to 90 μm . That change in the beam waist created about one order of magnitude increase in the beam intensity. For the Gaussian beam, the intensity is calculated by

$$I = \frac{4P}{\pi\omega^2}, \quad (98)$$

where P is the beam power. The “4” factor instead of 2 for usual Gaussian beams is to count for the retro-reflection effect of the PA beam. It is the same idea as if we have the same effect of two beams on top of each other. ω is the beam waist which 90 μm for our experiment. $I_{sat} = 1.24\text{mW}/\text{cm}^2$ for our transition at 811 nm in argon.

First we started with the high power scans. To start the investigation of the two dips -3.5 GHz and -1.5 GHz, we had to reproduce the conditions under which these scans were taken. In reference [1], where the graphs were produced, the scans were produced using a diode laser in ECDL Littman-Metcalf cavity configuration. The long scan, ~ 12 GHz range, was produced using a power locking technique. This idea depends on monitoring the power out from the diode as it scans. When the diode laser is about to jump to the next frequency cavity mode, the power out from the diode spikes really high. This power spikes can provide an error signal that can latter be fed into our locking circuit to our current controller to provide an error signal for the diode laser. This error signal mainly tweaks the diode laser current so that it remains on mode. When we used this technique, we found that the diodes were failing with an unusually high occurrence rate. That is why we began to simply take smaller frequency range scans and patch them together.

An absolute frequency reference was obtained from the Wavemeter. Scans from

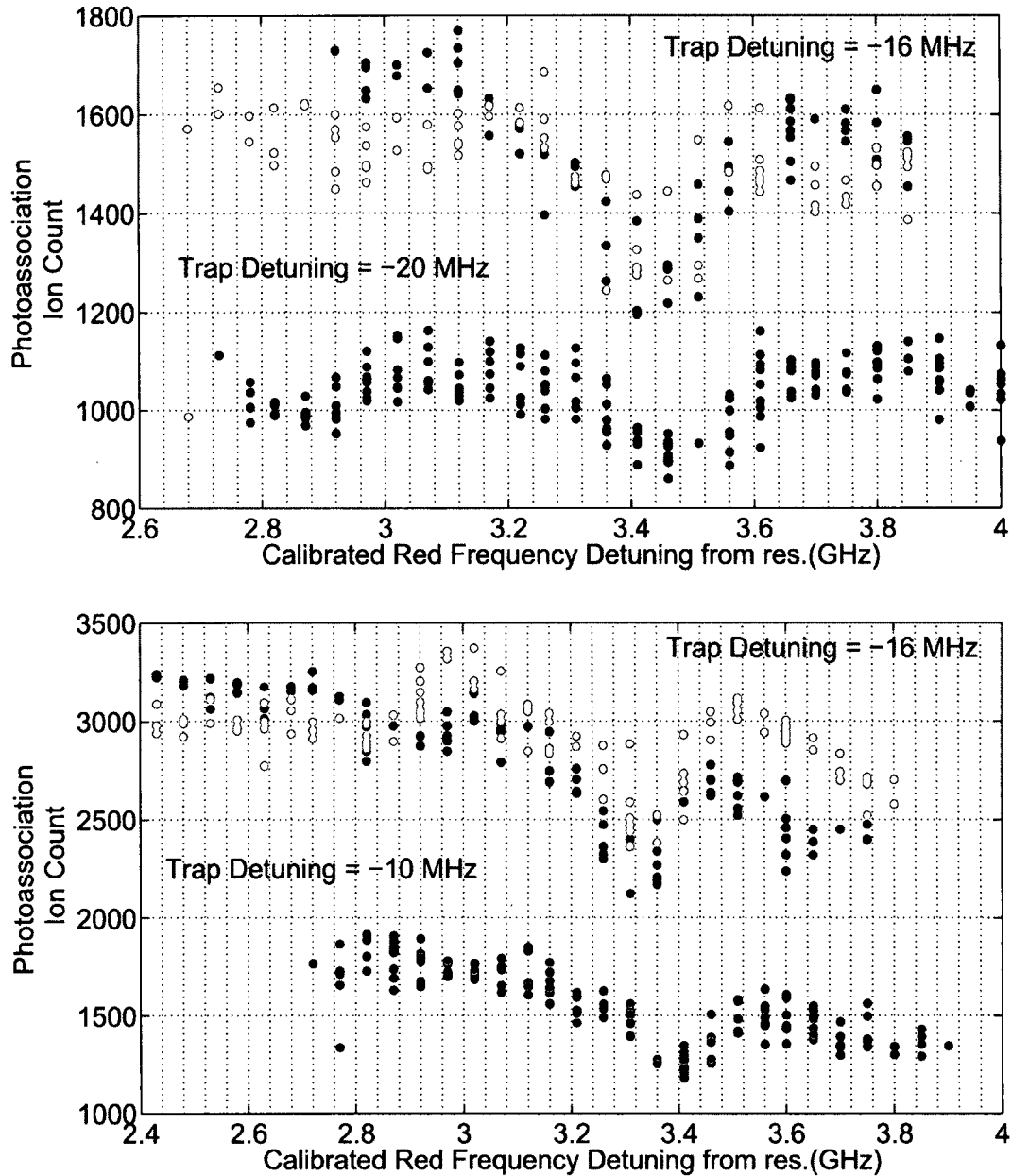


FIG. 54: The graphs show the dependence of the -3.4 GHz feature on the MOT density. The MOT density was changed by changing the MOT trap laser beams detuning. The graphs were taken at PA beam power of 80 mW. With a beam waist of $90 \mu\text{W}$. This is an intensity of $4.9 \times 10^5 I_{sat}$ and with retro reflection included $I=9.75 \times 10^5 I_{sat}$. The different colors for each detuning represent different scans that were taken to guarantee reproducibility and exclude artifacts from any discharge pressure fluctuation.

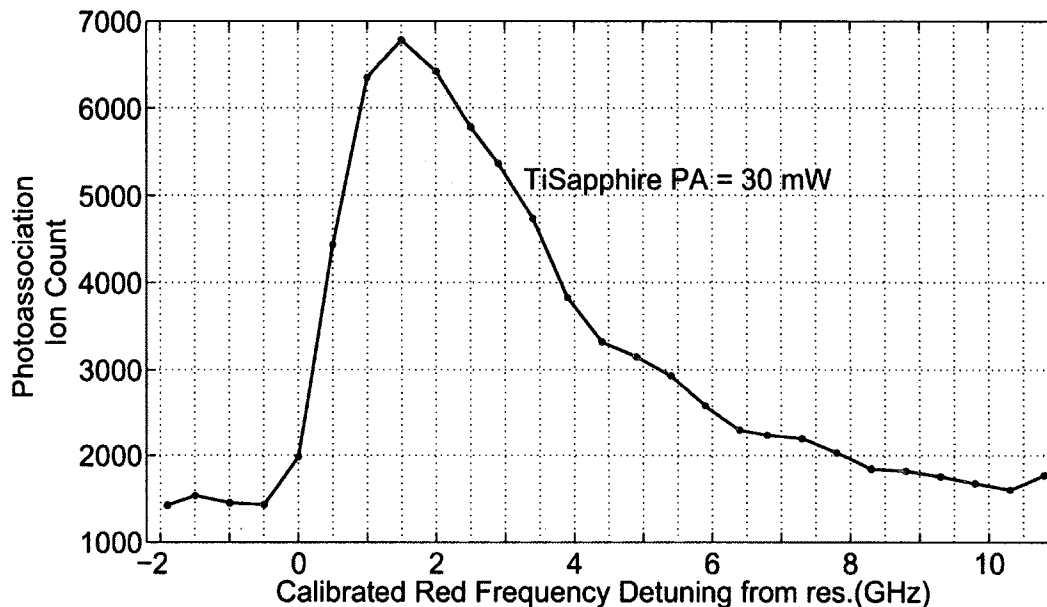


FIG. 55: The graph shows scan from the Ti:Sapphire laser source. The graph was taken at PA beam power of 30 mW. The x-axis is the red frequency detuning from resonance. Zero frequency detuning is at resonance.

the Ti:Sapphire laser were studied against our data from the Littman-Metcalf configuration ECDL cavity (LM-ECDL). It was found, as shown in Fig. 55, that at -3.5 GHz, a dip was always observed in the diode laser scans but was always missing in the Ti:Sapphire. This prompted us to perform a bandwidth measurement for the two lasers. Each laser beam was split into two parts, one part was directly sent to the photo-detector and the other part was launched into a very long fiber more than once. This produced a path difference between the original beam and the fiber output beam. The beat signal bandwidth was taken as a sign for the original laser bandwidth. The result of this test showed that the Ti:Sapphire had a smaller bandwidth than the diode laser as shown in Fig. 56. On the other hand, the sidebands were not visible on this test on the ECDL cavity.

Motivated by these findings and the fact that every ECDL had sidebands, a new ECDL cavity in Littrow configuration (L-ECDL) was built. The frequency at which these sidebands take place is related to its cavity length. The reason for choosing the Littrow configuration is that it enables the design of very short ECDL cavity. As a result, the sidebands are pushed out of our frequency range of interest. Two

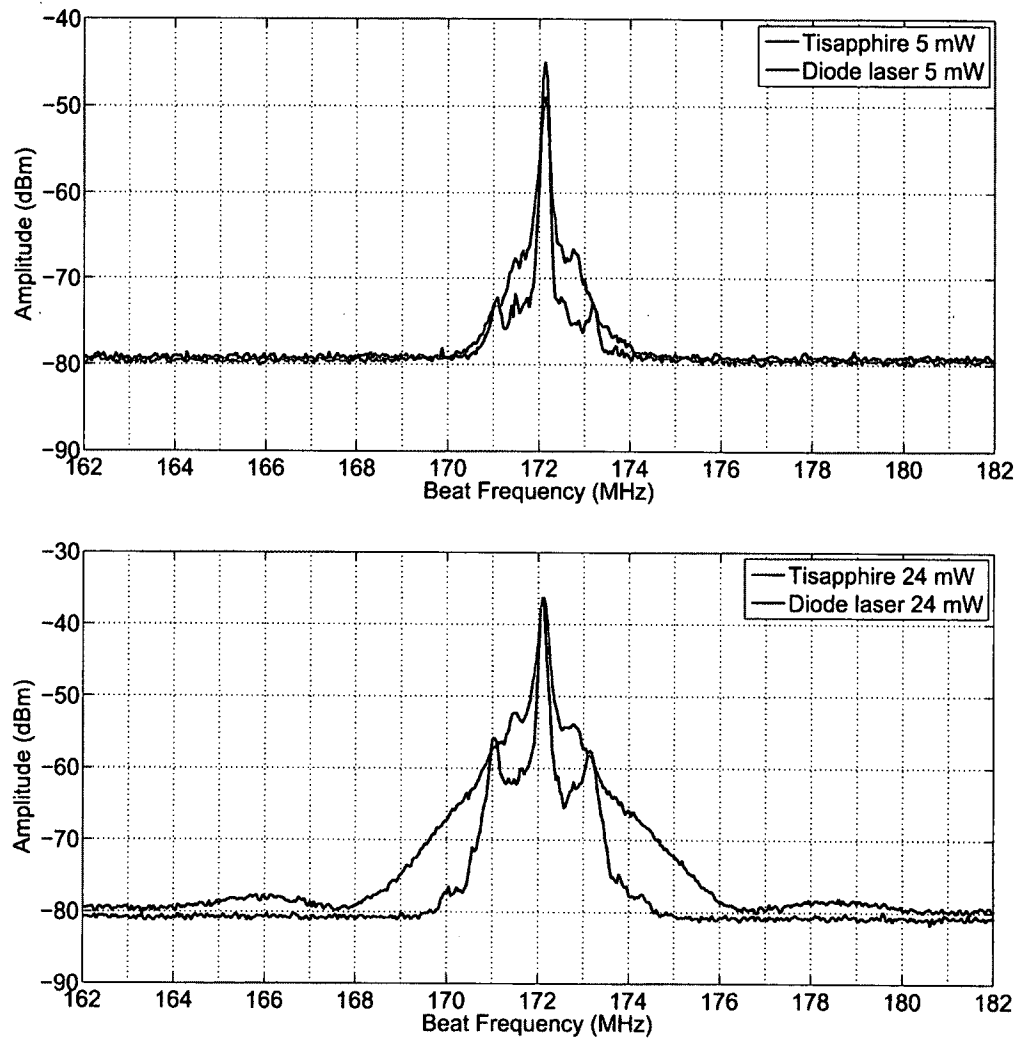


FIG. 56: The graphs show the bandwidth measurements for both the Ti:Sapphire laser and the diode laser. The measurement shows that the diode lasers have higher bandwidth than the Ti:Sapphire laser.

theories were suggested to explain these dips. Either the features were resulted from sideband on the (LM-ECDL) cavity or they were effects from the tapered amplifier spontaneous emission. In all the diode laser scans, the laser beam from the diode was used to seed the tapered amplifier to boost up the PA power. To exclude the second theory, laser from the unseeded tapered amplifier was combined with the Ti:Sapphire laser and sent to the experiment. Since no features appeared on the scans, the first theory became a strong candidate. We tested the scans from the (L-ECDL) against the scans from (LM-ECDL) at the same power and frequency range. Those two tests are shown in Fig. 57. The scans from (L-ECDL) did not show any dip at -3.5 GHz although they were present in the (LM-ECDL) scans. Next, we needed to confirm that the -3.5 GHz was a sideband effect from the (LM-ECDL). That is why artificial sidebands were added to the (L-ECDL) cavity at different frequencies 2.6 GHz and 3.1 GHz using a frequency modulator. The scans were repeated with the artificial sidebands as shown in Fig. 58. It was found that when the 2.6 GHz sideband was introduced, three dips appeared at (2.6 GHz, 5 GHz and at $2*2.6=5.2$ GHz). When the 3.1 GHz sideband was introduced, another three dips appeared at (3.1 GHz, 5 GHz and $2*3.1=6.1$ GHz). When no sidebands were added and the modulation was turned off, only one dip at 5 GHz was introduced. These findings led to the conclusion that the sidebands' effect was very visible on the scans. They can introduce dips at their own frequencies. The second conclusion was that the (L-ECDL) had sidebands at ~ 5 GHz and 10 GHz. Accordingly, our (LM-ECDL) had sidebands that are at ~ -1.7 GHz and -3.4 GHz. Those values were confirmed by calculating the sidebands using the cavity length.

To better understand the effect of the sideband, let us examine Eqn. 97. When the laser scans, it drags behind sidebands at ± 1.7 GHz and ± 3.4 GHz from the main laser frequency. When the main laser frequency hits -1.7 GHz, the positive sideband will be crossing resonance $\delta = 0$. Looking back into the scattering force equation, this will have a very strong scattering force that it does not require much intensity. That is why although the sidebands were not visible on the spectrum analyzer or detected on the wavemeter, their intensities were enough to create those dips. The same argument holds for the 3.4 GHz dip. The question now is why this effect is very visible on the red side and not as strong on the blue side. In other words, when the main laser crosses +1.7 GHz, the sideband is again going through resonance. The answer to that is because of the optical shielding. For the blue side, the ion

production is very weak that all the ion counts are mainly due to the background ion production. In other words, most of the atoms that interact with the PA laser are pushed apart and do not create any ion count. The sideband as well provides an escape channel for the atoms from the trap (atoms are simply kicked out from the trap) which again shields any interaction between them. To summarize, on the red side, the sidebands causes small ion loss while the other red laser frequencies create high counts signal. On the blue side, the sidebands causes small ion loss while the other blue laser frequencies also create small ion counts signal.

For the low power features, we studied the 200 MHz feature. Reproducing this feature was the hardest step. This feature is not spread over a wide range of frequencies as in the case for the -1.7 GHz and -3.4 GHz dips. That is why it required very high frequency calibration and very small and stable step size as we scan the lasers. This was provided using the beat lock design. The scans were done using a 5 MHz frequency step. The feature was tested against different ECDL configurations Fig. 59. It was observed for both LM-ECDL and L-ECDL which suggests an independence on the cavity configuration and hence the cavity sidebands. Also the theory of scattering from the AOM zeroth order was tested. The flashing of the PA beam was done using an AOM which is controlled by an rf switch. The way AOMs work as explained before is that they scatter the input light beam into the first order beam that is frequency shifted from the input zeroth order beam. The problem is that sometime the zeroth order light still leaks through with the first order. This leakage is very small that we can neglect for most cases. The question was whether the feature was a result of the PA AOM zeroth order scattering. We tested that by changing the frequency of the AOM at which the first order is sent from 64 MHz to 84 MHz. Note that the negative first order on the AOM was sent as a PA beam to the experiment. This scans the zeroth order through resonance as the PA frequency scans through the red side frequency. For all the AOM frequency changes, no change in the position where the feature takes place was observed. This is shown in Fig. 59. The third test was made to inspect the effect of the rf discharge where the metastable argon atoms are created. We wanted to know weather or not it was broadcasting rf noise affecting the laser frequency. The frequency of the discharge was changed to 153 MHz. The rf discharge usually runs at 145 MHz. Changing the discharge rf operating frequency further dramatically affects the number of metastable atom production. No effect was observed on the 170 MHz dip from this frequency shift.

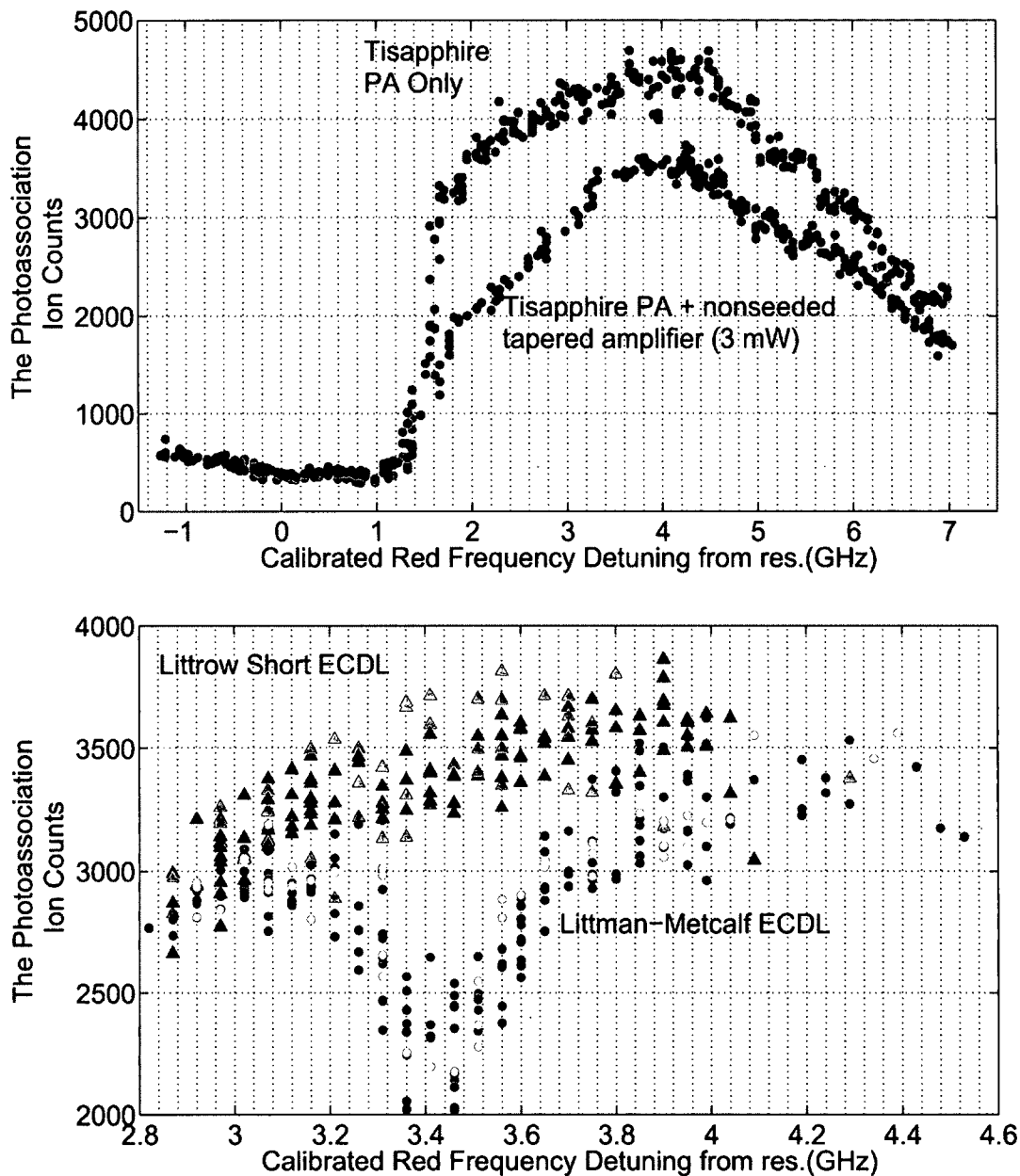


FIG. 57: The first graph shows the check of the scan of the Ti:Sapphire alone (~ 30 mW) against the scan from the Ti:Sapphire combined with the laser of the unseeded tapered amplifier (3 mW). It is apparent that the only effect of the tapered amplifier laser is to deplete the MOT atoms at every frequency. The second graph shows the difference between scans made using (L-ECDL) and (LM-ECDL). Both of the two scans were done using a 100 mW of PA power. Different colors on every curve correspond to different scans to assure the reproducibility of these features.

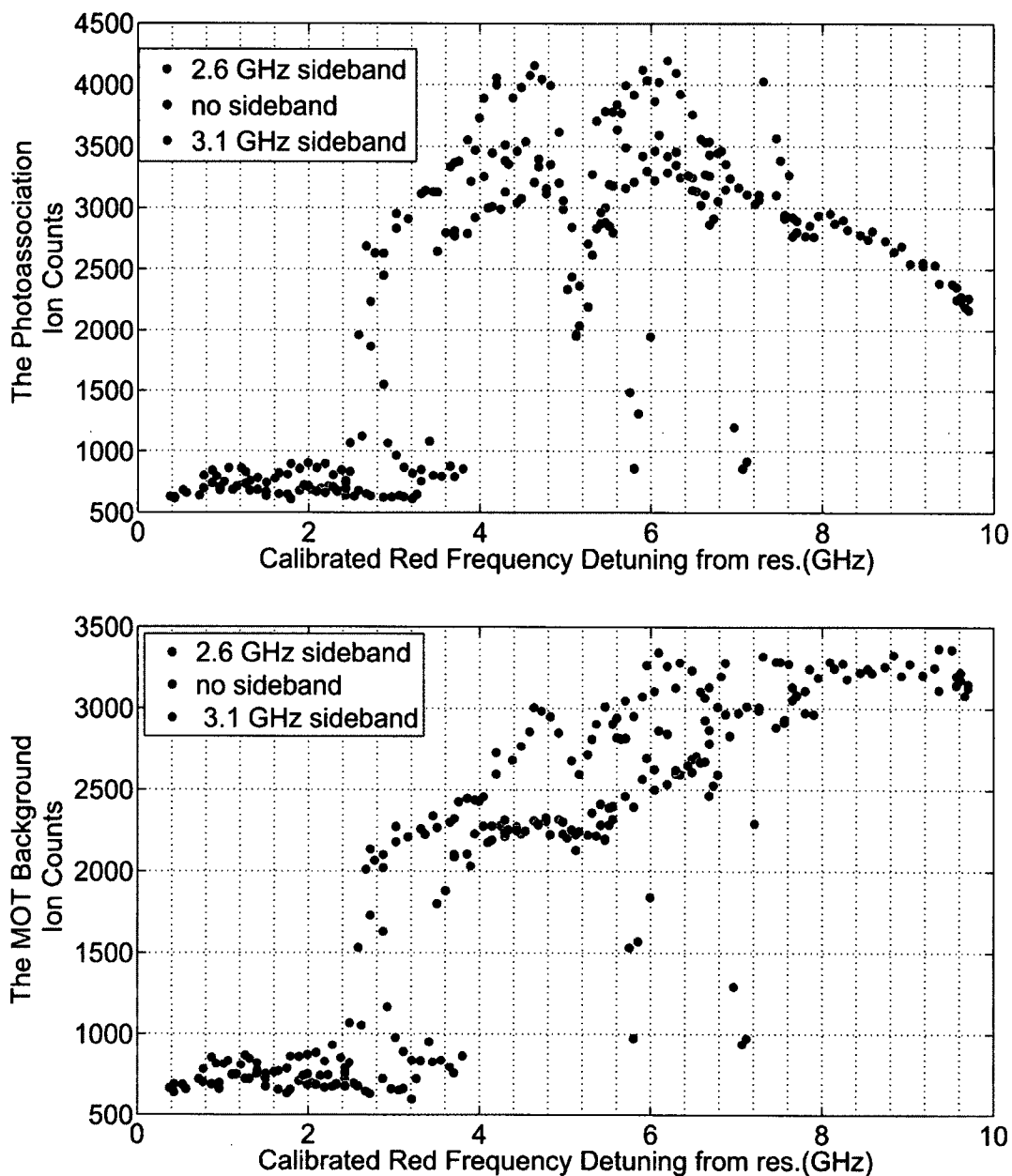


FIG. 58: The graphs show the effect of adding artificial sidebands on the laser in (L-ECDL) versus no sidebands. The blue is for no sidebands where one dip appear at ~ 5 GHz. The red is for adding sidebands at 2.6 GHz where three dips appeared at (~ 2.6 GHz, 5 GHz, 5.8 GHz). The green is for adding sidebands at 3.1 GHz where three dips appeared at (~ 3.1 GHz, 5 GHz, 7 GHz).

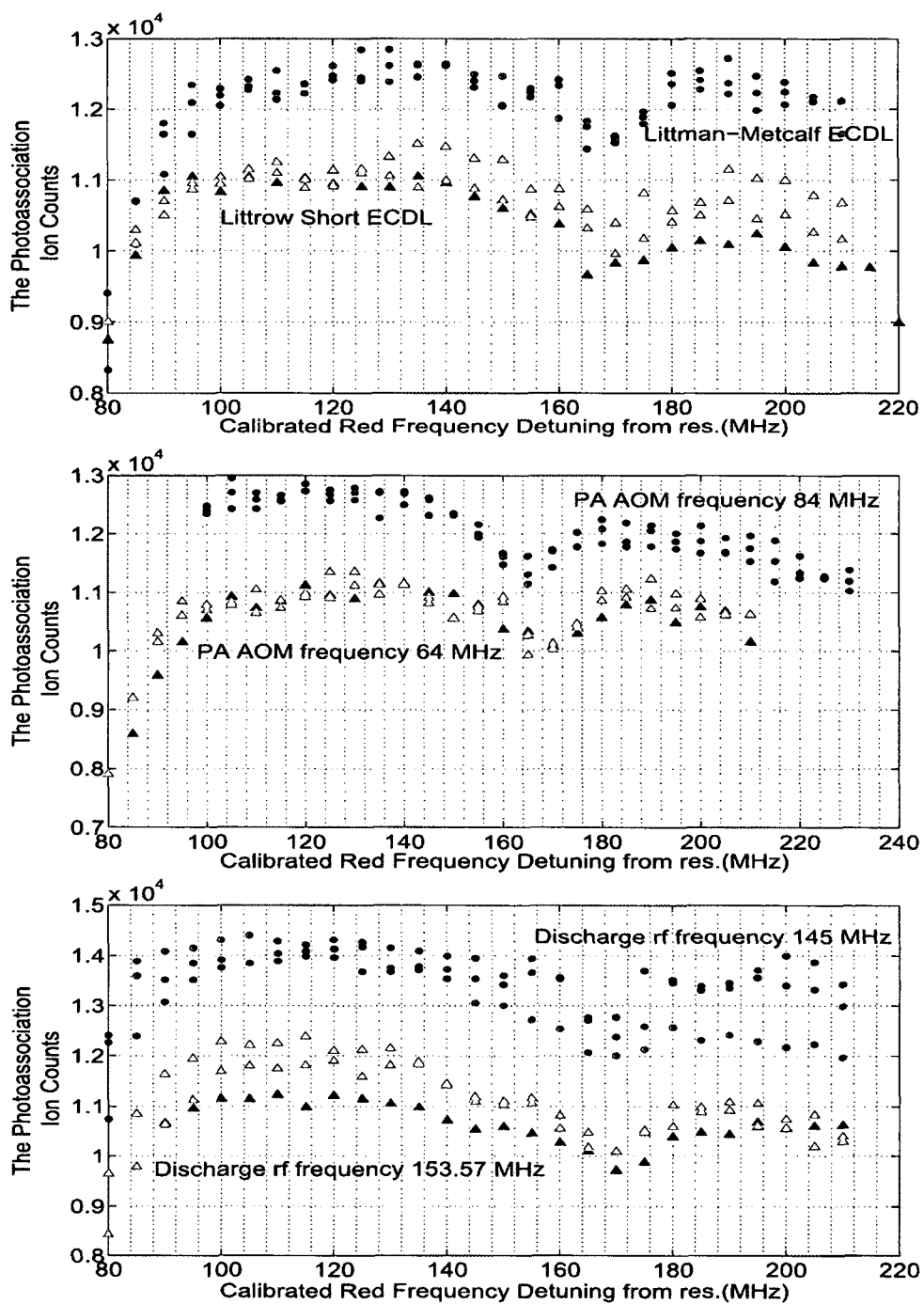


FIG. 59: The graphs show the different tests made on the 170 MHz dip feature. The first graph tested the ECDL cavity effect (Littman-Metcalf versus Littrow). The second graph tested the AOM scattering effect (AOM frequencies 64 MHz and 84 MHz). The third graph tested the rf signal broadcast effect from the rf discharge cell (153 MHz and 145 MHz). Different colors show different scans to guarantee reproducibility of the data.

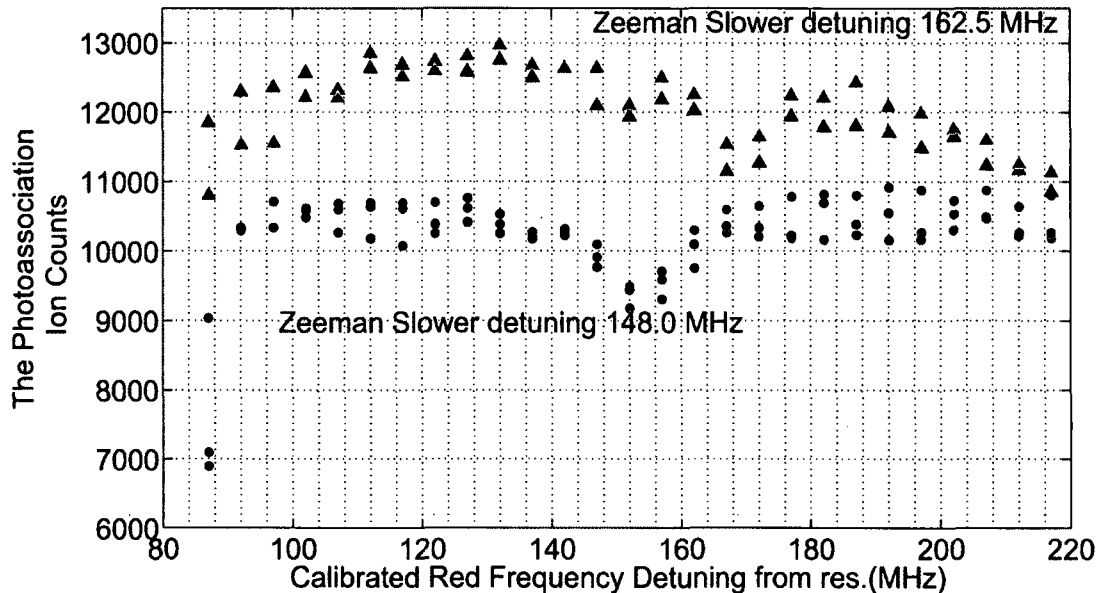


FIG. 60: The graph is used to show the effect of changing the Zeeman slower laser beam detuning on the dip. When the laser beam detuning changes from 162.5 MHz to 148.0 MHz, the dip position is displaced by the same amount.

This is shown in Fig. 59.

Finally, in our timing scheme the Zeeman slower beams are never turned off. The reason for that is, for a flashing Zeeman slower beam, the MOT will need much longer time to load after every single PA shot. This will enormously increase the data acquisition time for the whole scan. Since our Zeeman slower laser beam detuning was -162.5 MHz, a test was done where this frequency was changed. It was found that a frequency shift in the Zeeman slower detuning corresponds to a frequency shift in the feature's position as shown in Fig. 60. This suggests that the feature happens at the same frequency as the Zeeman beam detuning. To test this new theory, a "fake" Zeeman slower beam was sent into the chamber at different frequencies -125 (-140) MHz. The fake Zeeman slower is a beam that was always ON to resemble the effect of the Zeeman slower laser beam. The result of this test is that two dips appeared (at -160 and -125(-140) MHz respectively) as shown in Fig. 61. In the case of the fake Zeeman slower beam being at -140 MHz, the spectrum change appeared as a broadening of the original feature at ~ 160 MHz. It was found that the second dip does not depend on the direction or the angle at which the fake Zeeman beam is sent

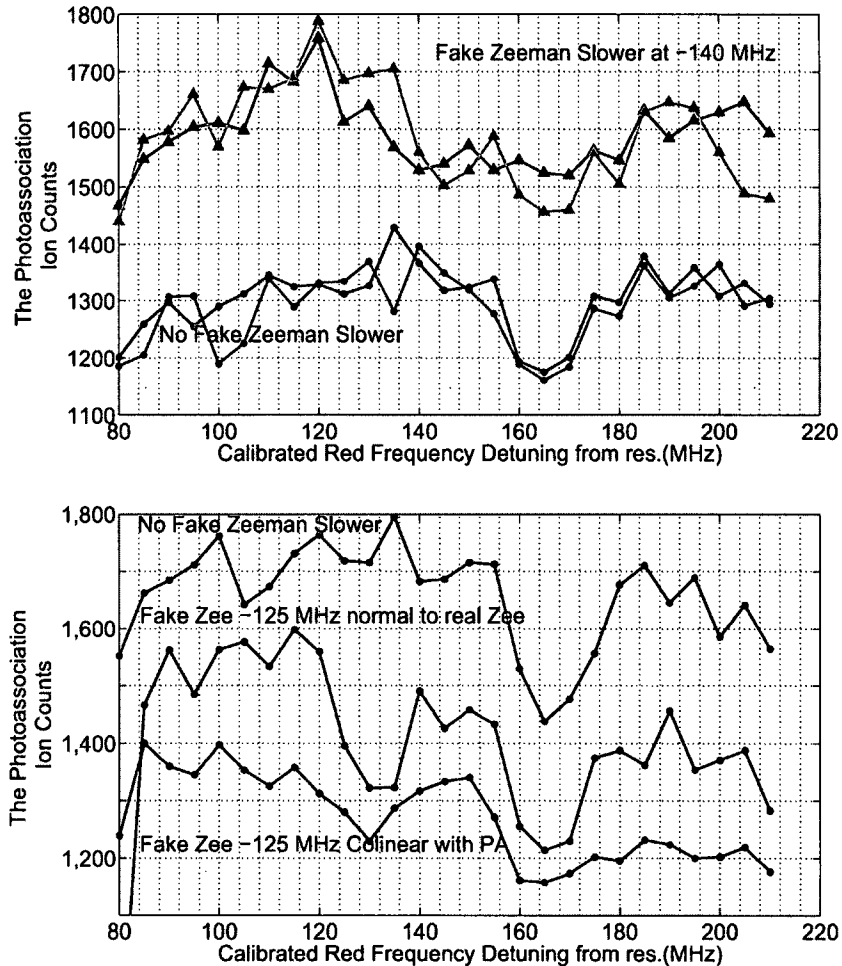


FIG. 61: The graphs show the effect of adding a new laser beam that is always on to resemble the effect of the Zeeman slower laser beam. The “fake” Zeeman beam was set at two different frequencies of -140 MHz for the first graph and at -125 MHz for the second graph. The first graph shows a broadening of the 160 MHz dip which is due to having two dips at -160 MHz and -140 MHz combined together, but not resolved. The second graph shows two separate dips at -160 MHz and -125 MHz. The second graph also shows the angular effect of having the fake Zeeman slower beam at 90° angle to the true Zeeman slower versus having it collinear with the PA laser beam.

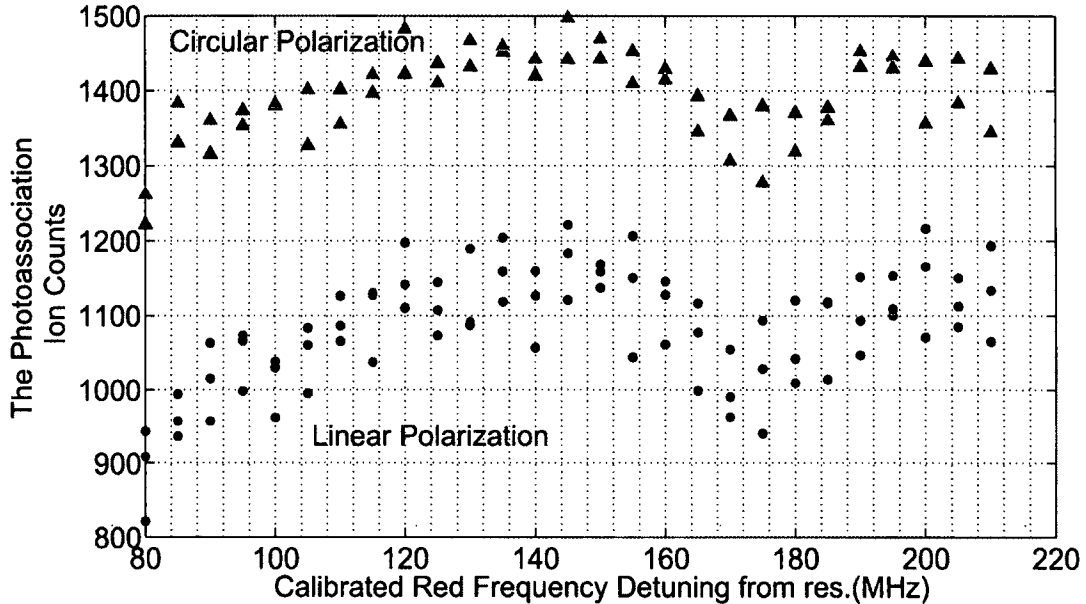


FIG. 62: The graph shows the polarization dependence of the 160 MHz feature. The polarization of the PA beam was changed between linear and circular and no change in the feature was observed.

as shown in Fig. 61. Finally the feature dependence on the PA beam polarization was tested and no polarization dependence was observed as shown in Fig. 62. It is important to note that the error estimation of our data still holds from the first experiment. All the tests were done with the same number of cycles per data point as experiment one. This means that the statistical deviation of the data is ± 100 . This is true for all the scans except for scans shown in Fig. 61. In this scan the number of cycles per data point is much smaller. The deviation of these data can be estimated about ± 25 ion counts.

The Argon PA features experiment conclusion

When we started this experiment, we were trying to track every feature observed in the Fig. 3. The two high intensity features at -1.7 GHz and -3.4 GHz were results from the sidebands on the ECDL cavity. We were able to change their positions by simply changing the cavity length (Littrow (cavity length of 2.8 cm) versus Littman-Metcalf (cavity length of 8.5 cm)). As for the two low intensity features -170 MHz and -80 MHz, only the -170 MHz dip was observed. It was found that this dip is a two color effect. One photon is from the Zeeman slower that is always on and the second

is from the PA photon when it has the same frequency as the Zeeman slower photon. This feature is independent of the direction of the two photons which excludes the four wave mixing explanation. It is also independent of the beam polarization dependence. Unfortunately, the nature of this feature is still undetermined. As for the -80 MHz dip, this dip was only observed once in Fig. 3. We were not able to reproduce this feature even at low intensity and with longer MOT recovery time after each PA shot.

After tracing the origin of all these dips, we can conclude that they were all artifacts of the specific experimental conditions. The next step is to design an experimental set up where we can exclude all of these effects. We can then make a molecular PA scan and try to look for vibrational resonances on the PA spectrum. That is what we are going to show in the next experiment.

4.3 EXPERIMENT 3: CORRECTED PA SPECTRUM FOR BOTH ARGON AND KRYPTON

With all of the knowledge learned from the previous experiments in which the effect of artifacts was conclusively demonstrated, experiment 3 was designed to produce a PA spectrum free from artifacts. In other words, this experiment was aimed to create a clean long scan for both argon and krypton at both high and low PA intensity. The first step in getting these scans was to use the shortest possible ECDL cavity. The reason for that is the short cavity guarantees a far (in frequency terms) sidebands away from our scan limits (from $\sim -5\text{GHz}$ to $\sim +1.5\text{GHz}$). The second modification we made to our experiment was building a long range beat lock where we can scan the PA laser up to 5 GHz. The circuit built was designed to go up to 7 GHz however the frequency signal generated after 5 GHz was not as stable as below 5 GHz. The beat lock did not only enable a PA long scan, but also it enabled a very stable and accurate frequency step in every data point. The stability of the frequency step enabled the conditions of the PA laser to remain constant long enough to build up enough statistics. To describe in detail the experiment statistics, every data point was taken by turning off the MOT trap for 200 μs while the PA laser beam is turned on. For these 200 μs the photon counter is allowed to add up the ion counts generated from the ion detector. After 2000 μs from the beginning of the timing pulse (1800 μs from the MOT turning back on), the second shot comes in and the same cycle repeats. Every data point on the graph results from adding up the ion counts for 2000 cycles from the cycles described before. We wanted to make sure that the MOT returned to its original size before the following shot. That is why right before the MOT is turned off ChB on the photon counter is allowed to add up the number of counts from the ion detector for 200 μs . These counts are added up for 2000 times to get one data point. After each data point is obtained with enough statistics, the beat lock system was moved by the Labview program to the next frequency data point where the whole process starts all over again. For both the low and high power scans, the frequency step was chosen to be 5 MHz. Although going down to 2 MHz frequency step was available, this would have significantly increased the data acquisition time. If we had used 2 MHz step size, we would have run into experiment stability issues. In simplest words, right now with our timing scheme the acquisition time for every data point takes about 2000 cycles \times 2000 μs (the period of every cycle)= 4000 ms. That is in addition to the dead time of the detection

system after the collection of every data point which is 5 ms at least. This could give the reader an estimate about the time required to finish every single scan for a step of 5 MHz versus a step of 2 MHz.

The spatial characteristics for the PA laser beam in this experiment is that the PA beam is coupled through a fiber. It is launched through a fiber launcher with a C260 Thorlabs collimation lens (focal length= 15.29 mm). It takes the beam diameter from 2.5 μm right out from the fiber to 3000 μm . Through 30 cm path the PA laser goes through a couple of mirror reflections into a 400 mm lens. This creates a beam waist at the MOT position of 90 μm (beam diameter of 180 μm). For the intensity calculations, the beam intensity was calculated by $I = 4 * P/(\pi\omega^2)$. The factor of 4 instead of 2 is to count for the retro reflection effect of the PA beam. For the $^{40}\text{Ar}^*$ 811.75 nm transition, the saturation intensity $I_{sat} = 1.44\text{mW}/\text{cm}^2$. For the $^{84}\text{Kr}^*$ 811.51 nm transition, the saturation intensity $I_{sat} = 1.36\text{mW}/\text{cm}^2$. The graphs on the intensity maps for every element are labeled in reference to their intensity. The intensity is expressed in terms of saturation intensity units. The reason for writing the intensity in terms of saturation intensity is that this gives us a measure of how strong the atoms in the MOT feel the effect of the laser. The strength of the effect of a laser on the atoms does not only depend on the laser intensity. It also depends on the detuning of this laser from the resonance transition for the atoms and how fast the atoms decay from the new state. This information is all included in the saturation intensity. For example, when the intensity of the light is much less than the saturation intensity, the atoms' population is mostly in the ground state. On the other hand, for very high intensity much larger than the saturation intensity, the atoms' population is equally distributed between ground and excited state.

The third trick was used to cover the whole frequency range. Since the beat lock was able to cover the range of frequency between 150 MHz and 5000 MHz, AOM shifts had to be used. The shift here means the frequency difference between the reference laser (locked to saturation absorption point or at zero point of frequency) and the PA laser sent through the AOM (for flashing purposes) to the experiment. The PA flashing AOM was fixed at 80 MHz where the positive order was sent to the experiment. The trick was adding another AOM before sending the reference laser to the saturation absorption discharge tube. This AOM will have no effect on the PA beam since it only affects the reference laser. This AOM was set to 190 MHz. Both the negative and the positive first orders of the AOM were used. For the negative

first order, the PA original was put at $+190 \text{ MHz} + \text{the beat frequency} + \text{the PA AOM frequency shift (+80 MHz)}$. This creates a frequency displacement offset of $+270 \text{ MHz}$ between the two lasers. Then, the beat lock starts scanning towards the red (negative) side of frequencies. As for the positive first order of the AOM, this creates a $-190 \text{ MHz} + (\text{the beat lock frequency}) + \text{the PA AOM frequency shift (+80 MHz)}$. This creates a frequency displacement offset of -110 MHz from which the PA laser starts scanning blue (or positive) wise. The reason for going through all this is to ensure same laser conditions all along the PA scan and the change only happens either electronically or on the reference laser path.

The graphs shown in Fig. 63 and 64 are divided into two parts. Part 1) is where the PA laser powers were relatively high. It covered the frequency range between (-5 GHz and $+1.5 \text{ GHz}$). Part 2) is where the PA laser powers were relatively low. It covered the frequency range between (-1.5 GHz and $+0.5 \text{ GHz}$). The graphs show the typical behavior of getting wider PA peaks as we go higher in intensity. This can be explained as being able to populate further detuned states because of the higher intensity. The resolution between the different molecular states was not possible even with our high resolution beat frequency scanning technique. The high resolution between molecular features was expected to appear as a separation between different peaks at different molecular levels. This result is in accordance with results observed from the neon, xenon and krypton PA experiments shown in Fig. 1 and 2. In those experiments, the resolution between different molecular levels was not observed either. The main difference between those PA scans and our experiment performed here is that thanks to the tapered amplifier, we were able to access much higher intensity ranges.

The PA spectrum for both Ar and Kr experiment conclusion.

Our findings can be explained with the help of Fig. 17. In this graph, molecular levels are graphed against internuclear separation distance for both argon and krypton. With our highest intensities obtained in our experiments, we could only populate molecular levels that are up to $\sim 4 \text{ GHz}$ detuned from the atomic resonance transition. It is important to note that we were able to populate the molecular levels in this 4 GHz range. An evidence for that is having higher counts on the red side than the blue side counts along the frequency scan range. A detailed explanation of the ion generation process is in the photoassociation section. The question now is why we were unable to distinguish between every molecular level even with the

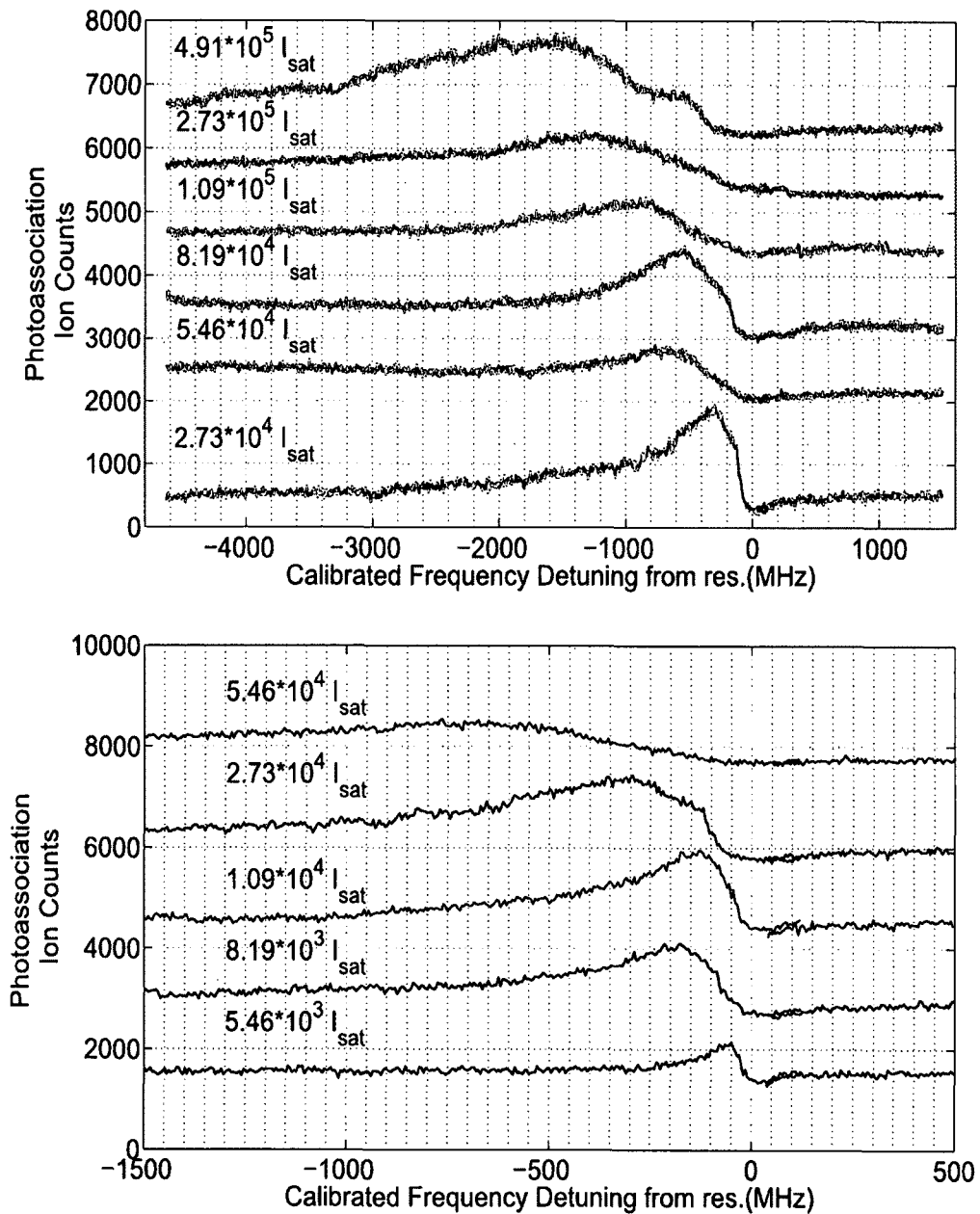


FIG. 63: The graphs show the photoassociation spectrum for argon for higher power limit (top graph) and low power limit (bottom graph). Each single graph is labeled by its own intensity expressed in terms of saturation intensity (1.44 mW/cm^2). The top graph has frequency range between $\sim -5 \text{ GHz}$ and $\sim +1.5 \text{ GHz}$. The bottom graph has frequency limits between -1.5 GHz and $+0.5 \text{ GHz}$.

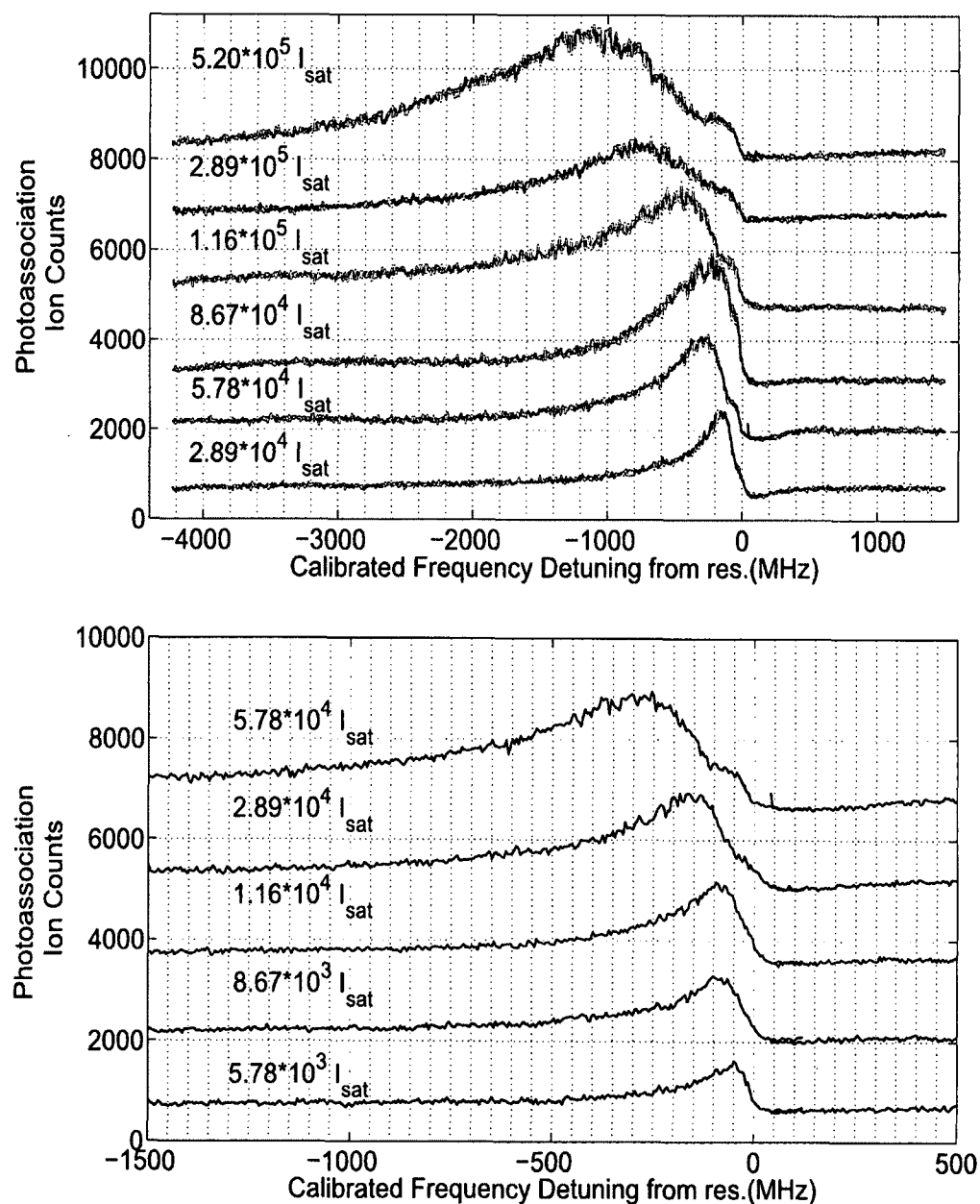


FIG. 64: The graphs show the photoassociation spectrum for krypton for higher power limit (top graph) and low power limit (bottom graph). Each single graph is labeled by its own intensity expressed in terms of saturation intensity (1.36 mW/cm^2). The top graph has frequency range between $\sim -5 \text{ GHz}$ and $\sim +1.5 \text{ GHz}$. The bottom graph has frequency limits between -1.5 GHz and $+0.5 \text{ GHz}$.

high resolution scan technique. Looking at Fig. 17, the molecular levels that can be populated within 4 GHz detuning range are very tightly packed. In other words, the separation between the molecular energy levels is so small that they are merging together to form a molecular energy band. The ion counts created from the excitation to every molecular energy level form a very wide peak that covers the range of the molecular energy band.

It is also noted that as a comparison between argon and krypton, the PA peaks were much wider at the same intensity in Ar compared to Kr. As shown in Fig. 17, the divergence between different molecular energy levels takes place much faster and at much higher internuclear separation in krypton than in argon.

By the end of this experiment we had performed the PA spectrum around the atomic transition $ns[3/2]_2 \rightarrow np[5/2]_3$, where $n=4$ for argon and $n=5$ for krypton. In these spectra, all the vibrational sublevels were washed together. Our detection methods were not able to resolve between different transitions in different vibrational levels. That is why we changed our interest to the PA spectrum around another atomic transition $ns[3/2]_2 \rightarrow np[5/2]_2$. The study of the vibrational sublevels around a different atomic transition might yield an insight on how molecules in those levels are formed.

4.4 EXPERIMENT 4: STUDY OF PURELY LONG RANGE STATES FOR BOTH ARGON AND KRYPTON

Long range states in krypton associated with the $5s[3/2]_2$ to $5p[5/2]_2$ transition were detected in Ref. [2]. Also the calculations of the long range potential in rare gases were shown in Ref. [10]. With all these motivations, an experiment was initiated where we attempted to study long range states in argon and krypton. To recall, the Purely-Long-range (PLR) potential wells are formed as a result of the non-crossings between the molecular potentials. They are very interesting to study since they have a very large inner and outer turning point. In other words, atoms interactions in those states can happen at large internuclear displacement. In fact for the study provided in [2], PLR states were detected as a loss channel in the MOT ion signal at the time of the exposure to the PA light.

In this experiment, the PA light was scanned about the new atomic transition limit between $ns[3/2]_2 \rightarrow np[5/2]_2$ where $n = 4$ for argon and $n = 5$ for the case of krypton. This was a challenge since this transition is strongly coupled to the element's ground state. This means that after the atoms interaction with this beam for a few cycles, they will end up in the atom's ground state (not in the metastable state as in the previous experiments). The only way to capture this atom back into the MOT is to load it back into the rf discharge. Then they have to go through the deceleration process in the Zeeman slower and so on until they end up back in the MOT. Right now, this recycling technique is not used in our system. Using this recycling technique will not affect the duration of loading the MOT atoms back. This means that the closer the PA laser to the atomic transition, the more atoms will escape the MOT trap. This in turn requires longer time for the MOT to reload before we send the next PA signal. As a result, the whole duration of the scan increases.

Different timing schemes were used to ensure that the MOT had enough time to reload after every single PA shot. We also tried allowing the MOT to stay on while the PA light was shined to guarantee constant reloading of the MOT. Also Zeeman slower flashing was tried to eliminate any two color effects on the MOT. Zeeman slower flashing means turning the Zeeman laser light off while the PA light was turned ON. Also the same timing scheme explained in Ref. [2] was tried as shown in Fig. 65. In this scheme, the trap was turned off for $17 \mu\text{s}$ meanwhile the PA is turned on for $5 \mu\text{s}$. Every cycle was repeated after 2 ms. Unfortunately, for all of these techniques no change in the ion signal was detected when the PA light was

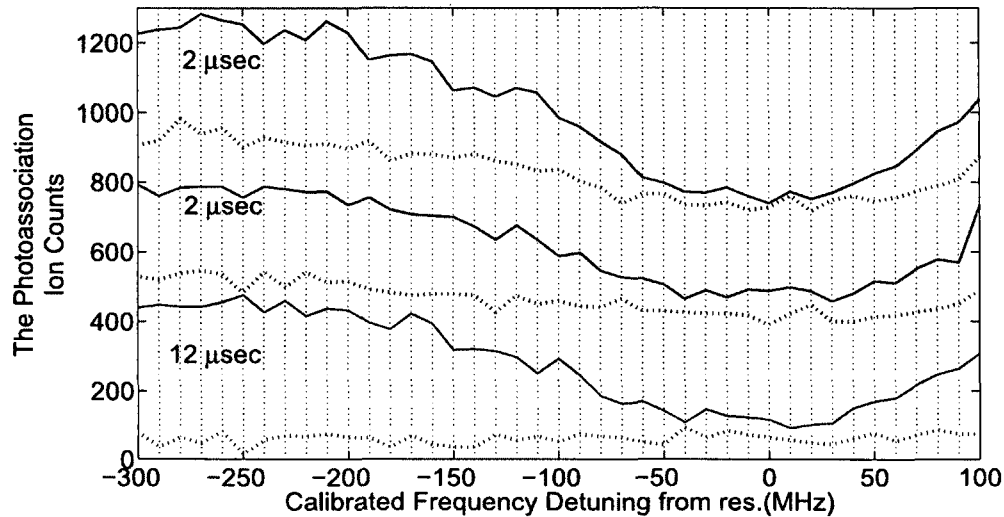


FIG. 65: These scans are using a timing scheme where the trap is turned off for $17 \mu\text{s}$ and the PA is turned on for $5 \mu\text{s}$. The delay between when the trap turns off and the PA turns on was changed between $12 \mu\text{s}$ and $2 \mu\text{s}$. In the graph, the dashed lines are for the PA signal and the solid curves are for the MOT background signal.

turned ON. The only obvious result seen is that as soon as the MOT trap beams are turned off all the ion counts created by the MOT are very small. Later addition of the PA beam only makes the reloading of the MOT after the shot harder. This agrees with the fact that atomic quench transition is a strong transition. The probability of such transition is very high that adding the PA photons simply kills most of the atoms in the MOT by loading them into the ground state. That is why the action of quenching the atoms from the MOT by the PA overwhelms any PLR detection.

Analyzing Fig. 66 where different timing schemes were used in argon, we reached the following conclusions. 1) First, the PA signals which are the dashed line in the graphs show almost constant magnitude. That is consistent with the atoms being killed from the MOT and from the atomic beam as well. The atomic beam is the background metastable atoms that were about to be loaded to the MOT. This PA signal is independent on the PA frequency for example it does not rise higher at certain frequencies. It is always \sim zero. 2) Second, the MOT background signals which are the solid curves were taken originally to measure the effect of the PA on the MOT after it reloads before the next PA shot. The graph shows that as the period of the cycle gets longer the MOT has enough time to reload to its original

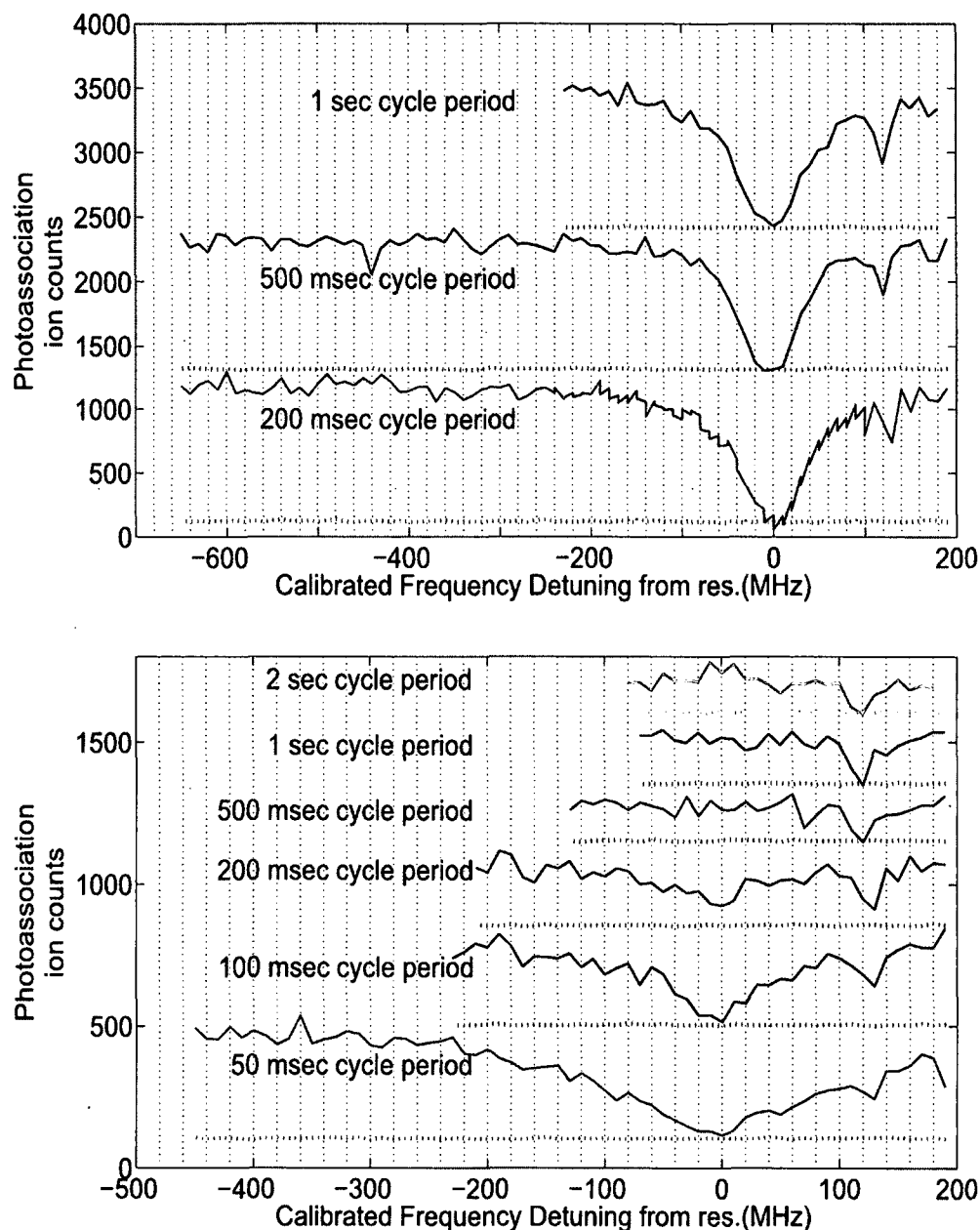


FIG. 66: The graphs show the effect of having a different timing schemes on the PA signal. The dashed lines are almost straight to resemble the PA signal detected. The MOT background signals which are the solid curves show that the MOT recovery time is affected by the PA frequency. Those scans were taken at power of $120 \mu\text{W}$ which corresponds to $5 \times 10^3 I_{sat}$ in intensity terms. It is also important to note that they were taken with no mechanical shutter added. The main difference between the two graphs is in the delay of reading the MOT background counts.

size. This is clear for low frequencies as 2 Hz and 1 Hz. The MOT restores back to its original size even though the PA signal was exactly at resonance frequency. On the graph, this is the point where calibrated frequency detuning was zero MHz. In conclusion, we can say that the PA's light does not create any extra ion signal, as for the MOT it only affects its loading speed. This means that as the PA frequency is closer to resonance, the MOT needs more time to reload after every PA pulse. This is consistent with the PA removing more metastable atoms that could have been reloaded back into the MOT after the end of the PA pulse.

Studying Fig. 66, we can note that almost all the MOT background graphs shows a “dip” in the signal at the $\sim +125$ MHz. This corresponds to the AOM zeroth order. This dip was observable and very strong even after giving the MOT full time to recover from the PA shot and return to its original size. This is apparent in the bottom graph in Fig. 66. It is very important to note that the main difference between the two graphs in Fig. 66 is the delay in reading the MOT background signal. The top graph was mainly focused on measuring how strong was the PA effect on the MOT background signal. The bottom graph was focused on measuring how much did the MOT recover after each shot. The very interesting observation is that even with when the MOT totally recover from the PA resonance signal, it still suffers from a dip at +125 MHz. One of the artifacts that was visual on our spectrum was the effect generated from the AOM zeroth order (0^{th}) scattering. Although this scattering had very small intensity, it still was strong enough to kill the ion counts when it reached resonance. To check that the dip is really generated from the AOM zeroth order, a test was made as shown in Fig. 67. The PA laser was allowed to scan with the AOM turned off so there was absolutely no optical power in the light's first order of the AOM. The result of this test is that the dip still appeared at the same position. This means that the dip was not generated from the first order (1^{st}) of the AOM. This makes sense since the ion counts for the background was collected when the PA light (1^{st} order) was off. Only when the 0^{th} of the AOM was physically blocked that this dip disappeared. The question that might rise now is that why does the 0^{th} order creates an effect on the ion signal but the 1^{st} order does not? The answer to this is that when the 1^{st} order arrives at the MOT, the trap beams were turned off so the original signal is very small. On the other hand, when the 0^{th} order of the AOM effect was measured, the MOT was on and the original ion counts was high. That is why for the rest of the experiment, a beam shutter was added in front

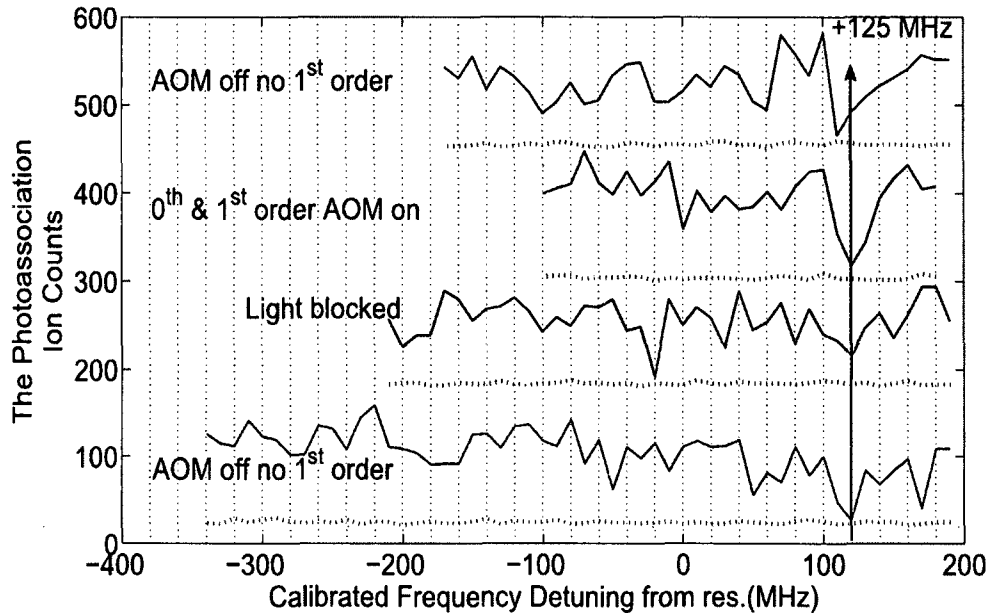


FIG. 67: Those graphs show the effect of the 0^{th} order of the AOM on the MOT background signal. The graph shows the dashed lines as the PA signal which is still a straight line. It also shows the MOT background signal when the AOM is on and off and when the light is blocked. Those scans were taken at PA power of $120 \mu\text{W}$ which corresponds to $5 \times 10^3 I_{\text{sat}}$ in intensity terms.

of the PA beam to block the 0^{th} order from affecting the MOT reloading.

More interactions between the cold atoms sample and the laser beam mean we get better signal statistics. This is why two beam waists were tried. The first one was the focused beam waist at the MOT site $\sim 90 \mu\text{m}$. In this frame we accessed the high intensity limit. Recall that $I = 4P/\pi\omega^2$, so smaller ω means higher I . The second beam waist used was 1.1 mm compared to a MOT size of 0.6 mm in diameter [13]. This means that the beam covered the whole MOT to ensure better number of interaction incidences. In other words, using a larger beam ensures that more atoms will see the PA light. No sign of ion formation was observed.

Another test was used where the MOT evolution along every ON/OFF cycle was studied. Usually, we collected the ion counts when the PA light is on and added them at every single frequency to create data points. In the new technique, the frequency of the PA laser was fixed using the beat lock. Data points were collected at different time bins during the ON/OFF cycle for the MOT using a Multichannel

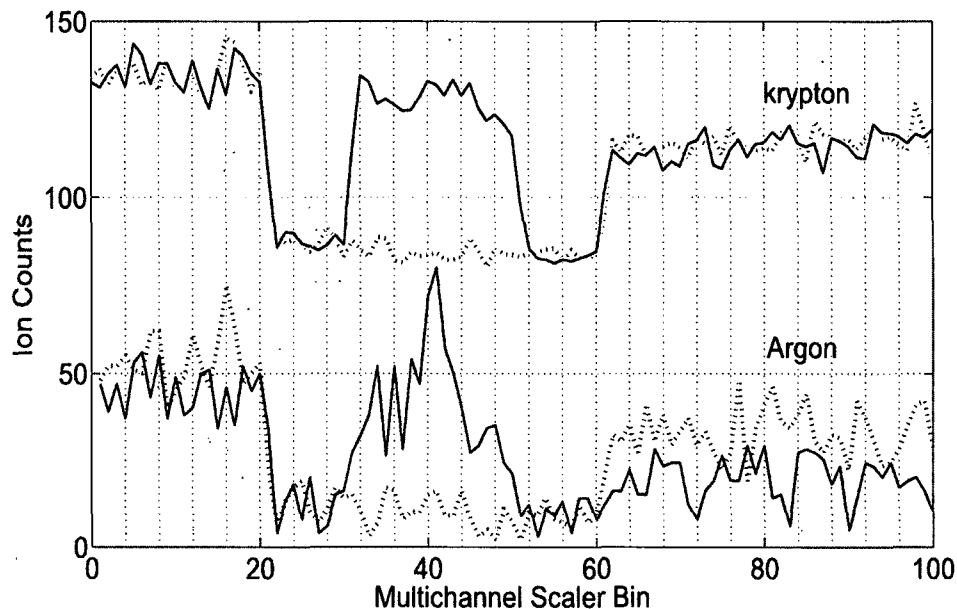


FIG. 68: This graph shows the Multichannel Scaler for both $ns[3/2]_2 \rightarrow np[5/2]_3$ for argon and krypton (red and green respectively) against $ns[3/2]_2 \rightarrow np[5/2]_2$ for argon and krypton (dashed blue and dashed yellow respectively). The timing scheme is trap off at bin 20 and on at bin 60. PA is on at bin 30 and off at bin 50.

Scaler (MCS). The idea was to look for any changes in the ion counts as the PA beam was turned on or off.

Those types of scans were compared for both argon and krypton for both the two atomic transition limits as shown in Fig. 68. The first limit was the $ns[3/2]_2 \rightarrow np[5/2]_3$, where we were able to create PA ion counts as in the previous experiments. It is visible that the PA signal would get stronger as the power of the PA light is higher. The PA signal will also get longer with the longer duration of exposure as shown in Fig. 69. The second limit was the $ns[3/2]_2 \rightarrow np[5/2]_2$ transition, where we are looking for any effects rising from the PA. It is very important to explain the timing schemes shown in the figures. The bin width was fixed at $10.24 \mu\text{s}$ and the MCS was allowed to add 32,767 records to obtain these scans. For all of these scans the MOT was allowed to fully load before turning off the trap beam at bin 20. While it was off, the PA light was turned on at bin 30 and turned back off at bin 50. Later at bin 60, the trap lights were turned back on and the MOT was allowed to reload. By comparing the scans for the two transition, we can see that PA ion

counts are always visual with $ns[3/2]_2 \rightarrow np[5/2]_3$ as in the previous experiments. The strength of its effect changes with the power and the duration of the exposure. As for $ns[3/2]_2 \rightarrow np[5/2]_2$ transition, absolutely no change in the ion counts was detected. The stronger the PA and the longer the exposure gate, the harder it is to reload the MOT.

One of the effects that could change our data is where in the PA laser is parked in terms of frequency. That is why different frequencies were tested for both focused and unfocused beams. Also different PA powers were tested as well. This was the case for both argon and krypton. Some of those scans were shown in Fig. 70 for argon and in Fig. 71 for krypton. These graphs were shown as examples of the data scans that we got for most of our frequency and power space values. For all of the multichannel scaler scans, the error deviation of the ion counts can be approximated about ± 25 .

The PLR in Argon and Krypton experiment conclusion.

In conclusion, we started off this experiment hoping to resolve resonances at the vibrational sublevels on our molecular wells. That is why we performed PAS around this new atomic limit. This experiment was performed about the $ns[3/2]_2 \rightarrow np[5/2]_2$ atomic transition limit instead of $ns[3/2]_2 \rightarrow np[5/2]_3$ which was used for the previous experiment. The downside of this difference is that the new transitions are highly coupled to the atoms' ground state. This means that atoms interacting with the PA light have a higher probability of going to the ground state. This is an atomic transition that does not create ions. In other words, in these types of experiments, there is no balance between the destruction of the MOT ion counts and the PAS ion generation. This of course does not exclude the molecular production probability. It only excludes the ion detection method as a valuable way of detecting the molecular production, which was the similar conclusion stated in Ref. [7]. On the other hand, these findings does not agree with the conclusion of Ref. [2]. For future work, a photon detection method should be added. The molecular production around those atomic limits can be associated with photon emission. Photon detection at different frequencies can be used as a sign of molecules created. This detection method proved to be successful for detecting those states in both helium and krypton [2, 7]. The application of the photon detection method in this experiment may give us information about molecules' formation.

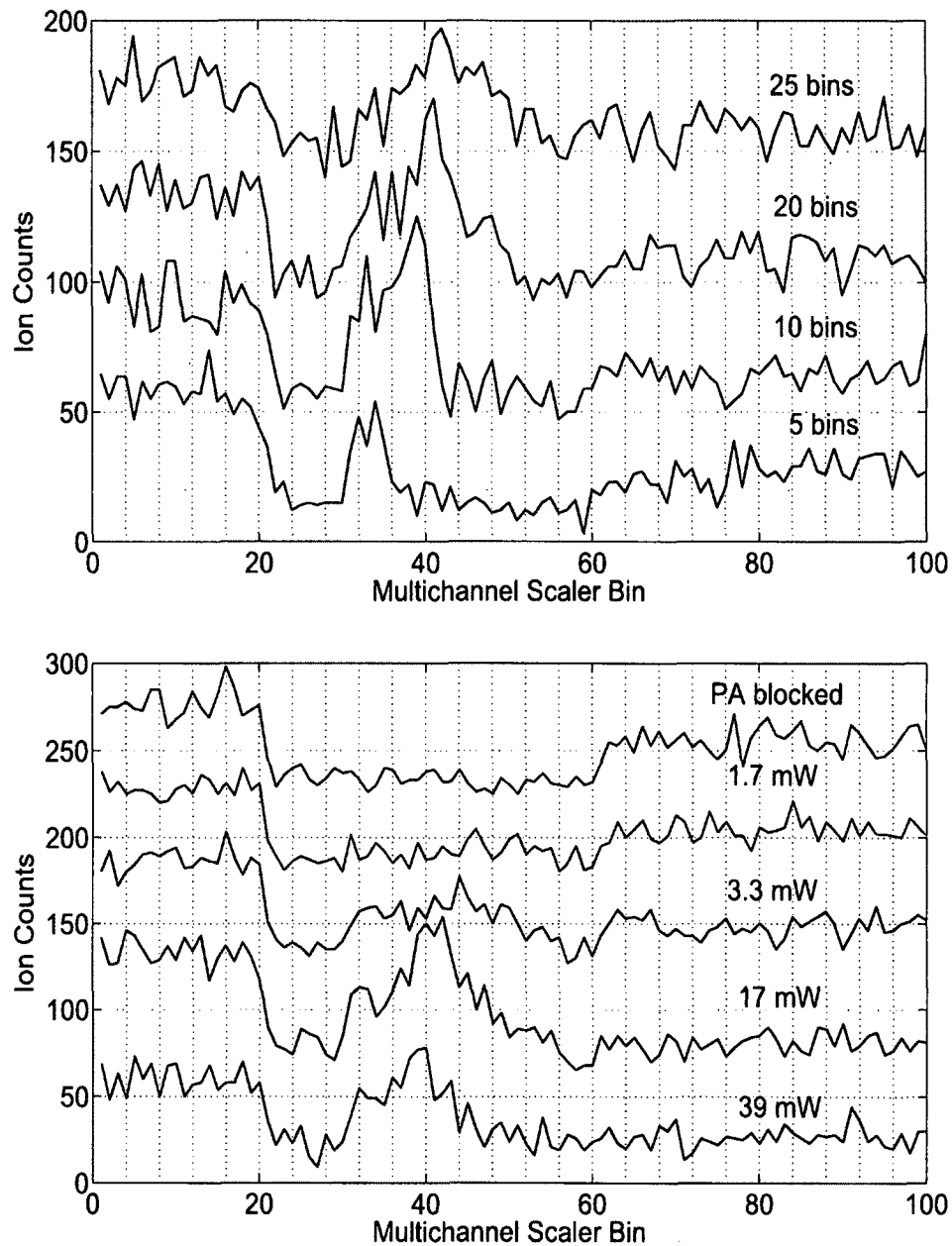


FIG. 69: The graphs show the Multichannel scaler signal as observed in the $4s[3/2]_2 \rightarrow 4p[5/2]_3$ trapping transition for argon. It is a relation between the bin number and the ion counts. The trap beams were turned off at bin 20 and back on at bin 60. The PA was turned on at bin 30. For the top graph the duration of the PA on time was changed. For the bottom graph the PA was turned off at bin 50. For all of these graphs the bin width was $10.24 \mu\text{s}$ and it was allowed to add for 32,767 records.

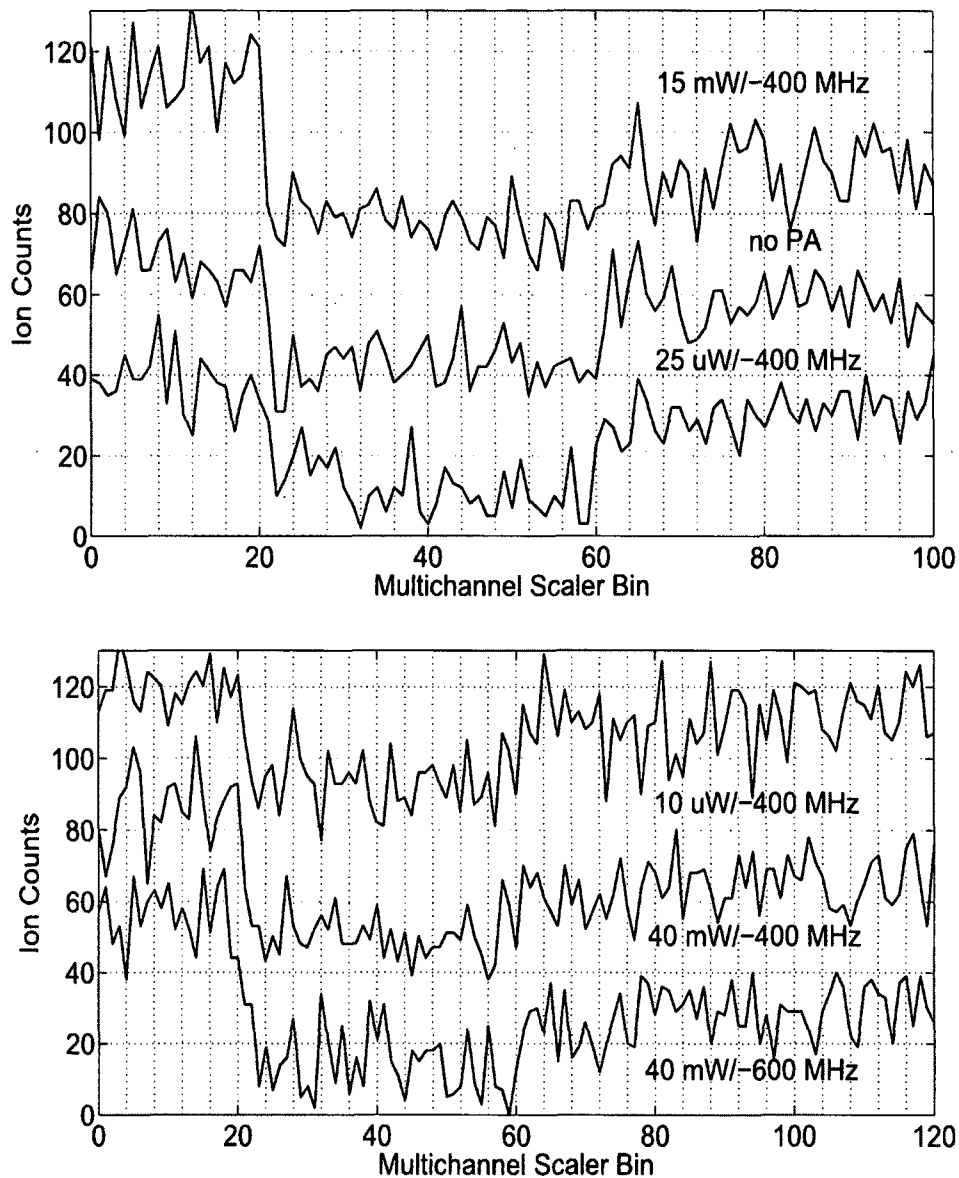


FIG. 70: The graphs show the Multichannel scaler signal for argon. The top graph was taken for focused beam so the beam waist was $90 \mu\text{m}$ and the bottom graph is for unfocused beam so the beam waist was 1.1 mm . The power is shown on the graph as well as the PA frequency detuning while taking the graph. The timing scheme is trap off at bin 20 and on at bin 60. PA on at bin 30 and off at bin 50.

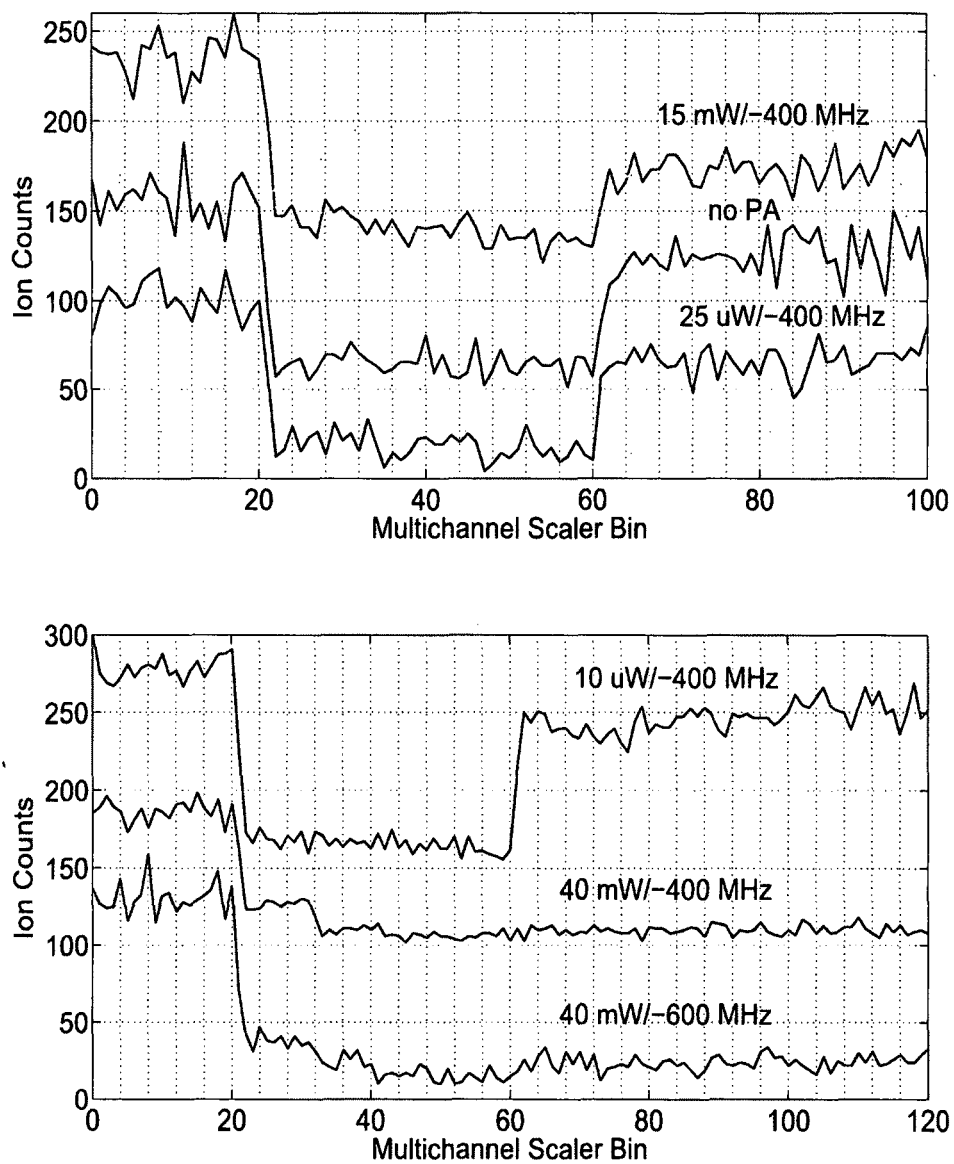


FIG. 71: The graphs show the Multichannel scaler signal for krypton. The top graph was taken for focused beam so the beam waist was $90 \mu\text{m}$ and the bottom graph is for unfocused beam so the beam waist was 1.1 mm . The power is shown on the graph as well as the PA frequency detuning while taking the graph. The timing scheme is trap off at bin 20 and on at bin 60. PA on at bin 30 and off at bin 50.

CHAPTER 5

CONCLUSION AND PROSPECTS FOR THE FUTURE

When we started our research, our goal was to study the features observed in the scans produced in Ref. [1]. After managing to reproduce these features, it is clear now that most of those features originate from atomic transitions in the MOT trapped atoms. As a result of our study, we were able to exclude the artifacts that create such features. Afterwards, we started performing our new PAS for both argon and krypton. We were able to produce PAS free from artifacts for both the two elements, however no vibrational features were resolved on those scans. Motivated by our findings and previous literature studies, we started studying the PLR states. Unfortunately, we were never able to detect any of the molecular resonances.

At the end of our experiments, we gained a better understanding of the experimental system. We can also trace the different effects that could change our spectrum shape. We have designed and built a stable and reliable laser scanning tool (beat lock). With all of these new tools, we can start performing PAS for a dual species MOT. The idea for that is to simultaneously load the MOT with both argon and krypton. Much of the preparation for dual noble gas operation of the apparatus has been completed already, though some additional optical development work is needed. The main challenge that we face in this experiment is that the wavelengths corresponding to the two atomic transitions used in argon and krypton are close. The wavelengths are 811.53 nm for argon and 811.29 nm for krypton. This makes the combination of the two beams to form the trap and the Zeeman slower light not trivial. This is because this combination has to maintain the correct polarization and with minimal loss of power. We have managed to establish a design to combine the two beams together which will be tested in the following months.

As soon as we have the new dual Ar^*/Kr^* MOT, we can perform PAS and search for evidence of excitation to excited states of the ArKr molecule. In this dissertation, we have covered the PA spectra for two interacting argon atoms or two interacting krypton atoms. When we fold in the dual species interaction spectrum, we can distinguish between features from the homonuclear and heteronuclear molecules.

This in turn can yield information about the virtually unstudied structure of these molecular states. It will also help us study of the dynamics of the PA process.

We also plan to begin a search for the production of ground state Ar₂, Kr₂ and ArKr using multi photon techniques. These techniques are now being developed in separate experiments in our research laboratory.

BIBLIOGRAPHY

- [1] M. K. Shaffer, G. Ranjit, C. I. Sukenik, and M. Walhout, *Phys. Rev. A* **83** (2011).
- [2] Z. S. Smith, A. Harmon, J. Banister, R. Norman, K. H. Pot, and M. Walhout, *Phys. Rev. A* **81**, 013407 (2010).
- [3] K. A. Suominen, K. Burnett, P. S. Julienne, M. Walhout, C. O. U. Sterr, M. Hoogerland, and S. L. Rolston, *Phys. Rev. A* **53** (1996).
- [4] R. D. Glover, J. E. Calvert, D. E. Laban, and R. T. Sang, *J. Phys. B: At. Mol. Opt. Phys.* **44**, 245202 (2011).
- [5] H. Katori and F. Shimizu, *Phys. Rev. Lett* **73** (1994).
- [6] N. Herschbach, P. J. J. Toll, W. Vassen, W. Hogervost, G. Woestenenk, J. W. Thomsen, P. van der Straten, and A. Niehaus, *Phys. Rev. Lett* **84** (2000).
- [7] J. Leonard, M. Walhout, A. P. Mosk, T. Muller, M. Leduc, and C. Cohn-Tannoudji, *Phys. Rev. Lett* **91** (2003).
- [8] H. J. Metcalf and P. van der Straten, *Laser Cooling and Trapping* (Springer-Verlag Inc., New York, 1999).
- [9] B. H. Bransden and C. J. Joachain, *Physics of Atoms and Molecules* (John Wiley & Sons. Inc., New York, 1983).
- [10] E. J. D. Vredenbregt, J. G. C. Tempelaars, H. C. W. Beijerinck, and B. J. Verhaar, *Phys. Rev. A* **57** (1998).
- [11] M. K. Shaffer, Ph.D. thesis, Old Dominion University (2008).
- [12] M. T. Bell and T. P. Softley, *Mol. Phys.* **107** (2009).
- [13] H. C. Busch, Ph.D. thesis, Old Dominion University (2004).
- [14] C. J. Foot, *Atomic Physics. Oxford Master Series in Atomic, Optical and Laser Physics* (Oxford University Press, New York, 2005).

- [15] T. P. Inc, *Specifications & Configurations High Power Diode Lasers and Amplifiers*, Toptica, New York (2009).
- [16] G. Ranjit, Ph.D. thesis, Old Dominion University (2010).
- [17] V. Bagnato, L. Marcassa, C. Tsao, Y. Wang, and J. Weiner, *Phys. Rev. Lett.* **70**, 3225 (1993).
- [18] C. M. Dion, C. Drag, O. Dulieu, B. Laburthe Tolra, F. Masnou-Seeuws, and P. Pillet, *Phys. Rev. Lett.* **86**, 2253 (2001).
- [19] C. Degenhardt, T. Binnewies, G. Wilpers, U. Sterr, F. Riehle, C. Lisdat, and E. Tiemann, *Phys. Rev. A* **67**, 043408 (2003).
- [20] C. Drag, B. Tolra, O. Dulieu, D. Comparat, M. Vatasescu, S. Boussen, S. Guibal, A. Crubellier, and P. Pillet, *Quantum Electronics, IEEE Journal of* **36**, 1378 (2000).
- [21] S. B. Nagel, P. G. Mickelson, A. D. Saenz, Y. N. Martinez, Y. C. Chen, T. C. Killian, P. Pellegrini, and R. Côté, *Phys. Rev. Lett.* **94**, 083004 (2005).
- [22] Y. Takasu, K. Komori, K. Honda, M. Kumakura, T. Yabuzaki, and Y. Takahashi, *Phys. Rev. Lett.* **93**, 123202 (2004).
- [23] L. P. Ratliff, M. E. Wagshul, P. D. Lett, S. L. Rolston, and W. D. Philips, *Chem. Phys.* **101** (1994).
- [24] H. R. Thorsheim, J. Weiner, and P. S. Julienne, *Phys. Rev. Lett.* **58** (1987).
- [25] E. R. I. Abraham, W. I. McAlexander, H. T. C. Stoof, and R. G. Hulet, *Phys. Rev. A* **53**, 3092 (1996).
- [26] U. Schlöder, C. Silber, T. Deuschle, and C. Zimmermann, *Phys. Rev. A* **66**, 061403 (2002).
- [27] A. Amelink, K. M. Jones, P. D. Lett, P. v. d. Straten, and H. G. M. Heideman, *Phys. Rev. A* **62**, 013408 (2000).
- [28] A. Amelink, K. M. Jones, P. D. Lett, P. v. d. Straten, and H. G. M. Heideman, *Phys. Rev. A* **61**, 042707 (2000).

- [29] L. E. E. de Araujo, J. D. Weinstein, S. D. Gensemer, F. K. Fatemi, K. M. Jones, P. D. Lett, and E. Tiesinga, *Journal of Chemical Physics* **119**, 2062 (2003), ISSN 00219606.
- [30] F. K. Fatemi, K. M. Jones, P. D. Lett, and E. Tiesinga, *Phys. Rev. A* **66**, 053401 (2002).
- [31] P. D. Lett, K. Helmerson, W. D. Phillips, L. P. Ratliff, S. L. Rolston, and M. E. Wagshul, *Phys. Rev. Lett.* **71**, 2200 (1993).
- [32] J. P. Shaffer, W. Chalupczak, and N. P. Bigelow, *Phys. Rev. Lett.* **83**, 3621 (1999).
- [33] H. R. Thorsheim, J. Weiner, and P. S. Julienne, *Phys. Rev. Lett.* **58**, 2420 (1987).
- [34] J. P. Burke, C. H. Greene, J. L. Bohn, H. Wang, P. L. Gould, and W. C. Stwalley, *Phys. Rev. A* **60**, 4417 (1999).
- [35] A. N. Nikolov, J. R. Ensher, E. E. Eyler, H. Wang, W. C. Stwalley, and P. L. Gould, *Phys. Rev. Lett.* **84**, 246 (2000).
- [36] H. Wang and P. Gould, *Journal of Chemical Physics* **106**, 7899 (1997), ISSN 00219606.
- [37] C. Amiot, O. Dulieu, R. F. Gutterres, and F. Masnou-Seeuws, *Phys. Rev. A* **66**, 052506 (2002).
- [38] *The European Physical Journal D - Atomic, Molecular, Optical and Plasma Physics* **11** (2000), ISSN 1434-6060.
- [39] *The European Physical Journal D - Atomic, Molecular, Optical and Plasma Physics* **5** (1999), ISSN 1434-6060.
- [40] *The European Physical Journal D - Atomic, Molecular, Optical and Plasma Physics* **21** (2002), ISSN 1434-6060.
- [41] R. A. Cline, J. D. Miller, and D. J. Heinzen, *Phys. Rev. Lett.* **73**, 2636 (1994).

- [42] T. Mullins, W. Salzmann, S. Götz, M. Albert, J. Eng, R. Wester, M. Weidemüller, F. Weise, A. Merli, S. M. Weber, et al., *Phys. Rev. A* **80**, 063416 (2009).
- [43] A. Merli, F. Eimer, F. Weise, A. Lindinger, W. Salzmann, T. Mullins, S. Götz, R. Wester, M. Weidemüller, R. Ağanoglu, et al., *Phys. Rev. A* **80**, 063417 (2009).
- [44] H. C. Mastwijk, J. W. Thomsen, P. van der Straten, and A. Niehaus, *Phys. Rev. Lett* **80** (1998).
- [45] K. J. Matherson, R. D. Glover, D. E. Laban, and R. T. Sang, *Phys. Rev. A* **78**, 042712 (2008).
- [46] K. J. Matherson, R. D. Glover, D. E. Laban, and R. T. Sang, *Rev. of Sci. Instr.* **78**, 073102 (2007).
- [47] M. Walhout, U. Sterr, C. Orzel, M. Hoogerland, and S. L. Rolston, *Phys. Rev. Lett* **74** (1995).
- [48] J. Weiner, V. S. Bagnato, S. Zilio, and P. S. Julienne, *Rev. Mod. Phys.* **71**, 1 (1999).
- [49] H. Metcalf and P. van-der Straten, *Journal of Opt. Soc.* **20**, 887 (2003).
- [50] G. W. F. Drake, *Springer Handbook of Atomic, Molecular, and Optical Physics* (Springer Science & Business Media, USA, 2006).
- [51] W. D. Phillips and H. Metcalf, *Physical review letters* **48** (1981).
- [52] Z. Xiong, Y. Long, H. Xiao, X. Zhang, L. He, and B. Lu, *Chinese Optical letters* **9** (2011).
- [53] G. E. Marti, R. Olf, E. Vogt, A. Ottl, and D. M. Stamper-Kurn, *Physical review letters* **81** (2010).
- [54] M. Bober, J. Zachorowski, and W. Gawlik, *Optica Applicata* **XL** (2010).
- [55] T. C. Killian, T. Pattard, T. Pohl, and J. M. Rost, *Phys. Rep.* **449**, 77 (2007).
- [56] J. Weiner, V. S. Bagnato, S. Zilio, and P. S. Julienne, *Rev. of Mod. Phys.* **71** (1999).

- [57] P. D. Lett, W. D. Phillips, S. L. Rolston, C. E. Tanner, R. N. Watts, and C. Westbrook, *J. Opt. Soc. Am. B* **6** (1989).
- [58] L. H. S. Chu, J. E. Bjorkhilm, A. Cable, and A. Ashkin, *Physical review letters* **55** (1985).
- [59] J. Dalibard and C. Cohentannoudji, *Journal of Opt. Soc.* **6**, 2023 (1989).
- [60] E. L. Raab, M. Prentiss, A. Cable, S. Chu, and D. E. Pritchard, *Phys. Rev. Lett.* **59** (1987).
- [61] W. Vassen, C. Cohen-Tannoudji, M. Leduc, D. Boiron, C. I. Westbrook, A. Truscott, K. Baldwin, G. Birkl, P. Cancio, and M. Trippenbach, *Rev. Mod. Phys.* **84**, 175 (2012).
- [62] K. M. Jones, E. Tiesinga, P. D. Lett, and P. S. Julienne, *Rev. of Modern Physics* **78**, 423 (2006).
- [63] J. I. Steinfeld, *An Introduction to Modern Molecular Spectroscopy* (The MIT Press, Cambridge, Massachusetts, 1985).
- [64] H. Lefebvre-Brion and R. W. Field, *The Spectra and Dynamics of Diatomic Molecules* (Elsevier Inc., San Diego, CA, 2004).
- [65] G. Herzberg, *Molecular Spectra and Molecular Structure* (Krieger Publishing Company, Malabar, Florida, 1991).
- [66] J. Goodisman and E. Loebl, *Diatomic Interaction Potential Theory: Applications* (Academic Press, New York, 2013), ISBN 9781483191645.
- [67] J. Brown and A. Carrington, *Rotational Spectroscopy of Diatomic Molecules* (Cambridge University Press, UK, 2003).
- [68] R. LeRoy and R. B. Bernstein, *J. Chem. Phys.* **52**, 3869 (1970).
- [69] R. J. LeRoy, *Semiclassical Methods in Molecular Scattering and Spectroscopy* (Reidel, Dordrecht, 1980).
- [70] M. R. Winchester and R. Payling, *Spec. Acta part B* **59**, 607 (2004).

- [71] B. E. Bernacki, P. R. Hemmer, S. P. Smith, and S. Ezekiel, *Opt. Lett.* **13**, 725 (1988).
- [72] B. Dahmani, L. Hollberg, and R. Drullinger, **12**, 876 (1987).
- [73] M. de Labachellerie and P. Cerez, *Opt. Commun.* **55**, 174 (1985).
- [74] G. Tino, L. Hollberg, A. Sasso, M. Inguscio, and M. Barsanti, *Phys. Rev. Lett* **64**, 2999 (1990).
- [75] J. Sell, W. Miller, D. Wright, B. V. Zhdanov, and R. Knize, *Appl. Phys. Lett.* **16** (1991).
- [76] M. G. Littman and H. J. Metcalf, *Appl. Opt* **17**, 2224 (1978).
- [77] K. C. Harvey and C. J. Myatt, *OPTICS LETTERS* **16** (1991).
- [78] W. M. Wang, K. T. V. Grattan, A. W. Palmer, and W. J. O. Boyle, *Journal of lightwave technology* **12** (1994).
- [79] K. Wall and A. Sanchez, *Journal of lightwave technology, The Lincoln Laboratory Journal* **3** (1990).
- [80] S. M. K., R. G. G., and C. I. Sukenik, *Review Of Scientific Instruments* **79**, 046102 (2008).
- [81] P. D. Lett, P. S. Julienne, and W. D. Phillips, *Annu. Rev. Phys. Chem.* **64**, 423 (1995).
- [82] S. Kato, R. Yamazaki, K. Shibata, R. Yamamoto, H. Yamada, and Y. Takahashi, *Phys. Rev. A* **86**, 043411 (2012).

VITA

Maha Khaled Omar
Department of Physics
Old Dominion University
Norfolk, VA 23529

Education

Ph.D. in Physics, Old Dominion University, Norfolk, VA, May 2015.

M.S. in Physics, Old Dominion University, Norfolk, VA, May 2012.

B.SC in Physics, Tanta University, Egypt, May 2006.

Experience

Graduate Research Assistant in Physics Department in Old Dominion University, Norfolk, VA, May 2009 to present.

Teaching Assistant in Physics Department in Old Dominion University, Norfolk, VA, 2009 to May 2010 and from May 2012 to present.

Graduate Assistant in Physics Department, Tanta University, Egypt, From September 2006 to September 2008.

Teaching Assistant in Physics Department, Tanta University, Egypt, From September 2006 to September 2008.